

**EVOLUTION AND CONTROL OF COUPLED FLOW SEPARATION  
AND STREAMWISE VORTICITY CONCENTRATIONS WITHIN  
OFFSET DIFFUSERS**

A Dissertation  
Presented to  
The Academic Faculty

by

Travis John Burrows

In Partial Fulfillment  
of the Requirements for the Degree  
Doctor of Philosophy in Mechanical Engineering in the  
Woodruff School of Mechanical Engineering

Georgia Institute of Technology  
December 2020

**COPYRIGHT © 2020 BY TRAVIS J. BURROWS**

**EVOLUTION AND CONTROL OF COUPLED FLOW SEPARATION  
AND STREAMWISE VORTICITY CONCENTRATIONS WITHIN  
OFFSET DIFFUSERS**

Approved by:

Dr. Ari Glezer, Advisor  
School of Mechanical Engineering  
*Georgia Institute of Technology*

Dr. Bojan Vukasinovic  
School of Mechanical Engineering  
*Georgia Institute of Technology*

Dr. Devesh Ranjan  
School of Mechanical Engineering  
*Georgia Institute of Technology*

Dr. James Mace  
Technical Fellow  
*The Boeing Company*

Dr. Timothy Lieuwen  
School of Aerospace Engineering  
*Georgia Institute of Technology*

Date Approved: August 14, 2020

## ACKNOWLEDGEMENTS

First and foremost, I would like to thank my thesis advisor, Dr. Ari Glezer, who to the very end pushed me to work harder. Dr. Bojan Vukasinovic, thank you for in the early years teaching me so much about experimental methods and troubleshooting, and in the later years guiding me on technical writing. Thank you to my other committee members Dr. Timothy Lieuwen, Dr. Devesh Ranjan, and Dr. James Mace for providing your time and perspective for guiding my thesis proposal and defense. Dr. Slava Yorish, I am indebted to you for all the times you helped me solve experimental problems.

I could not have made it without the support and comradery of my fellow students in FMRL and ME. Dr. Tom Lambert, thanks for inspiring me to get better at programming. Dr. Tom Boziuk, thanks for being a reliable coffee-making partner. Sourabh Jha and Yuehan Tan, thanks for always being willing to help with experiments. I could not have gotten through quals without Mason Chilmoneczyk, Peter Griffiths, Curtis Peterson and Alon Katz. Thanks also to Derek Nichols, Edward Lee, York Huang, and Gabriel Peyredieu Du Charlat.

Thanks to my family for supporting me through this endeavor and the many steps it took to get here. Lastly, thanks to my wife Sam Petti, who has been a constant source of encouragement.

Support from the Office of Naval Research, monitored by Dr. Steve Martens, is gratefully acknowledged.

# TABLE OF CONTENTS

<b>ACKNOWLEDGEMENTS</b>	<b>iii</b>
<b>LIST OF TABLES</b>	<b>vi</b>
<b>LIST OF FIGURES</b>	<b>vii</b>
<b>LIST OF SYMBOLS AND ABBREVIATIONS</b>	<b>xxi</b>
<b>SUMMARY</b>	<b>xxiv</b>
<b>CHAPTER 1. Introduction</b>	<b>1</b>
1.1 Thesis Structure	3
1.2 Offset Diffuser Flow Physics	4
1.3 Technical Rationale of the Present Investigations	5
1.4 Literature Review	7
1.4.1 Inlet Flows	7
1.4.2 Passive Flow Control in Diffusers	7
1.4.3 Active Flow Control in Diffusers	9
1.4.4 Hybrid Flow Control in Diffusers	11
1.4.5 Trapped Vorticity Flow Control in Diffusers	13
1.4.6 Flow Control in Inlets	14
<b>CHAPTER 2. Experimental Setup and Methodology</b>	<b>16</b>
2.1 The Wind Tunnel	16
2.2 Diffuser Test Sections	19
2.3 Diagnostics	21
2.3.1 Pressure Measurements	21
2.3.2 Pressure Sensitive Paint	27
2.3.3 Particle Image Velocimetry	31
2.3.4 Surface Oil-flow Visualization	36
2.3.5 Uncertainty	37
2.4 Flow Control Techniques	38
2.4.1 Fluidic Oscillating Jets	39
2.4.2 Aerodynamic Bleed	40
<b>CHAPTER 3. Offset Diffuser</b>	<b>42</b>
3.1 Introduction	42
3.2 Characterization of the Base Flow in the Presence of the Surface Recess	45
3.3 Effects of Jet Actuation Coupled with the Wall Recess	51
3.4 Effects of Actuation on the Diffuser's Boundary Layer	57
3.5 Flow Control Optimization	65
<b>CHAPTER 4. Serpentine Diffuser</b>	<b>76</b>
4.1 Introduction	76
4.2 Characterization of the Base Flow	78



<b>4.3</b>	<b>Flow Control Effects</b>	<b>87</b>
<b>4.4</b>	<b>Effects of the Width of the Actuator Array</b>	<b>91</b>
4.4.1	The Time-Averaged Flow	91
4.4.2	Dynamic Effects	102
<b>CHAPTER 5.</b>	<b>Transonic Shock in a Serpentine Diffuser</b>	<b>121</b>
<b>5.1</b>	<b>Introduction</b>	<b>121</b>
<b>5.2</b>	<b>Characterization of the Base Flow in the Diffuser's First Turn</b>	<b>123</b>
<b>5.3</b>	<b>Effects of Fluidic Actuation</b>	<b>132</b>
<b>CHAPTER 6.</b>	<b>Serpentine Diffuser with Cowl Inlet</b>	<b>146</b>
<b>6.1</b>	<b>Introduction</b>	<b>146</b>
<b>6.2</b>	<b>Base Flow Characterization</b>	<b>148</b>
<b>6.3</b>	<b>Aerodynamic Bleed using Auxiliary Inlets</b>	<b>162</b>
6.3.1	Bleed Effect within the Cowl Inlet	164
6.3.2	Bleed Effect within the Diffuser and at the AIP	175
<b>6.4</b>	<b>Auxiliary Inlet Slots with Active Flow Control</b>	<b>184</b>
<b>CHAPTER 7.</b>	<b>Conclusions</b>	<b>189</b>
<b>7.1</b>	<b>Offset Diffuser (SD-1)</b>	<b>189</b>
<b>7.2</b>	<b>Serpentine Diffuser (SD-2)</b>	<b>191</b>
<b>7.3</b>	<b>Transonic Shock in a Serpentine Diffuser (SD-2)</b>	<b>193</b>
<b>7.4</b>	<b>Serpentine Diffuser with Cowl Inlet</b>	<b>195</b>
<b>7.5</b>	<b>Closing Remarks</b>	<b>197</b>
<b>APPENDIX A:</b>	<b>Pressure Sensitive Paint</b>	<b>199</b>
<b>A.1</b>	<b>Background</b>	<b>199</b>
<b>A.2</b>	<b>Hardware</b>	<b>200</b>
<b>A.3</b>	<b>Postprocessing</b>	<b>203</b>
<b>A.4</b>	<b>Image De-warping</b>	<b>205</b>
<b>REFERENCES</b>		<b>208</b>

## LIST OF TABLES

Table 2.1	Test section configurations for each research chapter.	21
Table 4.1	Parameter values for cases within broad optimum region.	96
Table 5.1	Ratio of pressure downstream of shock front to pressure upstream of shock front for each $M_{AIP}$ in Figure 5.3.	124

## LIST OF FIGURES

Figure 2.1	Pull-down wind tunnel.	16
Figure 2.2	Section view of the SD-2 test section attached to the contraction and square-to-D adapter.	17
Figure 2.3	SD-2 test section with cowl inlet and ground plane top view (a), side view (b), and front view (c), isolated from wind tunnel.	18
Figure 2.4	Side and front views of diffusers SD-1 (a, b) and SD-2 (c, d), and coordinate system.	20
Figure 2.5	Static (green) and total (red) pressure port locations on the SD-1 (a) and SD-2 (b) diffuser geometries, centerlines (left) and AIP (right).	21
Figure 2.6	Photo of the AIP total pressure rake (a), a total pressure color raster plot generated with rake data (b), and a photo of the rake installed at the downstream (right) end of diffuser test section (c). $i$ and $j$ are AIP total pressure port coordinates for ring $i$ and rake $j$ .	23
Figure 2.7	Repeated measurements of AIP total pressure ratio of base flow at $MAIP \approx 0.54$ in SD-2 diffuser on dates 4/4/2016, 9/21/2016, 1/12/2017, 1/23/2017, 8/29/2017, 11/14/2017.	25
Figure 2.8	Schematic of the integrated camera and UV LEDs illuminating the PSP domain on the SD-2 diffuser second turn.	28
Figure 2.9	Flow-facing side of the integrated stereolithography PSP insert containing a camera and four LEDs.	28
Figure 2.10	Pressure sensitive paint calibration curve relating intensity ratio to pressure ratio.	29
Figure 2.11	PSP pressure color raster plot, showing an inactive jet array on top, and static pressure ports in central and lower regions.	30
Figure 2.12	Top view (a), and front view (b), of laser path from laser (grey), through multiple spherical lenses (blue), mirrors (black), and a cylindrical lens (orange).	32

Figure 2.13	Top (a), back (b), front (c), and section (d) views of the camera (gray), lens (blue), and laser (green) setup for diffuser (blue) planar PIV.	33
Figure 2.14	Left (a), front (b), and bottom (c) views of stereo PIV camera and laser setup.	34
Figure 2.15	Example raw PIV image (a), image after high-pass Butterworth filtering (b), and time-average SPIV field, colored by $u$ velocity with $v, w$ in-plane vectors (c).	36
Figure 2.16	Section view of SD-2 test section with integrated flow control inserts on the first and second turns.	38
Figure 2.17	Top view (a), isometric section view (b), and side section view (c) of flow control insert containing array of fluidically oscillating jets and embedded plenum. Arrow describes flow direction along centerline. Coordinate directions are included for reference.	38
Figure 2.18	Drawing of no-feedback-loop fluidic oscillating jet, with length scale	39
Figure 2.19	Schematic of the cowl aerodynamic bleed through the three arrays of slots. Coordinate directions are included for reference.	41
Figure 3.1	Cross sectional view of the center plane of diffuser SD-1 centerline in the absence (a) and presence (c) of the trapped-vortex recess. The corresponding color raster plots of the total pressure at the AIP are shown in (b) and (d), respectively. Coordinate system is included for reference.	43
Figure 3.2	Top view of helicity iso-surfaces along the lower surface in the base flow with recess (cf. Figure 3.1c). Coordinate system directions are included for reference.	44
Figure 3.3	Profiles of Mach number scaled by freestream Mach number $M_f$ (a) and the scaled Mach RMS fluctuations (Equation 3.1) (b) near the bottom surface ( $z/D=0.65$ ) at three spanwise locations $y/D = -0.35$ (blue), 0 (black), 0.35 (red).	46
Figure 3.4	Surface oil-flow visualization over the recess insert at $MAIP = 0.58$ (the flow is from left to right). The red dashed line marks flow reattachment, and blue arrows marking a central saddle and two side nodes.	46
Figure 3.5	Locations of hot wire anemometry and particle image velocimetry within the center plane of the diffuser between the	47

recess and the AIP. Hot wire (HW) measurements were acquired at  $x/D = -1.7$  and  $-0.6$ . The particle image velocimetry was acquired at  $x/D = -1.55$  (18 x 32 mm) and  $x/D = -0.4$  (14 x 26 mm).

- |             |   |    |
|-------------|---|----|
| Figure 3.6  | Time-averaged profiles of streamwise velocity [ $MAIP = 0.36$ ( $\circ$ ), $0.45$ ( $\square$ ), $0.58$ ( $\Delta$ ), and $0.7$ ( $\diamond$ )] at $x/D = -1.55$ (a, c) and $x/D = -0.4$ (b, d), in both scaled normal distance to the wall $z_w/D$ (a, b) and canonical boundary-layer wall (c, d) coordinates $y^+$ and $U^+$ . The logarithmic law $U^+ = 2.5 \ln y^+ + 5.5$ is shown for reference in (c, d) using a dashed line. | 48 |
| Figure 3.7  | Color raster plots of total pressure at the AIP in the presence of the recess $MAIP = 0.36$ (a), $0.45$ (b), $0.58$ (c), $0.64$ (d), and $0.7$ (e).   | 50 |
| Figure 3.8  | CAD drawings of the diffuser's flow control module that integrates the recess with an array of fluidic oscillating jets (a), and a front view of the jet array (b) with coordinate directions for reference.  | 51 |
| Figure 3.9  | Surface oil-flow visualization over the recess insert at $MAIP = 0.58$ and $Cq \approx 0.7\%$ (the flow is from left to right). The image shows the traces of the actuation jets on the left and marked alternating saddles and nodes along the attachment line (red dashed).   | 52 |
| Figure 3.10 | Surface oil-flow visualization along the inner surface of the diffuser looking downstream at the AIP (the total pressure rake is visible on the left side of each image) in the absence (a, c) and presence (b, d) of actuation ( $Cq = 0.7\%$ ) at $MAIP = 0.58$ (a, b) and $0.7$ (c, d). The dashed lines mark base (yellow) and actuated (red) flow trajectory.  | 53 |
| Figure 3.11 | Color raster plots of the total pressure at the AIP in the presence of actuation: $Cq$ , $MAIP = 1\%$ , $0.36$ (a), $0.9\%$ , $0.45$ (b), $0.75\%$ , $0.58$ (c), $0.7\%$ , $0.64$ (d), and $0.68\%$ , $0.7$ (e).  | 54 |
| Figure 3.12 | Variation of the absolute (a) and relative (b) AIP total pressure distortion $DPCP_{avg}$ with actuation mass flow rate coefficient $Cq$ at $MAIP = 0.36, 0.45, 0.58, 0.64$ , and $0.7$ .   | 55 |
| Figure 3.13 | Variation of the AIP total pressure distortion $DPCP_{avg}$ with the flow control mass flow rate coefficient $Cq$ at $MAIP = 0.7$ . Corresponding color raster plots of the AIP total pressure are also shown for reference.  | 57 |

Figure 3.14	The time-averaged cross stream distributions of $\rho^* \cdot M$ (a, c) and $(\rho^* \cdot M)_{\text{rms}}$ (b, d) in the center plane at the upstream, $x/D = -1.7$ (a, b) and downstream $x/D = -0.6$ (c, d) ports in the absence (open symbols) and presence (solid symbols) of actuation $MAIP = 0.36$ ( $\circ$ ), $0.45$ ( $\square$ ), and $0.58$ ( $\triangle$ ), and $Cq = 0.7\%$ ( $\blacktriangle$ ), $0.9\%$ ( $\blacksquare$ ), and $1\%$ ( $\bullet$ ).	58
Figure 3.15	The time-averaged cross stream distributions of $\rho^* \cdot M$ (a, c) and $(\rho^* \cdot M)_{\text{rms}}$ (b, d) in the center plane at the upstream, $x/D = -1.7$ (a, b) and downstream $x/D = -0.6$ (c, d) ports for $MAIP = 0.67$ in the absence ( $\circ$ ) and presence of actuation at $Cq = 0.2\%$ ( $\blacksquare$ ), $0.5\%$ ( $\blacktriangle$ ), and $0.7\%$ ( $\blacklozenge$ ).	60
Figure 3.16	Time-averaged distributions of $\rho^* \cdot M$ (a, b, e, f) and $(\rho^* \cdot M)_{\text{rms}}$ (c, d, g, h) in the center plane at the upstream, $x/D = -1.7$ (a–d) and downstream, $x/D = -0.6$ (e–h) ports in the absence (a, e, c, g) and presence (b, d, f, h) of actuation at $Cq = 0.6\%$ and $MAIP = 0.36$ , $0.45$ , and $0.58$ .	61
Figure 3.17	Power spectra of $\rho^* \cdot M$ at the $x/D = -0.6$ measurement station in the absence ( $—$ , $Cq = 0$ ) and presence ( $—$ , $Cq = 0.6$ ) of actuation for $MAIP = 0.58$ at $zw/D = 0.015$ (a), $0.039$ (b), $0.133$ (c), and $0.245$ (d) above the surface.	62
Figure 3.18	Time-averaged profiles of streamwise velocity in the absence (black, open symbol) and presence (color, closed symbol) of actuation at $x/D = -1.55$ (a–d) and $x/D = -0.4$ (f–h). Each column corresponds to a Mach number $MAIP = 0.36$ (a, e), $0.45$ (b, f), $0.58$ (c, g), and $0.7$ (d, h). Within each plot, $Cq$ is indicated by color and varies from $0.4\% - 1.1\%$ (a, e), $0.3\% - 0.9\%$ (b, f), $0.3\% - 0.8\%$ (c, g), and $0.2\% - 0.7\%$ (d, h), where increasing $Cq$ is colored from blue (lowest) to green (middle) to red (highest).	64
Figure 3.19	Color raster plots of distributions of the total pressure $pt/pto$ at the AIP in the presence of actuation by $n = 21$ (a – d), $13$ (e – h), and $7$ (i – l) central jets at $MAIP = 0.7$ and $Cq = 0$ (e, i), $0.8\%$ (a, j), $0.15\%$ (k), $0.25\%$ (f), $0.3\%$ (b, g), $0.38\%$ (c, l), $0.63\%$ (h), and $0.7\%$ (d).	66
Figure 3.20	Variation of the average circumferential distortion $DPCP_{\text{avg}}$ (solid lines) and of $MAIP$ (dashed lines) with $Cq$ (a) and $Cq/n$ (b) for $n = 21$ (yellow), $13$ (green), and $7$ (black).	67
Figure 3.21	Variation of the total pressure distortion $DPCP_{\text{avg}}$ with $\Delta MAIP/Mo$ at $MAIP = 0.7$ in the absence ( $\circ$ ) and presence of	68

actuation:  $n = 21$  (●), 19 (●), 17 (●), 15 (●), 13 (●), 11 (●), 9 (●), and 7 (●) active jets.

Figure 3.22	The variation with $Cq$ of the average circumferential distortion $DPCP_{avg}$ along with corresponding color raster plots of the total pressure distributions at the AIP for the optimal jet configuration $n = 13$ .	70
Figure 3.23	Images of surface oil visualization over the wall recess at $MAIP = 0.7$ in the absence (a) and presence (b) of actuation by the central $n = 13$ jets at $Cq = 0.25\%$ . The images are marked by saddles (labeled S) and nodes (labeled N), and the attachment line (red).	71
Figure 3.24	Isometric (a,c) and normal (b,d) view of iso-surfaces of Q-criterion colored by local Mach number in simulations of the diffuser flow over the recess at $MAIP = 0.7$ in the absence (a, b) and presence (d, e) of actuation ( $Cq = 0.25\%$ ).	72
Figure 3.25	Helicity iso-surfaces colored by helicity sign in the absence (a) and presence (c) of actuation within the diffuser, and color raster plots of the corresponding experimental total pressure distributions at the AIP (c and d, respectively) for $MAIP = 0.7$ , $n = 13$ , and $Cq = 0.25\%$ . Coordinate directions included for reference in (a).	74
Figure 4.1	A streamwise cross section along the center plane of the serpentine diffuser showing the locations of interchangeable inserts marked in red (a), and a color raster plot of the total pressure distribution at the AIP measured by the 40-probe rake ( $MAIP=0.54$ ) (b).	77
Figure 4.2	Surface oil visualization in the base flow ( $MAIP = 0.54$ ) over the first turn bottom surface (a, $-3.45 < x/D < -2.52$ ), and second turn top surface (b, $-2.07 < x/D < -0.82$ ) flow control inserts (cf. Figure 4.1a). The flow is from left to right, and the arrows indicate sense of secondary vortices. Domains enclosed in dotted black lines indicate separated regions.	78
Figure 4.3	Perspective view of counter-rotating vortices lifting off from spiral nodes [76].	79
Figure 4.4	Color raster plots of the total pressure at the AIP for the base flow at $MAIP = 0.29$ (a), 0.34 (b), 0.38 (c), 0.43 (d), 0.47 (e), 0.51 (f), 0.54 (g), and 0.58 (h). Arrows in (h) mark sense of streamwise vortices.	80

Figure 4.5	Variation of $C_p$ in the base flow along the span of the diffuser for $-0.5 < y/D < 0.5$ at $x/D = -1.9$ (a) and $-1$ (b), and streamwise variation of $C_p$ along the centerline ( $y = 0$ ) for $-3.5 < x/D < 0$ on the bottom (c) and top (d) surfaces for $MAIP = 0.29$ (●), $0.34$ (●), $0.38$ (●), $0.43$ (●), $0.47$ (●), $0.51$ (●), $0.54$ (●), and $0.58$ (●).	81
Figure 4.6	Color raster plots of surface pressure in the base flow measured using PSP at $MAIP = 0.41$ (a), $0.45$ (b), $0.47$ (c), $0.49$ (d), $0.50$ (e), and $0.53$ (f). Blue dashed region in (c) marks low-pressure region just upstream of jets. Red dashed domain in (c) marks region of elevated pressure. Black dashed domain in (f) bounds the elevated pressure region (separation). Black circles in (e) mark pressure ports at $x/D = -1$ (cf. Figure 4.5b). Flow is from top to bottom.	83
Figure 4.7	Color raster plots of the time-averaged (a) and instantaneous (b) total pressure at the AIP, and power spectra of the total pressure fluctuations at transducers A ( $i = 1, j = 5$ ) (c) and B ( $i = 1, j = 1$ ) (d), $MAIP = 0.342$ , <b>0.382</b> , <b>0.421</b> , $0.459$ , <b>0.492</b> , <b>0.527</b> .	85
Figure 4.8	a) Schematic rendition of the yawed jet array just upstream of the second turn separated region (marked in green in b); and b) a CAD image of a cross section of the actuation module installed in the diffuser.	87
Figure 4.9	Color raster plots of the total pressure at the AIP for $MAIP = 0.54$ and $Cq = 0\%$ (a), $0.09\%$ (b), $0.18\%$ (c), $0.27\%$ (d), $0.36\%$ (e), $0.45\%$ (f), $0.54\%$ (g), $0.63\%$ (h), $0.72\%$ (i), and $0.81\%$ (j).	88
Figure 4.10	Surface oil visualization over the second turn flow control insert at $MAIP = 0.54$ using an array of 17 jets at $Cq = 0$ (a), $0.18\%$ (b), $0.36\%$ (c), and $0.54\%$ (d). Dashed regions mark estimated separation extent.	89
Figure 4.11	Surface oil visualization at $MAIP = 0.54$ over the second turn flow control insert, with $Cq/n \approx 4 \times 10^{-4}$ and varying number of active jets. $Cq, n = 0.72\%$ , 17 (a), $0.62\%$ , 15 (b), $0.54\%$ , 13 (c), $0.46\%$ , 11 (d), $0.37\%$ , 9 (e), $0.29\%$ , 7 (f), $0.21\%$ , 5 (g), and $0.12\%$ , 3 (h). Red dashed lines mark spanwise extent of effected attachment domain (a, c). Yellow dashed lines mark gap between naturally attached flow and controlled-attached flow (d, e).	92
Figure 4.12	Color raster plots of the total pressure at the AIP at $MAIP = 0.54$ that are labeled by the number of active jets $n$ with $Cq = 0.72\%$ (a), $0.62\%$ (b), $0.54\%$ (c), $0.46\%$ (d), $0.37\%$ (e), $0.29\%$ (f), $0.21\%$ (g), and $0.12\%$ (h).	93



Figure 4.13	Variation of the relative change in the mean circumferential distortion parameter $DPCP_{avg}$ with $Cq$ for $n = 3, 5, 7, 9, 11, 13, 15,$ and $17$ jets ( $MAIP = 0.54$ ).	95
Figure 4.14	Variation with $Cq$ ( $n = 13$ ) of the distortion parameters $DPCP_{avg}$ (a), $DPCP_t$ (b), $DPCP_h$ (c), $DPRP_t$ (d), and $DPRP_h$ (e) and of Pressure Recovery (f), for $MAIP = 0.4, 0.44, 0.48, 0.52$ .	97
Figure 4.15	Images of surface oil visualizations (a, c) and corresponding color raster plots of surface pressure measured using PSP (b, d) in the base flow (a-b, $Cq = 0$ ) and in the presence of actuation (c-d, $Cq = 0.5\%$ , $n = 13$ ) at $MAIP = 0.54$ . Yellow dashed lines mark vortex traces (a). Corresponding high-pressure regions marked in (b) with black dotted lines.	98
Figure 4.16	Simulations of the base (a-d) and controlled (e-h) flows ( $n = 13$ , $Cq = 0.4\%$ , $MAIP = 0.54$ ) showing the evolution of time-averaged cross sections of the counter-rotating vortex pair (streamwise vorticity, a-b, e-f), iso-surfaces of streamwise vorticity (c, g), and the corresponding measured color raster plots of the total pressure distributions at the AIP (d, h).	100
Figure 4.17	Color raster plots of the RMS fluctuations of the total pressure at the AIP at $Cq/n \approx 4 \times 10^{-4}$ and varying number of active jets, such that $Cq$ , $n = 0\%$ , 0 (a), 12%, 3 (b), 29%, 7 (c), and 0.54%, 13 (d) at $MAIP = 0.54$ .	102
Figure 4.18	Circumferential distortion parameter $DPCP_{avg}/DPCP_{avg,0}$ (a), and total pressure RMS / RMS <sub>0</sub> for $n = 3, 7, 13$ , at $MAIP = 0.49$ .	103
Figure 4.19	Probability density function of a time-resolved $DPCP_{avg}$ parameter (a) and its corresponding power spectra (b) for $n = 0, 3, 7$ , and $13$ active jets.	105
Figure 4.20	Power spectra of time-resolved $DPCP$ for each ring of the 40-probe rake $i = 1-5$ (a-e) and its corresponding probability density functions (f-j) for $n = 0, 3, 7$ , and $13$ active jets.	108
Figure 4.21	The first five ( $m = 1-5$ ) POD modes of instantaneous total pressure for the unforced flow (a-e), and for varying jet configurations $n = 3$ (f-j), 7 (k-o), and 13 (p-t). Energy fraction in percentage are indicated in the center of each POD plot.	109
Figure 4.22	Power spectra of the time coefficients of POD modes $m = 1$ (a), and 5 (b) in the base flow.	111

Figure 4.23	Energy spectra of the first SPOD mode for the base flow ( $n = 0$ ) and with $n = 3$ , 7, and 13 actuation jets.	112
Figure 4.24	The first SPOD mode for the frequencies 475 (a-d), and 1,000 Hz (e-h), for $n = 0$ (a,e), 3 (b,f), 7 (c,g), and 13 (d,h).	113
Figure 4.25	Color raster plots of the total-pressure power spectra integrated over the band $f = 900$ -1,100 Hz for $n = 0$ (a), 3 (b), 7 (c), and 13 (d).	114
Figure 4.26	AIP face-averaged RMS fluctuations of total pressure (a), maximum instantaneous $DPCP_{avg}$ (b), and time-average $DPCP_{avg} / DPCP_{avg,0}$ (c) at $MAIP = 0.38, 0.42, 0.46, 0.5$ , and $n = 13$ .	116
Figure 4.27	AIP time-average total pressure (a, d), RMS fluctuations (b, e), and the total pressure at the instant of maximum $DPCP_{avg}$ (c, f) for cases $n = 0$ (a-c) and 13 (d-f).	117
Figure 4.28	Diagram showing ports chosen for individual power spectra in Figure 4.29. Ports chosen lie on three rakes, $j = 1, 2, 8$ , and all five radial rings, where $i = 1$ is radially innermost, and $i = 5$ is radially outermost.	118
Figure 4.29	Horizontal color raster bars of spectral magnitudes (up to 10 kHz) of the total pressure measured by each of the AIP sensors as marked in the accompanying schematic. These bars are arranged by sensor numbers in two vertical columns for the base flow (a) and in the presence of actuation by 13 jets (b). Representative power spectra in the absence (—) and presence (—) of actuation are shown for sensors: (1,1) (c), (4,1) (d), (1,8) (e), and (2,8) (f).	120
Figure 5.1	a) Isometric sectional view of the serpentine SD-2 diffuser showing the actuation insert at the first turn with the integrated spanwise jet array (the full array includes 23 actuation jets) and dynamic pressure sensor marked by black ellipse; and b) Outline of the diffuser's cross section along its center plane showing the setup for the illumination of the surface pressure sensitive paint (cf. Section 2.3.2), and the PIV planes. The insert extends from $x/D = -3.4$ to $-2.7$ . The global coordinate system is also included for reference.	122
Figure 5.2	Cross stream profiles of $x$ velocity component $U$ , normalized by the local maximum velocity, at $x/D = -3.5, y = 0$ , (cf. Figure 5.1b) a) PIV measurements $MAIP = 0.45$ ( $\times$ ), $0.53$ ( $\diamond$ ), $0.6$ ( $\circ$ ), $0.64$	123

(+), and 0.69 ( $\Delta$ ); and b) Simulation across the diffuser's height [78],  $MAIP = 0.53$  (blue line) superposed with the measurements.

- Figure 5.3 Color raster plots of surface pressure distributions over half the span of the base flow over the bottom surface of SD-2 first turn measured using PSP (a-e), and corresponding surface oil visualization (f-j) at  $MAIP = 0.54$  (a,f), 0.58 (b,g), 0.6 (c,h), 0.61 (d,i), and 0.66 (e,j). The solid black ellipse marks low pressure region (a). The blue dashed line marks diffuser corner, green dashed line marks the center span ( $y = 0$ ). In the oil visualization images, the black dotted line marks the horseshoe-shaped separation region, and the yellow solid lines mark the shock wave footprints. 125
- Figure 5.4 Color raster plots in cross stream (z-x) planes (referenced to the diffuser's global coordinates) of the time-averaged distributions of the spanwise vorticity overlaid with equidistant grid of vectors of the time-averaged velocity at  $MAIP = 0.54$  measured at: a)  $x/D = -3, 12 \times 15$  mm, and b)  $x/D = -2.5, 12 \times 10$  mm (cf. Figure 5.1b). 128
- Figure 5.5 Surface oil visualization at  $MAIP = 0.54$  on the bottom surface of the diffuser's first turn extending from  $x/D = -2.5$  (left) to 0 (right). Solid yellow lines mark signatures of streamwise counter-rotating vortices. The image also shows the 40-probe total pressure rake at the AIP on the far right. 129
- Figure 5.6 Color raster plots of the total pressure distribution at the AIP in the base flow at  $MAIP = 0.54$  (a), 0.61 (b), 0.66 (c). 130
- Figure 5.7 Color raster plots of surface pressure distributions over half the span of the base flow over the concave surface of the diffuser's first turn measured using PSP in the absence (a-c) and presence (d-f) of fluidic actuation at  $Cq = 0.75\%$ , and  $MAIP = 0.54$  (a, d), 0.61 (b, e), 0.66 (c, f). Dotted black line in (a) indicates the position of the jet array, orange dotted line in (c) marks shock front, the dashed rectangle in (d) marks traces of low pressure streaks induced by the actuation jets, and the red dashed lines in (e) and (f) mark the edges of low-pressure regions. 131
- Figure 5.8 Surface oil visualization on the first turn convex (bottom) surface at  $MAIP = 0.54$  with inactive (a-c) and active ( $Cq = 0.75\%$ , d-f) actuation jets (a, d), 0.61 (b, e), 0.66 (c, f). Each of the oil visualization images is matched with color raster plots of distributions of the estimated local Mach number near the surface that are overlaid over the half-span of the flow. In b, c, e, and f black lines mark the approximate location of the shock across 134

half the span. The first and second shock fronts are labeled A and B, respectively. Dashed ellipse in (c) marks region of constant Mach number. Dot in (a) marks position of dynamic pressure sensor.

Figure 5.9	Power spectra of surface pressure fluctuations downstream of the shock at $Cq = 0$ (black) and 0.75% (color) for $MAIP = 0.54$ (a), 0.61 (b), 0.66 (c).	137
Figure 5.10	Color raster plot of the mean spanwise vorticity component with overlaid mean velocity profiles as in Figure 5.4a and b, respectively.	138
Figure 5.11	Oil visualization on the concave (bottom) diffuser surface for $-2.5 < x/D < 0$ at $MAIP = 0.54$ with $Cq = 0.35\%$ . The yellow lines mark vortex trajectories.	139
Figure 5.12	Color raster plots of distributions of the total pressure at the AIP in the absence (a-c) and presence (d-f) of actuation ( $Cq = 0.75\%$ ), at $MAIP = 0.54$ (a, d), 0.61 (b, e), and 0.66 (c, f).	140
Figure 5.13	Variations with $Cq$ of the average circumferential distortion $DPCP_{avg}$ (a) and total pressure recovery $PR$ (b) for $MAIP = 0.54$ (●), 0.61 (●), and 0.66 (●).	142
Figure 5.14	Color raster plots of distributions of the total pressure at the AIP for $MAIP = 0.54$ (a-d), and 0.61 (e-h), for $Cq = 0$ (a, e), 0.25% (b, f), 0.5% (c, g), and 0.75% (d, h).	143
Figure 5.15	Effects of actuation at varying $MAIP$ (normalized by $MAIP_o = 0.54$ ) on $DPCP_{avg}$ (a), and total $PR$ (b) in the base and controlled flows (open and solid symbols, respectively).	144
Figure 6.1	Section view of the serrated cowl and ground plane serving as an inlet for the SD-2 diffuser.	147
Figure 6.2	The evolution of streamwise vortices within the coupled cowl-diffuser captured in the simulations of Lakebrink and Mani, [79]. The vortices are visualized using surfaces of streamwise vorticity (red is positive, blue is negative) originating at the serrated edges of the cowl and at the corner between the cowl and the inlet ground plane. The sense of each vortex is marked by arrows.	148
Figure 6.3	Surface oil visualization on the inner cowl surface (a) and the ground plane underneath (c) at $M_{AIP} = 0.5$ . Black dotted rectangle in (a) marks the enlarged region shown in (b). Yellow dashed lines highlight the surface markings of the vortex path.	150

Red rectangle mark regions in which the oil traces point normal to the streamwise direction.

Figure 6.4	Spanwise projection of cross-stream and streamwise-normal SPIV planes relative to the bleed slots on the surface of the cowl (cf. Sections 2.4.2, 6.3), at $x/D = -4.89$ (a), $-4.7$ (b), $-4.58$ (c), $-4.43$ (d), $-4.28$ (e), $-4.12$ (f).	151
Figure 6.5	Color raster plots of distributions of the streamwise vorticity (a-f), and TKE (g-l) of the base flow within the spanwise planes at $x/D = -4.89$ (a, g), $-4.7$ (b, h), $-4.58$ (c, i), $-4.43$ (d, j), $-4.28$ (e, k), $-4.12$ (f, l), at $M_{AIP} = 0.5$ . The dashed line in each image marks the centerline $y = 0$ , and solid lines bounding the domains mark the intersection of the diffuser's inner surface with the measurement planes.	152
Figure 6.6	Streamwise distributions of the centerline pressure coefficient $C_p$ along the lower (a) and upper (b) surfaces of the diffuser in the base flow measured at $M_{AIP} = 0.3$ (×), $0.35$ (×), $0.4$ (×), $0.45$ (×), and $0.5$ (×). The experimental measurements are compared with numerical simulations for $M_{AIP} = 0.5$ (dashed line, Lakebrink and Mani [79]).	154
Figure 6.7	Color raster plots of time-average total pressure at the AIP for $M_{AIP} = 0.3$ (a), $0.35$ (b), $0.4$ (c), $0.425$ (d), $0.45$ (e), $0.475$ (f), and $0.5$ (g).	156
Figure 6.8	Streamwise variation of average total pressure recovery from the numerical simulations of Lakebrink and Mani [79] at $M_{AIP} = 0.5$ , along the diffuser with the cowl inlet diffuser shown for reference above.	157
Figure 6.9	Steady state (×) and time-averaged (—) circumferential distortion $DP_{CP_{avg}}$ (a), and pressure recovery $PR$ (b), for $0.12 \leq M_{AIP} \leq 0.5$ . The 95% confidence interval is marked with a blue shaded region about the time-averaged data.	158
Figure 6.10	Color raster plots of the total pressure distributions at the AIP at the instant of peak $DP_{CP_{avg}}$ (a, b, c) and AIP total pressure RMS fluctuations (d, e, f) for $M_{AIP} = 0.3$ (a, d), $0.4$ (b, e), $0.5$ (c, f).	160
Figure 6.11	Vertical color raster bars of spectral magnitudes (b, up to 10 kHz) of the total pressure measured by each of the AIP sensors at $M_{AIP} = 0.5$ in each of the circumferential rings as shown schematically above in (a). The bars are grouped by ring number and the data	161

for each sensor are arranged in CW order starting at the red line in (a). The bars shaded in gray represent missing data.

Figure 6.12	Schematic of bleed flow through the three auxiliary inlet slots.	162
Figure 6.13	Surface oil visualization on the inner surface of the cowl with three auxiliary spanwise inlet slots at $M_{AIP} = 0.5$ . Yellow arrow highlights direction of oil streaks in the corner downstream of slots.	163
Figure 6.14	Color raster plots of vorticity (a-f), and TKE (g-l) fields within the auxiliary inlet cowl, within the spanwise planes at $x/D = -4.89$ (a, g), $-4.7$ (b, h), $-4.58$ (c, i), $-4.43$ (d, j), $-4.28$ (e, k), $-4.12$ (f, l), at $M_{AIP} = 0.5$ . Dashed line is test section centerline $y = 0$ , and the bounding solid lines mark the intersection of the diffuser's inner surface with the measurement planes.	165
Figure 6.15	Definition of $\beta$ for $\Gamma_2$ in Equation 6.2 [81]	167
Figure 6.16	The extent of the vortex cores as defined by Equation 6.2 marked by blue shading and the vortex centers marked by red dots in the flows through the base cowl (a-f, cf. Figure 6.5) and the cowl with the auxiliary bleed inlets (g-l, cf. Figure 6.14), at $x/D = -4.89$ (a, g), $-4.7$ (b, h), $-4.58$ (c, i), $-4.43$ (d, j), $-4.28$ (e, k), $-4.12$ (f, l).	169
Figure 6.17	The change in the $y$ and $z$ positions of the centers of the vortex cores relative to the vortex position in the base flow plane at $x/D = -4.8$ ( $\bullet$ ), and scaled by $D$ , for center vortex pair (a) and the corner vortices (b) for base ( $\bullet$ ) and auxiliary inlet ( $\blacktriangle$ ) at $x/D = -4.89, -4.7, -4.58, -4.43, -4.28, -4.12$ .	170
Figure 6.18	The circulation $\Gamma$ of the streamwise vortices (a) and the corresponding streamwise velocity $U$ through their cores as defined in Figure 6.16 (b) for the center and corner vortices in the base cowl (solid lines) and the cowl with the auxiliary bleed inlet (dashed lines).	171
Figure 6.19	Highest density regions [84] representing 75% of the distribution of the vortex positions in the base (a) and auxiliary inlet cowl (b) at $x/D = -4.7, -4.58, -4.43, -4.28, -4.12$ , where the most probable point (mode) is marked with a solid circle.	174
Figure 6.20	Streamwise distributions of the centerline pressure coefficient $C_p$ along the lower (a) and upper (b) surfaces of the diffuser in the presence of bleed through the cowl's surface measured at $M_{AIP} = 0.3$ ( $\times$ ), $0.35$ ( $\times$ ), $0.4$ ( $\times$ ), $0.45$ ( $\times$ ), and $0.5$ ( $\times$ ). The experimental measurements are compared with numerical	175

	simulations for $M_{AIP} = 0.5$ (dashed line) (Lakebrink and Mani [79])).	
Figure 6.21	Streamwise variation of average pressure recovery along the diffuser with the cowl inlet in the absence (—) and presence (—) of bleed from the numerical simulations of Lakebrink and Mani [79] at $M_{AIP} = 0.5$ .	177
Figure 6.22	Color raster plots of the time-average total pressure at the AIP in the presence of cowl bleed for $M_{AIP} = 0.3$ (a), 0.4 (b), 0.5 (c), and 0.6 (d).	178
Figure 6.23	Color raster plots of the RMS fluctuations of the total pressure (a-d) and total pressure distribution associated with peak $DPCP_{avg}$ distortion (e-h), at $M_{AIP} = 0.3$ (a,e), 0.4 (b,f), 0.5 (c,g), 0.6 (d,h) in the presence of bleed actuation.	179
Figure 6.24	Vertical color raster bars of spectral magnitudes (up to 10 kHz) of the total pressure measured by each of the AIP sensors in each of the circumferential rings as shown schematically in Figure 6.11a at $M_{AIP} = 0.5$ . The bars are grouped by ring number and the data for each sensor are arranged in CW order (cf. Figure 6.11a). The bars shaded in gray represent missing data. The data in the absence and presence of bleed are shown in (a) and (b), respectively. Also shown are corresponding color raster plots of distributions of the time-averaged total pressure (c,e) and total pressure RMS fluctuations (d,f) at the AIP, and a power spectra for the two previously mentioned cases at the port marked in the spectra bars (a,b) and AIP plots (c-f).	181
Figure 6.25	Base cowl and auxiliary inlet bleed $DPCP_{avg}$ (a) and pressure recovery (b) steady state (×), time-averaged (—), and 95% confidence interval (shaded) for $M_{AIP} = 0.12 - 0.6$ .	182
Figure 6.26	Schematic diagram of the diffuser cross section (a) and the location of the spanwise actuation jet array in the second turn (b, as in Chapter 4).	184
Figure 6.27	Variation with $C_q$ of the $DPCP_{avg}$ (a) and of the pressure recovery $PR$ (b), and corresponding color raster plots of the total pressure at the AIP for $C_q = 0$ (c), 0.25% (d), and 0.45 (e) all for $M_{AIP} = 0.6$ .	185
Figure 6.28	Vertical color raster bars of spectral magnitudes (up to 10 kHz) of the total pressure measured by each of the AIP sensors in each of the circumferential rings (a,b) as shown schematically in Figure 6.11a at $M_{AIP} = 0.5$ . The bars are grouped by ring number	187

and the data for each sensor are arranged in CW order starting (cf. Figure 6.11a). The bars shaded in gray represent missing data. The data in the absence and presence of bleed are shown in (a) and (b), respectively. Also shown are corresponding color raster plots of the time-averaged total pressure (c,e) and total pressure RMS fluctuations (d,f) at the AIP, and power spectra for the two previously mentioned cases at the port marked in the spectra bars (a,b) and AIP plots (c-f).

Figure A.1	Flow-facing side of the integrated stereolithography PSP insert containing a camera and four LEDs.	200
Figure A.2	PSP calibration curve relating intensity ratio to pressure ratio.	204
Figure A.3	Color raster plot of pressure from PSP, showing an inactive jet array on top, and static pressure ports in central and lower parts of domain.	205
Figure A.4	Colorized PSP camera image before correction (a), after 2D dewarping (b), and after mapping to 3D (c). Points on surface (●) were used for mapping.	206



## LIST OF SYMBOLS AND ABBREVIATIONS

### Abbreviations

AIP	Aerodynamic Interface Plane
BLI	Boundary-layer ingesting
HDR	Highest density region
PDF	Probability density function
PIV	Particle image velocimetry
POD	Proper orthogonal decomposition
PR	Pressure recovery
PSD	Power spectral density
PSP	Pressure sensitive paint
RMS	Root mean square
RMSF	Root mean square fluctuations
SPOD	Spectral proper orthogonal decomposition
TKE	Turbulent kinetic energy
TSP	Temperature sensitive paint
V/STOL	Vertical and/or short take-off and landing

### Symbols

$C_p$	Coefficient of pressure
$C_q$	Jet mass flow rate coefficient
$D$	Diffuser AIP diameter
$DPCP_{avg}$	Average SAE circumferential distortion descriptor

$DPCP_{avg,o}$	Reference $DPCP_{avg}$
$DPCP_h$	SAE circumferential distortion at hub
$DPCP_i$	SAE circumferential distortion for ring $i$
$DPCP_t$	SAE circumferential distortion at tip
$f$	Frequency
$H$	Diffuser throat height
$i$	AIP total-pressure rake ring index
$I$	PSP pixel intensity
$m$	Mode number
$M$	Mach number
$M_{AIP}$	Face-averaged Mach number at AIP
$\Delta M_{AIP}$	Relative change in $M_{AIP}$
$M_f$	Free-stream Mach number
$M_o$	Reference/nominal Mach number
$n$	Number of active jets
$p$	Static pressure
$p_t$	Total pressure
$p_{t,0}$	Reference total-pressure (ambient)
$RMS_0$	Reference RMS
$U$	$x$ -direction velocity
$U^+$	$U/u_\tau$
$x$	Global coordinate system dimension
$y$	Global coordinate system dimension
$y^+$	Wall coordinate
$z$	Global coordinate system dimension

$z_w$  Normal distance to wall

## Greek Symbols

$\Gamma$  Circulation

$\Gamma_1$  Gamma 1 vortex criterion

$\Gamma_2$  Gamma 2 vortex criterion

$\nu$  Kinematic viscosity

$\zeta$  Vorticity

$\rho$  Air density

$\rho_o$  Reference density

$\rho^*$   $\rho/\rho_o$

$\tau$  Wall shear stress

## SUMMARY

The flow in offset or serpentine diffusers is dominated by streamwise vorticity concentrations that advect of low-momentum fluid from the diffuser's surfaces into the core flow. These effects contribute to overall losses and give rise to flow distortion along the diffuser. Because the formation of these vortices is strongly coupled to locally separated flow domains over the curved surfaces in the diffuser's turns, the present experimental investigations exploit this coupling for controlling their evolution to mitigate the induced flow distortion and losses. The present investigations progress from a relatively mild offset diffuser in which the coupling mechanism between a concentration of trapped vorticity and the formation of streamwise vortices can be investigated to a more severe, serpentine configuration that is ultimately equipped with a cowl inlet. Active flow control based on fluidic actuation is used to control the formation and evolution of the vortices and thereby mitigate their adverse effects. The fundamental mechanisms by which the actuation methods (fluidic oscillating jets, autonomous bleed) control the flow are investigated using static and total pressures, pressure sensitive paint (PSP), particle image velocimetry (PIV), and surface oil visualization. It is shown that the evolution (strength and topology) of these vortices and hence their adverse effects can be considerably altered both at the inlet cowl and at the separation domains over the diffuser's turns with significant reductions in flow distortions and losses.

## CHAPTER 1. INTRODUCTION

This thesis has two primary objectives: (1) elucidation of the fundamental flow mechanisms in offset and serpentine diffusers, and (2) design and implementation of active flow control technologies for mitigation of the adverse effects of secondary flows within these diffusers. These objectives can be realized by addressing the specific goals:

1. *Identify the fundamental flow mechanisms that give rise to flow distortion and losses in offset diffusers and their characteristic temporal and spatial scales.*

Flow distortion within offset diffusers is typically measured at the aerodynamic interface plane (AIP) by the uniformity and symmetry of azimuthal distributions of the flow's total pressure and is can adversely affect engine performance. The losses associated with flow separation within the diffuser (typically over concave surfaces within the diffuser's turns) leads to distortion that is accentuated by the formation of streamwise vertical structures that induce blockage and displace low-momentum fluid towards the core flow. The coupling between the separation domains and the streamwise vortices can be exploited for mitigation of the adverse effects by using active flow control technologies.

2. *Determine active flow control (AFC) methodologies for alleviating their detrimental effects.*

Surface-mounted flow control actuators can modify near-surface flow structure and lead to significant mitigation of separation. A particular requirement from the present implementation of flow control is that the secondary vertical flow structures that contribute significantly to the distortion and originate at the internal flow surfaces are advected away

from the surfaces and therefore their control must be addressed at the surface. The present investigations are based on surface-mounted fluidic flow control using arrays of fluidically oscillating jets and assesses the actuation potential based on improvements in flow distortion and reduction in losses.

*3. Identify the primary AFC parameters and their effect on control authority.*

The effects of flow control parameters such as the actuation mass flow rate, number, and spanwise spacing of the actuation jets is investigated. The present investigations show that there is a clear optimum of actuation flow rate and that low flow rates can often increase losses or distortion, but that there is also an upper limit above which increased flow rate either has no or detrimental effect on distortion and losses. Furthermore, the number and spacing of actuation jets within a jet array jets can be selected for increased per-jet effects with significant reduction in jet mass flow rate. An important element of the investigations is to determine the effects of the actuation on the apparent stability of the streamwise vortical structure especially the stability of the vortices that are formed by the cowl inlet.

*4. Determine the range of effectiveness and potential limitations of the AFC actuation.*

Surface-mounted flow control devices can be effective at modifying near-surface flow structure when the base flow develops internal separation domains and/or shock waves of the concave turning surfaces. The range of effectiveness is determined based on the improvement relative to the base flow and is clearly dependent on optimal placement of the actuators relative to the domain of the flow that is to be controlled. Also, while surface-mounted actuation affords the capability to affect vorticity concentrations that

originate at the surface, control of the evolution of these vortices once they are advected into the core flow may be limited.

## **1.1 Thesis Structure**

The thesis is organized in chapters as follows:

*Chapter 1* includes the overview and the review of prior relevant investigations including an overview of flow in offset and serpentine diffusers and the effects of the inlet cowl, flow control based on trapped vorticity, and passive and active flow control.

*Chapter 2* describes the experimental setup including the wind tunnel in which the offset and serpentine diffuser models are placed, the offset and serpentine diffuser test sections including the flow control actuation insets, the representative cowl inlet that was used in the present experiments, and the experimental techniques (particle image velocimetry, pressure sensitive paint and total/static pressure measurements)

*Chapter 3* discusses the investigations of the indirect control of the streamwise vortices by manipulation of separate flow domains that lead to their formation. These investigations are conducted in an isolated, mild offset diffuser.

*Chapters 4 and 5* describe implementation of the flow control technique developed in Chapter 3 in the second and first turns of an isolated aggressive serpentine diffuser, respectively. While the flow in the second turn is dominated by an isolated separation domain on the concave surface, the flow in the first turn includes a transonic shock that is followed by a shock-induced separation domain.

*Chapter 6* focuses on the effects of a cowl inlet on the internal flow of the isolated serpentine diffuser of Chapters 4 and 5, the formation of an inlet vortex system that dominates the evolution of the flow within the diffuser and methodology for controlling these vortices.

*Chapter 7* summarizes the present findings results and the implications of this work.

## **1.2 Offset Diffuser Flow Physics**

Internal surface curvature in offset and serpentine diffusers can engender centrifugal pressure gradients that induce secondary flows and the formation of large, counter-rotating streamwise vortices [1, 2]. Furthermore, compact diffuser designs result in steep adverse streamwise pressure gradients over their internal surfaces that lead to rapid increase in boundary-layer thickness and potential local flow separation that can couple to the formation of streamwise vortices [3]. The formation of these secondary flow structures in propulsion systems leads to significant flow distortion and losses that can adversely affect engine performance. Therefore, the present investigations seek to indirectly control the evolution of these secondary flows by controlling the near-surface vorticity concentrations within the separation domains to which the streamwise vortices are coupled with the objective of diminishing their unfavorable effects. To accomplish this, spanwise arrays of discrete fluidic oscillating jets are utilized as control elements building on earlier investigations of separation control in which such fluidic actuators were used effectively in both internal (cf. Section 1.4.3), and external flows [4] including shock-induced flow separation [5].



### **1.3 Technical Rationale of the Present Investigations**

The present investigations were initiated in a mild, low-expansion offset diffuser (denoted SD-1), which did not exhibit an internal separated flow domain nor global counter-rotating secondary flow. This segment of the investigations had two primary objectives. First, to demonstrate the coupling between a region of trapped spanwise vorticity concentration mimicking local separation and the formation of a counter-rotating streamwise vortex pair that is typical of aggressive offset diffusers. The second objective was to demonstrate that active control of the trapped vorticity can indirectly control the evolution of the streamwise vortices. In order to utilize this geometry as a test bed for this flow control approach, the inner diffuser surface was modified to include an integrated recess along the concave surface at the flow turn to form concentration of trapped vorticity whose upstream and downstream edges each nearly span the inner (concave) flow surface. To manipulate the trapped vorticity, an array of discrete fluidic oscillating jets was placed upstream of the recess, issuing tangentially to the surface, and was contoured to match the upstream boundary of the separation.

The investigations in the offset diffuser demonstrated that the fluidic actuation could affect the separated domain, and, more importantly, mitigate the adverse effects in terms of flow distortion and losses. These findings were used in the main study which was conducted in an aggressive serpentine diffuser (denoted SD-2) in which the flow separates on the concave surface of each of the turns and couples to the formation of streamwise vortices. The separated flow over the second-turn concave surface forms a closed separation bubble that spans about a third of the surface span. Using the results from SD-1, an array of fluidically-oscillating jets was placed just upstream of the leading edge of

the separation domain and knowledge of the sense of the naturally occurring streamwise vortices prompted yawing of individual jets on each side of and away from the centerline to create predominantly single-sign streamwise vorticity of opposite sense to the prevailing sense of vorticity in the streamwise vortex that is naturally formed by the separation domain. The present investigations also showed that the separation along the concave first-turn surface is significantly exacerbated by formation of transonic shock at elevated flow rates, which imposes an upper operating limit of the diffuser. This motivated additional study of a possible extension of the diffuser operation range by application of flow control aimed at weakening of the shock and mitigation the coupled first-turn flow separation and secondary flows. This is accomplished using a separated array of actuators upstream of the shock that targets the shock evolution indirectly by controlling the coupled separation immediately downstream of the shock.

In the final stage of this research, an additional step is taken to mimic aircraft-integrated diffusers, by drawing the flow into the diffuser through a serrated cowl inlet. While such inlets are typically optimized for other parts of the flight envelope during takeoff, they form secondary streamwise vortices that dramatically hinder the engine operation. These inlet vortices that form along the cowl lips are similar to the vortices that are formed over delta wings, and they subsequently dominate the flow dynamics within the diffuser. Aerodynamic bleed, which has been shown to be able to effectively modify vortical structures in delta wings [6-8], is integrated into the cowl lips to directly interact with the cowl lip vortices through the introduction of momentum and small-scale vorticity near the surface and thereby significantly mitigate the effects of these vortices on the diffuser flow.

## 1.4 Literature Review

### 1.4.1 Inlet Flows

Poor performance of supersonic inlets in low speed conditions has been a known issue for decades. The crux of the issue is described well by Henne [9]: “High speed cruise favors thin inlet lips to keep the inlet mass flow ratio high and to keep the nacelle size and, therefore, drag as small as possible. However, high performance at low speed conditions, such as zero forward speed with crosswind and low forward speed with high angle of attack, favors thick inlet lips to efficiently turn the flow into the inlet.” The effect of a sharp lip in low-speed flow was theoretically characterized by Fradenburgh and Wyatt in 1954 [10] using momentum balance analysis on a cylindrical air inlet at subsonic free-stream Mach numbers. With this analysis they estimated total-pressure recovery as a function of freestream and inlet Mach numbers. At lower freestream Mach numbers, and especially in the case of zero freestream Mach number, the total pressure recovery plummets, greatly reducing aircraft engine performance. A supersonic inlet model was tested experimentally and found results in reasonable agreement to the theory. Lower pressure recovery means that if an aircraft needs to operate at that condition, it will need to have a larger engine, greatly increasing the weight and size of the aircraft.

### 1.4.2 Passive Flow Control in Diffusers

The most common passive flow-control device is the vortex generator. Brown et al. [11] tested one and two rows of rectangular, vane-type vortex generators, which were designed based on inviscid-vortex-image theory, in a short, trumpet-shaped Lockheed SST subsonic diffuser, at a diffuser entrance Mach of 0.8. It was found that these vortex

generators both increased total-pressure recovery and decreased the total-pressure distortion by 40%. Vakili et al. [12] used two rows of wing-shaped vortex generators in a counter-rotating configuration to successfully eliminate boundary-layer separation, reducing distortion by 30%, and increasing total-pressure recovery by 1%. Reichert and Wendt [13] tested wishbone and tapered-fin style vanes in a diffusing s-duct with an inlet Mach number of 0.6, and found that wishbone-style were ineffective, while tapered-fin style were effective in generating vortices of opposite sense to the naturally-occurring vortices in the flow, resulting in a slight improvement of total-pressure recovery, and 50% reduction in maximum circumferential distortion. Anderson and Gibb [14] numerically and experimentally investigated the usage of co-rotating rectangular vortex generators in a M2129 inlet s-duct. They were able to numerically predict and experimentally measure an 80% drop in steady and unsteady distortion at an inlet Mach number of 0.8. Hamstra et al. [15] used CFD in conjunction with design of experiments (DOE) to optimize the shape and location of an array of micro-vane vortex generators at each of the two bends in a 4:1 aspect ratio ultra-compact serpentine diffuser at throat Mach numbers up to 0.65. These micro-vanes effected a decrease in DC60 distortion and RMS turbulence of 50%, and an increase in total-pressure recovery of 5%. Jirasek [16] also performed a numerical DOE study on vortex-generator height, length, spacing, angle, and distance from separation, and applied the results to a dual-bend UAV inlet with a fixed AIP Mach number of 0.5. Experimental tests found the optimal vane configuration to reduce DC60 by more than 50%, while leaving total-pressure recovery almost unchanged. Holden and Babinsky [17] investigated the effect of vane and wedge sub-boundary-layer vortex generators on the interaction between normal shockwaves and boundary-layers in supersonic flow and found both to

reduce shock-induced separation. Yi et al [18] improved Anderson and Gibb's [14] vortex generators in a M2129 s-duct using gradient-based optimization to further reduce distortion by 79%, with negligible impact to total-pressure recovery. Recently, Tanguy et al. [19] performed stereo PIV at the AIP of an s-duct diffuser to investigate the effect of semi-delta wing vortex generators on total-pressure distortion and recovery, as well as swirl-distortion unsteadiness. They found that vortex generators could reduce DC60 distortion by almost 50% at an inlet Mach number of 0.6 and reduce peak-swirl unsteadiness by 61 percent. Similarly, Gil-Prieto et al. [20] studied steady and dynamic swirl distortion in multiple s-duct configurations and identified swirl patterns with proper orthogonal decomposition (POD). In addition, Tanguy et al. [21] performed a dynamic analysis of distortion on diffusers with multiple degrees of vertical offset, comparing the unsteadiness, and demonstrated extreme-value theory as a tool for unsteady distortion assessment.

#### *1.4.3 Active Flow Control in Diffusers*

Active flow control (AFC) has also been used to improve diffuser performance with less drag penalty than passive vortex generators. Two common techniques are mass flow insertion using continuous jets, or mass removal using suction. In 1985, Ball [22] separately tested area suction and slot blowing in a 3D offset diffuser at throat Mach of 0.7, and was able to reduce the boundary-layer thickness through suction, increase pressure recovery by 1% with blowing (2% airflow ratio) or suction (5% airflow ratio), and decreased distortion by 28% using suction. Scribner et al. [23] used microjets in a serpentine diffuser, operating at an inlet Mach number of 0.55, to reduce circumferential distortion by 70%, while improving pressure recovery by 2%, with a jet mass flow rate coefficient  $C_q$  of 1%. Anderson et al. [24] numerically investigated microjets' effect in a

redesigned M2129 inlet s-duct, and after a DOE optimization study, were able to reduce DC60 to below 0.1 with a  $C_q = 0.5\%$  at a throat Mach number  $M_t = 0.7$ . Gartner and Amitay [25] utilized a variety of AFC devices, including pulsed jets, sweeping jets, and a blowing slot to improve total-pressure recovery in a rectangular diffuser. The slot was found to be not as effective as the sweeping and pulsed jet arrays, even when used with greater  $C_q$ . Rabe [26] tested microjets in a double-offset diffuser, attached to a bell-mouth inlet, with the bulk flow fluidically driven by a gas-turbine engine, and mass injection driven by bleed from that engine. With a bleed rate of 1% ( $M_t = 0.55$ ) at the cruise condition, circumferential distortion was reduced by more than 60%. Harrison et al. [27] simulated, and experimentally verified the favorable superposition of ejector-pump-like suction and blowing for a thick-boundary-layer ingesting serpentine diffuser at  $M = 0.85$  in the freestream. They found that a 50% reduction in DC60 from using a circumferential blowing scheme, which could be increased to 75% with the addition of suction. Garnier [28] performed a spectral analysis of the effectiveness of pulsed and continuous blowing to reattach flow at  $M_{AIP} = 0.2$  to 0.4 in an aggressive s-duct using an array of dynamic-pressure sensors. It was found that pulsed blowing effects dynamic-distortion fluctuations at the forcing frequency, but they were able to match performance of continuous jets at 50%  $C_q$ . Gissen et al. [5] utilized fluidic oscillating jets to delay subsonic, shock-induced separation and reduce shock fluctuations, and Souverein and Debieve [29] used vortex-generating jets to reduce separation-bubble size and in effect increase the shock frequency. Narayanaswamy et al. [30] utilized an alternative AFC technique, pulsed plasma jets, to control unsteadiness in shock-wave boundary-layer interactions. When pulsed at 2 kHz, wall-pressure-fluctuation magnitude was reduced by about 30% in the frequency band

associated with the separation unsteadiness. In addition to conventional jets, synthetic jets have been tested in internal flows for their effectiveness in improving performance. Amitay et al. [31] investigated separation control in a non-diffusing serpentine duct using an array of synthetic jets, and were able to completely reattach flow up to  $M = 0.2$ . Mathis et al. [32] also utilized synthetic jets to reattach flow at  $Re = 4.1 \cdot 10^4$  along a high curvature region of an s-duct diffuser and verified flow reattachment with particle image velocimetry (PIV).

#### *1.4.4 Hybrid Flow Control in Diffusers*

A hybrid control approach, which incorporates the advantages of both passive and active control, has been shown to be effective in the reduction of parasitic drag while maintaining fail-safe attributes and satisfying the need for adjustable flow control [33, 34]. Owens et al. [33] combined active and passive flow control using vanes and jets to improve performance of an offset diffuser over a range of flow rates, especially at low velocities for which the micro-vanes were not optimized. In an effort to reduce engine bleed, Anderson et al. [34] combined the micro-ramps used in their earlier work [35] with flow injection resulting in an almost tenfold reduction in required engine bleed. Vane vortex generators have been extensively studied as a means for controlling separation in adverse pressure gradients [36], as well as for use in s-ducts [37-39] and as the passive component of hybrid-flow-control systems [33, 40]. Delot, Garnier, and Pagan [41] experimentally evaluated the effectiveness of passive vortex generators and continuous and pulsed micro-jets for reducing distortion in an offset diffuser and reported a reduction of the circumferential distortion parameter DC60 by 50% at  $M_{AIP} = 0.2$  and up to 20% at  $M_{AIP} = 0.4$ . Harrison et al. [27] simulated and experimentally verified the effect of various blowing and suction

schemes for a BLI serpentine diffuser using swirl and circumferential-flow-distortion analysis. They realized a 50% reduction in total-pressure circumferential distortion parameter DC60 by using a circumferential blowing scheme. In addition, they noted that blowing and suction could be strategically combined to produce reductions in distortion of up to 75%. Gissen et al. [42] utilized a combination of vanes and synthetic jets to achieve a 35% reduction in circumferential distortion in a BLI offset diffuser operating at  $M_{AIP} = 0.55$ . Gartner and Amitay [43] studied the effect of introducing a honeycomb mesh upstream of an offset rectangular duct and showed improvements in the symmetry of the pressure distribution while minimally decreasing total-pressure recovery. The mesh accomplished this by pushing the saddle-saddle point, responsible for the onset of an instability leading to asymmetry, farther downstream. Gartner and Amitay [25] experimentally tested the effect of sweeping, pulsed, and two-dimensional jet actuators on the total-pressure recovery of a rectangular diffuser under transonic-flow conditions, and showed that sweeping jets produced the greater recovery at comparable mass-flow rates. Burrows et al. [44] modified the moldline of an offset diffuser to trap vorticity concentrations and utilized fluidic-oscillating jets to control the vorticity and ultimately reduce engine-face distortion by 68% with a  $C_q$  of 0.25%. The experimental results were used concomitantly with numerical simulations to elucidate physics for the base flow and its interactions with fluidic-oscillator jets, and how the flow-control ultimately succeeded in improving diffuser performance.



#### *1.4.5 Trapped Vorticity Flow Control in Diffusers*

A flow control approach used in the offset diffuser study (Chapter 4) relies on the existence of trapped vorticity in a diffuser, which would occur naturally in an actual inlet system as a result of boundary-layer separation. Manipulation of trapped vorticity is not new in either external or internal aerodynamics. Many interesting concepts have been developed for external aerodynamics, predominantly motivated by the notion that airfoil circulation can be either enhanced or reduced when vorticity becomes bound to the surface [45]. Early work by Hurley [46] considered improvements of low-speed characteristics of a nominally high-speed airfoil profile by introduction of a large forward flap that would trap a vortex over the leading suction side. In order to maintain ‘free-streamline’ attachment over the downstream flap surface (and full confinement of the vortex), Hurley utilized steady jets over the leading Coanda surface. Another concept, proposed by Kasper and published by Cox [47], made use of upstream and downstream flaps without any active control. Rossow [48] expanded on the application of trapped spanwise vorticity along the leading edge by utilization of end-plate suction for vortex stabilization and claimed an increase in the resulting lift coefficient of up to 10. More relevant to the present study, several prior investigations considered utilization of trapped vorticity in diffusers, primarily motivated by reduction of total-pressure losses. Ringleb [49] proposed the cusp diffuser, which is characterized by a vortex-shaped cusp on a portion of the diffuser meant to generate a stationary vortex rotating in the direction of the flow. In practice, it was found difficult to maintain a stable standing vortex, which was attributed to the skin friction within the cusps [3, 50]. In an attempt to improve upon the cusp diffuser, a trapped-vortex diffuser was developed by Heskestad [51], and further by Adkins [50]. This design utilized

an annular vortex chamber to trap low-momentum fluid which would otherwise lead to separation downstream in the diffuser. To maintain a vortex in the chamber, it was bled continuously such that flow from the diffuser constantly energized the vortex. Designed primarily for gas turbine combustors, it was surmised that about 3% of the bleed air flow would be needed. Subsequently, Adkins, Matharu, and Yost [52] refined this design to create a ‘hybrid diffuser’ which provided the same benefits with a third of the bleed, and also can achieve a 25% increase in recovery, relative to a conventional divergent duct of the same length, with no bleed. More recently, numerical investigations have been performed by Mariotti, Buresti, and Salvetti [53] on the effect of altering a two-dimensional diffuser surface to include contoured cavities. It was found that inclusion of one cavity increased total-pressure recovery by 6.9% and two cavities led to an increase of 9.6%.

#### *1.4.6 Flow Control in Inlets*

Aircraft that require high performance in both low- and high-speed conditions need a variable inlet. The vertical and/or short take-off and landing (V/STOL) fighter type aircraft were among the first to encounter this issue, because they must both hover (high inlet speed, zero free-stream Mach number) and cruise at a high speed. In the 1960s, during the development of the prototype Hawker P1127 V/STOL aircraft, an inflatable lip was designed and tested [54]. The idea was to inflate a rubber balloon on the lip to approximate a bell-mouth during low-speed operation and deflate it to create a sharp lip for high-speed operation. After testing, this solution was determined to be not feasible because the rubber would ripple and tear at high speeds.

The auxiliary inlet with passive flaps (blow-in doors) were ultimately chosen and implemented on Harrier production aircraft [55]. An auxiliary inlet is a bell-mouth-like slot going around the circumference of an inlet. This increases the inlet area and allows some mass flow to bypass the sharp lip, resulting in higher pressure recovery. Blow-in doors are passive hinged covers for the slots, which open with the pressure difference is lower inside the inlet (low-speed operation), and close when the opposite is true (high-speed operation). This approach, of creating extra inlet area for low speeds, has been used many times since its development. It has been used on transport aircraft, like the Boeing 707, 737-200, and 747, in addition to B-52, and MiG-29 [56]. The blow-in door was integrated into the General Dynamics YF-16 prototype fighter in the 1970s to provide extra stall margin during takeoff and landing [57]. Tests of variable cowl slots were conducted on an axisymmetric mixed-compression supersonic inlet in 1985 by Powell et al. [58] at freestream Mach numbers of 0, 0.1, and 0.2. They found that the slot was effective at reducing flow separation associated with the sharp lip at low speeds and was able to reduce the total pressure recovery and steady-state distortion. Garzon [59] investigates the benefits of integrating a translating cowl onto a supersonic business jet to improve low speed performance with CFD simulations at freestream Mach number 0.1. It was found that pressure recovery was improved but at a cost of increased pressure distortion, which was attributed to interaction with a boundary-layer diverter.

## CHAPTER 2. EXPERIMENTAL SETUP AND METHODOLOGY

### 2.1 The Wind Tunnel

The experimental investigations were performed in an open-return, pull-down, subsonic wind tunnel with exchangeable test sections as shown in Figure 2.1. The tunnel is driven in suction by a 150 hp blower and in most configurations the air enters the test section through an inlet contraction (contraction ratio 106:1) and exits the tunnel through a controlled low pressure drop heat exchanger. The investigations of the isolated diffuser discussed and presented in Chapters 3, 4, and 5 utilize the inlet contraction upstream of the diffuser's throat (Figure 2.1).

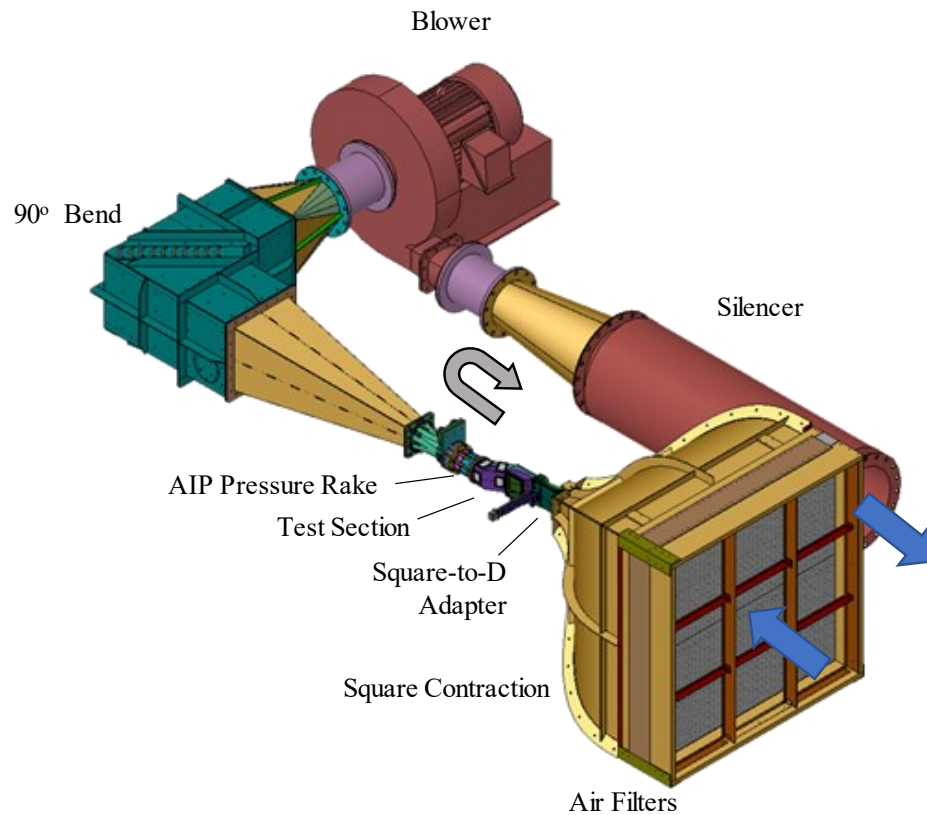


**Figure 2.1 Pull-down wind tunnel.**

The 106:1 contraction inlet cross-section measures 1.78 m x 1.78 m, and is reduced to 17.3 cm x 17.3 cm. The square outlet of the contraction is connected to the diffuser's D-shape inlet (Figure 2.4) through an adapter section (Figure 2.2). The diffuser section is described in Section 2.2, and is followed by a section of a rake of 40 probe total-pressure tubes which are used to measure the mass flow rate through the facility (see Section 2.3.1.1), and quantify the pressure field at the plane where an aircraft engine would be installed, called the Aerodynamic Interface Plane (AIP). Following the pressure rake section, the flow is expanded through a diffuser (not the test section) and a 90 degree turn into the system's blower (150 HP, New York Blower, powered by Rockwell Automation GV6000 variable frequency drive). The blower's outlet is connected to a flow silencer (AAF TDM 24-4N) to reduce noise, and a water-cooled low-pressure drop heat exchanger (not shown) that is cooled by a dedicated chiller.

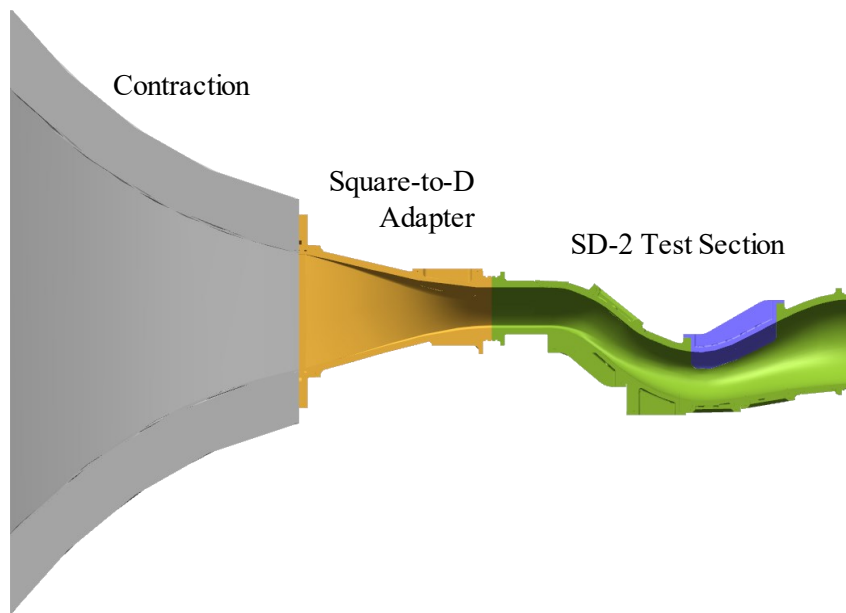


**Figure 2.2 Section view of the SD-2 test section attached to the contraction and square-to-D adapter. Not all of contraction is shown.**

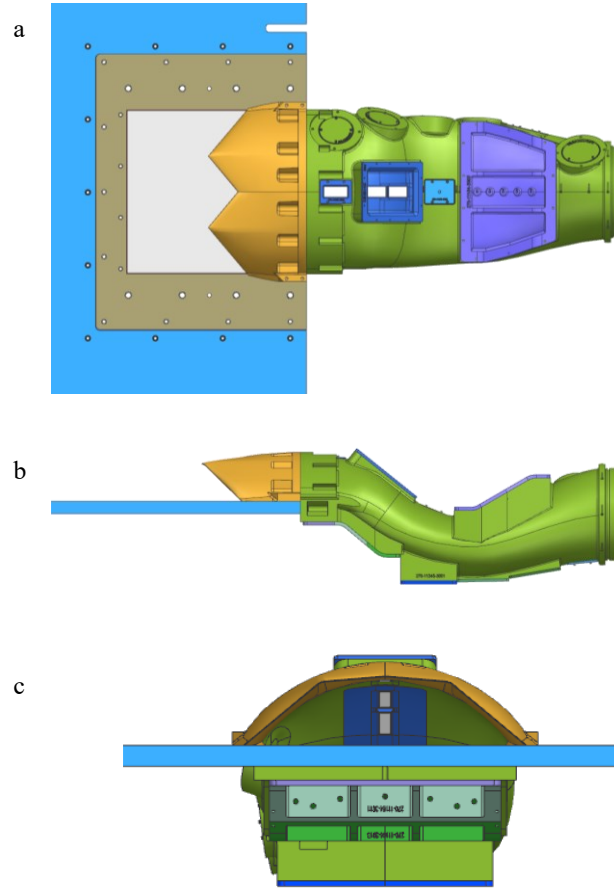


**Figure 2.3 SD-2 test section with cowl inlet and ground plane top view (a), side view (b), and front view (c), isolated from wind tunnel.**

In Chapter 6, a cowl inlet and ground plane replace the 106:1 area-ratio contraction to better approximate the flow in a diffuser with an inlet that is integrated onto an aircraft wing. Three views of the inlet integration are shown, with the top view (Figure 2.3a) showing the cowl serrated edge and the ground plane with glass behind the cowl for PIV. To fully visualize the geometry, the side view (Figure 2.3b) and front view (Figure 2.3c) are included. The ground plane measures 1.91 m x 1.91 m and is supported by L brackets on the floor and I-beams above. It is made from 19 mm plywood and has 16 mm thick glass window for PIV measurements inside the cowl inlet.

## 2.2 Diffuser Test Sections

Two different diffuser configurations which have simplified geometries of realistic aircraft subsonic diffusers, denoted SD-1 and SD-2, were built by the Boeing Company for the present investigations (Figure 2.4a-d). Figure 2.4 shows two views of the diffusers, with color coding for the throat (dark blue, solid), center and side-wall lines (blue, solid), and AIP (light blue, dashed). The first configuration was an offset diffuser (SD-1, Figure 2.4a-b, cf. Ch. 3) having a circular outlet with diameter  $D = 12.7$  cm. The diffuser's inlet (throat) has a D-shape that is  $1.33 \cdot D$  wide and  $0.7 \cdot D$  high as shown in Figure 2.4b. The outlet mates to the 40-pressure probe section (i.e., the AIP) resulting in an expansion ratio of 1.07. The total length of the diffuser is  $3.08D$ , and its center-to-center offset is  $1.0D$ . The diffuser's body was machined from aluminum and it has multiple removable inserts for flow control modules and optical access for PIV (cf. Ch. 3). The diffuser centerline has a distinct recess, which is a modification made to induce a flow similar to that of a boundary-layer ingesting (BLI) diffuser.

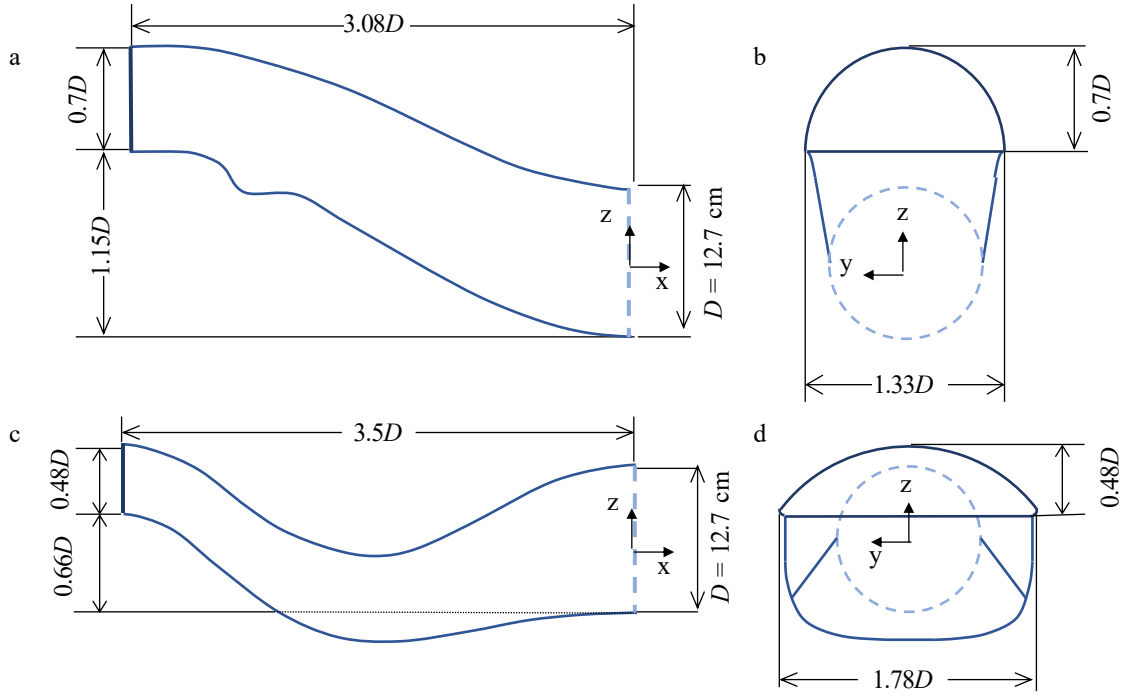


**Figure 2.4 Side and front views of diffusers SD-1 (a, b) and SD-2 (c, d), and coordinate system.**

Diffuser configuration SD-2 (Figure 2.4c and d, cf. Chapters 4, 5 and 6) is a more aggressive, two-turn serpentine diffuser. Its exit plane diameter is  $D = 12.7$  cm (dashed) and its D shape inlet (throat) is  $1.78D$  wide and  $0.48D$  high, its length is  $3.5D$  and it has an expansion ratio of 1.26. Diffuser SD-2 was manufactured using stereolithography and several versions were constructed over time with different optical access inserts, and different attachment arrangements for attaching the contraction (Chapter 4 and 5) and later on the inlet cowl and ground plane (Chapter 6). Table 2.1 shows the test section and inlet configuration that corresponds to each research chapter. In addition to the diffuser geometries, Figure 2.4 shows the common global coordinate system used in this thesis. The origin is at the center of the AIP, with  $x$  being the streamwise dimension, pointing downstream, and  $y$  and  $z$  being spanwise dimensions.



**Table 2.1 Test section configurations for each research chapter.**

<b>Chapter</b>	<b>Test Section</b>	<b>Inlet Configuration</b>
3	SD-1	Contraction
4,5	SD-2	Contraction
6	SD-2	Cowl Inlet

## 2.3 Diagnostics

### 2.3.1 Pressure Measurements

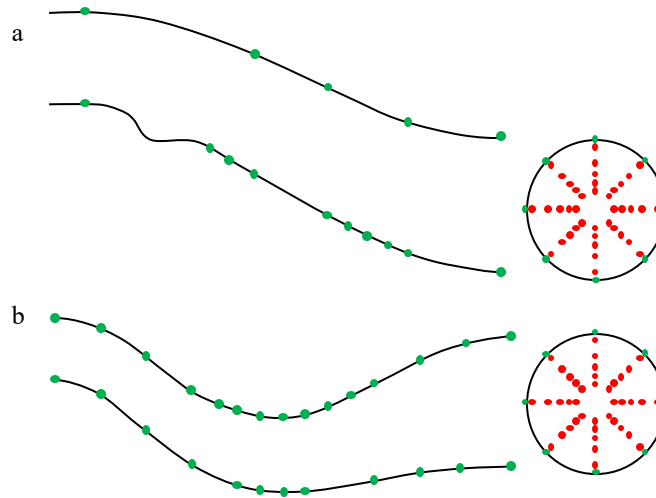


**Figure 2.5 Static (green) and total (red) pressure port locations on the SD-1 (a) and SD-2 (b) diffuser geometries, centerlines (left) and AIP (right).**

#### 2.3.1.1 Time-Averaged Pressure Measurements

Time-averaged static pressures are measured along the centerline of each diffuser and around the circumference of the AIP. The locations of the static pressure ports are shown in Figure 2.5 for SD-1 (Figure 2.5a) and SD-2 (Figure 2.5b), which are shown in green. The number of ports and location depend on the design of the test section, but there are always centerline ports at the throat and AIP. At the AIP, there is a ring of eight equally spaced ports which are aligned to the eight total pressure rakes. Each total-pressure rake contains five ports, spaced to represent equal areas according to the ARP1420B SAE standard. These ports are also shown in Figure 2.5 (red).

An image of the rake used is shown in Figure 2.6a, which shows the eight rakes, each containing five probes. This array is used to generate a total pressure color raster plot as shown in Figure 2.6b. The quantity plotted is the ratio of the measured total pressure to the reference total pressure, or ambient pressure, that is measured with a barometer. With the forty-point measurements, the plot is generated by interpolation to create a visualization of the whole plane. Each individual port is assigned a coordinate for the ring  $i$  and rake  $j$  on which it is located. The installation of the pressure rake in the facility is shown in Figure 2.6c, which is placed just downstream (to the right) of the diffuser test section.

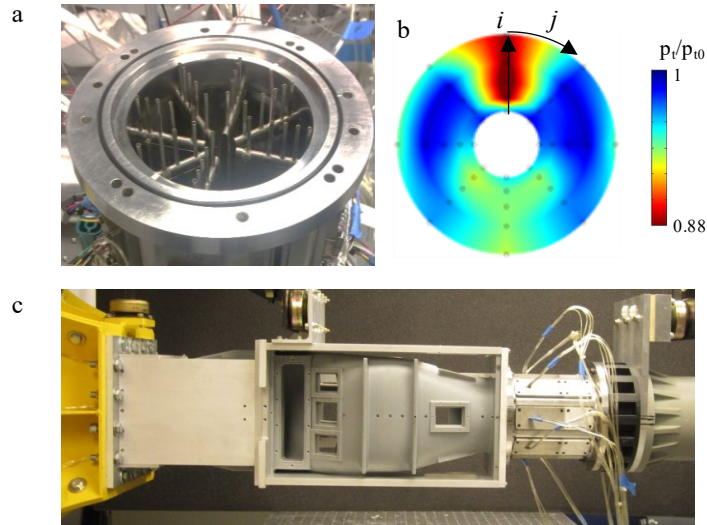


**Figure 2.6** Photo of the AIP total pressure rake (a), a total pressure color raster plot generated with rake data (b), and a photo of the rake installed at the downstream (right) end of diffuser test section (c).  $i$  and  $j$  are AIP total pressure port coordinates for ring  $i$  and rake  $j$ .

The time-averaged static pressures were measured using a pressure scanner (PSI Netscanner). The scanner system consists of a 98RK-1 scanner interface rack, which houses 5 pressure scanner modules, each containing 16 silicon piezoresistive sensors. The pressure range of each module is 34.5 kPa. The scanner can make multiple samples internally and return the averaged values. This feature is used in all experiments, where each sample received by the acquisition computer is an average of 64 samples that the scanner measured. Typically, at least 100 of these samples are taken and averaged, resulting in an effective average of 6400 samples. The accuracy of the PSI system is quoted as  $\pm 0.05\%$  full scale after rezeroing, which is conducted before every pressure measurement acquisition run. This accuracy specification means an absolute accuracy of  $\pm 17.25$  Pa for the previously mentioned modules. A test of the pressure system RMS was conducted by measuring instantaneous ambient pressure with an ambient reference (a value that should equal zero), after disabling the internal averaging mentioned above. The

results found an RMS of 5 Pa, which is the inherent fluctuations associated with the pressure sensors.

Because of the module range limit, and the fact that the facility can reach pressures that exceed the limit relative to atmosphere, a known reference pressure lower than ambient must be supplied to lower the measured pressure difference into the 34.5 kPa range. This is achieved by measuring a pressure along the centerline, often chosen to be the throat static pressure on the top surface, with a temperature-compensated differential transducer (MKS Baratron), while also splitting the pressure signal to connect to the reference pressure line of the pressure scanner. The measured pressures from the pressure scanner are then offset by the value produced by the secondary transducer. The differential transducer (MKS Baratron) measures the reference pressure relative to ambient, and ambient pressure is measured with a Princo Fortin mercury barometer. This barometer is manually inspected before each acquisition run to provide the final offset value to the pressure measurements.

The pressure scanner (PSI Netscanner) is interfaced to the local data acquisition computer using an ethernet connection while the differential transducer (MKS Baratron) is sampled directly using an A/D board (National Instruments) and data acquisition software (National Instruments LabView). The previously discussed internal averages are produced at about 3 Hz (not time-resolved), where acquisitions of 100 averages taking 33 seconds.

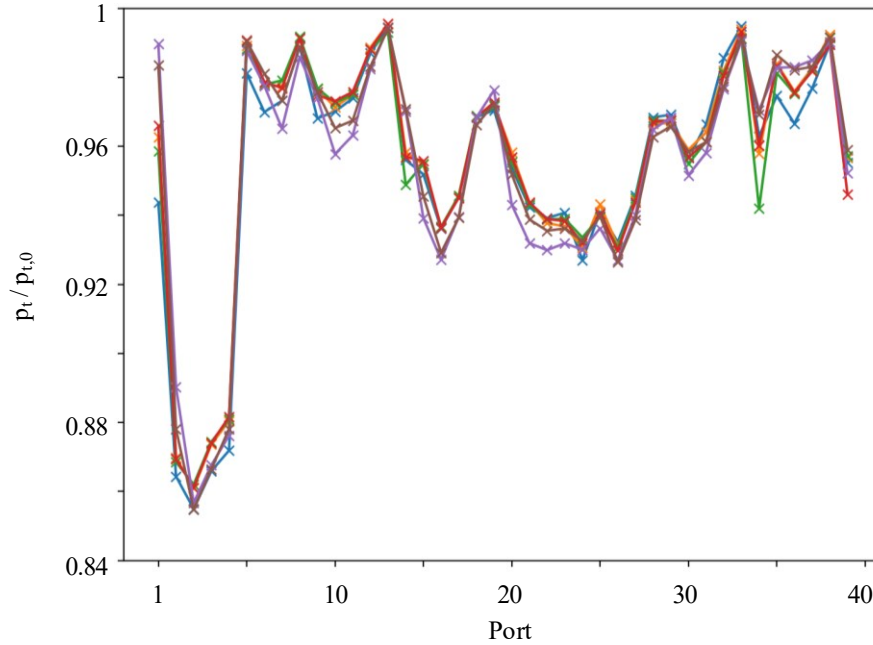


**Figure 2.7** Repeated measurements of AIP total pressure ratio of base flow at  $M_{AIP} \approx 0.54$  in SD-2 diffuser on dates 4/4/2016, 9/21/2016, 1/12/2017, 1/23/2017, 8/29/2017, 11/14/2017.

To further characterize the experimental repeatability of the steady-state pressure measurements, total pressure measurements from the SD-2 diffuser (cf. Figure 2.4) across a wide span of dates is plotted in Figure 2.7. The total pressure ratio (total pressure divided by ambient pressure) is plotted in a line plot by port in Figure 2.7 at  $M_{AIP} \approx 0.54$ . This plot shows that over the period of 19 months, a case can be reasonably repeated. Throughout this time, many adjustments were made to the facility, including the usage of different inserts (that have the same nominal geometry), and different instrumentation for various experiments. Most ports have very good agreement across the data sets, with a percent error of 1% from the mean of the shown datasets, with a couple ports reaching 2%.

### 2.3.1.2 Time-Resolved Pressure Measurements

Time-resolved measurements of the total-pressure were acquired in two separate entries during the present research (Chapters 4 and 6) using a dedicated system that was brought to the laboratory by Boeing personnel. The Boeing system is an identical replacement of the AIP pressure rake (Figure 2.6a) and its 40 total pressure tubes are each integrated with a high-frequency pressure transducers (Kulite XCEL-072) that allow for simultaneous sampling of the total pressures at up to 100 kHz. The differential transducers used have a range of 170 kPa, and a specified a maximum accuracy range of +/- 850 Pa.

The instantaneous pressure measurements are recorded using a dedicated data acquisition system. The Boeing rake also includes integrated total pressure probes for time-averaged measurements of the total pressure using the PSI scanner described in Section 2.3.1.1 to be used as the time-averaged reference for each of the time-dependent measurements.

### 2.3.1.3 AIP Derived Quantities

The AIP total pressure rake (time-averaged or time-resolved) is used to calculate quantities that describe pressure loss, AIP pressure uniformity/symmetry, and Mach number. Pressure loss is described by pressure recovery, which is the average of the forty total pressures scaled by ambient pressure. Pressure uniformity and symmetry is described by distortion, which is higher when there is more nonuniformity and more asymmetry. In particular, the main distortion parameter studied is  $DPCP_{avg}$ , which is the face-averaged circumferential distortion. The calculation is detailed in the SAE standard document ARP1420. The AIP Mach number is calculated from the total and static pressures with

Equation 2.1, where  $\overline{P}_T$  is the average AIP total pressure,  $\overline{P}_S$  is the average AIP static ring pressure, and  $\gamma$  is the heat capacity ratio of air.

$$M_{AIP} = \sqrt{\frac{2}{\gamma - 1} \left( \left( \frac{\overline{P}_T}{\overline{P}_S} \right)^{\frac{\gamma-1}{\gamma}} - 1 \right)} \quad 2.1$$

### 2.3.2 Pressure Sensitive Paint

#### 2.3.2.1 Background

Pressure sensitive paint (PSP) measurements, based on molecular photoluminescence [60], are conducted over the flow control module installed in the second turn of the diffuser yielding spatial distribution of the static pressure over the flow control insert (capturing the central separation domain and the outboard spanwise attached domain). In this experimental technique that was developed in the 1980s and 90s (Peterson and Fitzgerald [61], Kavandi et al. [62]) and later refined by Liu and Campbell [60], and Bell [63], the illuminated paint absorbs and emits light proportional to oxygen and thermal quenching at the surface. The thermal bias is typically compensated for through a second component of the paint that is only sensitive to temperature (TSP), where, in principle, both the PSP and TSP components have identical temperature sensitivity such that the paint/surface pressure ratio is related to the PSP and TSP intensity ratios as in Equation 2.2 [63, 64], where the subscripts  $P$  and  $T$  refer to the intensities of the PSP and TSP components and subscript  $o$  refers to the tunnel off case. The coefficients  $A$  and  $B$  must be determined experimentally through calibration.

$$\frac{I_{P,o}}{I_P} \cdot \frac{I_T}{I_{T,o}} = A + B \frac{p}{p_o} \quad 2.2$$

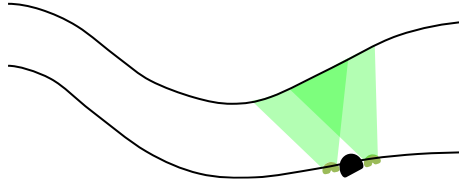


**Figure 2.8 Schematic of the integrated camera and UV LEDs illuminating the PSP domain on the SD-2 diffuser second turn.**

#### 2.3.2.2 Procedure

In the present experiments the PSP is used to measure the surface pressure over the first and second turns turn of the SD-2 diffuser (as shown schematically on the second turn in Figure 2.8). The paint is illuminated using a UV (400 nm) LED array, and the fluorescence is captured through an optical access port using a miniature camera integrated into the diffuser wall (Figure 2.9) such that the PSP surface is in the field of view. Using the ambient conditions as a reference, the light intensity is measured simultaneously with an array of static pressure ports over an insert in the diffuser's surface range of flow rates through the diffuser.

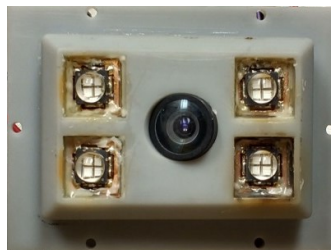


**Figure 2.9 Flow-facing side of the integrated stereolithography PSP insert containing a camera and four LEDs.**



The paint used is a dual-luminophore paint by Innovative Scientific Solutions, Inc. (ISSI) called BinaryFIB. It has a response time of 300 ms, an ideal excitation wavelength of 400nm, and emission wavelength range from 500 nm to 720 nm. Temperature sensitivity is 0.03% per degree Celsius, and pressure sensitivity is 0.6% per kPa. This paint was chosen because it is dual-luminophore – it contains TSP in addition to PSP molecules, such that temperature can be corrected for. In order to correct, however, two different wavelengths must be acquired simultaneously – one for pressure (~650 nm, red) and one for temperature (~550 nm, green). When the paint is excited by 400 nm light, it will emit light at those two other wavelengths, with an intensity proportional to the temperature and pressure on the surface.

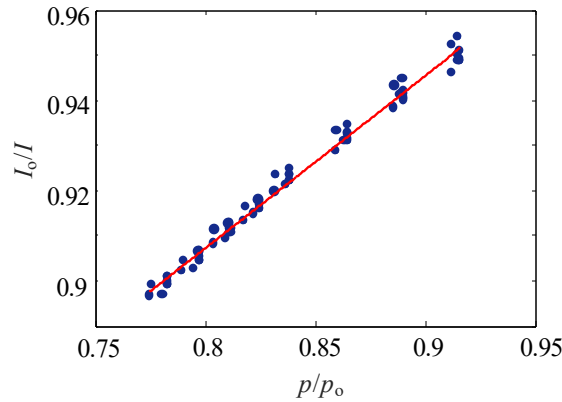


**Figure 2.10 Pressure sensitive paint calibration curve relating intensity ratio to pressure ratio.**

The PSP acquisition system consists of a camera and UV LEDs which are activated when the camera shutter is opened. Triggering is implemented in LabView, while the acquired image sequence is acquired and saved in Matlab. Using averaged tunnel-off and tunnel-on images, as well as simultaneous static pressure point measurements on the PSP surface, a linear calibration curve is fit (coefficients A and B are chosen for Equation 2.2)

to relate the change of intensity ratios to the change in pressure. This curve is then used to convert the images into pressure by isolating  $p$  on one side of Equation 2.2. An example calibration curve is shown in Figure 2.10, showing points associated with multiple point static pressure measurements at multiple flow rates, and the line fit through them to create the calibration curve. An example PSP pressure color raster plot from Chapter 4 is shown in Figure 2.11, which shows the previously mentioned static pressure ports (dots on lower half of image) on the surface used to create the calibration. See further detail of the PSP system and procedure in the appendix.

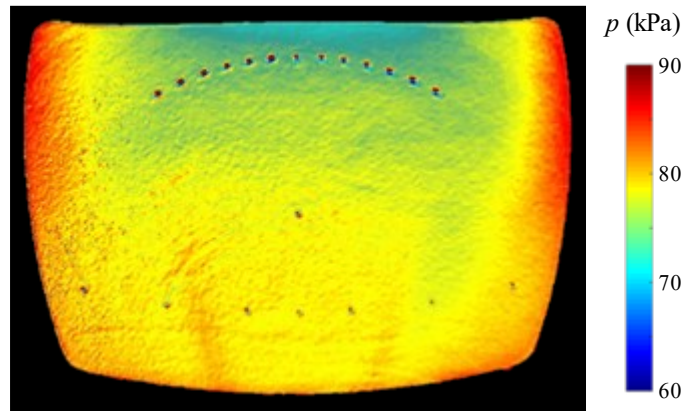


**Figure 2.11** PSP pressure color raster plot, showing an inactive jet array on top, and static pressure ports in central and lower regions.

### 2.3.2.3 Uncertainty and Repeatability

Many factors can contribute to the uncertainty of pressure sensitive paint measurements. This includes the uncertainty of every piece of equipment in the setup – camera shot noise, LED brightness consistency, and temperature variation are some examples. The paint used in this thesis, as noted in the above section, is inherently self-correcting with an embedded TSP component. The PSP component is designed by ISSI to

be equally as sensitive to temperature as the TSP component, while the TSP is designed to not have pressure dependence. The temperature variation found from the TSP is divided from the pressure signal indicated by the PSP, such that the final quantity (LHS of Equation 2.2) used to correlate to the static pressure simultaneously measured is independent of temperature ( $p$  on RHS of Equation 2.2). The division of the tunnel-off image also removes variance between experiments. The tunnel-off image quantifies the spatial variation due to light nonuniformity, paint non-uniformity, and camera view angle that are inherent to the experiment. This is then divided from the tunnel-on image, which removes these sources of spatial inconsistency.

### 2.3.3 *Particle Image Velocimetry*

High-speed planar and stereo particle image velocimetry (PIV and SPIV, respectively) were used in the present investigations to quantify velocity fields. Both types of PIV use a single laser sheet to illuminate seeding particles (fog). The beam from the laser head is guided by mirrors and lenses to create a thin laser sheet in the interrogation domain. An example laser path is shown in Figure 2.12, which shows the top and side views of a laser path that uses two spherical lenses, two mirrors, and a cylindrical lens to focus and spread the laser into a laser sheet.

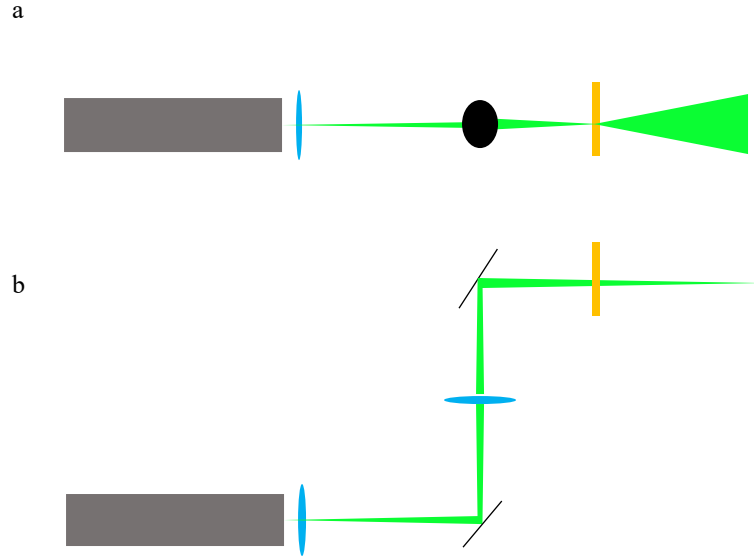


**Figure 2.12 Top view (a), and front view (b), of laser path from laser (grey), through multiple spherical lenses (blue), mirrors (black), and a cylindrical lens (orange).**

#### 2.3.3.1 Planar PIV

Planar PIV was used to measure the velocity field in cross stream planes along the center plane of the diffusers SD-1 and SD-2. In internal flows, PIV can be particularly challenging because optical access for both the laser and camera for each desired PIV interrogation domain must be designed into the test section when it is built. In the present investigations, optical access in SD-1 and SD-2 was enabled by using removable inserts with optical flat glass windows that were manufactured using stereolithography (SLA). Flat optical glass is integrated into the curved geometry by introducing fairings to minimize the disruption of the flow by sharp glass. Due to geometrical constraints, the camera often must have a non-perpendicular angle to the laser sheet, and a tilt angle must be introduced between the camera and lens to correct the focusing plane (Scheimpflug principle).

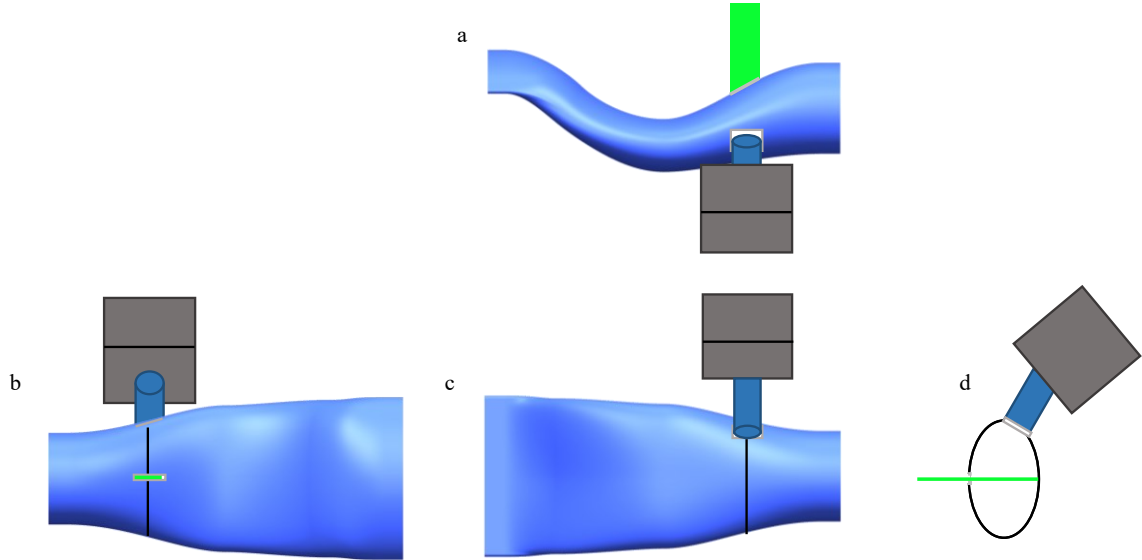


**Figure 2.13 Top (a), back (b), front (c), and section (d) views of the camera (gray), lens (blue), and laser (green) setup for diffuser (blue) planar PIV.**

The internal 2D PIV is conducted through optical access ports as shown in the diagram in Figure 2.13. The laser enters through the diffuser wall to illuminate the PIV interrogation domain. The camera images illuminated particles through a second optical access port and uses a tilt adapter to compensate for the angle between the camera and laser sheet. The equipment used consisted of a Quantronix Darwin Duo dual-cavity high speed YLF 527nm laser, with each cavity capable of a frequency up to 4 kHz and a pulse energy up to 25 mJ. The laser beam is shaped into a thin sheet with an array of spherical and cylindrical lenses (Figure 2.12), the configuration of which changes in each setup. A schematic of an example laser sheet is shown in Figure 2.13b and d, where the laser shines through an optical access port, and a camera uses a separate optical port to take images.

Two different Vision Research cameras were used in planar PIV experiments - the Phantom v12.1, and Phantom VEO 710L. Both models have a resolution of 1280 x 800, 12-bit pixel depth, and a pixel size of 20 microns. Typically, a tilt adapter and a Nikon

105mm f/2.8 Micro-Nikkor lens are mounted to the cameras. A LaVision high-speed programmable timing unit (PTU) is used to synchronize the camera and laser triggers. Particles to seed the flow were generated by a commercial theatrical fog blower (Rosco Vapour). PIV was conducted at frequencies from 1-2 kHz for one or more seconds.

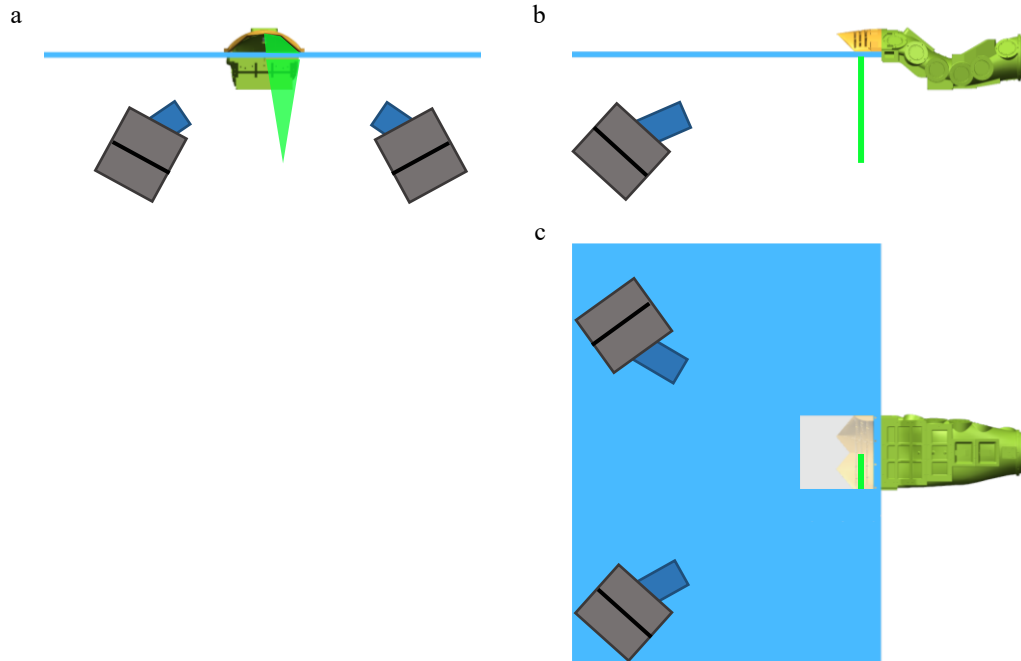


**Figure 2.14 Left (a), front (b), and bottom (c) views of stereo PIV camera and laser setup.**

### 2.3.3.2 Stereo PIV

Stereo PIV measurements (Chapter 6) were employed to investigate the flow through the cowl inlet (cf. Figure 2.3). The orientation of the plane is such that the bulk flow velocity component is the through-plane PIV component  $u$ , as shown in Figure 2.14.

In these experiments, a pair of Phantom VEO 710L cameras were used, along with the Photonics DM30 dual cavity high speed YLF laser, which can reach a frequency of 10

kHz and pulse energy of 65mJ. One of the biggest differences between this stereo setup and previous planar setups is the angle of the cameras relative to the laser sheet. Typically, the camera is angled on one axis relative to the laser sheet, but the cameras in this setup are angled on two axes (Figure 2.14b and c). Because of this, the axis along which the tilt must be applied is no longer obvious. It is still possible to fully correct for the angle and focus on the PIV plane, but the process is iterative. The tilt axis must be adjustable relative to the camera sensor, such that an optimal tilt angle can be found that corrects for both the angle of the lens shown in Figure 2.14b, and the angle shown in Figure 2.14c.

An example of the stereo PIV data processing steps is shown in Figure 2.15. A raw image from the cowl inlet SPIV (Chapter 6) is shown in Figure 2.15a, where a corner of the cross-section is shown in the lower right, and the centerline is close to the left edge. This image contains many undesirable artifacts like intense laser reflections along the top inner wall, and extra reflection repetitions from the thick optical glass. This is addressed with a high-pass Butterworth filter, which removes features that oscillate at lower frequencies in time, like reflections, and keeps high-frequency information (particles), the result of which is shown in Figure 2.15b. See details on Butterworth filtering algorithm at Ref. [65], which is built into LaVision Davis software. This filtered image is processed to produce a 3-component vector field  $(u,v,w)$ . An example SPIV vector field with a contour of through-plane velocity ( $u$ ), and vectors showing in-plane velocity ( $v,w$ ) is shown in Figure 2.15c.

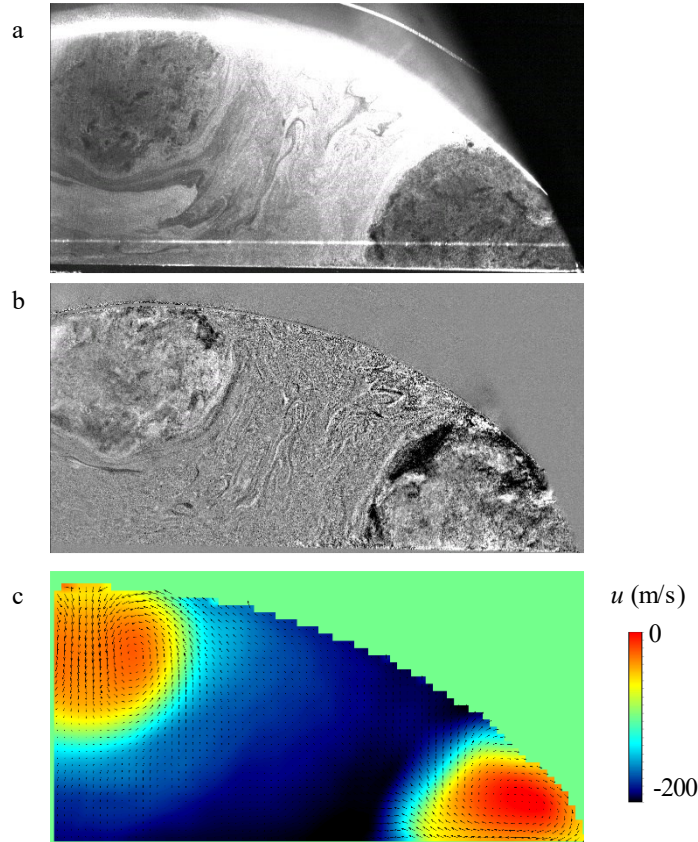


**Figure 2.15** Example raw PIV image (a), image after high-pass Butterworth filtering (b), and time-average SPIV field, colored by  $u$  velocity with  $v, w$  in-plane vectors (c).

#### 2.3.4 Surface Oil-flow Visualization

Oil paint is used to visualize flow topology on test section surfaces. The visualization is conducted on a surface that is painted black using white paint for contrast. Linseed oil and titanium dioxide white oil paint are mixed at a ratio that achieves an optimum viscosity for a given flow speed, such that the oil is thin enough to flow and create streaks, but thick enough to not be blown away completely. The paint is applied to the surface using a sponge, applying it uniformly where paint streaks are desired. The near-surface airflow leads to the formation of streaks in the oil layer where the flow is attached, and does not move the oil where the flow is slow (ostensibly below a threshold that depends



on the oil viscosity) or separated. This technique has been invaluable in characterizing diffuser flow and prototyping flow control devices.

### 2.3.5 *Uncertainty*

#### 2.3.5.1 Uncertainty of the Time-Averaged Pressure Measurements

As noted in Section 2.3.1.1, each of the pressure scanner modules has an absolute accuracy of  $\pm 17.25$  Pa for a single measurement. In the present investigations,  $N = 6,400$  instantaneous pressure measurements are sampled at about 200 Hz to obtain the time-averaged pressure. The computed propagated error is proportional to  $1/\sqrt{N}$ , and therefore, the error associated with the time-averaged pressure is well below 1%.

#### 2.3.5.2 Uncertainty in Particle Image Velocimetry

Errors in PIV measurements have been investigated by several authors [66, 67]. In the present analysis, it was intended to compute the compounded errors that are associated with the optical setup, the electronic hardware, and the data processing by measuring the nearly uniform incoming flow upstream of the cowl inlet. Unfortunately, owing to complications associated with the closure due to the COVID-19 pandemic, it was not possible to take measurements upstream of the inlet, and therefore the measurements within the core flow in the PIV plane at the upstream edge of the cowl (Chapter 6) were used to estimate this uncertainty. Clearly, the core flow within this section is already affected by potential fluctuations that are induced by the formation of the secondary vortices, and so the computed uncertainty represents an upper bound. The uncertainty is estimated by computing the fraction of the RMS fluctuations of the streamwise velocity within the core

flow that has negligible vorticity concentrations. Based on the PIV measurements at  $M_{AIP} = 0.4, 0.5$ , and  $0.6$ , the RMS fluctuations of the streamwise velocity were below 4% of the central core flow.

## 2.4 Flow Control Techniques

The present investigations employed two flow control techniques: fluidic oscillating jets and aerodynamic bleed.

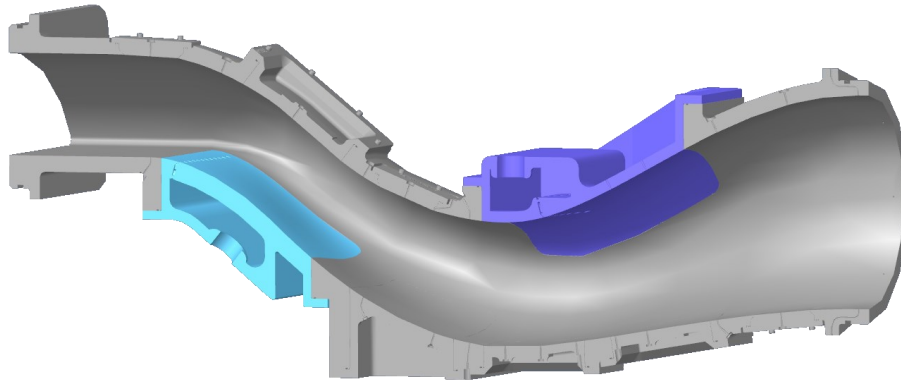


**Figure 2.16** Section view of SD-2 test section with integrated flow control inserts on the first and second turns.

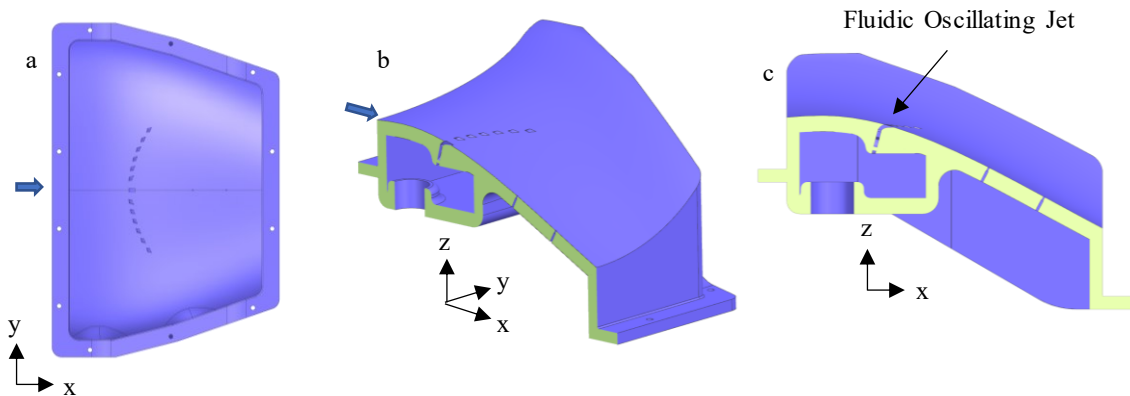


**Figure 2.17** Top view (a), isometric section view (b), and side section view (c) of flow control insert containing array of fluidically oscillating jets and embedded plenum. Arrow describes flow direction along centerline. Coordinate directions are included for reference.

### 2.4.1 Fluidic Oscillating Jets

The primary active flow control device used in the present study is the fluidically oscillating jet actuator, which is a device that exploits internal flow instability to form a sweeping jet using a steady air supply. Typically, a custom insert is designed to replace a stock insert of a test section, which has the same interior surface but with an integrated array of fluidic oscillating jets (cf. Figure 2.16). A design of a custom insert for SD-2, used in Chapter 4 and 6, is shown in Figure 2.17. Other examples of flow control inserts are the SD-1 insert shown in Figure 3.8 and the first-turn flow control insert in SD-2 shown in Figure 5.1a. A plenum (or cavity), shown in Figure 2.17b and c, distributes air evenly to the jets from a compressed air supply, which enters plenum through the hole shown in bottom of plenum in Figure 2.17b and c. The frequency of oscillation is in the range of 6-8 kHz and varies with flow rate.

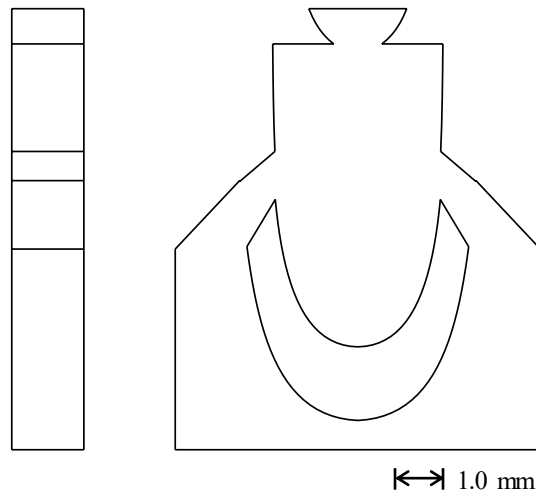


**Figure 2.18 Drawing of no-feedback-loop fluidic oscillating jet, with length scale.**

In the present investigations, the throat of a single oscillator measures  $1.5 \times 1.0$  mm, the exit orifice measures  $1.5 \times 2.0$  (Figure 2.18), and typical jet spacing is 6.3 mm center-to-center (Figure 2.17a). The jets are placed beneath the surface of the flow control insert, oriented normal to the surface with a channel that turns the exiting air tangential to the surface (Figure 2.17c). The array of tangential jets is effective at attaching naturally separated flow (Chapter 4). To quantify the jet mass flow input, the mass flow coefficient  $C_q$  used, which is shown in Equation 2.3, where  $\dot{m}_{AFC}$  is the total flow rate through the jet array, and  $\dot{m}_{TS}$  is the total flow rate through the test section. The mass flow rate through the jets is calculated by multiplying standard air density by the standard volume flow rate which is measured by an Aalborg gas flow meter that has a range of 1000 SLPM and an accuracy of +/- 15 SLPM. Further detail of the behavior of this fluidic oscillating jet geometry can be found in [44, 68], and general concepts of fluidic oscillators in [69].

$$C_q = \frac{\dot{m}_{AFC}}{\dot{m}_{TS}} \quad 2.3$$

#### 2.4.2 Aerodynamic Bleed

Aerodynamic bleed is a method of exploiting an existing pressure difference on two sides of a body by adding a slot or channel between them to enable flow from the high-pressure side to low-pressure side. This method has been implemented on airfoils [70] to reduce drag and/or increase lift, on and inlets to reduce losses associated with turning of air around an inlet with a sharp lip [55]. It has the inherent limitation that the flow rate cannot be controlled, as it is governed by the pressure difference and losses through the

channel. However, they can be opened and closed dynamically, depending on flow conditions. In cowl inlets, flaps that open and close bleed slots (blow-in doors) are used to allow air through in subsonic flow, when the supersonic inlets have high losses (see Chapter 1).

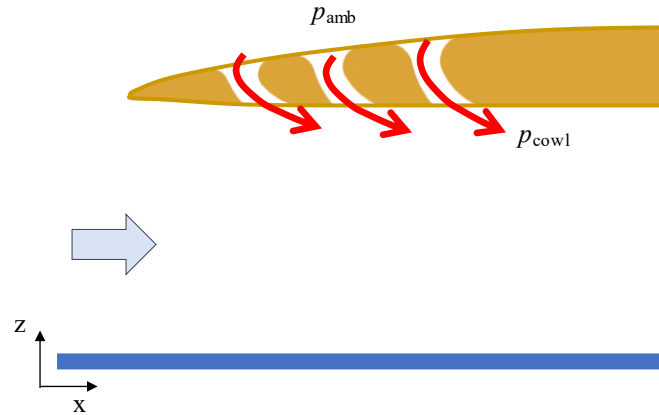


**Figure 2.19 Schematic of the cowl aerodynamic bleed through the three arrays of slots. Coordinate directions are included for reference.**

In Chapter 6, aerodynamic bleed slots are integrated into an inlet cowl to increase the inlet area and introduce a secondary source of inlet flow (auxiliary inlet). A sliced view of the slots integrated into the cowl inlet is shown in Figure 2.19, which have a bell-mouth-like design on the outer surface to minimize losses, and are angled downstream on the inner surface. This design was originally used in the context of Harrier vertical and/or short take-off and landing (V/STOL) aircraft and documented in Ref. [55].

## CHAPTER 3. OFFSET DIFFUSER

The present investigations were initiated in a mild, low-expansion offset diffuser (denoted SD-1), which did not exhibit an internal separated flow domain nor global counter-rotating secondary flow. This segment of the investigations had two primary objectives. First, to demonstrate the coupling between a region of trapped spanwise vorticity concentration mimicking local separation and the formation of a counter-rotating streamwise vortex pair that is typical of aggressive offset diffusers. The second objective was to demonstrate that active control of the trapped vorticity can indirectly control the evolution of the streamwise vortices. In order to utilize this geometry as a test bed for this flow control approach, the inner diffuser surface was modified to include an integrated recess along the concave surface at the flow turn to form concentration of trapped vorticity whose upstream and downstream edges each nearly span the inner (concave) flow surface. To manipulate the trapped vorticity, an array of discrete fluidic oscillating jets was placed upstream of the recess, issuing tangentially to the surface, and was contoured to match the upstream boundary of the separation.

### 3.1 Introduction

As noted in connection with Figure 2.4, diffuser SD-1 has D-shaped and circular cross sections at the throat and the exit plane, respectively. A streamwise cross section of the center plane of the unmodified diffuser geometry is shown along with a representative color raster plot of the resulting total pressure distribution at the AIP are shown in Figure 3.1a,b. The reasonably uniform total pressure distribution at the AIP indicates that the base flow is attached through the diffuser with minimal losses. In the present

investigations, the streamwise vortex pair that is normally formed by a closed separation bubble at the turn of aggressive offset diffusers [71] is engendered by introducing a local surface recess (Figure 3.1c) which introduces trapped vorticity concentrations, induced by local separation and reattachment. The signature of the vortex pair is shown by the color raster plot of the total pressure distribution at the AIP in Figure 3.1d. The sense of rotation is such that the vortices lift low momentum flow off the lower surface towards the center of the AIP that is evidenced by the low total pressure at the bottom center of Figure 3.1d.

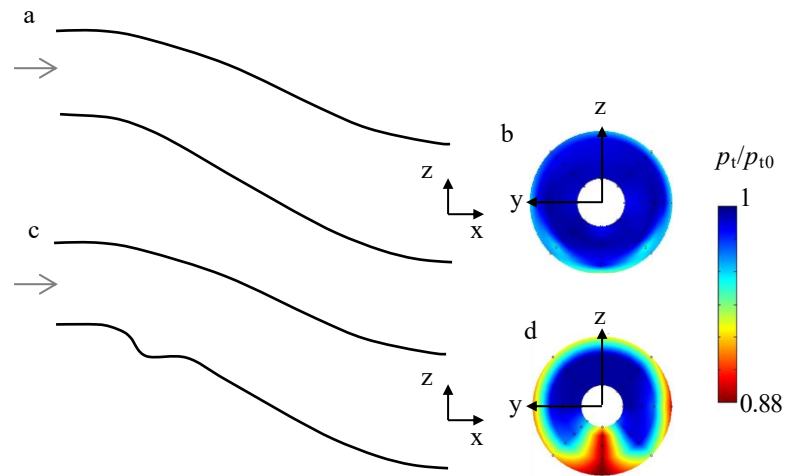


**Figure 3.1 Cross sectional view of the center plane of diffuser SD-1 centerline in the absence (a) and presence (c) of the trapped-vortex recess. The corresponding color raster plots of the total pressure at the AIP are shown in (b) and (d), respectively). Coordinate system is included for reference.**

Numerical simulations of the flow within the present diffuser (Lakebrink and Mani, [44]) capture the evolution of these streamwise vortices as shown in iso-surfaces of the helicity (integral of the inner product of velocity and vorticity having the sense of the vorticity [72]) in Figure 3.2. As noted in connection with Figure 3.1d, these data show that the sense of rotation of these vortices along the lower-surface of the diffuser is such that they move the low-momentum flow towards the center of the lower-surface and then

upward, away from the wall resulting in the total-pressure deficit in Figure 3.1d. The data in Figure 3.2 also highlights corner vortices along each of the outboard sides of the diffuser, which are shed from the edges of the recessed-cavity insert. It should be noted that the streamwise change in the sense of the helicity is associated with flow reattachment, which is caused by a change in the sign of streamwise velocity.

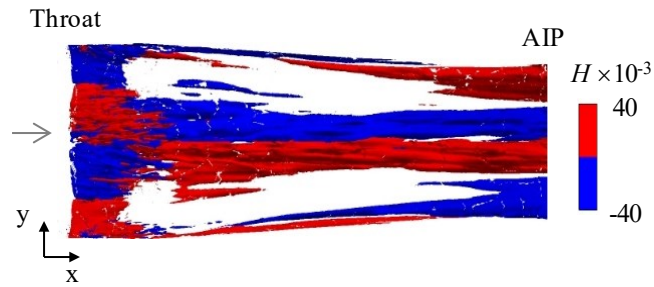


**Figure 3.2 Top view of helicity iso-surfaces along the lower surface in the base flow with recess (cf. Figure 3.1c). Coordinate system directions are included for reference.**

The total pressure contours in at the AIP in Figure 3.1d clearly highlight the detrimental effect of secondary streamwise vortices on flow distortion. The local separation bubble at the diffuser's turn engenders losses at the AIP which resemble the losses associated with a thick incoming boundary layer [71]. The receptivity of similar separated internal flows to manipulation with flow control (cf. Section 1.4.3) suggests that fluidic flow control approach can potentially have a significant effect on manipulating the evolution of the secondary vortices and thereby reduce their detrimental effects (distortion, pressure loss) on the diffuser flow. The effects of flow control on the diffuser secondary flow are investigated in the present chapter.



### 3.2 Characterization of the Base Flow in the Presence of the Surface Recess

Since the flow characteristics at the diffuser's entrance affect its evolution through the diffuser, the streamwise velocity across the boundary layer just downstream of the contraction (cf. Chapter 2) is measured using hot wire anemometry. The cross stream distributions of the Mach number scaled by freestream Mach number  $M_f$  and the corresponding scaled Mach number RMS fluctuations (Equation 3.1) at  $x/D = -4.2$  ( $x/D = -3.5$  is the diffuser's throat, cf. Figure 3.1) are shown in Figure 3.3, where  $D$  is the diffuser exit plane diameter of 12.7 cm (cf. Figure 2.4). The time-averaged and RMSF (Equation 3.1) Mach number are shown for three spanwise locations  $y/D = -0.35, 0$ , and  $0.35$  in Figure 3.3a and b, respectively. These plots indicate that the high-shear region within the boundary layer is about 2 mm thick, which is attributed to the large area-ratio contraction (Figure 2.1). Furthermore, the symmetry of the distributions about the center plane ( $y/D = 0$ ) indicates that the boundary layer along the flat portion of the D-shaped throat is spanwise-uniform. In the absence of the mold-line recess (cf. Figure 3.1a), the interaction between the thin boundary layer and the flow turning along the diffuser results in nearly negligible total-pressure distortion (a measure of asymmetry and non-uniformity) at the AIP as is evidenced in Figure 3.1b, where the average distortion parameter  $DP_{CP_{avg}}$  is about 0.008, compared to that with the recess in Figure 3.1d, which is 0.035, where the total pressure is much less uniform.

$$RMSF = \sqrt{\frac{1}{N} \sum_{i=1}^N (x_i - \bar{x})^2} \quad 3.1$$

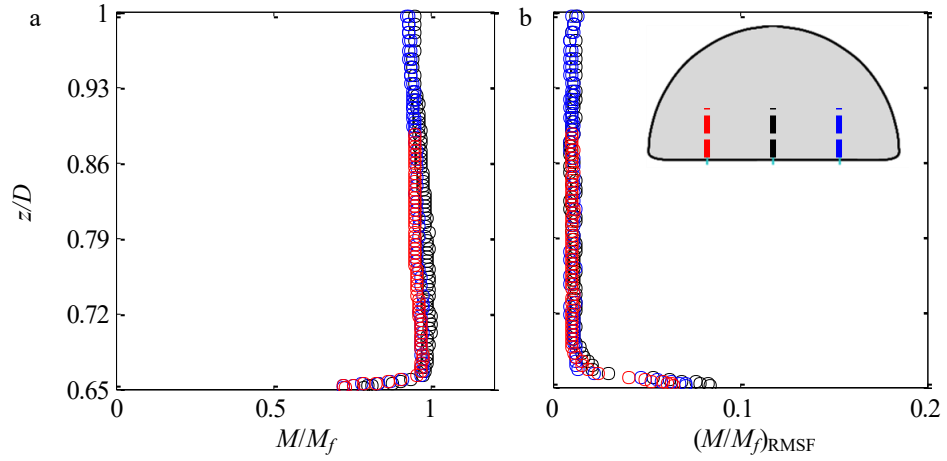


**Figure 3.3 Profiles of Mach number scaled by freestream Mach number  $M_f$  (a) and the scaled Mach RMS fluctuations (Equation 3.1) (b) near the bottom surface ( $z/D=0.65$ ) at three spanwise locations  $y/D = -0.35$  (blue),  $0$  (black),  $0.35$  (red).**

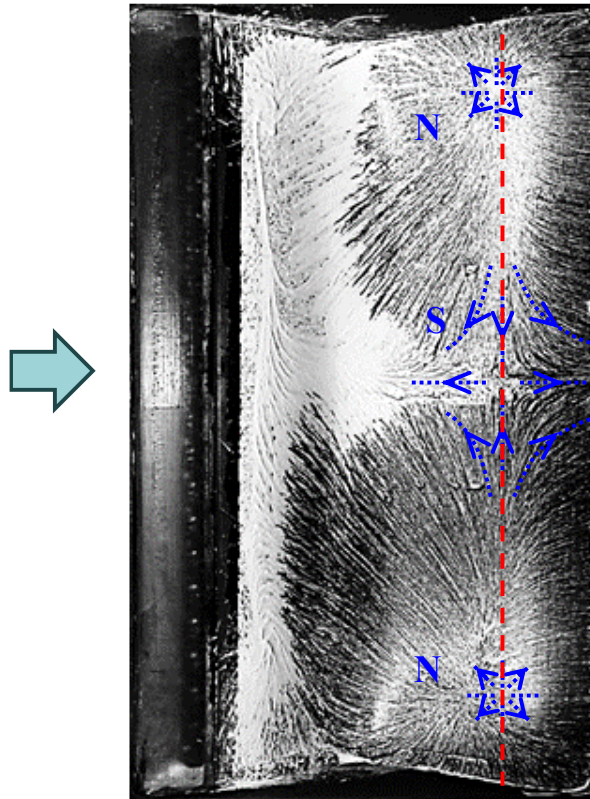


**Figure 3.4 Surface oil-flow visualization over the recess insert at  $M_{\text{AIP}} = 0.58$  (the flow is from left to right). The red dashed line marks flow reattachment, and blue arrows marking a central saddle and two side nodes.**

Following the characterization of the incoming flow, the mold-line recess is added to the diffuser using an insert (as described in Chapter 2 and in connection with Figure 3.1) to engender local separation. The local and global surface flow topologies resulting from the presence of the recess are characterized using surface oil-flow visualization (discussed in Chapter 2). The oil-flow traces within the recess are shown in Figure 3.4 for  $M_{AIP} = 0.58$ . Critical points (saddles and nodes, [73, 74]) of the flow are surmised from the topology of the oil traces and are marked in Figure 3.4. The flow separates at the upstream (left) end of the mold-line recess and reattaches along the dashed red line shown in Figure 3.4. The flow reattaches within two distinct spanwise domains that are separated by the central saddle point (marked “S”) between upstream and downstream flows. There are also two nodes (each marked “N”) close to each of the side walls. The corners of the D-shaped diffuser induce local flow reattachment at the nodes, which, in turn, affect the flow symmetry about the central plane through the saddle point and its direction towards the central plane.

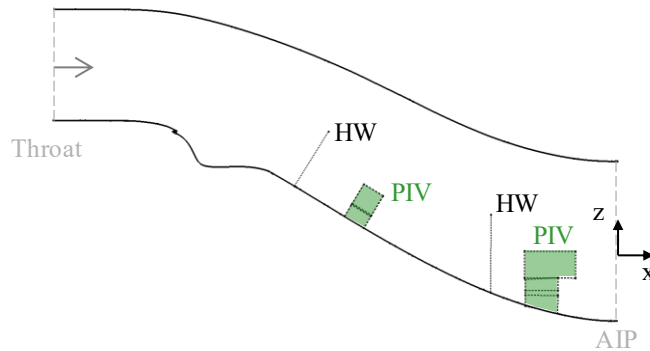


**Figure 3.5** Locations of hot wire anemometry and particle image velocimetry within the center plane of the diffuser between the recess and the AIP. Hot wire (HW) measurements were acquired at  $x/D = -1.7$  and  $-0.6$ . The particle image velocimetry was acquired at  $x/D = -1.55$  (18 x 32 mm) and  $x/D = -0.4$  (14 x 26 mm).

The effects of the trapped vorticity within the recess on the flow farther downstream were measured across the diffuser's center plane at multiple locations between the recess and the AIP using hot wire anemometry (HW,  $x/D = -1.7$  and  $-0.6$ ) and particle image velocimetry (PIV,  $x/D = -1.55$  and  $-0.4$ ) as shown in Figure 3.5.

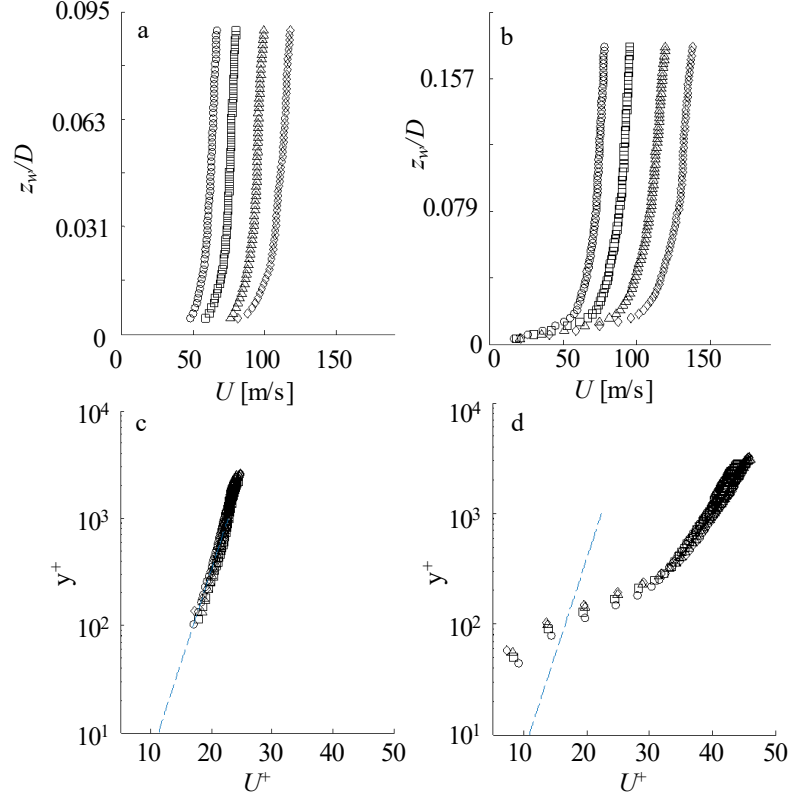


**Figure 3.6** Time-averaged profiles of streamwise velocity [ $M_{AIP} = 0.36$  ( $\circ$ ),  $0.45$  ( $\square$ ),  $0.58$  ( $\triangle$ ), and  $0.7$  ( $\diamond$ )] at  $x/D = -1.55$  (a, c) and  $x/D = -0.4$  (b, d), in both scaled normal distance to the wall  $z_w/D$  (a, b) and canonical boundary-layer wall (c, d) coordinates  $y^+$  and  $U^+$ . The logarithmic law  $U^+ = 2.5 \ln y^+ + 5.5$  is shown for reference in (c, d) using a dashed line.

The velocity field in the near-wall region is measured in the base flow in the presence of the recess at  $M_{AIP} = 0.36, 0.45, 0.58$ , and  $0.7$  using PIV at  $x/D = -1.55$  and  $-0.4$  (cf. Figure 3.5) utilizing a composite of two partially overlapping measurement domains. Boundary layer profiles extracted from each of the time-averaged flow fields are shown in

Figure 3.6, plotted against distance from the wall  $z_w$  scaled by the AIP diameter  $D$  in Figure 3.6a,b. Owing to surface reflection, the flow cannot be resolved within a narrow strip at the wall using PIV, and it is estimated that the closest measurements are about 0.5 mm above the surface. As the flow accelerates following reattachment within the recess, there is a significant velocity deficit in all profiles ( $x/D = -1.55$ , Figure 3.6a), which is indicated by the velocity continuing to increase, even at the points furthest from the surface. Given the adverse pressure gradient within the diffuser, it is expected that the boundary layer closer to the AIP would be thick, which is also clearly visible at  $x/D = -0.4$  (Figure 3.6b). The profile shapes at this station ( $x/D = -0.4$ ) are different from a canonical turbulent boundary layer profiles however, which is evidenced by the sharp change in slope at about  $z_w/D=0.02$ . This is ostensibly due to the three-dimensional motions that are induced within the diffuser by the presence of the recess (cf. Figure 3.1d) that in the center plane lead to advection of low-momentum flow from the bottom surface.

To further test how the time-averaged velocity profiles of the base flow with recess compare to canonical turbulent boundary layer profiles, the measured profiles are reduced to wall coordinates:  $U^+ = \bar{U}/u_\tau$  and  $y^+ = z_w u_\tau/\nu$ . In the process of scaling the profiles, the largest uncertainty is the estimated coefficients is in the velocity gradient at the wall, which cannot not be measured directly because of the reflections. Its initial value is calculated based on the first measurement point of the time-averaged profile, and it is corrected by a multiplication factor based on the numerically-resolved full boundary layer profiles by Lakebrink and Mani [44]. The scaled boundary layer profiles that correspond to Figure 3.6a and b are shown in Figure 3.6c and d, respectively. In addition, a canonical turbulent boundary layer log-law profile  $U^+ = 2.5 \ln y^+ + 5.5$  is plotted for reference. It can

be seen that the boundary layer profiles closer to the recess (Figure 3.6c) closely follow canonical log-low profile despite the fact that the bulk flow within the diffuser varies in the streamwise direction owing to the expansion. In contrast, the velocity profiles just upstream of the AIP ( $x/D = -0.4$ , Figure 3.6d) depart significantly from the canonical profiles as the secondary flow significantly impacts the central wall flow and reduces its momentum (which results in reduction in the total pressure shown in Figure 3.7). As the flow momentum close to the surface diminishes, the surface shear stress is lowered, which in turn increases  $U^+$  for a given outer flow speeds as is evident in the profiles shown in Figure 3.6d.

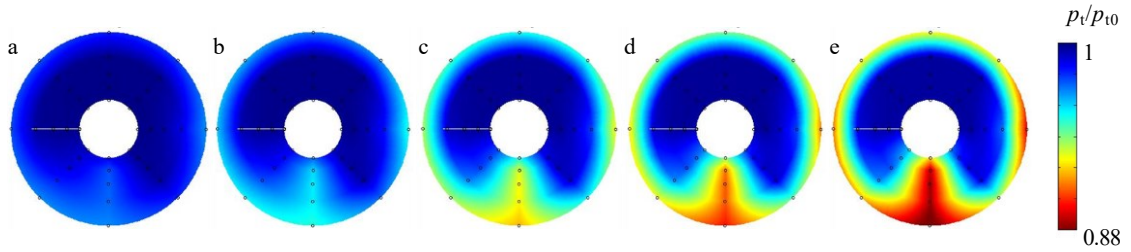


**Figure 3.7** Color raster plots of total pressure at the AIP in the presence of the recess  $M_{AIP} = 0.36$  (a),  $0.45$  (b),  $0.58$  (c),  $0.64$  (d), and  $0.7$  (e).

Finally, the effect of the trapped vorticity within the recess is characterized by distributions of the total pressure at the AIP shown in Figure 3.7a - e for  $M_{AIP} = 0.36, 0.45, 0.58, 0.64$ , and  $0.7$ , respectively. These data show that a sharp-cusped, laterally symmetric pressure deficit develops in the bottom-central region and intensifies with increasing  $M_{AIP}$ . This total-pressure deficit is qualitatively similar to that of a boundary-layer ingesting (BLI) offset diffuser in the absence of internal flow separation [71]. In the BLI offset diffuser, the total-pressure pattern at the AIP is induced by a pair of large-scale secondary vortices that distribute momentum deficit from the boundary layer of the flow that enters

the diffuser towards its bottom and up about its center plane as visible at the AIP. While in the present experiments the momentum deficit at the inlet to the diffuser is negligible, the deficit is generated downstream of the separation bubble in the surface recess and is accompanied by the formation of two large-scale counter-rotating vortical structures that sweep low-momentum fluid from the sidewalls towards the center of the duct.

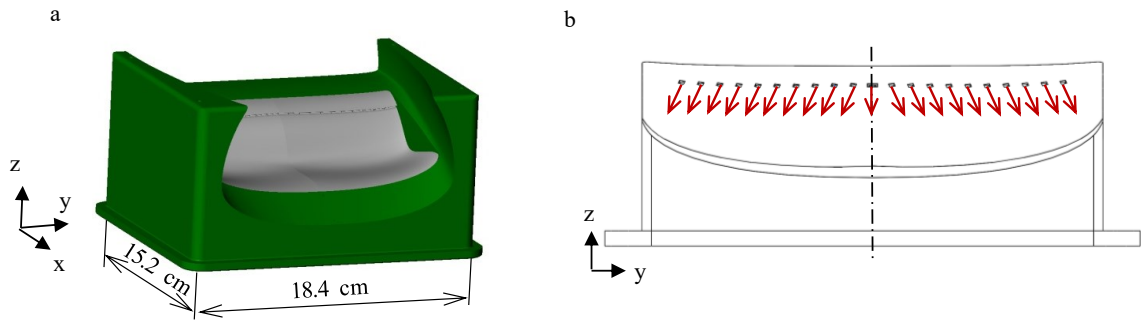


**Figure 3.8 CAD drawings of the diffuser's flow control module that integrates the recess with an array of fluidic oscillating jets (a), and a front view of the jet array (b) with coordinate directions for reference.**

### 3.3 Effects of Jet Actuation Coupled with the Wall Recess

Hybrid flow control is utilized to mitigate the effects of separation and secondary flow characterized in the presence of the wall recess described in Section 3.2. This is implemented by integrating the surface recess with a spanwise array of fluidic oscillating jets in a removable flow control insert, shown in Figure 3.8a that mates smoothly with both the upstream and downstream diffuser surfaces. The array of fluidic oscillating jets (Figure 3.8b) is positioned immediately upstream of the recess and includes an array of 21 jets that are equally spaced 7 mm apart. Each jet emanates from an orifice measuring  $1.5 \times 2$  mm tangentially to the local surface, and it oscillates laterally at frequencies between 7 – 9 kHz depending on the jet flow rate. The jets are used to control the strength and structure of

the trapped vortex, and thereby affect the flow throughout the diffuser. The main flow-control parameter is measured by  $C_q$ , which is the ratio between the mass flow rate through the jet array and the diffuser. In the present investigations  $C_q$  never exceeds 0.7%.

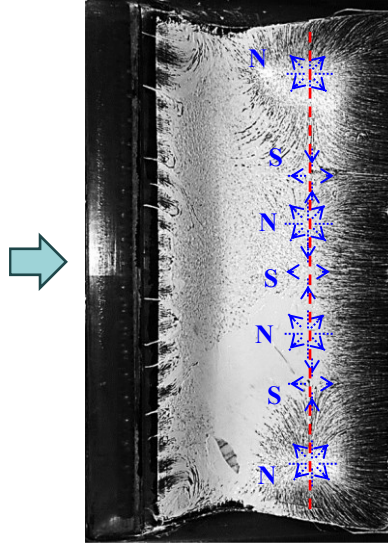


**Figure 3.9 Surface oil-flow visualization over the recess insert at  $M_{AIP} = 0.58$  and  $C_q \approx 0.7\%$  (the flow is from left to right). The image shows the traces of the actuation jets on the left and marked alternating saddles and nodes along the attachment line (red dashed).**

The effect of the array on local and global flow topology is first characterized using surface oil-flow visualization as shown in Figure 3.9. Separation occurs at the upstream edge of the recess, and the flow reattaches along the red line in Figure 3.9. As expected, there is an imprint of the flow control jets just downstream from the actuator array, on the upstream end of the recess. Their effect is reflected further downstream by the displacement of the reattachment line (red line) slightly upstream as compared to corresponding base flow in Figure 3.4. Besides changes in the scale of the separated region, its topology is also altered. The nodes associated with reattachment of the local corner base flow are still present, but their domain is reduced, as the nearest saddle is physically



much closer. Although it is not easily discernible from the oil accumulation, there are at least two additional nodes and a saddle, and possibly even additional pairs between the two outboard saddles. It is conjectured that this topology is associated with the discrete jet actuation. Regardless of the exact combination of the node and saddle points, the increased number of critical points straightens the flow downstream, indicated by the reduced angularity of the streaks after the array of saddles and nodes, indicating a quasi-two-dimensional flow downstream from reattachment.

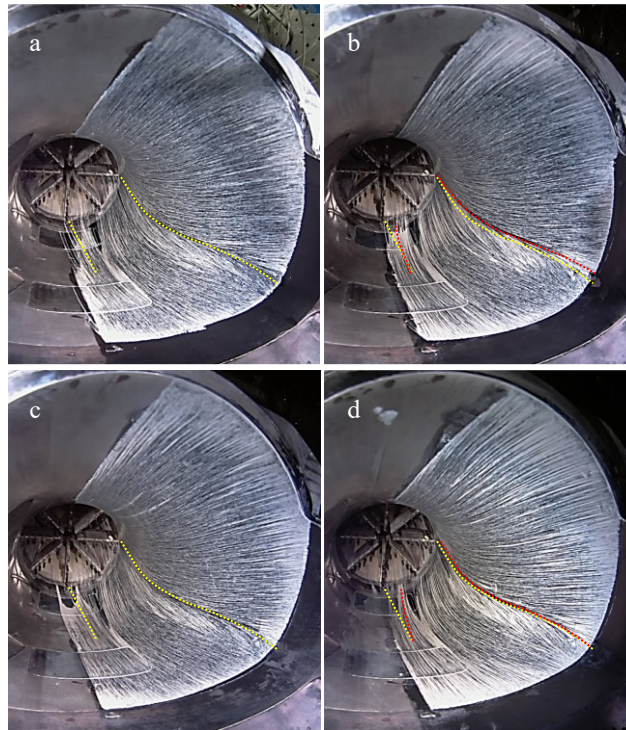


**Figure 3.10** Surface oil-flow visualization along the inner surface of the diffuser looking downstream at the AIP (the total pressure rake is visible on the left side of each image) in the absence (a, c) and presence (b, d) of actuation ( $C_q = 0.7\%$ ) at  $M_{AIP} = 0.58$  (a, b) and 0.7 (c, d). The dashed lines mark base (yellow) and actuated (red) flow trajectory.

The flow over the inner surface of the diffuser is visualized between the wall recess flow control insert and the AIP in the absence and presence of actuation ( $C_q = 0.7\%$ ) as

shown in Figure 3.10a-d for  $M_{AIP} = 0.58$  (a, b) and 0.7 (c, d). In the absence of actuation (Figure 3.10a and c) the oil streak clearly show an imprint of the streamwise vortex that is formed downstream from the wall recess and the angularity of the flow approaching the central bottom section of the AIP where the largest deficit in total pressure is measured (cf. Figure 3.7a–e). These features are marked by yellow dashed lines overlaid on top of the corresponding images. The effects of the actuation are similar at each Mach number (Figure 3.10b and d). First, the streamwise vortex trajectory is displaced azimuthally away from the center plane as marked by the red dashed line, and second, and, perhaps more importantly, the flow approaching the AIP is directed straight towards it (compare the red and yellow traces). The straightening of the flow within the diffuser which is also evident in Figure 3.9, indicates a significant reduction in distortion.

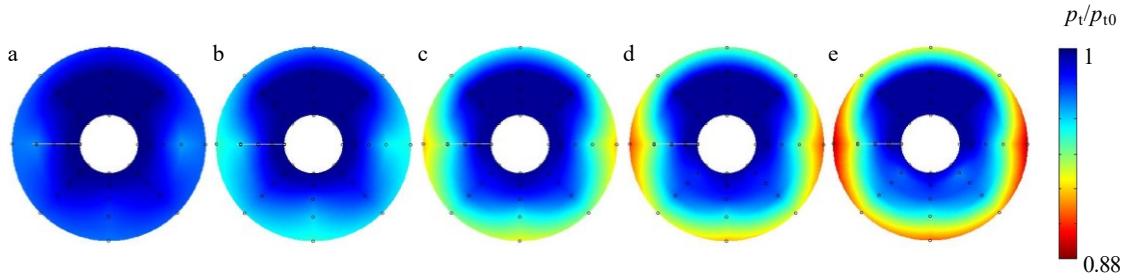


**Figure 3.11 Color raster plots of the total pressure at the AIP in the presence of actuation:  $C_q$ ,  $M_{AIP} = 1\%$ , 0.36 (a), 0.9%, 0.45 (b), 0.75%, 0.58 (c), 0.7%, 0.64 (d), and 0.68%, 0.7 (e).**

The effectiveness of hybrid-flow control is demonstrated using color raster plots of the total pressure at the AIP in Figure 3.11a–e for  $M_{AIP} = 0.36, 0.45, 0.58, 0.64$ , and 0.7, respectively. The pressure distributions patterns demonstrate that the jets effect a redistribution of low-momentum fluid from the bottom-central region to a thin layer of low-momentum fluid along the wall, which spans about three quarters of the AIP

circumference. As  $M_{AIP}$  increases, the intensity of the initial pressure deficit (Figure 3.7) increases, but it is clear that an increase in  $C_q$  is not necessary to achieve this effect. This qualitative change relative to the absence of actuation (Figure 3.7) indicates reduced distortion because the concentrated total-pressure deficit is nearly eliminated and the deficit becomes more azimuthally uniform. Such a redistribution of the total-pressure deficit is consistent with the application of a pair of counter-rotating vortices to the base flow with recess that have a sense of rotation that carries the low-momentum fluid out of the central bottom wall, and along the wall upward (clockwise in bottom left, counter-clockwise in bottom right of AIP). It is noted that this total-pressure redistribution is similar to the effect of active flow control in a BLI offset diffuser [71].

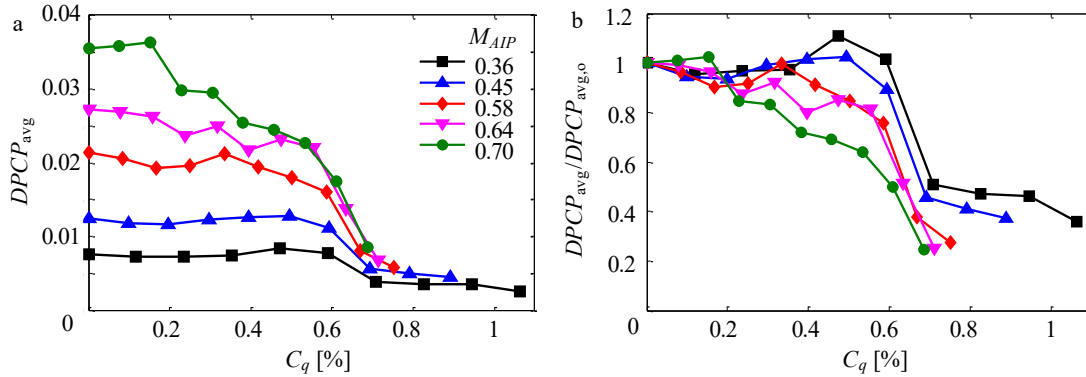


**Figure 3.12** Variation of the absolute (a) and relative (b) AIP total pressure distortion  $DPCP_{avg}$  with actuation mass flow rate coefficient  $C_q$  at  $M_{AIP} = 0.36, 0.45, 0.58, 0.64$ , and  $0.7$ .

The effects of the fluidic actuation on the AIP total-pressure distortion as measured by  $DPCP_{avg}$  are shown in Figure 3.12a over a range of  $C_q$  for each flow condition depicted in Figure 3.11. At the two lowest AIP Mach numbers the distortion is low in the base flow ( $C_q = 0$ ), and there is virtually no change at the lowest values of  $C_q$ . For

$C_q > 0.6\%$  a sudden small drop is observed, followed by a plateau with increasing  $C_q$ .  $DPCP_{\text{avg}}$  increases monotonically with Mach number, and for  $M_{\text{AIP}} > 0.45$  low levels of  $C_q$  induce a moderate decrease in  $DPCP_{\text{avg}}$ . For  $0.5\% < C_q < 0.7\%$ , sharp reductions in  $DPCP_{\text{avg}}$  are observed at all Mach numbers, the magnitude of which is commensurate with the distortion level in the baseline flow. Increasing  $C_q$  beyond  $0.7\%$  does not yield any significant benefit. These data show that the actuation effectiveness can be divided into three categories: (i) moderate reduction of  $DPCP_{\text{avg}}$  for  $C_q < 0.5\%$ , (ii) sharp reduction in  $DPCP_{\text{avg}}$  for  $0.5 < C_q < 0.7\%$  and (iii) saturation of flow-control effectiveness for  $C_q > 0.7\%$ . Another interesting insight can be gained by considering the reduction in total-pressure distortion between the presence and absence of actuation as shown in Figure 3.12b which indicates that actuation effectiveness increases with  $M_{\text{AIP}}$ . Although this finding may appear counterintuitive, in the absence of actuation the flow at lower Mach numbers has inherent lower levels of distortion, which makes it less susceptible to actuation.

Figure 3.13 illustrates the relationship between the AIP total pressure patterns and  $DPCP_{\text{avg}}$  for  $M_{\text{AIP}} = 0.7$ . As  $C_q$  increases from zero (base flow),  $DPCP_{\text{avg}}$  and the total pressure pattern change only slightly. As  $C_q$  increases further, the peak total-pressure deficit that protrudes upward towards the duct axis begins to retreat down toward the wall and spread radially outward at  $C_q = 0.3\%$ . This reduction in intensity provides nearly 20% reduction in  $DPCP_{\text{avg}}$ .  $DPCP_{\text{avg}}$  continues to decrease with increasing  $C_q$ , and a notable redistribution of the low momentum fluid up the diffuser wall is observed in the AIP patterns near  $C_q = 0.5\%$ . As already noted in the discussion of Figure 3.12, the largest response to the actuation is achieved for  $0.5\% < C_q < 0.7\%$ . In comparing the patterns for

$C_q = 0$  and 0.7%, one observes that the focused domain of low total pressure is completely swept up the inner surface of the diffuser.

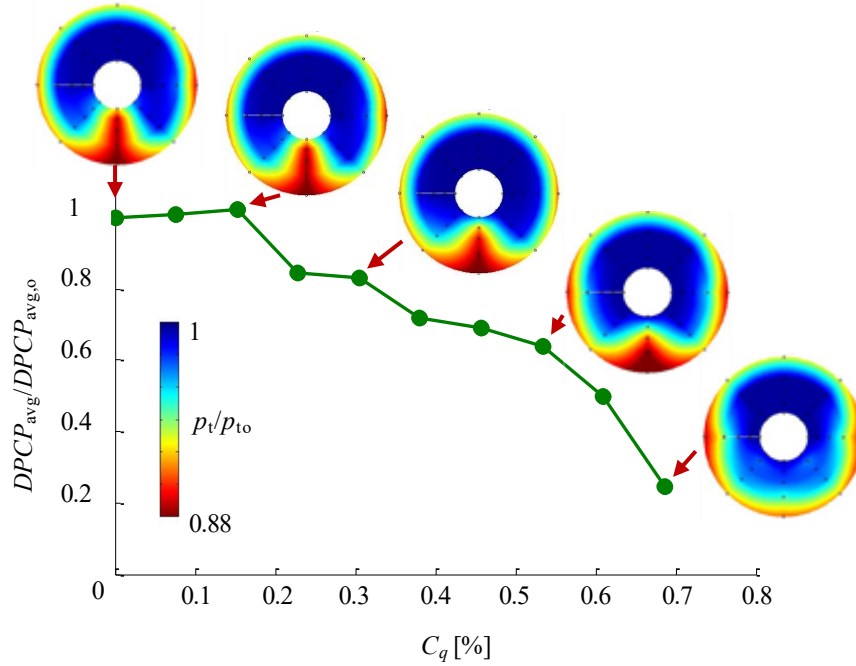


**Figure 3.13** Variation of the AIP total pressure distortion  $DPCP_{avg}$  with the flow control mass flow rate coefficient  $C_q$  at  $M_{AIP} = 0.7$ . Corresponding color raster plots of the AIP total pressure are also shown for reference.

### 3.4 Effects of Actuation on the Diffuser's Boundary Layer

Near-wall flow dynamics in the absence and presence of actuation are captured using hot wire and PIV measurements (cf. Figure 3.5). Figure 3.14 shows cross stream profiles of  $\rho^* \cdot M$  and  $(\rho M)_{rms}$ , which are generated by scaling the measured hot wire quantity  $\rho \cdot U$  by a density  $\rho_o$  and speed of sound  $c$  that are calculated from temperature and static pressure measured at the same cross-sections. This dimensionless quantity is plotted against the distance to the wall  $z_w$ , scaled by the diffuser AIP diameter  $D$  (12.7 cm).

Profiles for three diffuser AIP Mach numbers are shown, at both near reattachment ( $x/D = -1.7$ ) and near-AIP ( $x/D = -0.6$ ) measurement stations. It is interesting to note that downstream from the recirculating separation bubble that is formed by the recess (Figure 3.14a), the reattached flow induces velocity deficit only up to about  $z_w/D \approx 0.2$  above the surface in the uncontrolled flows. As the flow decelerates through the diffuser, the portion of the flow that experiences velocity deficit grows, and the bulk (unaffected) flow moves further from the wall, beyond the edge of the measured distribution ( $z_w/D \approx 0.49$ , Figure 3.14c).

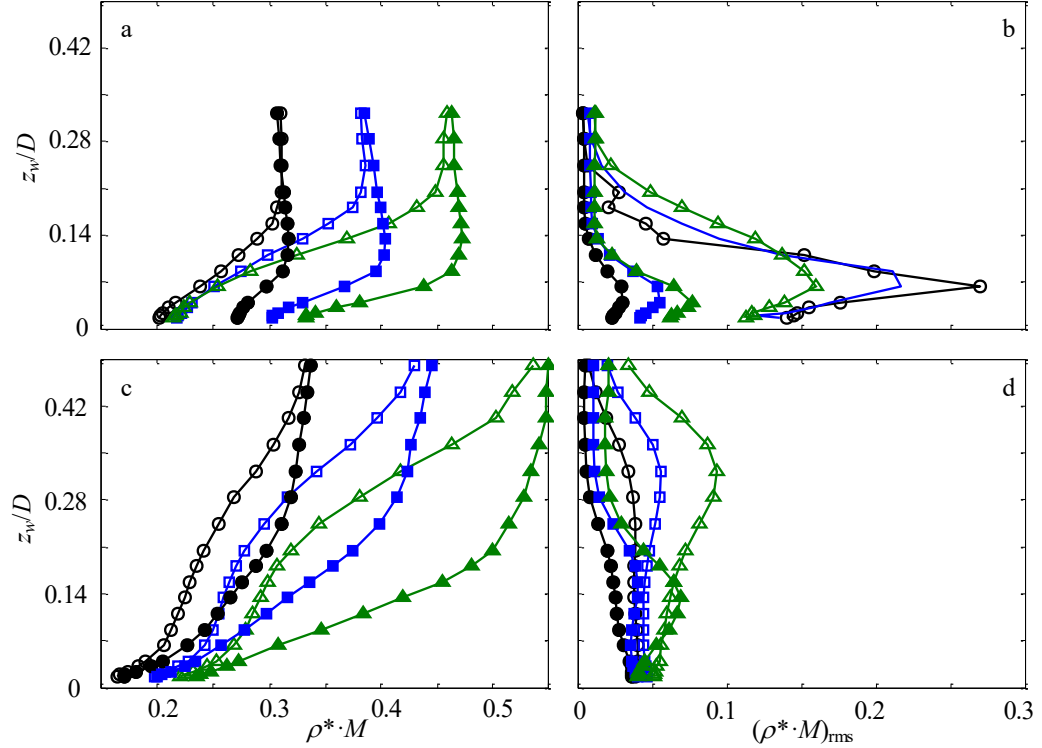


**Figure 3.14** The time-averaged cross stream distributions of  $\rho^* \cdot M$  (a, c) and  $(\rho^* \cdot M)_{rms}$  (b, d) in the center plane at the upstream,  $x/D = -1.7$  (a, b) and downstream  $x/D = -0.6$  (c, d) ports in the absence (open symbols) and presence (solid symbols) of actuation  $M_{AIP} = 0.36$  ( $\circ$ ),  $0.45$  ( $\square$ ), and  $0.58$  ( $\triangle$ ), and  $C_q = 0.7\%$  ( $\blacktriangle$ ),  $0.9\%$  ( $\blacksquare$ ), and  $1\%$  ( $\bullet$ ).

In the presence of actuation (solid symbols), the wall-induced velocity deficit at either station (Figure 3.14a,c) becomes significantly reduced and the layer of affected flow is pushed closer to the wall. The actuation effectiveness is more pronounced at higher diffuser Mach numbers, as the increase in velocity becomes proportional to the diffuser Mach number. This result is attributed to the fact that the control jets utilize the flow momentum when vectoring the diffuser flow and suppressing the separation bubble. Therefore, to the extent they are capable of vectoring flow of increasing momentum (as  $M_{AIP}$  is increased), they impose a stronger impact on the downstream flow.

The cross stream distributions of  $(\rho^* \cdot M)_{rms}$  (Figure 3.14b) upstream indicates strong flow fluctuations in the absence of actuation since this location is not far from flow reattachment. It is interesting to note that the peak levels of fluctuation appear to decrease with increasing  $M_{AIP}$ , which is attributed to faster streamwise dissipation of the smaller-scale fluctuations at higher Mach numbers. As the actuation is applied, there is a dramatic suppression of the RMS fluctuation levels more than 80% at  $M_{AIP} = 0.36$  (Figure 3.14b). At the downstream station ( $x/D = -0.6$ , Figure 3.14d), the high levels of fluctuations close to the wall are diminished and the peak fluctuations levels are associated with the highest shear of the velocity profiles, where the peak amplitudes are much lower than at the upstream station (Figure 3.14b), and, unlike the upstream station, increase with  $M_{AIP}$ . The effect of the actuation on  $(\rho^* \cdot M)_{rms}$  is similar at the downstream station, as the levels of fluctuations generally decrease with actuation, and the peak levels become pushed towards the wall in all cases.

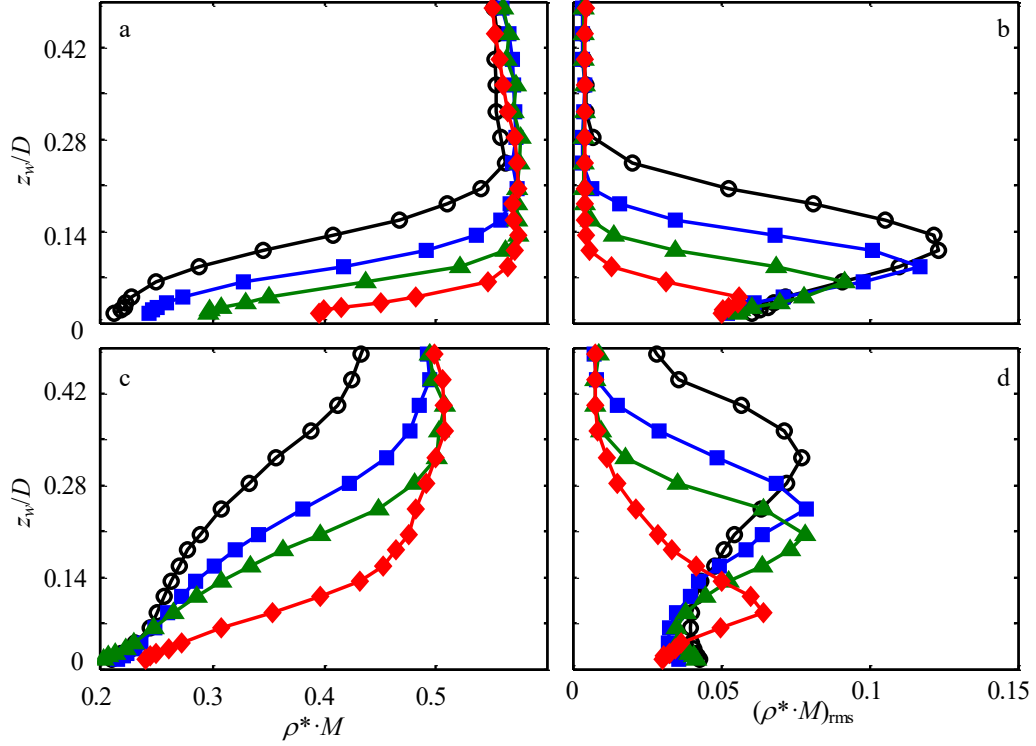


**Figure 3.15** The time-averaged cross stream distributions of  $\rho^* \cdot M$  (a, c) and  $(\rho^* \cdot M)_{rms}$  (b, d) in the center plane at the upstream,  $x/D = -1.7$  (a, b) and downstream  $x/D = -0.6$  (c, d) ports for  $M_{AIP} = 0.67$  in the absence ( $\circ$ ) and presence of actuation at  $C_q = 0.2\%$  ( $\blacksquare$ ),  $0.5\%$  ( $\blacktriangle$ ), and  $0.7\%$  ( $\blacklozenge$ ).

The effect of the varying the actuation mass flow rate coefficient  $C_q$ , is examined in Figure 3.15 for a  $M_{AIP} = 0.67$ . Both the distributions of  $\rho^* \cdot M$  and  $(\rho^* \cdot M)_{rms}$  are shown for in the absence and presence of actuation at  $C_q = 0.2, 0.5$ , and  $0.7\%$  downstream of reattachment and upstream of the AIP. A favorable effect is measured even at the lowest actuation level both in terms of the distributions of  $\rho^* \cdot M$  and  $(\rho^* \cdot M)_{rms}$ . The measurements at  $x/D = -1.7$  (Figure 3.15a) show proportional decrease of  $\rho^* \cdot M$  deficit as  $C_q$  is increased, while the  $(\rho^* \cdot M)_{rms}$  (Figure 3.15b) exhibits a proportional decrease in peak fluctuation amplitude along with simultaneous gradual displacement towards the wall. The distributions of  $\rho^* \cdot M$  at  $x/D = -0.6$  (Figure 3.15c) particularly emphasize the effectiveness



of the highest  $C_q$ , where the physical extent of the  $\rho^* \cdot M$  deficit has been limited to  $z_w/D = 0.35$  away from the wall, rather than that of the base flow extending outside of the measured domain. The corresponding distributions of  $(\rho^* \cdot M)_{\text{rms}}$  (Figure 3.15d) indicate a strong displacement towards the wall of the peak  $(\rho^* \cdot M)_{\text{rms}}$  with an increase in  $C_q$  and a mild effect on the suppression of the peak levels.

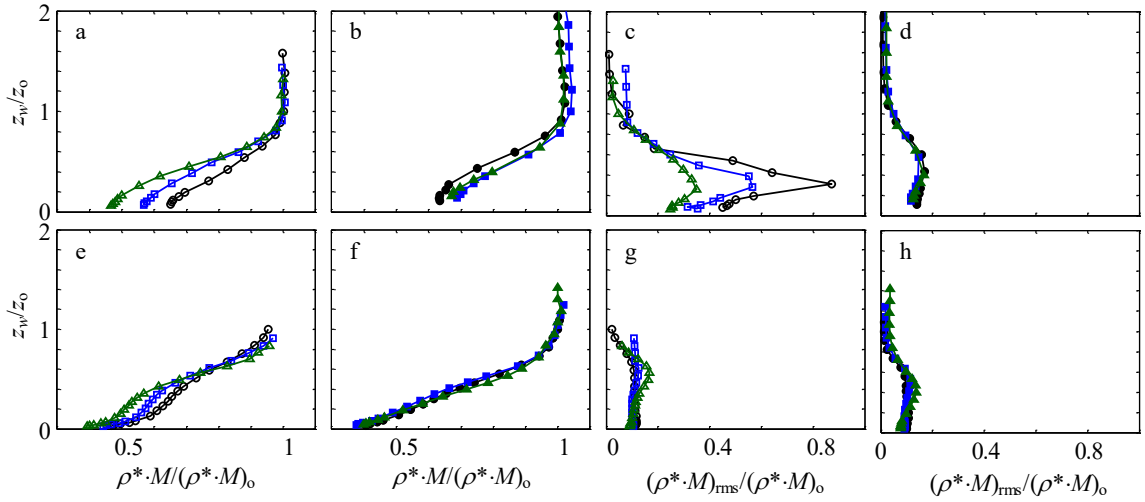


**Figure 3.16** Time-averaged distributions of  $\rho^* \cdot M$  (a, b, e, f) and  $(\rho^* \cdot M)_{\text{rms}}$  (c, d, g, h) in the center plane at the upstream,  $x/D = -1.7$  (a–d) and downstream,  $x/D = -0.6$  (e–h) ports in the absence (a, e, c, g) and presence (b, d, f, h) of actuation at  $C_q = 0.6\%$  and  $M_{\text{AIP}} = 0.36$ , **0.45**, and **0.58**.

To test how the diffuser flow responds to the same relative actuation level, flows at different Mach numbers are controlled by a fixed jet mass flow rate  $C_q$ . Figure 3.16 shows distributions of  $\rho^* \cdot M$  (left four plots) and  $(\rho^* \cdot M)_{\text{rms}}$  (right four plots) at the three diffuser flow rates ( $M_{\text{AIP}} = 0.36, 0.45, 0.58$ ), both at  $x/D = -1.7$  (Figure 3.16a–d) and  $x/D = -0.6$  (Figure 3.16e–h), where all profiles are scaled by the value and corresponding position at which the  $\rho^* \cdot M$  profile becomes invariant, moving away from the wall. In the absence of actuation, the distributions at  $x/D = -1.7$  (Figure 3.16a) indicate velocity deficit ( $0 < z_w/z_0$

$< 1$ , by scaling definition), where the deficit increases ( $\rho^* \cdot M$  decreases) with increasing  $M_{AIP}$ . As the flow decelerates in the streamwise direction, the distributions develop inflection points that are evident in Figure 3.16e. In the presence of actuation, the distributions collapse on top of each other at either measurement station (Figure 3.16b and f) indicating that  $C_q$  can be used to predict the flow evolution or to estimate the required actuation for a desired diffuser flow rate within this range. The distributions in the presence of actuation clearly show how the flow is altered in that the velocity deficit is reduced at  $x/D = -1.7$  and subsequently increases under the adverse pressure gradient (Figure 3.16f).

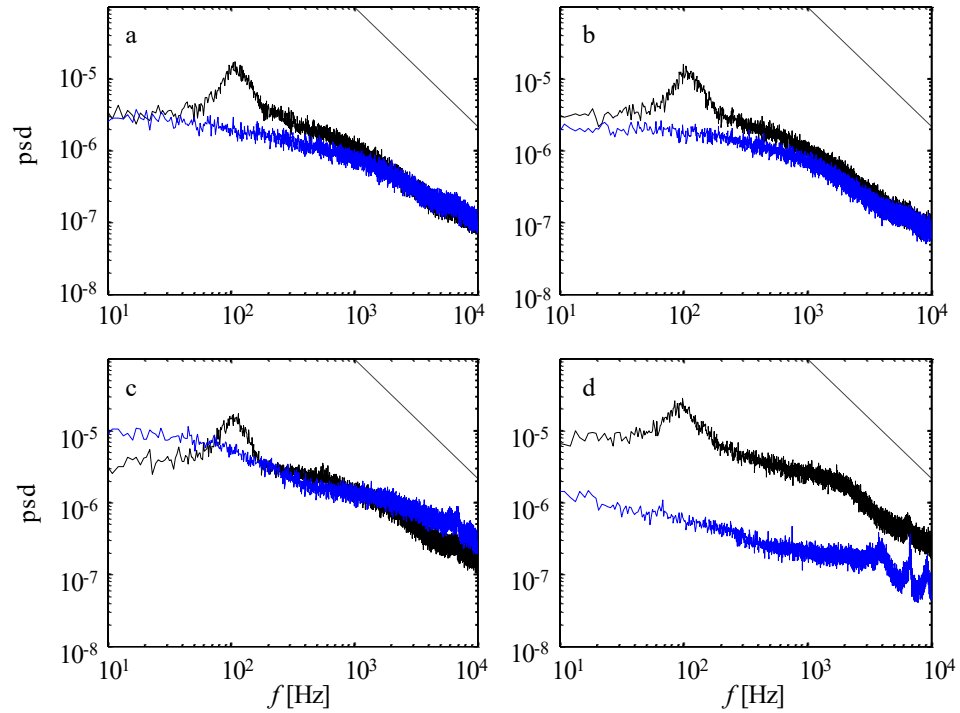


**Figure 3.17** Power spectra of  $\rho^* \cdot M$  at the  $x/D = -0.6$  measurement station in the absence (—,  $C_q = 0$ ) and presence (—,  $C_q = 0.6$ ) of actuation for  $M_{AIP} = 0.58$  at  $z_w/D = 0.015$  (a),  $0.039$  (b),  $0.133$  (c), and  $0.245$  (d) above the surface.

The distributions of  $(\rho^* \cdot M)_{rms}$  in the absence of actuation in Figure 3.16c and g show that downstream of reattachment (Figure 3.16c), its levels significantly increase, having

peaks at the elevations that correspond to the highest shear in the  $\rho^*M$  profiles, and the peak levels decrease with increased diffuser flow rate as discussed in connection to Figure 3.14. However, farther downstream higher rather than lower flow rates lead to higher peak fluctuations (compare Figure 3.16g to c), and overall, the levels of  $(\rho^*M)_{\text{rms}}$  are significantly lower. Once the actuation is applied,  $(\rho^*M)_{\text{rms}}$  becomes significantly suppressed at upstream (Figure 3.16d), while the levels and distributions downstream (Figure 3.16h) do not differ much from already low levels in the absence of actuation.

Additional insight into the effect of actuation on the diffuser flow is gained by spectral analysis of the fluctuations of  $\rho^*M$ . Figure 3.17 shows power spectra of the  $\rho^*M$  in the absence and presence of actuation at four characteristic heights above the surface for  $M_{\text{AIP}} = 0.58$ . The most notable feature of the spectra in the absence of actuation is the emergence of a spectral peak at around  $f = 100$  Hz, which is attributed to the unsteadiness of the trapped vorticity and reattachment within the recess. A common spectral feature in the presence of actuation at each elevation is that this spectral band becomes fully suppressed. Therefore, it is argued that the actuation does not only change global scales of separation, as shown in the oil visualization in Figure 3.4, Figure 3.9, and Figure 3.10, but also affects its dynamics, and suppresses its dominant unsteadiness.

The other spectral features in the presence of actuation compared to its absence appear to be elevation-dependent which can be partially attributed to the fixed spatial measurement point as the flow changes (cf. Figure 3.14c). Two spectra closest to the wall (Figure 3.17a and b) clearly indicate broadband suppression of fluctuations, asymptotically approaching the levels at the highest frequencies in the absence of actuation. An interesting

reversal is measured at  $z_w/D = 0.133$  (Figure 3.17c), where the controlled flow exhibit elevated levels of fluctuation through the entire spectra. This is not surprising, given that this elevation coincides with the peak levels of  $(\rho U)_{\text{rms}}$  in the presence of actuation as shown in Figure 3.14d. This is the only domain where in the levels are higher in the presence of actuation. Finally, the highest measurement point ( $z_w/D = 0.245$ ) reaches the bulk flow in the presence of actuation there is a dramatic drop in the fluctuation levels (Figure 3.17d) compared to the levels in the absence of actuation.

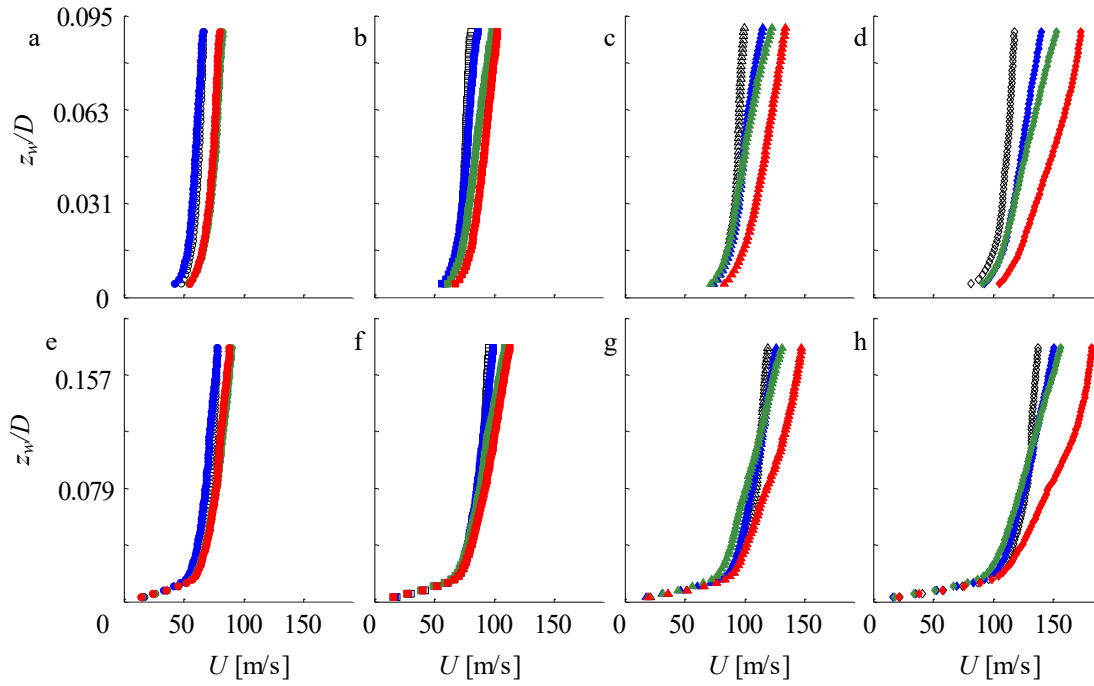


**Figure 3.18** Time-averaged profiles of streamwise velocity in the absence (black, open symbol) and presence (color, closed symbol) of actuation at  $x/D = -1.55$  (a–d) and  $x/D = -0.4$  (f–h). Each column corresponds to a Mach number  $M_{\text{AIP}} = 0.36$  (a, e),  $0.45$  (b, f),  $0.58$  (c, g), and  $0.7$  (d, h). Within each plot,  $C_q$  is indicated by color and varies from  $0.4\%$  -  $1.1\%$  (a, e),  $0.3\%$  -  $0.9\%$  (b, f),  $0.3\%$  -  $0.8\%$  (c, g), and  $0.2\%$  -  $0.7\%$  (d, h), where increasing  $C_q$  is colored from blue (lowest) to green (middle) to red (highest).

The effect of flow control on the boundary-layer is visualized with extracted velocity profiles from PIV in Figure 3.18, which include base flows from Figure 3.6 and

three actuation levels. Because the jet mass flow rate was fixed,  $C_q$  slightly decreases with increasing  $M_{AIP}$ , resulting in slightly different  $C_q$  ranges for each  $M_{AIP}$  (each column). As expected, the streamwise velocity increases with  $C_q$  both just downstream from reattachment ( $x/D = -1.55$ , Figure 3.18a–d) and just upstream from the AIP ( $x/D = -0.4$ , Figure 3.18e–h), with the highest effect most clearly seen at the highest level of  $C_q$  (shown in red). The effect of actuation differs between the two streamwise stations. At  $x/D = -1.55$ , (Figure 3.18a–d) there is an increase in velocity at the closest proximity to the surface while at  $x/D = -0.4$  (Figure 3.18f–h), the increase is predominantly away from the surface. Also, while at lower  $M_{AIP}$  the actuation does not significantly alter the shape of the velocity distributions (e.g., Figure 3.18a–b, e–f), the effect is stronger at higher  $M_{AIP}$  numbers (Figure 3.18c–d, g–h). In fact, it appears the actuation effectiveness increases with  $M_{AIP}$ , despite the decrease in  $C_q$  previously mentioned. The same trend is observed in the analysis of the face-averaged total pressure distortion parameter  $DPCP_{avg}$  with  $M_{AIP}$  and  $C_q$  (cf. Figure 3.12). It is argued that the apparent increase in actuation effectiveness stems from the attachment and the increase in the momentum of the diffuser’s core flow.

### 3.5 Flow Control Optimization

Following the characterization of fluidic actuation, further improvements in performance are sought by varying the number of active jets across the span. Utilization of subsets of the full array by disabling outboard jets is motivated by the desire to affect the centerline vortices more precisely. The effects of subarrays of the center 13 and 7 jets were compared with the of the full 21 jet array.

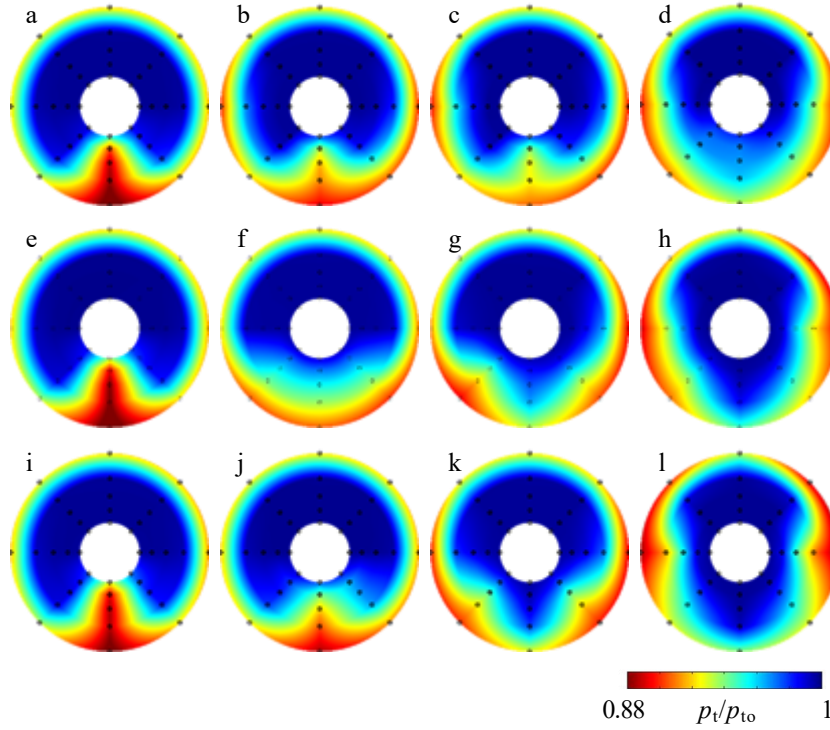


**Figure 3.19** Color raster plots of distributions of the total pressure  $p_t/p_{t0}$  at the AIP in the presence of actuation by  $n = 21$  (a – d), 13 (e – h), and 7 (i – l) central jets at  $M_{AIP} = 0.7$  and  $C_q = 0$  (e, i), 0.8% (a, j), 0.15% (k), 0.25% (f), 0.3% (b, g), 0.38% (c, l), 0.63% (h), and 0.7% (d).

The effect of the reduced actuation arrays are first examined using distributions of the AIP total pressure (Figure 3.19) for varying number of active jets in each row:  $n = 21$  (Figure 3.19a-d), 13 (Figure 3.19e-h), and 7 (Figure 3.19i-l), and increasing  $C_q$  values within each row (left to right). The qualitative trends with increasing  $C_q$  are largely independent of  $n$ , however, there are some important differences. For instance, redistribution of the deficit from the lower center domain to the upper wall appears gradual for the full jet configuration ( $n = 21$ ), while the lower number of jets ( $n = 13$ ) more significantly impacts the deficit at lower  $C_q$  (Figure 3.19f), which is followed by greater recovery at the center, but also greater losses along the upper wall with further increase in

$C_q$  (Figure 3.19h). The smallest array ( $n = 7$ ) does not as effectively suppress distortion at low  $C_q$ , while at the highest  $C_q$ , it raises total-pressure in the lower central deficit region, but has a side-effect of a significant increase in pressure deficit (reduction in total-pressure) along the sidewalls. (Figure 3.19l).

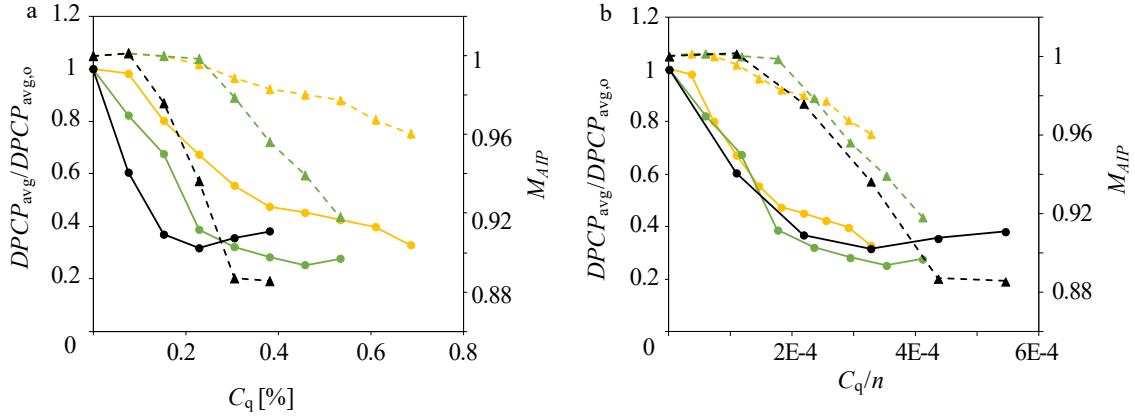


**Figure 3.20** Variation of the average circumferential distortion  $DPCP_{avg}$  (solid lines) and of  $M_{AIP}$  (dashed lines) with  $C_q$  (a) and  $C_q/n$  (b) for  $n = 21$  (yellow), 13 (green), and 7 (black).

The three actuation configurations discussed in Figure 3.19 are further characterized by the variation of  $DPCP_{avg}$ , with  $C_q$ , as well as by their effect on the AIP Mach number of the diffuser flow (Figure 3.20a). The change in  $M_{AIP}$  is useful for assessing the effect of the actuation on the overall losses because a decrease in  $M_{AIP}$  indicates increased losses. Figure 3.20a shows that the array with the fewest jets ( $n = 7$ ) starts reducing  $M_{AIP}$  at  $C_q = 0.1\%$ , as compared to the same effect with larger arrays that does not occur until about  $C_q = 0.25\%$ . In addition, these data show that the rate of decrease of  $M_{AIP}$  with  $C_q$  increases with a decrease in  $n$ . The levels of  $C_q$  at which  $M_{AIP}$  begins to decrease represents an upper bound for a subset of the flow control rates that could be considered optimal (reducing  $DPCP_{avg}$  without reducing  $M_{AIP}$ ). These data also indicate

that the rate of decrease in  $DPCP_{\text{avg}}$  is inversely proportional to the number of active jets. Although consideration of the distortion only would indicate that  $n = 7$  is optimal, consideration of the changes in  $M_{\text{AIP}}$  points to  $n = 13$  as the best performing array because at  $C_q = 0.25\%$  it results in a reduction of  $DPCP_{\text{avg}}$  to 0.015 while  $M_{\text{AIP}}$  remains invariant.

Since  $n$  is different for each of the array configurations, Figure 3.20b examines the dependence of both  $DPCP_{\text{avg}}$  and  $M_{\text{AIP}}$  on  $C_q$  per active jet ( $C_q/n$ ) rather than the total  $C_q$ . The dependence of  $DPCP_{\text{avg}}$  with  $C_q/n$  is independent of the number of active jets indicating that it is possible to reduce the total  $C_q$  while maintaining the same distortion reduction, since a lower  $n$  at the fixed  $C_q/n$  results in a lower total  $C_q$ . Although this part of the analysis points to  $n = 7$  as the best configuration, analysis of the dependence of  $M_{\text{AIP}}$  on  $C_q/n$  shows that  $M_{\text{AIP}}$  is invariant for the highest  $C_q$  for  $n = 13$  indicating this array is the most effective from the standpoint of both recovery and distortion.

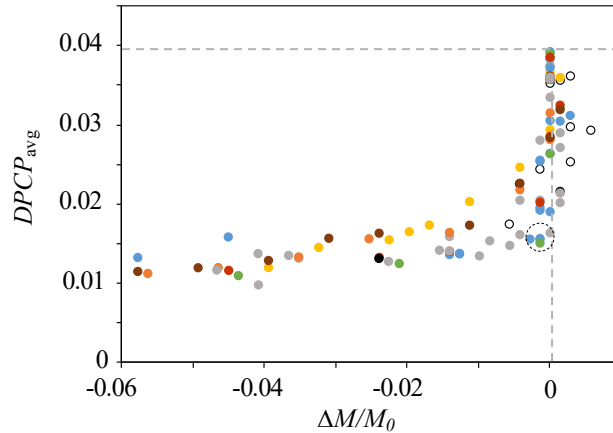


**Figure 3.21** Variation of the total pressure distortion  $DPCP_{\text{avg}}$  with  $\Delta M_{\text{AIP}}/M_0$  at  $M_{\text{AIP}} = 0.7$  in the absence ( $\circ$ ) and presence of actuation:  $n = 21$  ( $\bullet$ ), 19 ( $\bullet$ ), 17 ( $\bullet$ ), 15 ( $\bullet$ ), 13 ( $\bullet$ ), 11 ( $\bullet$ ), 9 ( $\bullet$ ), and 7 ( $\bullet$ ) active jets.



Given the clear trade-off of  $DPCP_{avg}$  and  $M_{AIP}$  with actuation, a comprehensive summary of the actuation effectiveness is shown in Figure 3.21 for eight jet configurations starting at a base flow  $M_{AIP} = 0.7$ . As  $C_q$  is varied, the test-section Mach number is altered due to the interactions of the jet array with the cross flow (Figure 3.20). Figure 3.21 therefore shows the variation of  $DPCP_{avg}$  with a percent change relative to the base flow  $\Delta M_{AIP}/M_o = (M_{AIP} - M_o)/M_o$  where  $M_o = 0.7$ . There is a common trend: as  $C_q$  is increased, there is at first a sharp decrease in distortion with little effect on  $M_{AIP}$  (moving from  $DPCP_{avg} \approx 0.04$  to  $DPCP_{avg} \approx 0.02$  along  $\Delta M_{AIP}/M_o \approx 0$ ). As saturation of the flow control's effect on distortion is reached ( $DPCP_{avg} \approx 0.015$ ) the jets reach the region with the best tradeoff between distortion and Mach number, where further increases in  $C_q$  result in reduction in  $M_{AIP}$  with no further significant reduction in distortion. These data further show that a reduction of about two-thirds in the distortion of the base flow can be attained with about half the number of active jets of the full array, at just a third of  $C_q$  compared to the full array control, and negligible change in Mach number. Based on the criteria discussed in connection with Figure 3.20, the two most effective arrays are  $n = 11$  and 13.

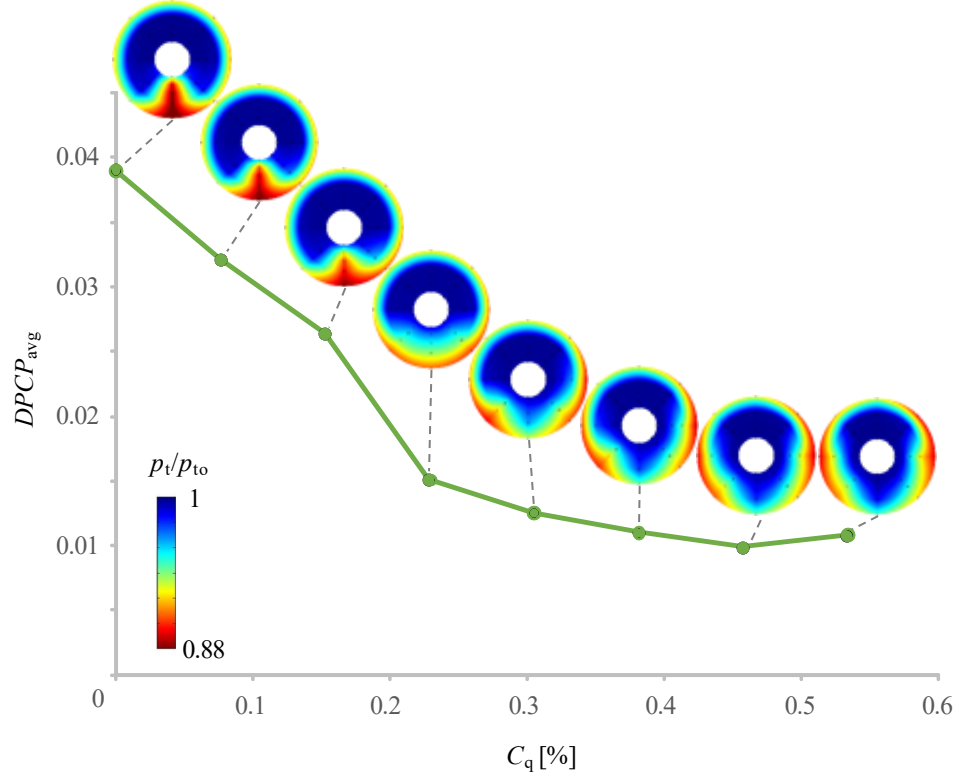


**Figure 3.22** The variation with  $C_q$  of the average circumferential distortion  $DPCP_{avg}$  along with corresponding color raster plots of the total pressure distributions at the AIP for the optimal jet configuration  $n = 13$ .

A more detailed representation of the AIP total-pressure distortion for the optimal number of jets,  $n = 13$ , is shown in Figure 3.22. Initially,  $DPCP_{avg}$  decreases with  $C_q$  as the lower-centerline losses are pushed azimuthally towards and along the surface in a thin near-wall layer. This trend breaks down when the losses below the centerline are spread around the AIP at  $C_q = 0.25\%$ . Beyond this, further increases in  $C_q$  continue to increase total pressure about the central domain and push the two segments of low-momentum fluid about the center plane farther azimuthally near the wall. These two effects oppose each other, resulting in a negligible reduction in distortion. This is a reason that the optimum  $C_q$  for this flow configuration is attained near  $C_q = 0.25\%$ .

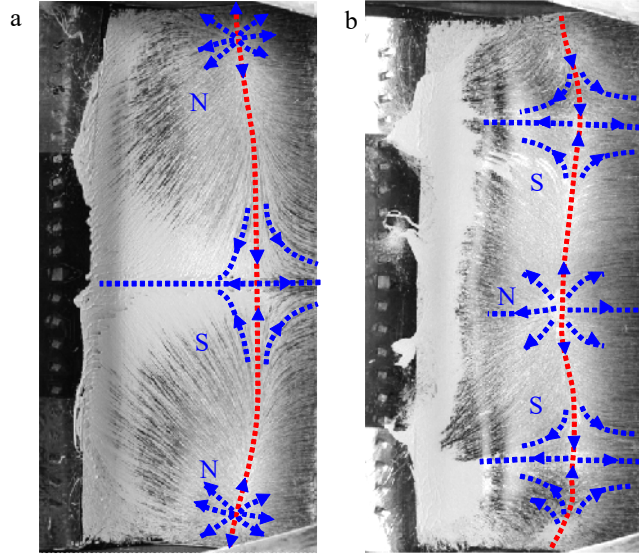


**Figure 3.23 Images of surface oil visualization over the wall recess at  $M_{AIP} = 0.7$  in the absence (a) and presence (b) of actuation by the central  $n = 13$  jets at  $C_q = 0.25\%$ . The images are marked by saddles (labeled S) and nodes (labeled N), and the attachment line (red).**

The effects of optimal actuation on the flow over the surface recess is detailed by surface oil visualization. Two images (base and optimal actuation) are shown in Figure 3.23 for  $M_{AIP} = 0.7$ , where the flow direction is left to right. The base flow (Figure 3.23a) is a higher Mach number version of Figure 3.4, and has the same topological structure as previously discussed, which includes two attachment nodes on the spanwise edges (top and bottom of image), along with a saddle along the centerline where the streams from the two nodes collide. The line that connects the nodes and saddle (red) is the line of flow reattachment. The separation line is upstream of the visualized domain. The effect of the actuation in Figure 3.23b is reflected by the reduction of the reattachment length of the separated flow domain and a significant change in the topology.

The flow topology of the reattaching flow is altered such that flow reattaches at a central node, in addition to nodes outside the visualized domain, which is implied by the

saddles on either side of the central node created by induced attachment. The primary reattachment region is defined as the span between the two saddles, which is about two-thirds of the span. This is similar to the effect of the full jet array seen in Figure 3.9, but the smaller jet array creates a lower number of critical points. Just as in the base flow, where the central saddle engenders a pair of counter-rotating vortices that lift off the surface at this saddle point, the two saddles in the optimal actuated flow each result in a pair of vortices, which do not create as much distortion as in the base flow (cf. Figure 3.21).

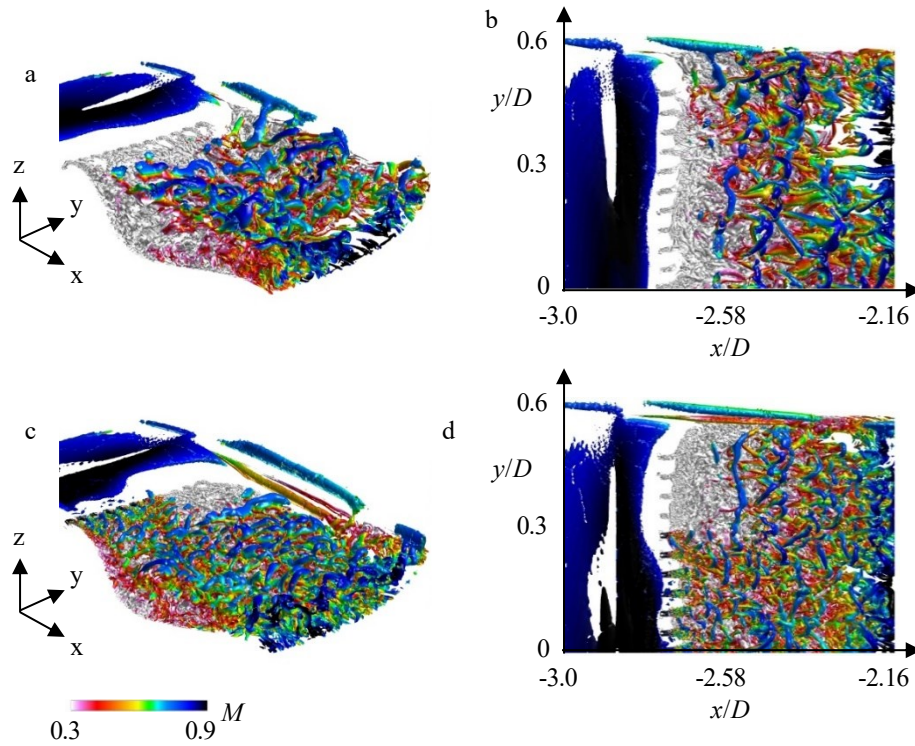


**Figure 3.24** Isometric (a,c) and normal (b,d) view of iso-surfaces of Q-criterion colored by local Mach number in simulations of the diffuser flow over the recess at  $M_{AIP} = 0.7$  in the absence (a, b) and presence (d, e) of actuation ( $C_q = 0.25\%$ ).

Numerical simulations (Lakebrink and Mani, [44]) of the diffuser flow in the absence and presence of optimal actuation ( $n = 13$ ,  $C_q = 0.25\%$ ) shed light on the three-

dimensional changes in the diffuser flow structure. Such detailed changes are difficult (if not impossible) to attain in the experiments. First, the instantaneous flow structures within the wall recess between the centerline ( $y/D = 0$ ) and the sidewall ( $y/D = 0.6$ ) are captured using the iso-surface of the  $q$ -criteria colored by local Mach number in the absence (Figure 3.24a and b) and presence (Figure 3.24c and d) of actuation. The views in Figure 3.24a and c are shown in isometric views (oriented from the centerline to the sidewall with flow from upper left to lower right) while Figure 3.24b and d are top-down views (the flow from left to right). The orifices of the control jets are visible upstream.

As the base flow separates off the upstream edge of the recess (Figure 3.24a and b), the resulting shear layer evolves into pockets of identifiable large-scale turbulent eddies, which appear to be fairly uniformly distributed across the span. Underneath the shear layer, the separated flow forms a recirculating flow which would be identified as a closed bubble in the time-averaged flow. In the presence of actuation, the flow exhibits several important features as depicted in Figure 3.24c and d. First, the active jets appear as intense, small-scale vortical motions that issue into the bulk flow. As a result, the lower left side of the flow in Figure 3.24c and bottom portion of the flow in Figure 3.24d exhibit trains of small-scale eddies that appear to quickly interact and presumably disrupt large-scale eddy formation and dynamics through enhanced mixing, production and dissipation of turbulent kinetic energy [75]. This region of the flow immediately downstream of the jets appears to be divided into two regions: a central region that is affected by the actuation, and a side region that initially begins to evolve similarly to the base flow, exhibiting similar flow structure of the evolving shear layer. Another feature in the presence of actuation is apparent when comparing the recirculating domains in the absence and presence of

actuation in Figure 3.24a and c, respectively. There is evidence of flow reattachment at the downstream edge of the bubble that is effected by the actuation and it is accompanied by an initial increase in mixing in the shear layer towards the lower surface so that it is better aligned with the core flow in the diffuser. Consequently, streamlined flow reattachment is accompanied by shortened and compressed recirculating bubble.

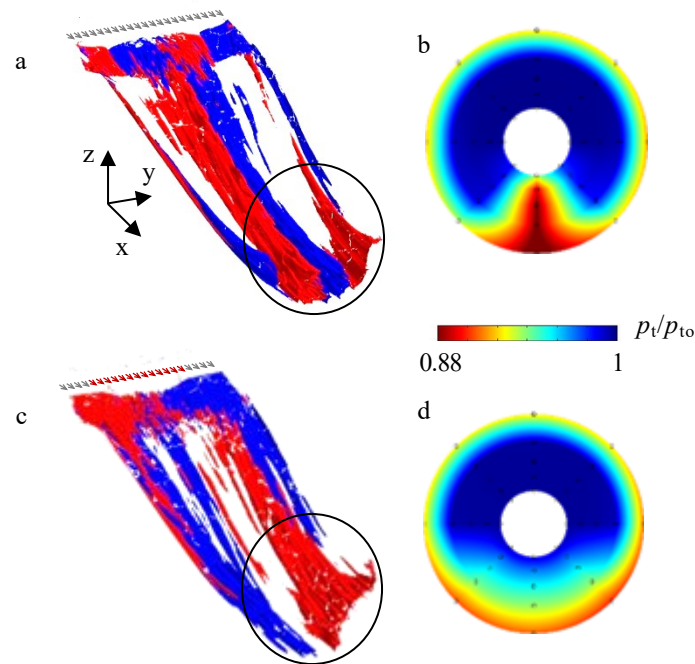


**Figure 3.25** Helicity iso-surfaces colored by helicity sign in the absence (a) and presence (c) of actuation within the diffuser, and color raster plots of the corresponding experimental total pressure distributions at the AIP (c and d, respectively) for  $M_{AIP} = 0.7$ ,  $n = 13$ , and  $C_q = 0.25\%$ . Coordinate directions included for reference in (a).

The underlying flow dynamics that give rise to flow distortion within the diffuser are illustrated using isometric views of simulated helicity surfaces extending from the onset of separation at the recess to the AIP in Figure 3.25a and c in the absence and presence ( $C_q = 0.25\%$ ) of actuation, respectively, along with corresponding measured distributions of

the total pressure at the AIP (Figure 3.25b and d). The helicity surfaces in the base flow (Figure 3.25a) show the formation of two streamwise vorticity concentrations symmetrically about each side of the center plane of the diffuser, that originate from the separated-flow domain at the turn of the diffuser. On each side of the center plane there is a weak counter-rotating vortex pair that forms near the corner of the diffuser. It is noteworthy that on each side, one of the counter-rotating concentrations is more pronounced (CW on the left and CCW on the right). More importantly, the strong central counter-rotating vortex pair that originates from the separation domain over the recess gives rise to upwelling of low momentum fluid at the center of the AIP (Figure 3.25b). The simulations support the assertion that these streamwise vortices originate where the two plow streams meet about the saddle reattachment in Figure 3.23a.

In the presence of actuation, the center vortices are significantly weakened and effectively disappear at the center of the AIP. Simultaneously, the stronger of the two counter-rotating vortices in each corner (CCW on the left and CW on the right) intensify. The result at the AIP is that the distortion caused by upwelling at the center subsides and there is only a small increase in pressure deficit. These flow structures can be connected to the topology at the local reattachment in the presence of fluidic actuation in Figure 3.23b. As the two opposing saddle points are formed closer to the side walls in the presence of actuation (Figure 3.25c and d), two strong sources of vorticity originate along these two sides in Figure 3.25d. Furthermore, flow reattachment over the center of the diffuser prevents formation of the central pair of counter-rotating streamwise vortices leading to nearly complete suppression of helicity about the center plane.

## CHAPTER 4. SERPENTINE DIFFUSER

The natural extension of the investigations in the SD-1 diffuser is the flow control application in a diffuser which creates naturally occurring separation and streamwise vortices (SD-2). In the present investigations, an upper-surface, second-turn separation bubble is found to naturally form, which spans about a third of the surface span and is also much more round along the upstream edge than was previously created in SD-1. Using the results from SD-1, an array of fluidically-oscillating jets was placed just upstream of the leading edge of the separation domain and knowledge of the sense of the naturally occurring streamwise vortices prompted yawing of individual jets on each side of and away from the centerline to create predominantly single-sign streamwise vorticity of opposite sense to the prevailing sense of vorticity in the streamwise vortex that is naturally formed by the separation domain.

### 4.1 Introduction

The serpentine, two-turn diffuser (denoted SD-2, Figure 4.1a) which is used in the present set of experiments has a D-shaped throat and circular exit cross-section (AIP), and is discussed in detail in Chapter 2. Like SD-1 (Chapter 3), this serpentine diffuser is investigated in isolation from an inlet by using a 106:1 area ratio contraction upstream of the throat.



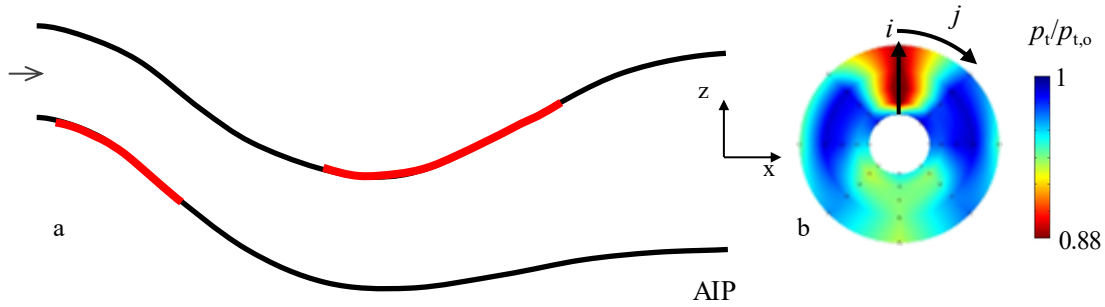


**Figure 4.1** A streamwise cross section along the center plane of the serpentine diffuser showing the locations of interchangeable inserts marked in red (a), and a color raster plot of the total pressure distribution at the AIP measured by the 40-probe rake ( $M_{AIP}=0.54$ ) (b).

Figure 4.1a shows the cross section along the diffuser's center plane, exhibiting the two internal turns that lead to flow separation the formation of secondary, streamwise vortices that are associated with pressure losses and flow distortion. The presence of the secondary flow is evidenced by the total pressure deficit at the AIP (Figure 4.1b), which appears to be more severe on the top surface. These data indicate that the losses associated with the second turn (on the top surface) are more severe than at the bottom surface, which might be attributed to a stronger second-turn separation or to the proximity of the second turn to the AIP (Figure 4.1b). Figure 4.1b also indicates the indexed notation of the radial and azimuthal positions of the forty total pressure probes which are discussed in detail in Chapter 2.

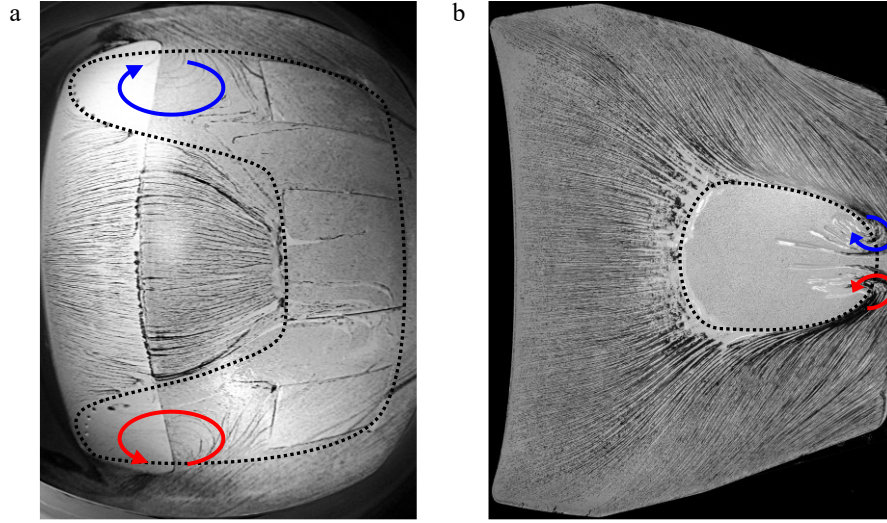


**Figure 4.2** Surface oil visualization in the base flow ( $M_{AIP} = 0.54$ ) over the first turn bottom surface (a,  $-3.45 < x/D < -2.52$ ), and second turn top surface (b,  $-2.07 < x/D < -0.82$ ) flow control inserts (cf. Figure 4.1a). The flow is from left to right, and the arrows indicate sense of secondary vortices. Domains enclosed in dotted black lines indicate separated regions.

## 4.2 Characterization of the Base Flow

Structural details of the base flow are first characterized using surface oil visualization (cf. Section 2.3.4) at  $M_{AIP} = 0.54$ . The respective characteristic features of the topology of the separated base flow at the upstream and downstream turns of the diffuser are shown in Figure 4.2a (bottom surface) and in Figure 4.2b (top surface). The images are recorded over the surfaces of the first- and second-turn inserts marked in Figure 4.1. The oil streaks over the first turn surface (Figure 4.2a) show the onset of separation at each corner of the duct (the separated domain is enclosed by a dotted line). The attached flow in the center domain (outside of dotted domain) is nearly symmetric about center span and its spanwise width diminishes in the streamwise direction (left to right) such that the flow over the surface becomes fully separated at about one third of the image width from the right edge of the image ( $x/D = -2.84$ ). As shown in Figure 4.2a, the separation line

(upstream border of separated domain) resembles an upstream-open horseshoe. The oil streaks also show the evolution of reverse flow along each the duct's corners that is counter-rotating (as marked by red and blue arrows), which indicates interaction with the counter-rotating streamwise vortices that form at the corners of the throat.

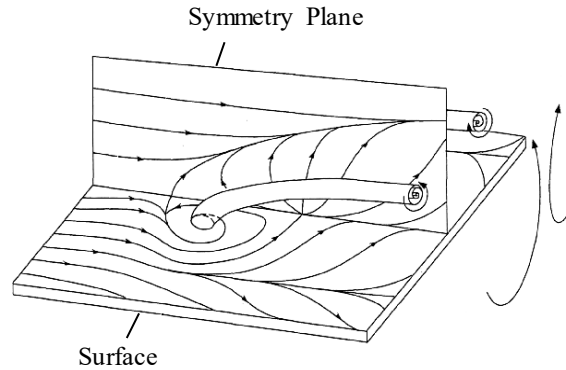


**Figure 4.3 Perspective view of counter-rotating vortices lifting off from spiral nodes [76].**

A second closed separation domain appears downstream of the second turn (Figure 4.2b), where a spanwise-compact separation bubble is formed symmetrically about the diffuser's center plane over about a third of the span, which is enclosed in the black dotted line. The oil streaks around this domain mark not only its spanwise edges but also indicate that these edges are bounded by counter-rotating streamwise vortices (spiral nodes marked by arrows). These vortices lift off the surface at these nodes at the downstream end of the separation region, similar to the illustration in Figure 4.3. The oil visualization in Figure 4.2b is used for the design of the spanwise jet-actuator array which is aligned with the upstream edge of the separation bubble.

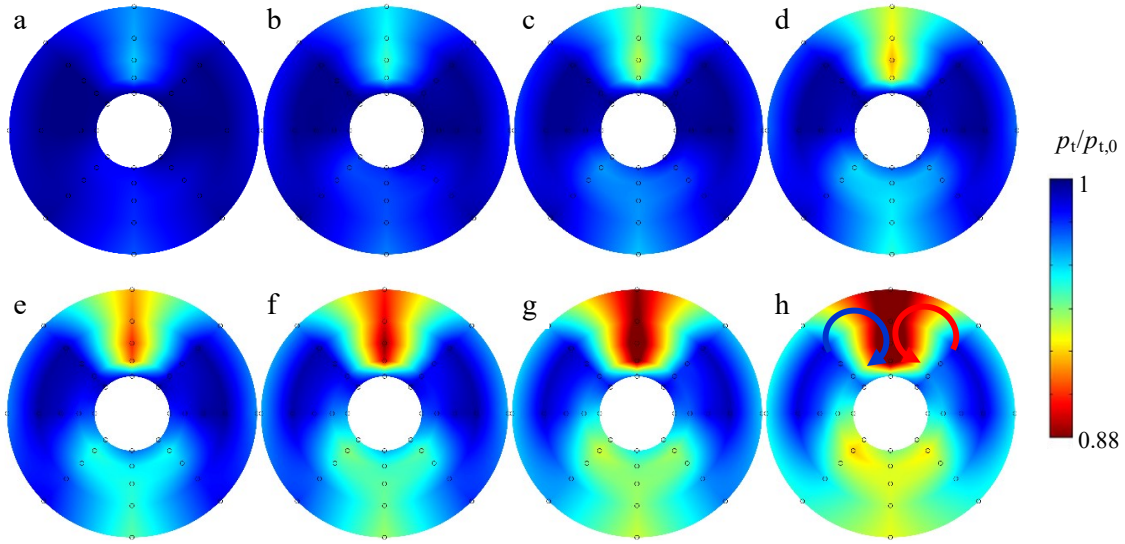


**Figure 4.4** Color raster plots of the total pressure at the AIP for the base flow at  $M_{AIP} = 0.29$  (a), 0.34 (b), 0.38 (c), 0.43 (d), 0.47 (e), 0.51 (f), 0.54 (g), and 0.58 (h). Arrows in (h) mark sense of streamwise vortices.

Pressure loss and distortion in the base flow are characterized using total pressure measurements at the AIP for  $0.29 < M_{AIP} < 0.58$  and are shown using color raster plots in Figure 4.4a-h. There are two primary regions of total pressure deficit: one each along the top and bottom surfaces that are associated with secondary flows and separation at the diffuser's bends. As the Mach number is increased, the regions of total pressure deficit increase in size and magnitude at the AIP, as indicated by larger areas of the AIP color raster plots having lower total pressure. This indicates increased advection of low-momentum fluid from the wall region into the core flow (marked by arrows in Figure 4.4h) by the secondary flow that lifts off the downstream edge of the second turn flow separation (arrows in Figure 4.2b). In addition, it can be seen that the losses manifested by the total pressure deficit with the first-turn separation over the lower-surface are less intense compared to the losses associated with separation at the second turn over the upper surface. These differences are attributed to the dissimilar separation domains at the two diffuser

turns, and the lesser distance the second-turn vortices have to dissipate before reaching the AIP. Moreover, the streamwise vortices that are formed along the upper surface couple to the spanwise edges of the separated domain, having the streamwise vortex pair lifting off the surface (Figure 4.3) at the tail end of the separation bubble in Figure 4.2b. This vortex pair appears to induce significant total pressure deficit in the top center of the AIP, most noticeable in in Figure 4.4f-h.

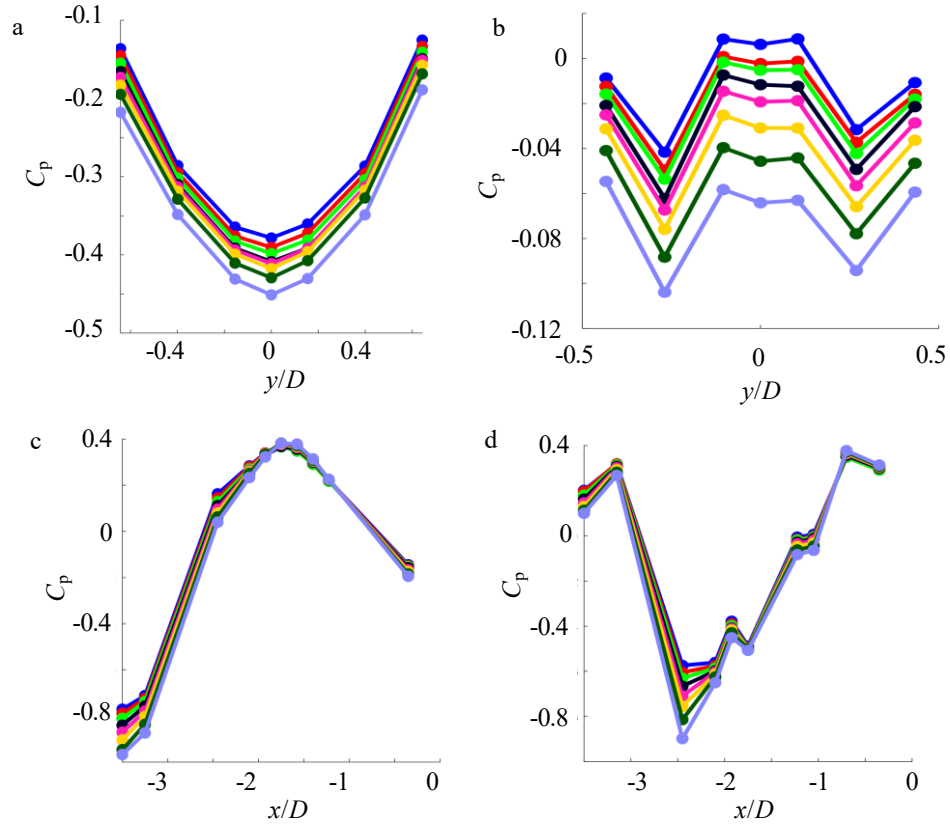


**Figure 4.5** Variation of  $C_p$  in the base flow along the span of the diffuser for  $-0.5 < y/D < 0.5$  at  $x/D = -1.9$  (a) and  $-1$  (b), and streamwise variation of  $C_p$  along the centerline ( $y = 0$ ) for  $-3.5 < x/D < 0$  on the bottom (c) and top (d) surfaces for  $M_{AIP} = 0.29$  (●),  $0.34$  (●),  $0.38$  (●),  $0.43$  (●),  $0.47$  (●),  $0.51$  (●),  $0.54$  (●), and  $0.58$  (●).

Further insight into the structure of the base flow is provided by analysis of static pressure distributions along the surface of the diffuser for the same  $M_{AIP}$  cases as shown in

Figure 4.4. The pressure coefficient  $C_p = 2(p/p_{ref} - 1)/(\kappa \cdot M^2)$  was computed using the average AIP static pressure as reference pressure and Mach number at the AIP. Figure 4.5a-d shows spanwise and streamwise distributions of  $C_p$  using spanwise pressure ports about the centerline at  $x/D = -1.9$  ( $-0.5 < y/H < 0.5$ ) and  $x/D = -1$  ( $-0.5 < y/D < 0.5$ ) and streamwise pressure ports at  $y = 0$  and  $-3.5 < x/D < 0$ . The family of spanwise pressure profiles at  $x/D = -1.9$  in Figure 4.5a, which is located upstream of the second-turn separation (Figure 4.2b) indicates the flow symmetry about the center plane, where the peak flow acceleration is along the centerline. The corresponding spanwise static pressure distributions at  $x/D = -1$  ( $-0.5 < y/D < 0.5$ ) is located across the second-turn separation bubble are shown in Figure 4.5b. The central three ports are within the separation bubble and show nearly-uniform pressure at all flow conditions, while the pressure dips on the right and left indicates some flow acceleration just outside of the separation domain, presumably due to the downwash effect of the bounding streamwise vortices (cf. Figure 4.2b). The outboard pressure distributions indicate deceleration of the flow that is attributed to upwash of the streamwise vortices.

The streamwise pressure distribution along the diffuser's lower diffuser surface in Figure 4.5c indicates that the flow enters the diffuser throat ( $x = 0$ ) with the highest velocity (lowest pressure) and begins to decelerate along the lower surface, up to a maximum static pressure at about  $x/D = -1.5$ , which is slightly downstream of the beginning of the diffuser's second turn ( $x/D = -1.75$  based on diffuser centerline). In the second turn, the flow accelerates and, consequently, the pressure decreases. The evolution of the pressure along the diffuser's upper surface (Figure 4.5d) is markedly different, owing to the fundamental differences between the two internal separation patterns. An initial pressure increase

between the first two pressure ports is followed by a sharp decrease up to the next pressure port, about  $x/D = -2.5$ . As the flow approaches the second turn along the upper surface ( $x/D > 2$ ), there is small net pressure increase, which is followed by a significant adverse pressure gradient that leads to flow separation. The two pressure ports about  $x/D = -1$  (upstream of the last two ports) are contained within the separated bubble and indicate that the pressure levels out. Once the flow reattaches, the last two ports indicate that the flow conforms to the diffuser geometry.

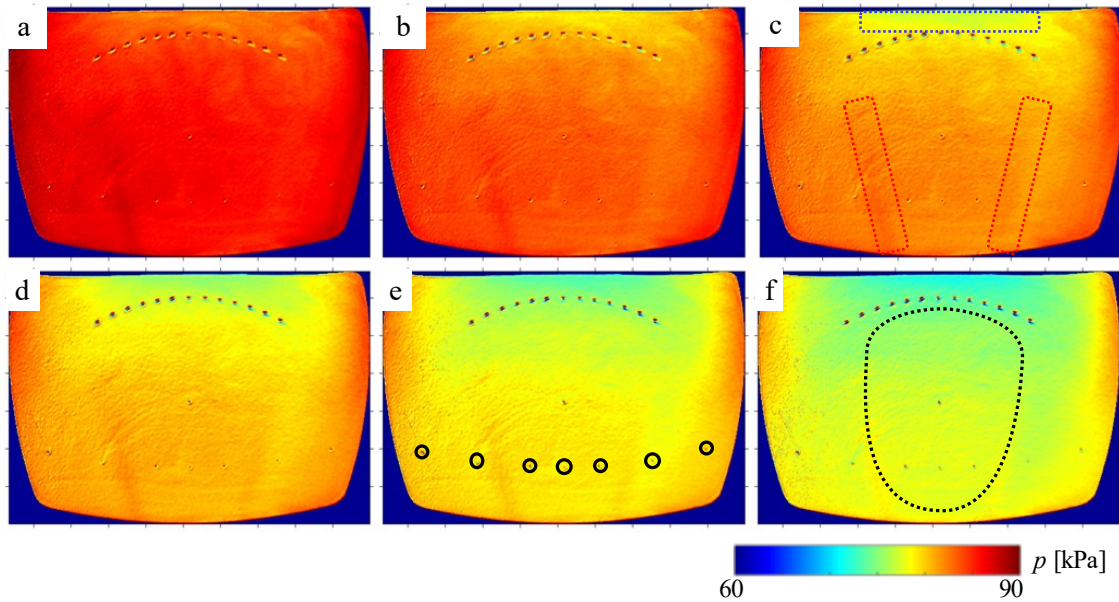


**Figure 4.6** Color raster plots of surface pressure in the base flow measured using PSP at  $M_{AIP} = 0.41$  (a), 0.45 (b), 0.47 (c), 0.49 (d), 0.50 (e), and 0.53 (f). Blue dashed region in (c) marks low-pressure region just upstream of jets. Red dashed domain in (c) marks region of elevated pressure. Black dashed domain in (f) bounds the elevated pressure region (separation). Black circles in (e) mark pressure ports at  $x/D = -1$  (cf. Figure 4.5b). Flow is from top to bottom.

Additional details of the second-turn separated domain are provided by color raster plots of surface static pressure in Figure 4.6a-f obtained using pressure-sensitive paint (PSP described in Ch. 2 and in the Appendix) over the second-turn flow control insert (within

the nominal domain  $-0.69 < y/D < 0.69$ ,  $-1.68 < x/D < -0.88$ ). These distributions are measured for  $0.32 < M_{AIP} < 0.53$ . The images show the orifices of the array of actuation jets and the spanwise array of static-pressure ports (ports circled in Figure 4.6e). In addition, various markings are visible in the PSP images, which is attributed to the texture of the PSP surface itself. These markings, which are consistent across Mach numbers, should be disregarded when analyzing the surface pressure trends.

As expected, surface pressure globally decreases with increasing diffuser Mach number. In general, all the pressure color raster plots in Figure 4.6 indicate that the oncoming flow upstream of the flow control jets induces a suction peak at the centerline (marked by blue dashed region in Figure 4.6c) with the pressure increasing outward towards both spanwise edges. The separation bubble downstream from the jet array is depicted by a region of elevated surface static pressure, which is most visible and outlined in Figure 4.6f. Its spanwise bounds are marked by the highest pressure-levels (marked by red dashed lines in Figure 4.6c) which coincide with the streamwise vortices along the spanwise edges of the bubble (cf. Figure 4.2). This trend is also in agreement with the direct spanwise pressure measurements across the span at  $x/D = -1$  (Figure 4.5b), where the port locations are marked in Figure 4.6e. A drop in the surface pressure is observed just outside of the bubble bounds, and its rise further outbound are both clearly captured by the PSP measurements.



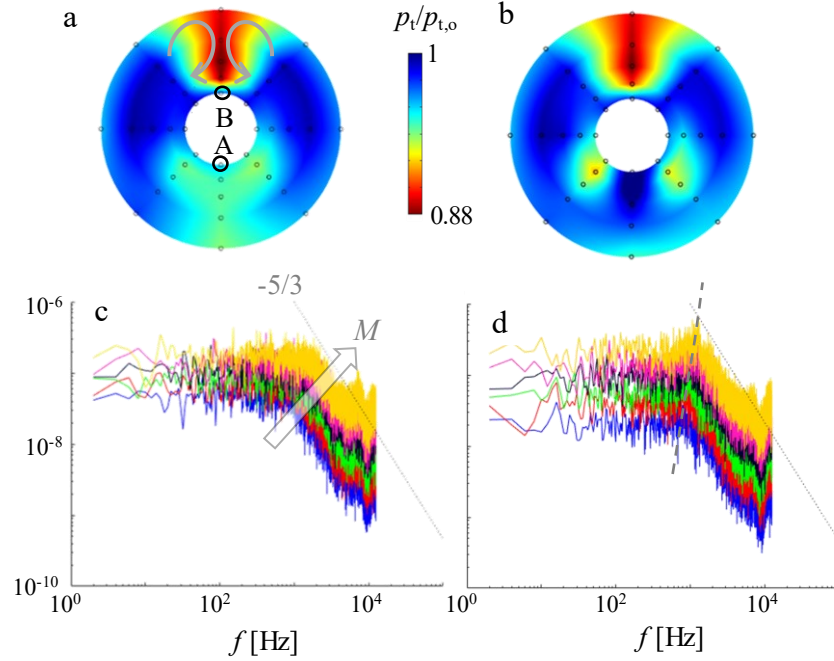


**Figure 4.7** Color raster plots of the time-averaged (a) and instantaneous (b) total pressure at the AIP, and power spectra of the total pressure fluctuations at transducers A ( $i = 1, j = 5$ ) (c) and B ( $i = 1, j = 1$ ) (d),  $M_{AIP} = \text{0.342, 0.382, 0.421, 0.459, 0.492, 0.527}$ .

In addition to time-averaged measurements, the flow at the AIP was also characterized using dynamic, time-resolved measurements of the AIP total pressures (cf. Section 2.3.1.2). This yields important topological assessment of the dynamics and intensity of coherent motions that are associated with the presence of the streamwise vortical structures in the base and controlled flows. Some dynamic measurements in the base flow are shown in Figure 4.7 (more detail in Section 4.4.2). For reference, Figure 4.7a shows distribution of the time-averaged total pressure at the AIP, which depicts the signatures of the two pairs of streamwise vortices, coupled to separation domains at the first turn (bottom surface) and second turn (top surface). Two AIP pressure transducers, marked in each separation domain (“A” in the top center inner ring and “B” in the bottom

center of the inner ring in Figure 4.7a), are selected to represent the two domains. A family of spectra of total pressure fluctuations for transducer “A” is shown in Figure 4.7c for six AIP Mach numbers ranging from 0.342 to 0.527. These spectra are relatively flat below 1 kHz followed by a sharp drop off at a slope closely following  $-5/3$ . As expected, the power of fluctuations monotonically increases with Mach number. A similar group of spectra for transducer “B” is shown in Figure 4.7d. However, compared to the fairly featureless spectra of transducer “A”, these spectra exhibit distinct peaks at about 1 kHz where the frequency of these peaks increases with the diffuser Mach number, from about 800 Hz at  $M_{AIP} = 0.342$  to 1300 Hz at  $M_{AIP} = 0.527$  (other nearby transducers also exhibit similar spectral peaks). In connection with the earlier discussion of the relationship between the topology of the pressure deficit and the counter-rotating streamwise vortices, it is argued that this frequency is associated with an instability of these vortex pairs.

Another important observation associated with the time-resolved measurements of the total pressure is that the time-averaged total pressure deficit on the bottom half of the AIP results from the unsteady motion of the vortices that are triggered farther upstream (at the first turn) and therefore may appear to be less coherent in the time averaged field at the AIP than that of the second turn. In fact, instantaneous pressure measurements show that the lower half of the AIP intermittently exhibits two distinct nodes of the total pressure deficit, as shown in Figure 4.7b that are ostensibly associated with two distinct streamwise vortices along the lower surface. The pressure data indicate that these vortices meander such that their cores are closer or farther apart by the time they reach the AIP and therefore this unsteadiness is manifested by an absence of a sharp spectral peak in the spectra of Figure 4.7c.

### 4.3 Flow Control Effects

To address the separation along the second turn, an array of fluidic oscillating jets are placed just upstream of the closed separation domain found in the surface oil visualization (Figure 4.2a). This is implemented using a flow control module which includes a spanwise array of fluidic oscillating jets whose width is about 50% of the test section span (17 jets spaced 6.35 mm apart) as illustrated in Figure 4.8a and described in Section 2.4. The jets in each half of the array are yawed away from the centerline to create predominantly single-sign vorticity concentrations of opposite sense to the naturally occurring streamwise vortices.

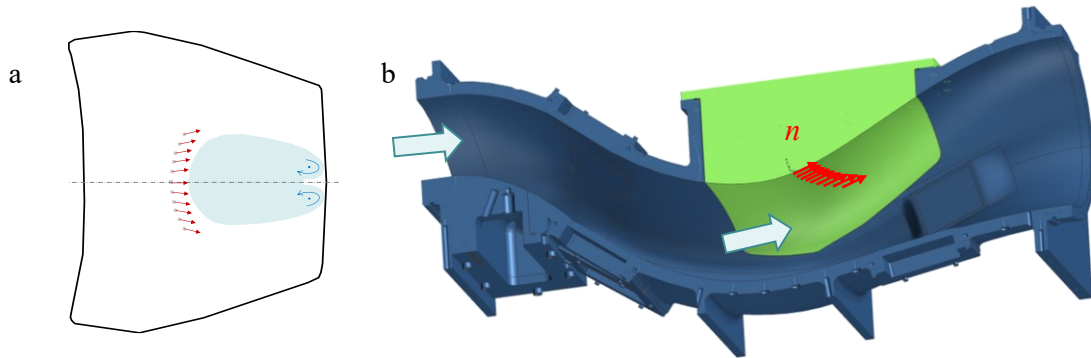


**Figure 4.8** a) Schematic rendition of the yawed jet array just upstream of the second turn separated region (marked in green in b); and b) a CAD image of a cross section of the actuation module installed in the diffuser.

As indicated in Figure 4.4, the distortion at the top half of the AIP is predominantly the result of the formation of a closed separation domain within the second turn and its coupling to a streamwise, counter-rotating vortex pair. A central element of the present investigations is the use of active flow control (AFC) for deliberate manipulation of the trapped vorticity within the separation region and its coupling to the secondary vortices within the top half of the diffuser. The effects of the actuation on separation in the first

turn (bottom surface) are discussed in Chapter 5. The effects of the actuation on the second-turn separation as depicted in total pressure distribution measured at the AIP are shown in Figure 4.9a-j for  $M_{AIP} = 0.54$  (the base flow is shown for reference in Figure 4.9a). The actuation is applied at  $C_q$  which is increased in equal increments of 0.09% up to 0.81% in Figure 4.9b-j.

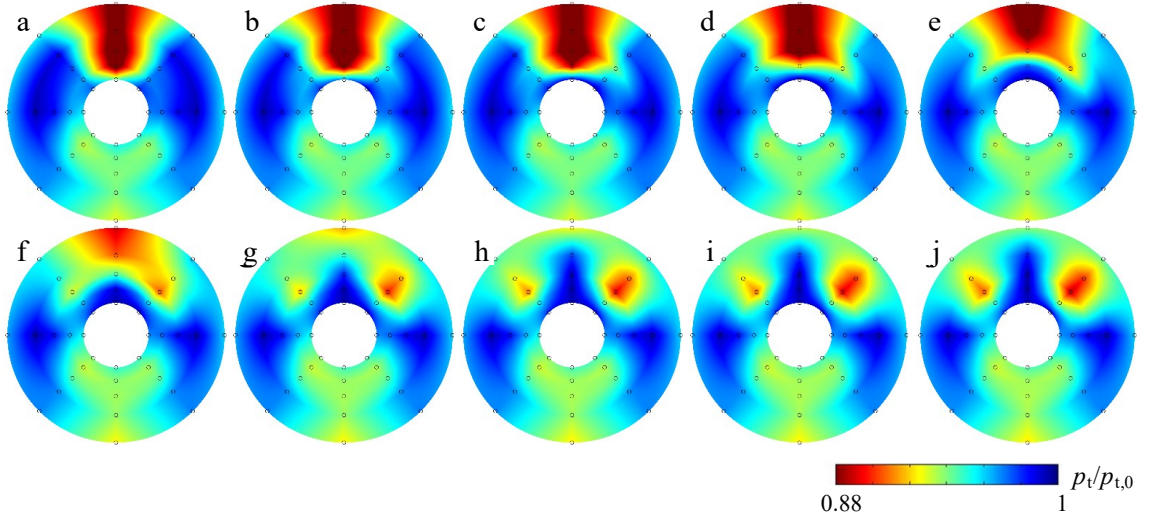


**Figure 4.9** Color raster plots of the total pressure at the AIP for  $M_{AIP} = 0.54$  and  $C_q = 0\%$  (a), 0.09% (b), 0.18% (c), 0.27% (d), 0.36% (e), 0.45% (f), 0.54% (g), 0.63% (h), 0.72% (i), and 0.81% (j).

The distortion  $DPCP_{avg}$  (cf. Section 2.3.1.3) in the base flow computed from the total pressure distribution at the AIP (Figure 4.9a) is  $DPCP_{avg} = 0.038$  and is predominantly affected by the upper-surface deficit. In the presence of actuation at low  $C_q$  (0.09%, 0.18%, and 0.27%, Figure 4.9b-d, respectively), there is a weak proportional flattening of the total pressure deficit along the upper AIP surface that reduces  $DPCP_{avg}$  by about 10%. As  $C_q$  increases past 0.45% (Figure 4.9f), in addition to further suppression of the deficit its shape appears to begin to split into two distinct domains. By  $C_q = 0.54\%$  (Figure 4.9g), instead of a connected deficit domain, two new small “nodes” of pressure deficit emerge at about

45° on each side of the centerline on either side of the top surface. With the further increase in  $C_q$  (Figure 4.9h – j), the high momentum flow penetrates deeper into the central top region (e.g., compare the central top wall between Figure 4.9g and j), but the low-momentum flow becomes increasingly concentrated into two nodes in the top central right and left positions of the AIP pressure contour. Therefore, there are the two competing effects, which are the further deficit decrease in the central region and further increase of deficit at the nodes. Overall, the application of the flow control leads to significant suppression of losses in the central region, increased losses in the nodes, and up to a 50% reduction in  $DPCP_{avg}$ .

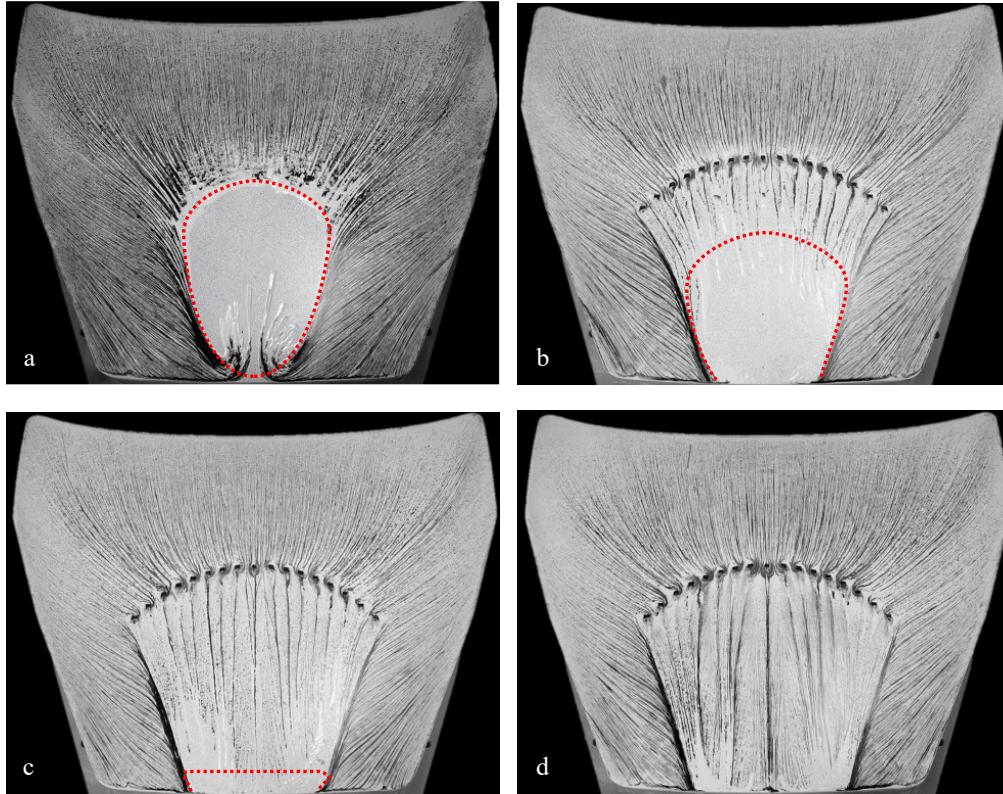


**Figure 4.10 Surface oil visualization over the second turn flow control insert at  $M_{AIP} = 0.54$  using an array of 17 jets at  $C_q = 0$  (a), 0.18% (b), 0.36% (c), and 0.54% (d). Dashed regions mark estimated separation extent.**

To assess how the flow control impacts the base flow, three flow-control cases shown in Figure 4.10 are further examined using surface oil visualization (the base flow is shown in Figure 4.10a for reference) for  $C_q = 0.18\%$ ,  $0.36\%$ , and  $0.54\%$  (Figure 4.10b-d, respectively). At  $C_q = 0.18\%$ , the oil streaks show clear imprints of streamwise vortices formed by each of the jets immediately downstream of the jet orifices. The actuation appears to delay the onset of separation (estimated separation marked by dashed lines) as is evidenced by the streaks indicating attachment that protrude downstream, but at the same time, the downstream end of the closed separation domain migrates farther downstream out of the field of view. In addition, the actuation seems to widen the spanwise spacing between the bounding vortices. It is conjectured that this slight displacement weakens the central upwash of the low-momentum fluid by the streamwise vortex pair that flattens the total pressure deficit in Figure 4.9c. The pressure losses at the upper segment of the AIP in Figure 4.9e are still present even at  $C_q = 0.36\%$ , although the jets are able to maintain the attached flow further into the separation bubble, as seen in Figure 4.10c where the previously separated region is almost fully attached. A clear outboard displacement of the streamwise vortices is at this  $C_q$  somewhat diminishes the central upwash as evidenced by increased total pressure in Figure 4.9e. Finally, at  $C_q = 0.54\%$  (Figure 4.10d), the flow appears to be attached within the entire central domain, as is evidenced by oil streaks continuing through the whole visualized domain. This leads to the weakening and even larger spanwise displacement of the secondary vortices (cf. Figure 4.9g). The larger displacement raises the central total pressure in Figure 4.9g since the upwash of low momentum fluid into the central upper region of the flow is reduced, and instead two separate nodes of total pressure deficit appear for each vortex.

## 4.4 Effects of the Width of the Actuator Array

Following the demonstration of the effectiveness of the full 17-jet array, an optimized jet configuration was sought by incrementally decreasing of the number of active jets, symmetrically on each side. This optimization study was motivated by the finding that past a certain total  $C_q$  for the 17 jet array, there was a trade-off in further improvements due to the opposing trends that were discussed in connection with Figure 4.9. Starting with the full jet array, the two outermost jets are iteratively excluded from the active jet array, yielding multiple actuation cases for which the number of central active jets was decreased by increments of two from 17 down to 3.

### 4.4.1 *The Time-Averaged Flow*

The effect of reducing the number of active jets is examined using oil visualization over the second-turn flow control surface, which is shown in Figure 4.11 where the mass flow rate through each jet is held roughly constant ( $C_q/n \approx 4 \times 10^{-4}$ ) while the number of jets is reduced. These oil streak images clearly show that, regardless of the number of active jets, the effect of flow attachment downstream of the active jets is maintained. As a consequence, the spanwise extent of the attached flow narrows with the reduction in  $n$  (shown by the spanwise extent of the streaks, marked in Figure 4.11a, c), and at first, the flow outside the controlled, attached domain also remains attached. This has a significant ramification on the spacing of the streamwise vortices that form along the boundary of the controlled and uncontrolled flow (the position of the vortices for  $n = 17$  is discussed in connection with Figure 4.10, and marked in Figure 4.11a). As  $n$  decreases, the gap between the naturally attached flow and controlled attachment widens which is visible



starting for  $n = 13$ , and marked in Figure 4.11d and e, but continues to widen through Figure 4.11h. The evolution of the flow within these gaps gives rise to local separation cells that further spread spanwise as the number of active jets decreases, as is evidenced by the progression from Figure 4.11c to h where the regions without oil streaks on either side of the controlled attachment grow in size monotonically.

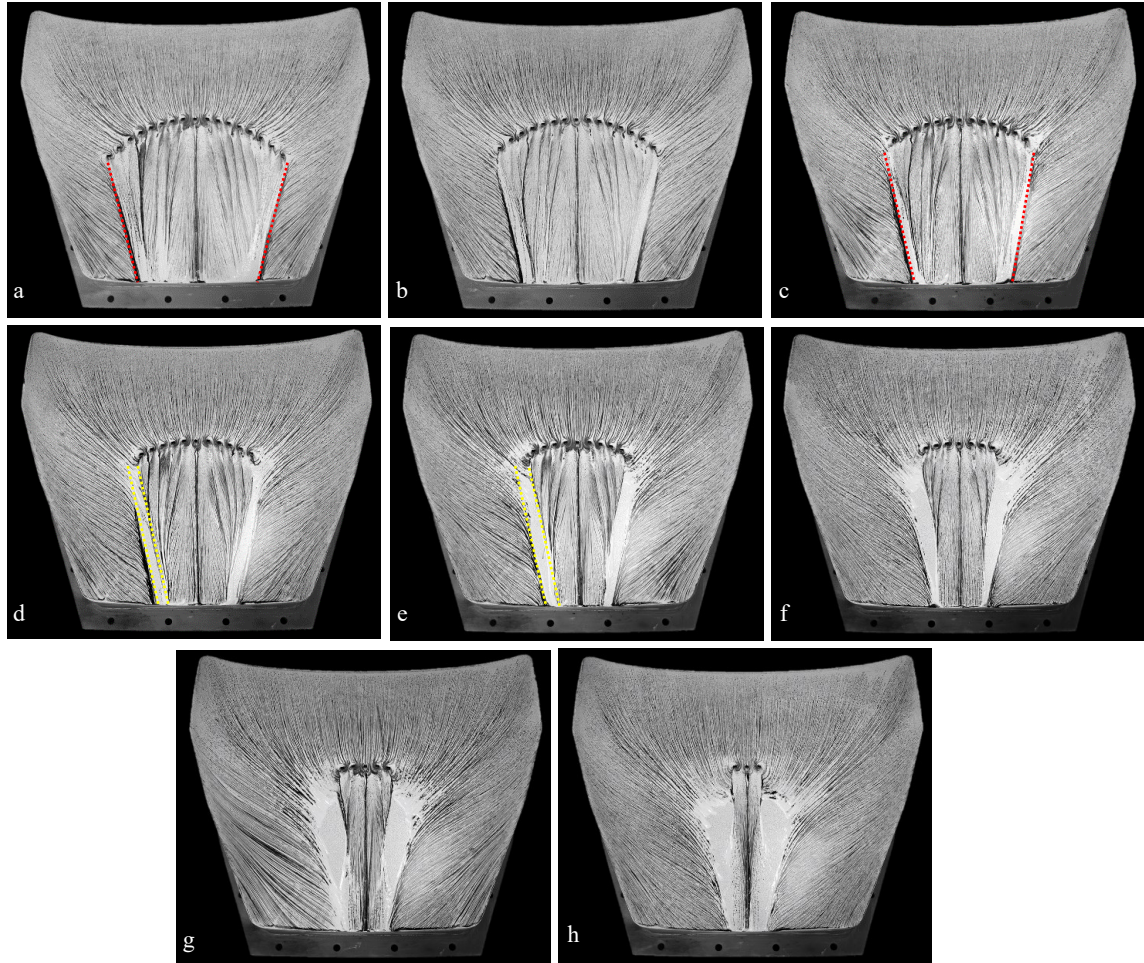


**Figure 4.11** Surface oil visualization at  $M_{AIP} = 0.54$  over the second turn flow control insert, with  $C_q/n \approx 4 \times 10^{-4}$  and varying number of active jets.  $C_q$ ,  $n = 0.72\%$ , 17 (a),  $0.62\%$ , 15 (b),  $0.54\%$ , 13 (c),  $0.46\%$ , 11 (d),  $0.37\%$ , 9 (e),  $0.29\%$ , 7 (f),  $0.21\%$ , 5 (g), and  $0.12\%$ , 3 (h). Red dashed lines mark spanwise extent of effected attachment domain (a, c). Yellow dashed lines mark gap between naturally attached flow and controlled-attached flow (d, e).



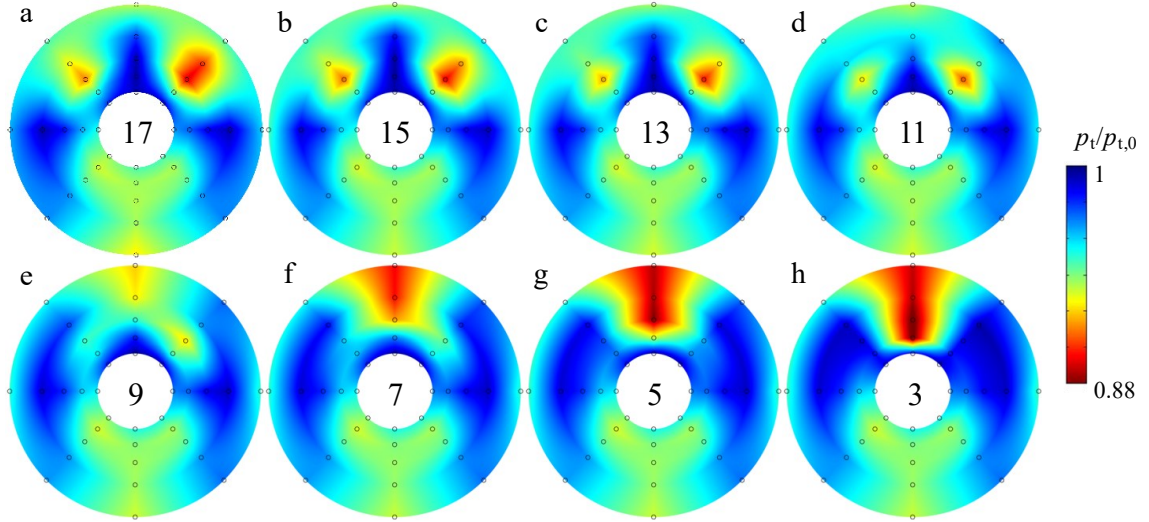


**Figure 4.12** Color raster plots of the total pressure at the AIP at  $M_{AIP} = 0.54$  that are labeled by the number of active jets  $n$  with  $C_q = 0.72\%$  (a),  $0.62\%$  (b),  $0.54\%$  (c),  $0.46\%$  (d),  $0.37\%$  (e),  $0.29\%$  (f),  $0.21\%$  (g), and  $0.12\%$  (h).

The effects of the actuation patterns in Figure 4.11 on the flow losses and distortion are assessed from measurements of the total pressure distributions at the AIP as shown in the Figure 4.12 for the same actuation cases. When the number of active jets varies between 17 and 11 (Figure 4.12a-d, respectively), the actuation displaces the secondary streamwise vortices along the upper surface, which is manifested by the two individual “nodes” of the total pressure deficit, indicated by the localized high pressure deficit regions on the top left and right of Figure 4.12. Despite the reduced separation between the vortices with decreasing  $n$ , the vortex behavior does not return to the coupled pair of vortices found in the base flow (Figure 4.9a), but continues to keep the vortices separated by a central high-pressure region.

However, as  $n$  is reduced to 9 (Figure 4.12e), the distinctly individual “nodal” vortex signatures diminish, and there is a simultaneous increase in the total pressure deficit along the top surface, resulting in a connected top-surface pressure deficit region. This

behavior coincides with an increase in the separation cells discussed in connection to Figure 4.11. It is argued that these separation cells induce flow losses (shown in Figure 4.12e-h), which, when combined with the decreasing spanwise separation between the streamwise vortices can lead to upwelling of low momentum fluid between them, as evidenced by the increase in pressure deficit with the reduction of  $n$  in Figure 4.12e-h. Therefore, reduction in the number of active jets past the point at which the separation pockets begin to grow locally induces attachment at the center of the flow (Figure 4.11) but does not mitigate separation enough to reduce pressure losses at the AIP associated with it.

Any further reduction in  $n$  (Figure 4.12f-h) does not prevent the central pressure deficit to form, effected by increasing advection of low momentum fluid towards the top center, much like the base flow streamwise vortices. Although not as severe, the distortion pattern for the three active jets (Figure 4.12h) does not differ much from the corresponding pattern in the base flow in Figure 4.9a. It should be noted, though, that the underlying flow dynamics of the base flow (governed by the two streamwise vortices detaching from the tail-end of the separation bubble, see Figure 4.10a) and that of the flow controlled by the three central jets is substantially different (cf. Section 4.4.2).

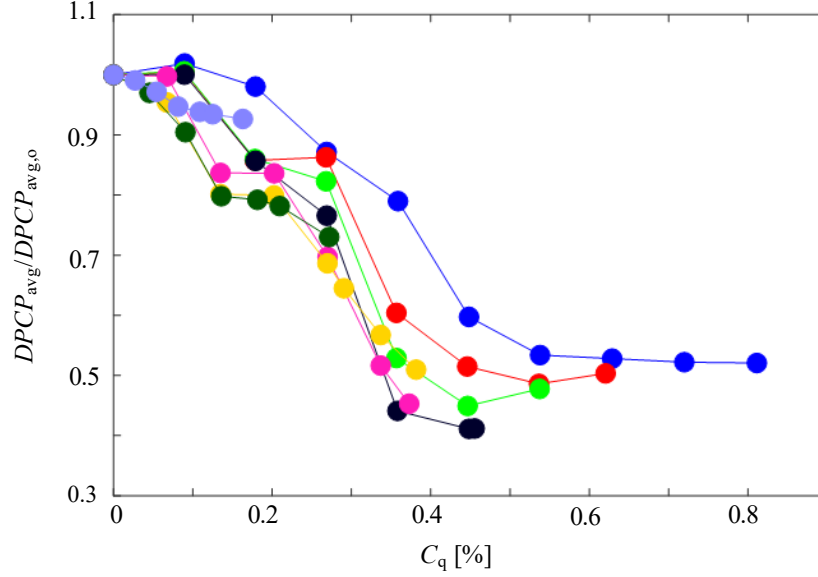


**Figure 4.13** Variation of the relative change in the mean circumferential distortion parameter  $DPCP_{avg}$  with  $C_q$  for  $n = 3, 5, 7, 9, 11, 13, 15$ , and  $17$  jets ( $M_{AIP} = 0.54$ ).

These eight jet array configurations are tested with a varying  $C_q$  and their effectiveness is assessed using  $DPCP_{avg}$ . Figure 4.13 shows  $DPCP_{avg}$  scaled by that of baseline ( $C_q = 0, DPCP_{avg,o}$ ) for each of the jet arrays tested. These data show several interesting features in the variation of  $DPCP_{avg}$  with  $n$  and  $C_q$ . First, the flow response to small  $C_q$  improves with reduction of the number of jets; only five active jets yield a 20% reduction in distortion at  $C_q = 0.125\%$ . This trend emphasizes the importance of the local jet effect, where for a given total  $C_q$ , mass flow rate per jet ( $C_q/n$ ) increases with decreasing number of jets. However, there is a limit of the distortion reduction that can be achieved with a fixed number of jets, which limits the utilization of smaller actuation arrays. For instance, the 3-jet array cannot effect more than 10% improvement, while the 5-jet array plateaus at less than 30% improvement. When examined for the optimal configuration, it is found that there is no sharp cutoff that points to an optimal  $n$ . These results suggest that the probable optimum lies between  $n = 9$  and  $n = 13$  jets. A broad optimum is clearly

beneficial for practical applications, allowing for a wider operational range that would result in significant reduction in distortion. Furthermore, these initial optimization results indicate that nearly 60% reduction in  $DPCP_{\text{avg}}$  could be achieved with  $C_q < 0.5\%$ , compared to nearly 50% reduction at  $C_q = 0.63\%$  for the  $n = 17$  configuration.

In the present study the selection of the ‘optimal’ jet array is restricted to considerations of three parameters namely, the actuation mass flow rate ( $C_q$ ), the changes in the AIP Mach number ( $M_{\text{AIP}}$ ) that are brought about by the actuation, and the distortion ( $DPCP_{\text{avg}}$ ). Considering these parameters, the desire is to minimize both  $C_q$  and  $DPCP_{\text{avg}}$ , and while maximizing  $M_{\text{AIP}}$  for a given blower power in the experimental facility. The optimum that is discussed in the context of the present investigations is clearly a “soft optimum” based on the actual experimental runs. Values for the parameters associated with the broadly optimum cases in Figure 4.13 are shown in Table 4.1. The case of  $n = 13$  jets is chosen for the purposes of further analysis.

**Table 4.1 Parameter values for cases within broad optimum region.**

<b>n</b>	<b><math>M_{\text{AIP}}</math></b>	<b><math>DPCP_{\text{avg}}</math></b>	<b><math>C_q</math></b>
9	0.537	0.0164	0.28%
11	0.540	0.0149	0.35%
13	0.538	0.0163	0.34%

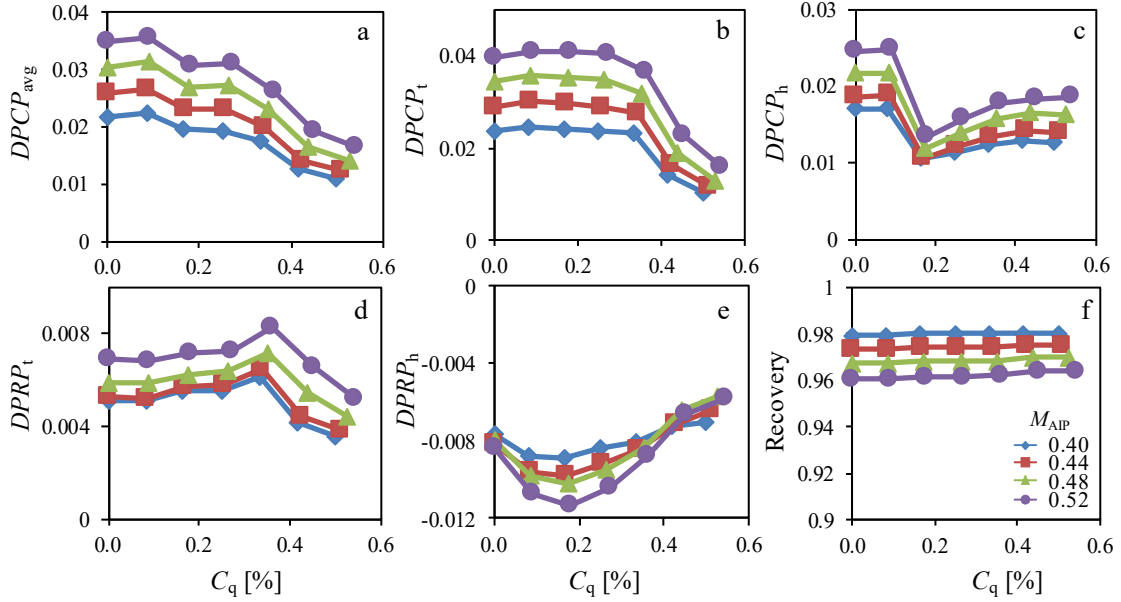


**Figure 4.14** Variation with  $C_q$  ( $n = 13$ ) of the distortion parameters  $DPCP_{avg}$  (a),  $DPCP_t$  (b),  $DPCP_h$  (c),  $DPRP_t$  (d), and  $DPRP_h$  (e) and of Pressure Recovery (f), for  $M_{AIP} = 0.4, 0.44, 0.48, 0.52$ .

The performance of an optimal jet array configuration ( $n = 13$ ) is characterized in more detail for a range of actuation flow rates using time-averaged distortion parameters and the recovery at  $M_{AIP} = 0.40, 0.44, 0.48, 0.52$  (Figure 4.14). The distortion parameters include: circumferential face-averaged (Figure 4.14a), tip (Figure 4.14b) and hub (Figure 4.14c), and radial tip (Figure 4.14d) and hub (Figure 4.14e), and the pressure recovery (Figure 4.14f). These data show that the trends with variation of  $C_q$  are similar over the range of tested Mach numbers. The circumferential face-averaged distortion parameter  $DPCP_{avg}$  decreases by 50 to 55% at about  $C_q = 0.52\%$  for all  $M_{AIP}$  (Figure 4.14a).  $DPCP_t$  (Figure 4.14b) is nearly invariant with  $C_q$  until the evolution of the streamwise vortices in the base flow is altered (and partially suppressed) at higher  $C_q$ . The corresponding variation of the radial tip distortion (Figure 4.14e) follows the same trend, although at lower magnitude. The initial sharp drop in  $DPCP_h$  (Figure 4.14c) at low  $C_q$  is followed by a weak

increase with  $C_q$  (to 0.3 and then remains invariant), while the radial equivalent (Figure 4.14f) is not detrimental for any of the operating parameters. Finally, the significant decrease in the averaged circumferential distortion is accompanied by a weak increase in recovery (Figure 4.14f).

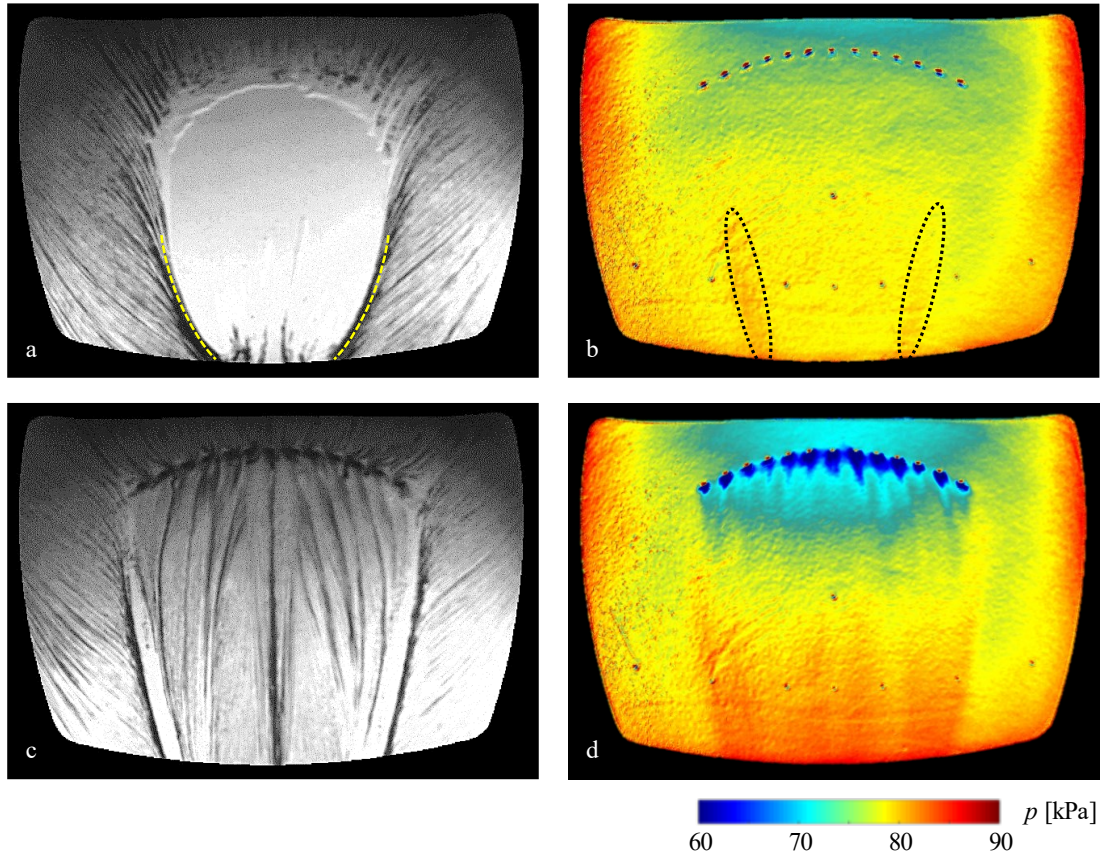


**Figure 4.15** Images of surface oil visualizations (a, c) and corresponding color raster plots of surface pressure measured using PSP (b, d) in the base flow (a-b,  $C_q = 0$ ) and in the presence of actuation (c-d,  $C_q = 0.5\%$ ,  $n = 13$ ) at  $M_{AIP} = 0.54$ . Yellow dashed lines mark vortex traces (a). Corresponding high-pressure regions marked in (b) with black dotted lines.

To summarize the time-average effects of the optimal  $n = 13$  flow control configuration, the effects on flow topology is investigated using PSP and discussed with respect to the base flows in Figure 4.15. Color raster plots of static surface pressure derived

from PSP measurements are shown in Figure 4.15b and d, for the base and controlled ( $C_q = 0.54\%$ ) flows, respectively. The camera used for the PSP measurements is also utilized to record the corresponding oil visualizations (Figure 4.15a,b). The oil visualization images in the base flow (Figure 4.15a) show the presence of the separation bubble and the formation of streamwise vortices at its edges as discussed in connection with Figure 4.10, marked in Figure 4.15a with yellow dashed lines. The presence of these vortices is marked by black dotted lines in the corresponding surface pressure distribution in Figure 4.15b, which show elevated pressure on the surface, possibly due to vortex downwash. In the presence of actuation, Figure 4.15c shows the controlled attachment region with signatures of the bounding vortex on the sides as discussed in connection with Figure 4.11. The surface pressure distribution (Figure 4.15d) shows that the issuing jets induce a local low-pressure region immediately downstream of the actuation orifices. The lower surface pressure upstream of the actuator array indicates that the upstream flow is accelerated by the actuation jet ostensibly owing to strong entrainment (jet pump effect) and a local reduction in the losses through the diffuser. It is interesting to note that once the flow becomes reattached following separation in the base flow, the surface pressure downstream of the jet orifices increases relative to the base flow. This pressure increase is indicative of the streamwise decrease in the global speed of the flow through the diffuser.



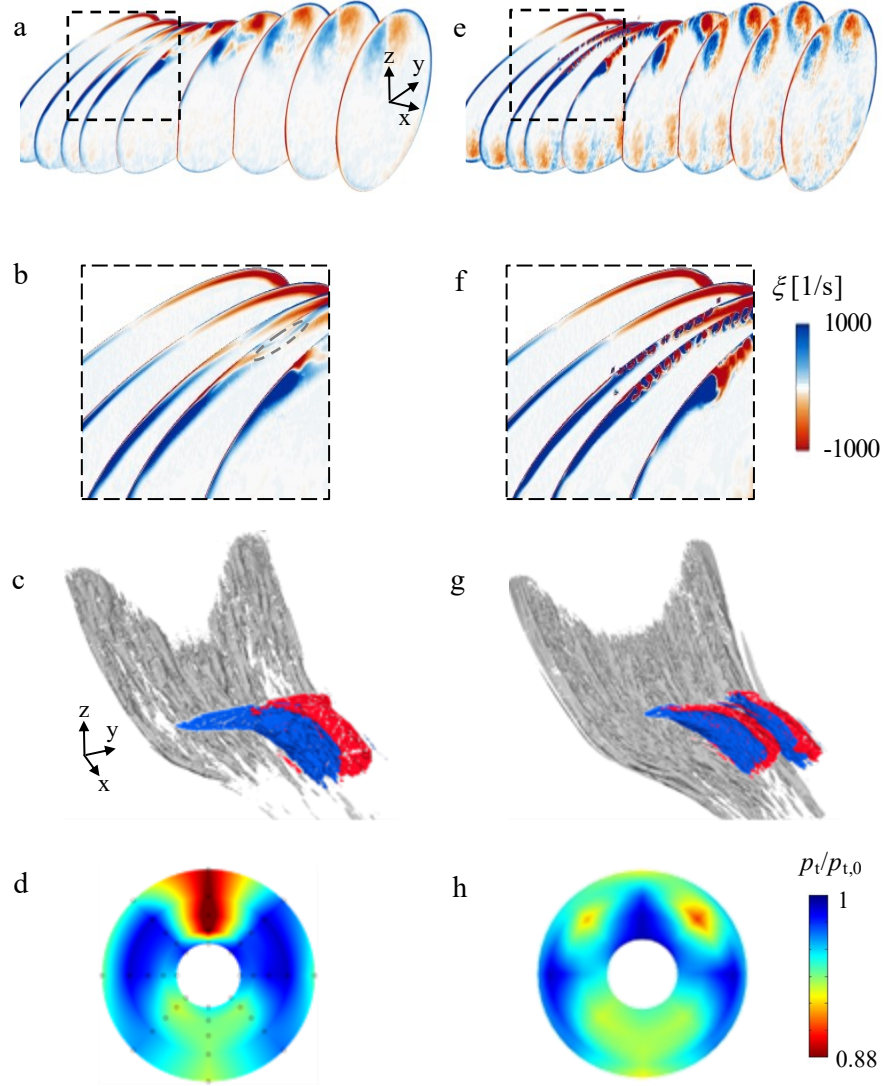


**Figure 4.16 Simulations of the base (a-d) and controlled (e-h) flows ( $n = 13$ ,  $C_q = 0.4\%$ ,  $M_{AIP} = 0.54$ ) showing the evolution of time-averaged cross sections of the counter-rotating vortex pair (streamwise vorticity, a-b, e-f), iso-surfaces of streamwise vorticity (c, g), and the corresponding measured color raster plots of the total pressure distributions at the AIP (d, h).**

Time-averaged CFD simulations are used to investigate the coupling between the separated domain downstream of the second turn of the diffuser and the rolling of streamwise vortices at its spanwise edges (Figure 4.2b). The rollup is depicted in sectional distributions of streamwise vorticity concentrations in successive cross sections from just before the jet array ( $x/D = -1.75$ ) to the AIP ( $x = 0$ ) (Figure 4.16a), and the topology of the



resulting streamwise vortex pair is shown in Figure 4.16c. These data show that the counter-rotating vortex pair leads to the advection of low-momentum fluid from the inner surface of the diffuser into the core flow, giving rise to significant total pressure losses at the top half of the measured AIP cross section (Figure 4.16d). The rollup of the vortices along the diffuser walls is shown in the closeup view in Figure 4.16b. A thin layer of vortices evolves into a vortex that bounds one side of the second-turn separated region. In this visualization, the separation is the region between these vortices, and is marked with the gray dashed line in Figure 4.16b.

Actuation is applied using an array of 13 jets at  $C_q = 0.4\%$ , which as discussed in connection with Figure 4.13, and alters the structure of the base streamwise vortices significantly. As noted in Chapter 2, the actuation jets are deliberately skewed in the spanwise direction (symmetrically about the centerline) and therefore result in the formation of discrete streamwise vortices having the opposite sense as the streamwise vortex of the base flow on that side (clockwise on the left and counter-clockwise on the right of the center plane). Similar to Figure 4.16a, time-averaged sectional distributions of streamwise vorticity in the presence of actuation are shown in successive cross sections in Figure 4.16e and a closeup of the actuation effect in Figure 4.16f. The upstream-most slice shows a thin layer of vorticity approaching the jets. The third slice, just after the jet array, shows the formation of small-scale streamwise vortex pairs that are predominantly single-sign, which farther downstream (last four slices) coalesce into a concentrated vortex sheet that becomes wrapped along the inboard side of each of the vortices of the main base flow vortex pair. Each of these vortex sheets has a sense that is opposite relative to the vortex it is wrapped around. Therefore, the actuation effectively (and indirectly) controls the

strength and structure of the base flow vortex pair leading to a significant reduction in the circumferential distortion at the AIP by up to 60% at  $M_{AIP} = 0.54$ .

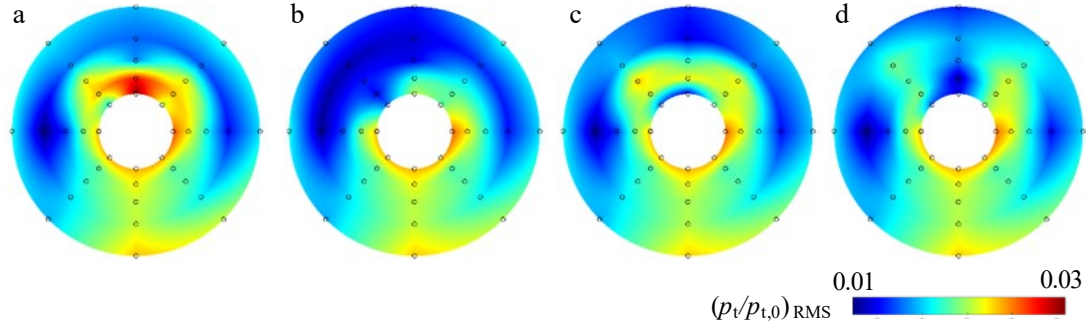


**Figure 4.17** Color raster plots of the RMS fluctuations of the total pressure at the AIP at  $C_q/n \approx 4 \times 10^{-4}$  and varying number of active jets, such that  $C_q$ ,  $n = 0\%$ , 0 (a), 12%, 3 (b), 29%, 7 (c), and 0.54%, 13 (d) at  $M_{AIP} = 0.54$ .

#### 4.4.2 Dynamic Effects

The effect of flow control for the optimal 13 jet array, along with 7 and 3 jet arrays, are further examined and compared to base flow using dynamic pressure measurements (Chapter 2.3.1.2). Color raster plots of the RMS fluctuations of the total pressure (Figure 4.17) show that high RMS levels of the base flow (Figure 4.17a) are distributed about the upper hub domain and are attributed to the instability of the upper pair of streamwise vortices. Aside from the hub region, the RMS fluctuations in the base flow are somewhat elevated along the lower surface, which is associated with the dynamics of the vortex pair that originate from the first turn. When actuation is applied using the central three jet (Figure 4.17b), the upper hub RMS fluctuations is suppressed, implying that one of the effects of the actuation is stabilization of the upper vortex pair. When actuation is effected using seven jets there is an increase in RMS fluctuations compared to the three-jet array. Nonetheless, the high-power fluctuations of the base flow become diffused over the

extended upper hub area by the actuation. This trend in redistribution of the high levels of the total pressure RMS fluctuations evolves further as actuation is expanded to a 13-jet array (Figure 4.17d). The elevated RMS levels appear as a “dual node” structure, or isolated regions in the top right and top left rakes ( $j = 2$  and  $8$ ), separated by low-RMS central domain. These two “nodes” align with the two distinct pressure deficit regions in the time-averaged total pressure in the presence of actuation (Figure 4.12c). It should be noted that the best case of flow control in terms of pressure recovery and distortion ( $n = 13$ ) does not exhibit the lowest RMS fluctuations (it is lowest for  $n = 3$ , cf. Figure 4.18b), owing to the dynamics of the interaction between the base flow and actuation-induced vorticity concentrations that mitigates distortion and assists pressure recovery.

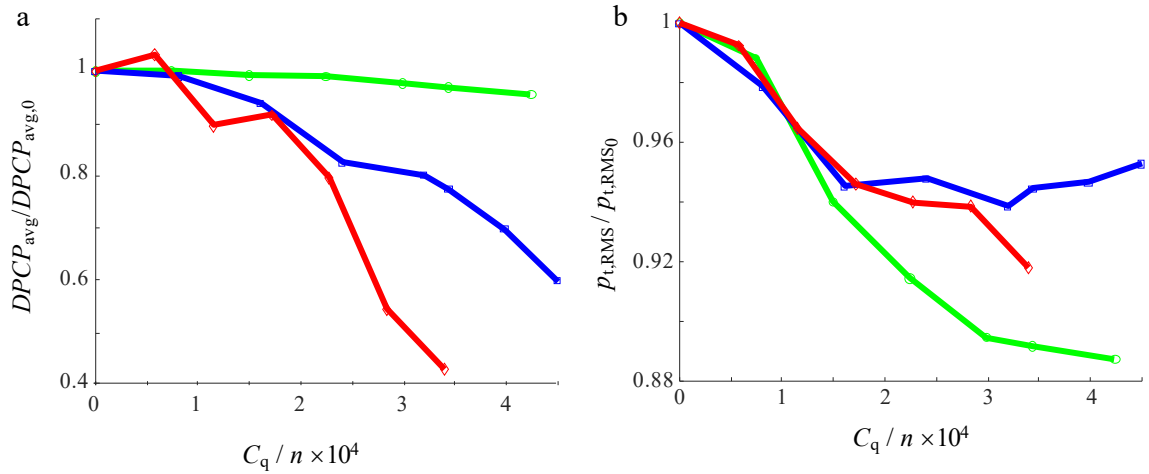


**Figure 4.18** Circumferential distortion parameter  $DPCP_{avg} / DPCP_{avg,0}$  (a), and total pressure RMS / RMS<sub>0</sub> for  $n = 3, 7, 13$ , at  $M_{AIP} = 0.49$ .

Another interesting observation is emphasized in Figure 4.18 in which three characteristic actuation cases  $n = 3, 7$ , and  $13$  are compared. Both the time-averaged distortion and RMS fluctuations of the AIP total pressure are shown for each of these

control cases, with total  $C_q$  kept invariant and equally distributed between the active jets. Figure 4.18a shows the variation with  $C_q/n$  of the time-average  $DPCP_{avg}$  (normalized by base flow distortion  $DPCP_{avg,0}$ ) while Figure 4.18b presents the total pressure RMS fluctuations (normalized by base flow RMS) at  $M_{AIP} = 0.49$ . As seen in Figure 4.18a, actuation by the three central jets does not significantly affect the flow distortion. However, the corresponding time resolved measurements (Figure 4.18b) indicate that this control reduces the flow unsteadiness, which, combined with virtually no effect on the distortion, suggests that this particular flow control approach actually stabilizes the vortex pair responsible for the total pressure deficit along the upper diffuser surface. This stabilization is also evident in Figure 4.17b, where low levels of the total pressure RMS expand outward from the upper surface of the diffuser compared to the base flow (Figure 4.17a). The other two jet arrays, which reduce the time-average total pressure distortion as seen in Figure 4.18a, decrease the RMS levels (Figure 4.18b) with increasing  $C_q$  until levelling out at around  $C_q/n = 2 \times 10^{-4}$ . This effect can be explained by the competing effects of the reduced RMS levels due to the suppression of flow separation along the upper surface and weakening of the corresponding vortex pair, while at the same time exhibiting increases in the RMS levels at the two previously mentioned “nodes”. In a sense, the total pressure distortion suppression in the average is achieved by the disruption and mixing of the dominant streamwise vortex pair by enhancing their interaction and increasing their local unsteadiness.

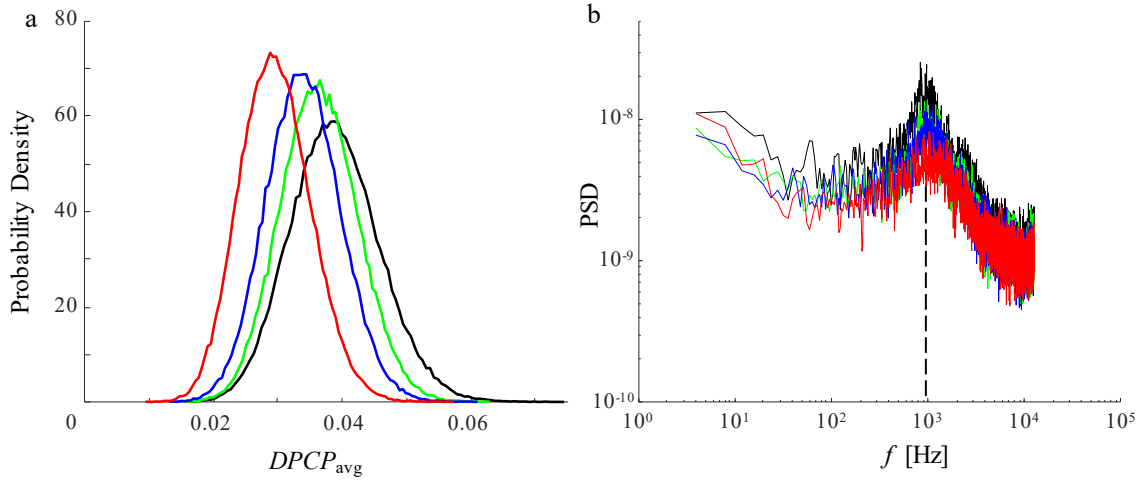


**Figure 4.19 Probability density function of a time-resolved  $DPCP_{avg}$  parameter (a) and its corresponding power spectra (b) for  $n = 0, 3, 7$ , and  $13$  active jets.**

Further insight into time-resolved flow distortion is attained by calculation of the instantaneous circumferential face-averaged distortion parameter  $DPCP_{avg}(t)$  for each realization  $t$  of the 40-probe rake measurements. Figure 4.19a shows the probability density function of the time-resolved  $DPCP_{avg}$  in the absence of actuation and for  $n = 3, 7$ , and  $13$  active jets. These distributions indicate a clear shift of the curves towards lower distortion levels in addition to a decrease in standard deviation, as evidenced by the narrowing of the distributions, with an increasing number of active jets. These curves also indicate a wide range of distortion values, distributed symmetrically about the most probable distortion. For instance, although the time-averaged  $DPCP_{avg}$  of the base flow is estimated to be about 0.038, its distribution indicates peak values up to about 0.076. As the most effective flow control approach is applied ( $n = 13$ ), the most probable distortion levels are reduced from 0.038 to 0.030 and the peaks of  $DPCP_{avg}$  are also reduced by about 25%. Although it was already shown that the corresponding reduction in  $DPCP_{avg}$  of the time-average flow is over 50%, the PDFs in Figure 4.19a indicate that the most expected

levels of the time-resolved distortion decrease by about 22%. This discrepancy is attributed to the smearing effect of time-averaging highly unsteady total pressure distributions, where the time-average misrepresents the instantaneous conditions. Lastly, the dominant frequency measured about the upper wall vortices of about 1 kHz (Figure 4.7c) clearly propagates into the distortion parameter dynamics, as seen in all spectra of  $DPCP_{avg}(t)$  in Figure 4.19b. It should be also noted that, despite the presence of this spectral peak in all of the cases, there is a slight shift in its corresponding frequency with different actuation approaches. Furthermore, the energy level of the dominant frequency somewhat decreases with an increase in the number of active jets.

In addition to the instantaneous analysis of the face-averaged  $DPCP_{avg}$ , the circumferential distortion for each ring  $i$  of the 40-probe rake,  $DPCP(i)$ , is assessed as well. The face-averaged descriptor gives an indication of the overall distortion, but individual distortions over azimuthal probe arrays can give a better idea of the radial contribution of  $DPCP_{avg}$ . These individual spectra and probability density functions of the  $DPCP$  distributions are shown in Figure 4.20 varying from the innermost ring ( $i = 1$ ), Figure 4.20a and f, to the outermost ring ( $i = 5$ ), Figure 4.20e and j (cf. Figure 4.1b that shows the rake and defines  $i$ ). It is apparent that the innermost ring, which is closest to the core diffuser flow, is the least affected by the actuation in terms of pressure distortion. There is minimal difference between the different numbers of jets  $n$  in both the magnitude of spectral peaks and the distribution of values of  $DPCP$  indicated in the PDF. This innermost ring,  $i = 1$ , is the furthest from the actuation, which is along the diffuser surface, closest to the outermost ring  $i = 5$ . Low momentum fluid at the AIP does not penetrate this far into the diffuser core flow from the surface. The next innermost ring,  $i = 2$ , however,

is affected by actuation, as evidenced by the spectra (Figure 4.20b) and PDF (Figure 4.20g). The magnitude of the base flow distortion in this ring is widely varying, without a dominant distortion magnitude as indicated by the low probability density maximum in Figure 4.20g. The base spectra has a peak at 1 kHz, which becomes suppressed even with  $n = 3$  (in Figure 4.20b). When  $n = 7$  or 13, the spectra is rendered featureless, and the distribution of *DPCP* is dramatically improved as is evidenced by the much lower most probable distortion value, and a narrower distribution about these lower values. The ring  $i = 3$  has the most consistent improvement as  $n$  is increased, which is evident by the decrease in power spectral density, particularly at  $f = 1$  kHz and below, and the consistent shifting of the PDF to lower distortion values as  $n$  is increased. Rings  $i = 4$  and 5 also have a spectral peak at 1 kHz, though it is less prominent than rings  $i = 2$  and 3. The effect of  $n$  on the fluctuations and distributions of *DPCP* is not as dramatic as  $i = 2$  and 3 in these outer regions. The effect of increase in  $n$  in ring  $i = 4$  is flattening the spectra (Figure 4.20d), by decreasing the magnitude of the spectral peaks around 1 kHz, and increasing fluctuation power at around 10 kHz, which is attributed to operating frequency the actuation jets (cf. Section 2.4.1). In both rings  $i = 4$  and 5, actuation with 3 or 7 jets has a comparable effect on the distribution of *DPCP*, while an increase to 13 actuation jets results in a distinctly larger reduction in the magnitude of *DPCP*.

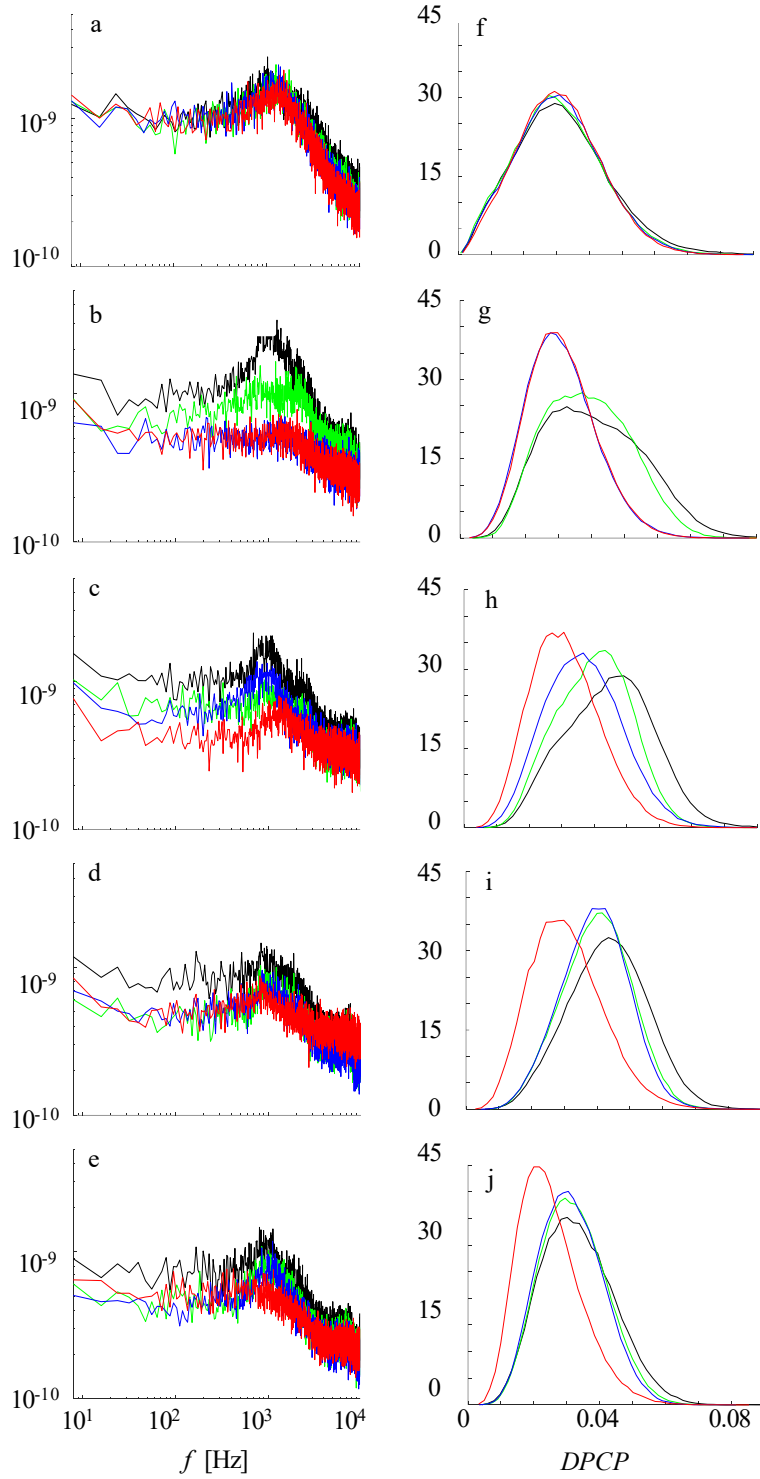


**Figure 4.20** Power spectra of time-resolved *DPCP* for each ring of the 40-probe rake  $i = 1-5$  (a-e) and its corresponding probability density functions (f-j) for  $n = 0, 3, 7$ , and **13** active jets.



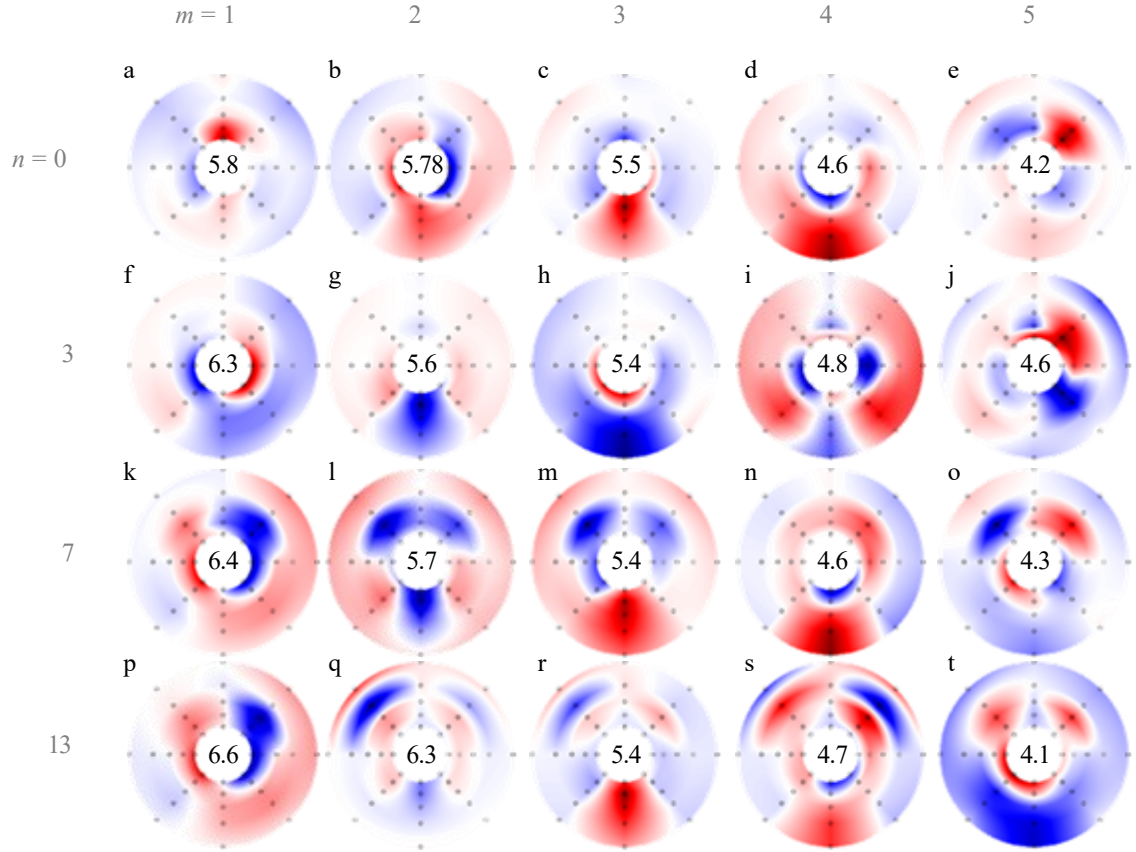


**Figure 4.21** The first five ( $m = 1-5$ ) POD modes of instantaneous total pressure for the unforced flow (a-e), and for varying jet configurations  $n = 3$  (f-j), 7 (k-o), and 13 (p-t). Energy fraction in percentage are indicated in the center of each POD plot.

The coherent structures associated with the time-resolved total pressure fluctuations at the AIP are identified using proper orthogonal decomposition (POD). The first five modes for the base flow and in the presence of  $n = 3, 7$ , and 13 actuation jets are shown in Figure 4.21(a-e), (f-j), (k-o), and (p-t), respectively. The energy fraction of each mode is indicated in the center of each color raster plot in percentage, where the sum of all fractions for all 40 modes of a given  $n$  equals one, and they monotonically decrease with increasing mode number.

In the base flow, the first mode corresponds to the same region identified with the highest RMS fluctuations in Figure 4.17a ( $i = 1, j = 1$ ). The following modes still have a comparable energy fractions, which is an indicator that they have similar relative significance in the flow. Modes 2 and 5 are likely related to the upper-surface unsteadiness, as the most intense regions of the mode are in the upper half of the AIP, while the third and fourth modes appear related to the lower surface pressure fluctuations, for the same reason.

When examining the POD mode  $m = 1$  in the presence of actuation (Figure 4.21 f, k, p), it is noteworthy that the dominant modes do not have the same structure as in the base flow. Instead, their structure resembles mode  $m = 2$  of the base flow (Figure 4.21b), indicating that the actuation suppresses the flow dynamics that gives rise to the first base flow mode. This is most apparent for  $n = 3$ , where the time-average total pressure pattern (Figure 4.12h) is visually most similar to the baseline, but its first mode resembles the second mode of the base flow and its modes 2 and 3 are structurally similar to modes 3 and 4 of the base flow. Therefore, the effect of actuation by 3 jets is essentially manifested solely in eliminating the dominant instability of the upper-surface vortex pair that is represented by the first base POD mode. This is in accord with the discussion of the RMS pressure fluctuations in Figure 4.17 where the RMS of  $n = 3$  is structurally similar to the RMS of  $n = 0$ , except for the high intensity region in the top of the AIP hub ( $i = 1, j = 1$ ). Actuation with  $n > 3$  jets also eliminate the base flow first mode (Figure 4.21a), but have a more profound effect of other dynamics, which is represented by modes  $m > 1$  that do not match any shown modes from  $n = 0$ . These distinctly different modes ultimately manifest themselves in the alteration of the time-averaged total pressure distributions in Figure 4.12.

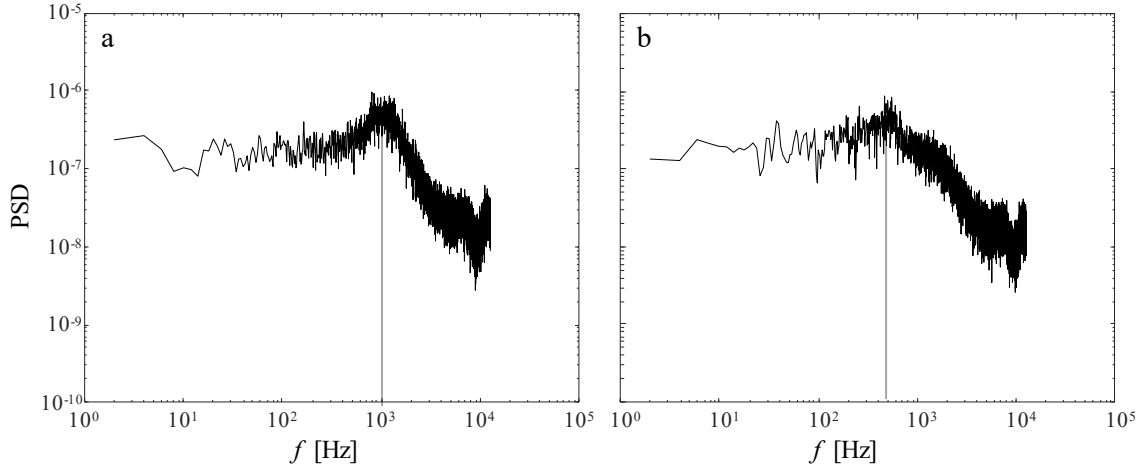


**Figure 4.22** Power spectra of the time coefficients of POD modes  $m = 1$  (a), and 5 (b) in the base flow.

Finally, it is noted that spectra of the time coefficients of POD modes 1 and 5 in the base flow (Figure 4.22a and b, respectively) exhibit characteristic peaks in the power spectra. Mode 1 contains a peak at 1 kHz, while mode 5 contains a peak at about 500 Hz. Since POD modes are not related to a single flow frequency, each mode represents phenomena at many different time scales or frequencies [77]. Therefore, the spectral peaks shown in Figure 4.22 indicate that the contributions of these modes are from predominantly at frequencies 1,000 and 500 Hz, respectively, but also less significantly across the whole spectrum.

Spectral POD (SPOD), whose modes depend on both space and time, is used to identify flow phenomena associated with individual frequencies (Towne et al. [77]), as opposed to conventional space-only POD whose modes are each associated with a wide range of frequencies (e.g. Figure 4.22). This modal decomposition technique is useful for understanding what spatial structures are associated with specific frequencies. The energy of the first ( $m = 1$ ) SPOD mode for each frequency is plotted as spectra for base flow and

in the presence of actuation with  $n = 3, 7$ , and  $13$  jets in Figure 4.23. The large peak found below  $100$  Hz is attributed to signal noise, which is also found in the total pressure spectra in Figure 4.29. Figure 4.24 shows the first mode ( $m = 1$ ) for the base flow and for  $n = 3, 7$ , and  $13$  actuation jets for the two spectral peaks that were identified in the SPOD energy spectra of the first mode in the base flow in Figure 4.23).

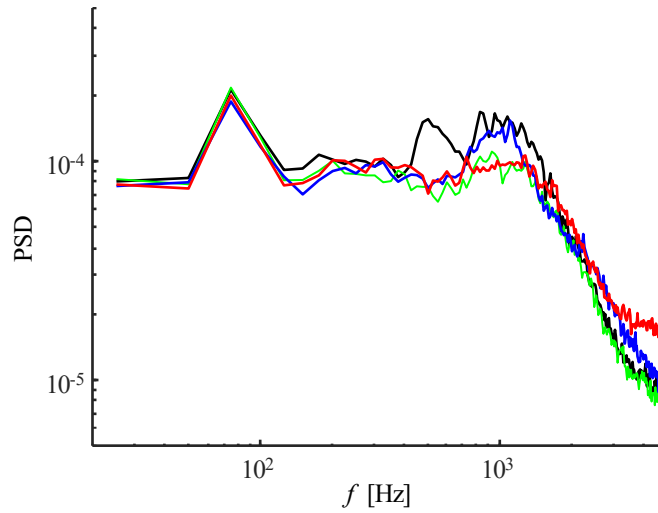


**Figure 4.23** Energy spectra of the first SPOD mode for the base flow ( $n = 0$ ) and with  $n = 3, 7$ , and  $13$  actuation jets.

The SPOD modes further detail the coherent temporal structures, and have a clear connection to the space-only POD modes in Figure 4.21. The first mode in the base flow at  $1$  kHz in Figure 4.24e has a similar structure to the first POD mode of the base flow, which can be expected based on the spectral peak at  $1$  kHz of the time coefficient in Figure 4.22a. The same connection can be drawn between the first SPOD mode of the base flow at  $475$  Hz and the fifth POD mode of the base flow, whose time-coefficient has a spectral peak around  $500$  Hz.

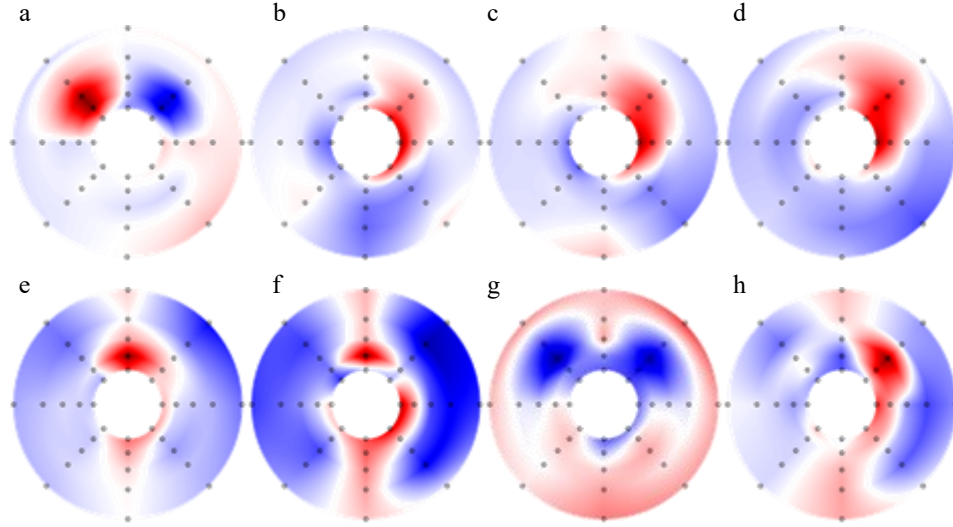


**Figure 4.24** The first SPOD mode for the frequencies 475 (a-d), and 1,000 Hz (e-h), for  $n = 0$  (a,e), 3 (b,f), 7 (c,g), and 13 (d,h).

Upon examination of the spectrum in Figure 4.23, the base flow is found to have a peak at  $\sim 475$  Hz which is eliminated by the actuation with all jet array configurations. The SPOD modes associated with this frequency (Figure 4.24a-d) indicate a structural change associated with this frequency in the presence of actuation - the two-node structure of the first baseline 475 Hz SPOD mode (Figure 4.24a) is no longer present at this frequency (Figure 4.24b-d). This indicates that the unsteadiness in the base flow associated with  $\sim 475$  Hz is suppressed when actuation is used with any of the jet arrays.

At  $f = 1000$  Hz, it is apparent that the mode corresponding to actuation with 3 jets (Figure 4.24f) exhibits a similar structure to that of the base flow (Figure 4.24e). However, as the spectral peak at this frequency (1000 Hz) is suppressed for this flow control case (Figure 4.23), it is argued that one effect of the  $n = 3$  jet array is the reduction of fluctuations at this frequency, without modification of the spatial structure. This substantiates the discussions of the  $n = 3$  case in connection with space-only POD modes (Figure 4.21).

Interestingly, the power spectra for  $n = 7$  indicates a peak at 1 kHz that actuation with 3 and 13 jets do not feature (Figure 4.23). This suggests that there are significant flow fluctuations at this frequency, but with a different spatial structure than that of the base flow. In addition, it is observed that this structure (Figure 4.24g) somewhat resembles the corresponding second and third POD modes (Figure 4.21l,m), which also have time-coefficient spectral peaks at this frequency. This similarity further relates the POD and SPOD analysis, as each POD mode can consist of multiple SPOD modes, as also noted by Towne et al. [77].

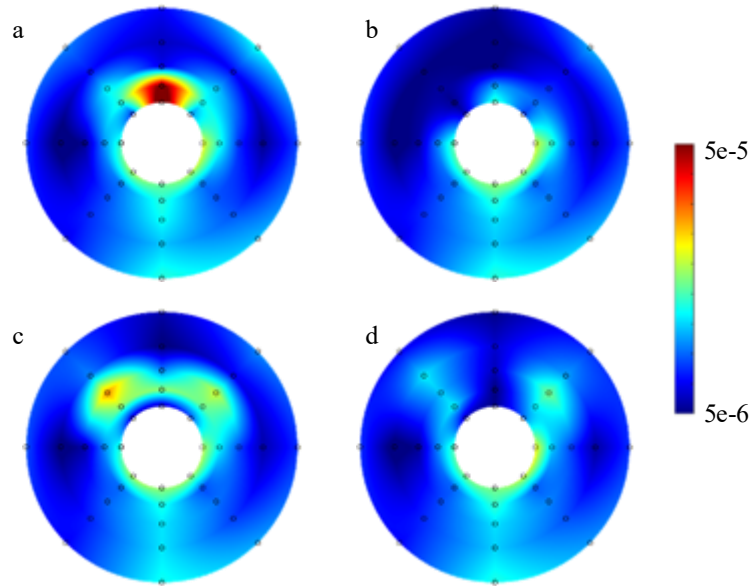


**Figure 4.25** Color raster plots of the total-pressure power spectra integrated over the band  $f = 900-1,100$  Hz for  $n = 0$  (a), 3 (b), 7 (c), and 13 (d).

Another indicator of the flow regions associated with the frequency of 1 kHz is sought by integration of total pressure power spectra from 900 Hz to 1100 Hz. Figure 4.25 shows color raster plots of this quantity for each of the four cases studied ( $n = 0, 3, 7, 13$ ). The base flow (Figure 4.25a) contains high energy levels of this band at the top of the hub ( $i = 1, j = 1$ ), which coincides with the region of peak RMS fluctuations seen in Figure

4.17a. This flow feature is captured in both POD and SPOD and is attributed to the unsteady interaction of the pair of counter-rotating vortices along the top diffuser surface.

When the flow control  $n = 3$  is utilized (Figure 4.25b), this 1 kHz energy band becomes greatly suppressed about the hub ( $i = 1$ ) and no other regions of fluctuation within this frequency band appear elsewhere. This is also in agreement with an earlier observation that, when  $n = 3$ , the flow POD structure (Figure 4.21) was quite similar to the base flow, except lacking the first base flow POD mode. SPOD energy spectra (Figure 4.23) and 1kHz modes (Figure 4.24e,f) provide further insight, that the coherent 1 kHz structure of the base flow does not disappear with  $n = 3$  jet actuation, but its relative significance is reduced as compared to the other frequencies. When  $n = 7$  (Figure 4.25c), the high energy band of the base flow disappears; however, a lesser intensity, larger area of this amplified band emerges around the original domain, indicating a spreading effect. This spreading has a somewhat similar shape to the first 1 kHz SPOD mode (Figure 4.24g) and is also in accord to the SPOD spectra (Figure 4.23), indicating that the fluctuations increase from  $n = 3$  to  $n = 7$ . Lastly, when  $n = 13$  (Figure 4.25d), regions of moderate energy level of the examined band appear in the regions that correspond to the low time-averaged total pressure (cf. Figure 4.12c).

The variation of the AIP face-averaged RMS fluctuations ( $p_{t,RMSF}$ ) and peak instantaneous  $DPCP_{avg}$  ( $DPCP_{peak}$ ), with the actuation flow rate  $C_q$  are shown in Figure 4.26 a and b, respectively, for  $M_{AIP} = 0.38, 0.42, 0.46$ , and  $0.5$ . These data show that while the base flow ( $C_q = 0$ )  $p_{t,RMSF}$  and  $DPCP_{peak}$  increase with  $M_{AIP}$ ,  $p_{t,RMSF}$  and  $DPCP_{peak}$  decrease with increasing  $C_q$  regardless of  $M_{AIP}$ . Increasing  $C_q$  results in a stronger suppression of the  $DPCP_{peak}$  as compared to the effect on  $p_{t,RMSF}$ . For  $M_{AIP} = 0.5$  and

highest  $C_q$  (0.44%), the peak distortion decreases below that of  $M_{AIP} = 0.42$  in the base flow ( $C_q = 0$ ). Figure 4.26c shows that the time-averaged  $DPCP_{avg}$  scaled by the value at baseline ( $C_q = 0, DPCP_{avg,0}$ ) for all Mach numbers collapses onto a single curve, indicating that the relative decrease of time-average distortion is independent of  $M_{AIP}$  within the present range, and that it depends only on  $C_q$ .

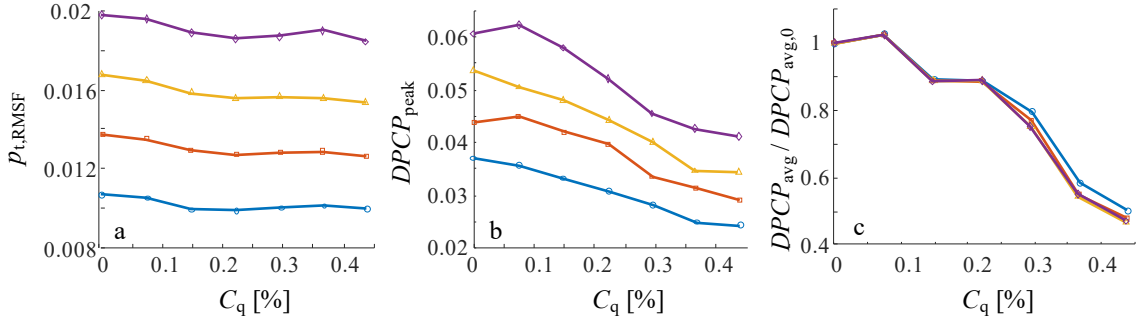


**Figure 4.26** AIP face-averaged RMS fluctuations of total pressure (a), maximum instantaneous  $DPCP_{avg}$  (b), and time-average  $DPCP_{avg} / DPCP_{avg,0}$  (c) at  $M_{AIP} = 0.38, 0.42, 0.46, 0.5$ , and  $n = 13$ .

The effects of optimal actuation ( $n = 13$ ) relative to the base flow are shown in Figure 4.27 using color raster plots of the time-averaged and RMS fluctuations of the total pressure and of the total pressure at the time of the peak distortion  $DPCP_{avg}$ . As noted in connection with Figure 4.16, the effectiveness of the actuation is manifested by bifurcation of the base-flow streamwise vortex pair along the upper surface as a result of the small-scale concentrations of streamwise vorticity imposed by the fluidic oscillating jets which effectively weakens the total pressure deficit at the AIP in the presence of actuation (Figure 4.27d) compared to the pressure deficit in the base flow (Figure 4.27a). In addition, concentrations of high RMS about the hub (Figure 4.27b) are redistributed and mark the interactions of the streamwise vorticity induced by the actuation with the base flow vortices



as shown in Figure 4.27e. Finally, the total pressure distribution at the instant of highest  $DPCP_{\text{avg}}(t)$  shows a strong suppression of the total pressure deficit along the upper surface of the AIP downstream of where the actuation is applied (Figure 4.27f). Interestingly, successful suppression over the top surface intensifies the peak total pressure deficit on the opposite, lower surface in the absence of actuation at the first turn of the diffuser. These data show an overall significant suppression in the peak AIP distortion in the presence of actuation along with the time-averaged suppression.

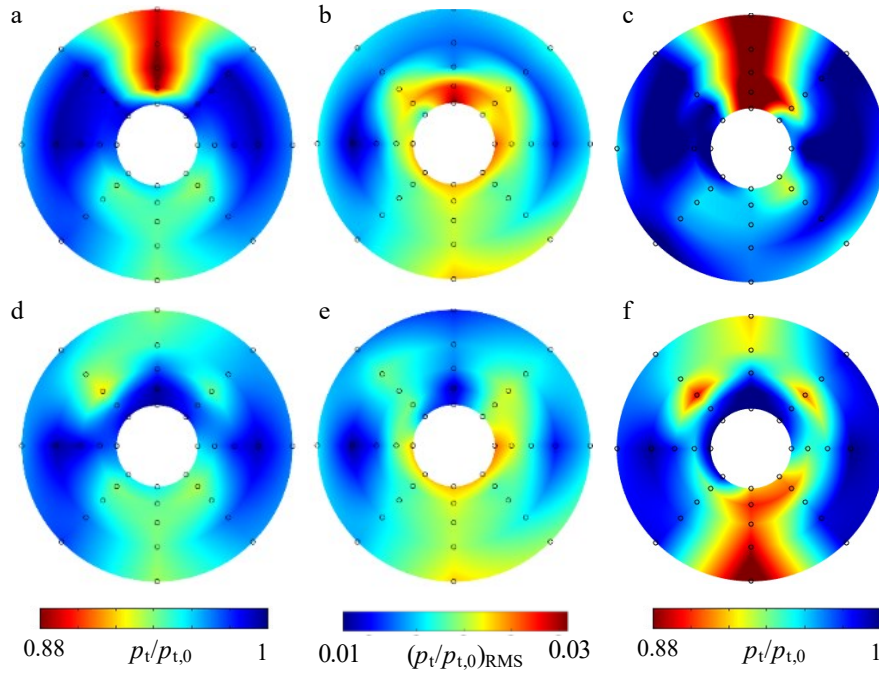


**Figure 4.27** AIP time-average total pressure (a, d), RMS fluctuations (b, e), and the total pressure at the instant of maximum  $DPCP_{\text{avg}}$  (c, f) for cases  $n = 0$  (a-c) and 13 (d-f).

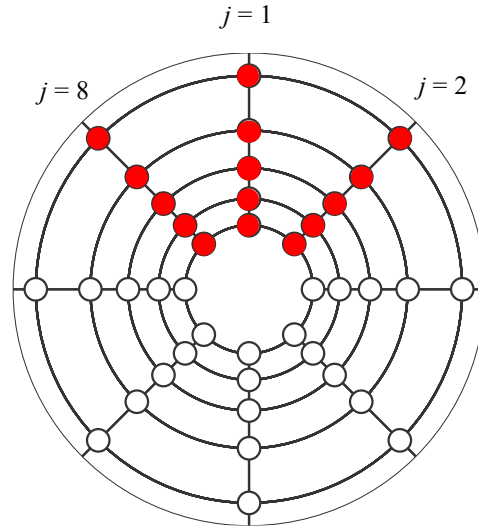


**Figure 4.28** Diagram showing ports chosen for individual power spectra in Figure 4.29. Ports chosen lie on three rakes,  $j = 1, 2, 8$ , and all five radial rings, where  $i = 1$  is radially innermost, and  $i = 5$  is radially outermost.

The dynamic effects of the optimized actuation over the upper half (cf. Figure 4.28) of the AIP are also analyzed by comparing the spectral content of the total pressure time series as shown in Figure 4.29 using horizontal color raster bars of the spectral magnitudes up to 10 kHz for each of the sensors. These bars stacked and arranged by sensor numbers from  $i = 1$  to  $i = 5$  for  $j = 8, 1, 2$  for the base flow (Figure 4.29a) and in the presence of actuation (Figure 4.29b). The common peak at about 100 Hz is associated with blower signal noise and should not be considered as a feature of the flow.

These spectra show that the primary effect of the actuation is manifested by broadband suppression of the spectral peaks (for example, consider the power spectra of the base and controlled flows at sensor (1,1) in Figure 4.29c). Of particular note are the spectral peaks at 500 Hz especially in ports (2,8) and (3,8), and their symmetric counterparts (2,2) and (3,2), which are suppressed in the presence of actuation and there are lower peaks at 1 kHz. It is interesting that these locations ((2,8), (3,8), (2,2), (3,2))

coincide with the nodal structure of the SPOD dominant mode ( $m = 1$ ) at 1,000 Hz of the  $n = 13$  controlled flow (Figure 4.24h), and also positioned in the dominant SPOD mode of the base flow at 475 Hz (cf. Figure 4.24a). This shift in the characteristic frequency is also emphasized in direct comparison between the uncontrolled and controlled spectra at (2,8), which are shown in Figure 4.29f. At a couple of locations, there is an increase in the total pressure fluctuations in the presence of actuation flow, as seen at (4,8) and (4,2). These two ports are symmetric across the center plane, and are in the regions in which the time-averaged AIP total pressure is diminished (Figure 4.27d), i.e., they directly characterize two regions of the forced interaction between the controlled and ‘natural’ streamwise vortices on either side of the center plane of symmetry.

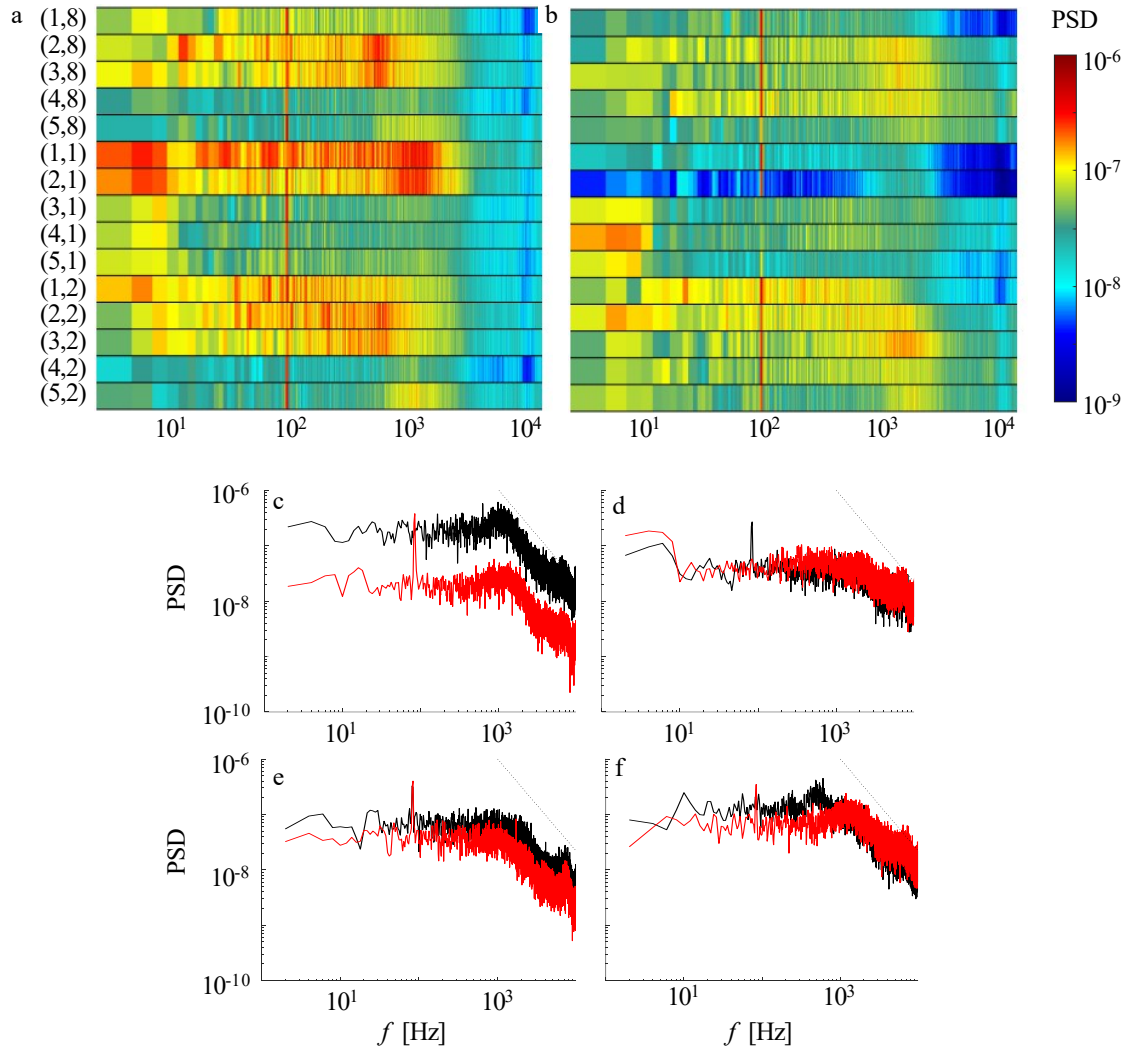


**Figure 4.29** Horizontal color raster bars of spectral magnitudes (up to 10 kHz) of the total pressure measured by each of the AIP sensors as marked in the accompanying schematic. These bars are arranged by sensor numbers in two vertical columns for the base flow (a) and in the presence of actuation by 13 jets (b). Representative power spectra in the absence (—) and presence (—) of actuation are shown for sensors: (1,1) (c), (4,1) (d), (1,8) (e), and (2,8) (f).

## **CHAPTER 5.    TRANSONIC SHOCK IN A SERPENTINE DIFFUSER**

The study of the flow structure in the serpentine diffuser SD-2 is extended to higher Mach numbers, where the total pressure loss and distortion along the concave surface of the first turn becomes more prominent due to the appearance of a transonic shock in the first turn. Mitigation of the detrimental effects of the shock is sought by application of flow control actuation with the objective of weakening the shock and alleviating the coupling between the first-turn flow separation and the secondary vortices. This is accomplished using a separated array of actuators upstream of the shock that targets the shock evolution indirectly by controlling the separation immediately downstream of the shock. Pressure sensitive paint and surface oil visualization were used to characterize the footprint, topology, and strength of the shock in the absence and presence of flow control with specific attention to the interaction between the shock, flow separation, and the formation of streamwise vortices.

### **5.1    Introduction**

The objective of the present study is to extend the upper limit of the diffuser's operating range into the transonic regime by using fluidic actuation to mitigate the pressure losses associated with the formation of a local shock wave on the concave surface of the diffuser first turn. The presence of the shock can exacerbate local separation that leads to the formation of secondary streamwise vortices and consequently results in elevated distortion at the AIP.

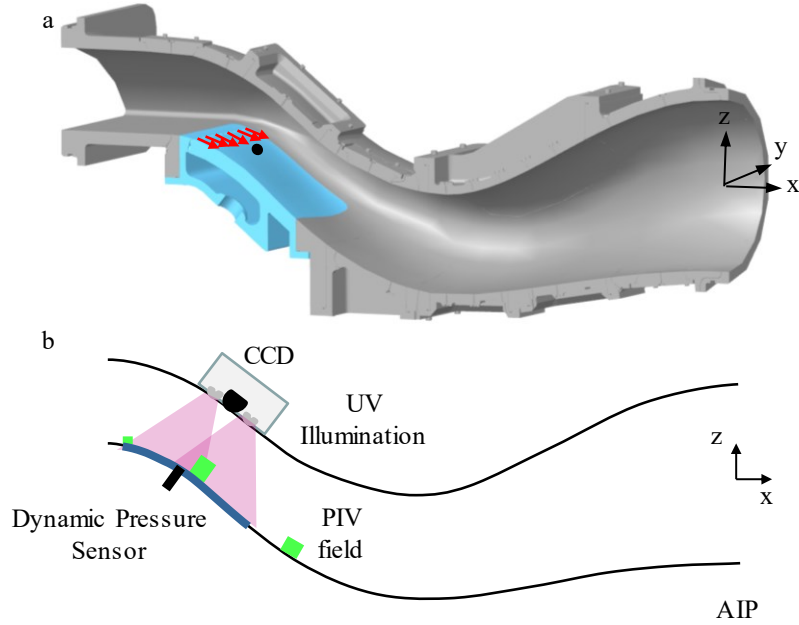


**Figure 5.1** a) Isometric sectional view of the serpentine SD-2 diffuser showing the actuation insert at the first turn with the integrated spanwise jet array (the full array includes 23 actuation jets) and dynamic pressure sensor marked by black ellipse; and b) Outline of the diffuser's cross section along its center plane showing the setup for the illumination of the surface pressure sensitive paint (cf. Section 2.3.2), and the PIV planes. The insert extends from  $x/D = -3.4$  to  $-2.7$ . The global coordinate system is also included for reference.

The fluidic actuation module (highlighted in blue in Figure 5.1a) is similar to the modules that used in Chapters 3 and 4 and includes a spanwise array of 23 fluidically-oscillating jet (6.35 mm apart) of the same design (cf. Section 2.4). The actuation jet array spans the width of the diffuser's bottom surface at  $x/D = -3.35$ . The diagnostics are shown schematically in Figure 5.1b, including the setup for illumination of the surface pressure sensitive paint (PSP, cf. Section 2.3.2) within the domain  $-3.45 < x/D < -2.71$ ,  $0 < y/D < 0.76$ , and imaging domains for planar particle image velocimetry, each measuring about  $15 \times 15$  mm and centered at  $x/D = -3.5$ ,  $-3$ , and  $-2.5$  (upstream to downstream). In addition, surface oil visualization is conducted on the same surface as

PSP highlighted in Figure 5.1a. Lastly, a high-frequency pressure sensor (sampled at 200 kHz) is mounted at  $x/D = -3.23$ ,  $y/D = 0.44$  for time-resolved pressure measurements, and is shown schematically in Figure 5.1a and b.

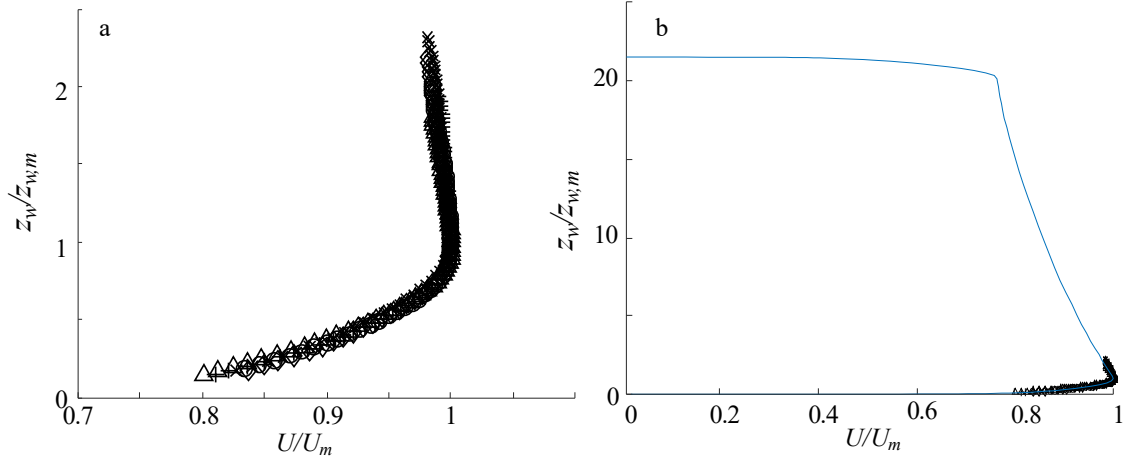


**Figure 5.2** Cross stream profiles of  $x$  velocity component  $U$ , normalized by the local maximum velocity, at  $x/D = -3.5$ ,  $y = 0$ , (cf. Figure 5.1b) a) PIV measurements  $M_{AIP} = 0.45$  ( $\times$ ),  $0.53$  ( $\diamond$ ),  $0.6$  ( $\circ$ ),  $0.64$  ( $+$ ), and  $0.69$  ( $\Delta$ ); and b) Simulation across the diffuser's height [78],  $M_{AIP} = 0.53$  (blue line) superposed with the measurements.

## 5.2 Characterization of the Base Flow in the Diffuser's First Turn

The near-surface flow along the bottom surface of the first turn at the center plane ( $y = 0$ ) is characterized using PIV measurements at the throat ( $x/D = -3.5$ , cf. Figure 5.1b) for  $M_{AIP} = 0.45$ ,  $0.53$ ,  $0.6$ ,  $0.64$ , and  $0.69$ , and the time-averaged cross stream distribution of the streamwise velocity  $U$  normalized by magnitude of the profile velocity peak  $U_m$  is shown in Figure 5.2a. The coordinate  $z_w$  is a distance from the lower surface at  $x/D = -3.5$  ( $z_w = 0$  corresponds to  $z/D = 0.16$ ) and normalized by the distance from the wall of the velocity peak,  $z_{w,m}$ . This scaling is used because it collapses all velocity profiles onto a single curve, showing that though the magnitude and position of the near-surface peak

velocity changes with  $M_{AIP}$ , relative to this maximum point, all profiles are similar. The numerical simulations of Lakebrink and Mani [78] at  $M_{AIP} = 0.6$  yield the time-averaged velocity distribution across the throat as shown in blue in Figure 5.2b. Near the wall where PIV measurements are taken ( $z_w/z_{w,m} < 2.5$ ), the numerical results are in good agreement. The throat velocity distribution is clearly affected by the D-shaped cross section of the duct (cf. Figure 2.4), which is not uniform or symmetric and exhibits higher velocity close to the bottom ( $z_w = 0$ ) surface as compared to the velocity close to opposite wall ( $z_w \approx 22$ ). This is a result of incoming air non-uniformly accelerating when the square-cross-section contraction evolves into a D-shape to lead the air to the throat.

**Table 5.1 Ratio of pressure downstream of shock front to pressure upstream of shock front for each  $M_{AIP}$  in Figure 5.3.**

$M_{AIP}$	Pressure Ratio
0.54	1.06
0.58	1.21
0.60	1.29
0.61	1.36
0.66	1.46



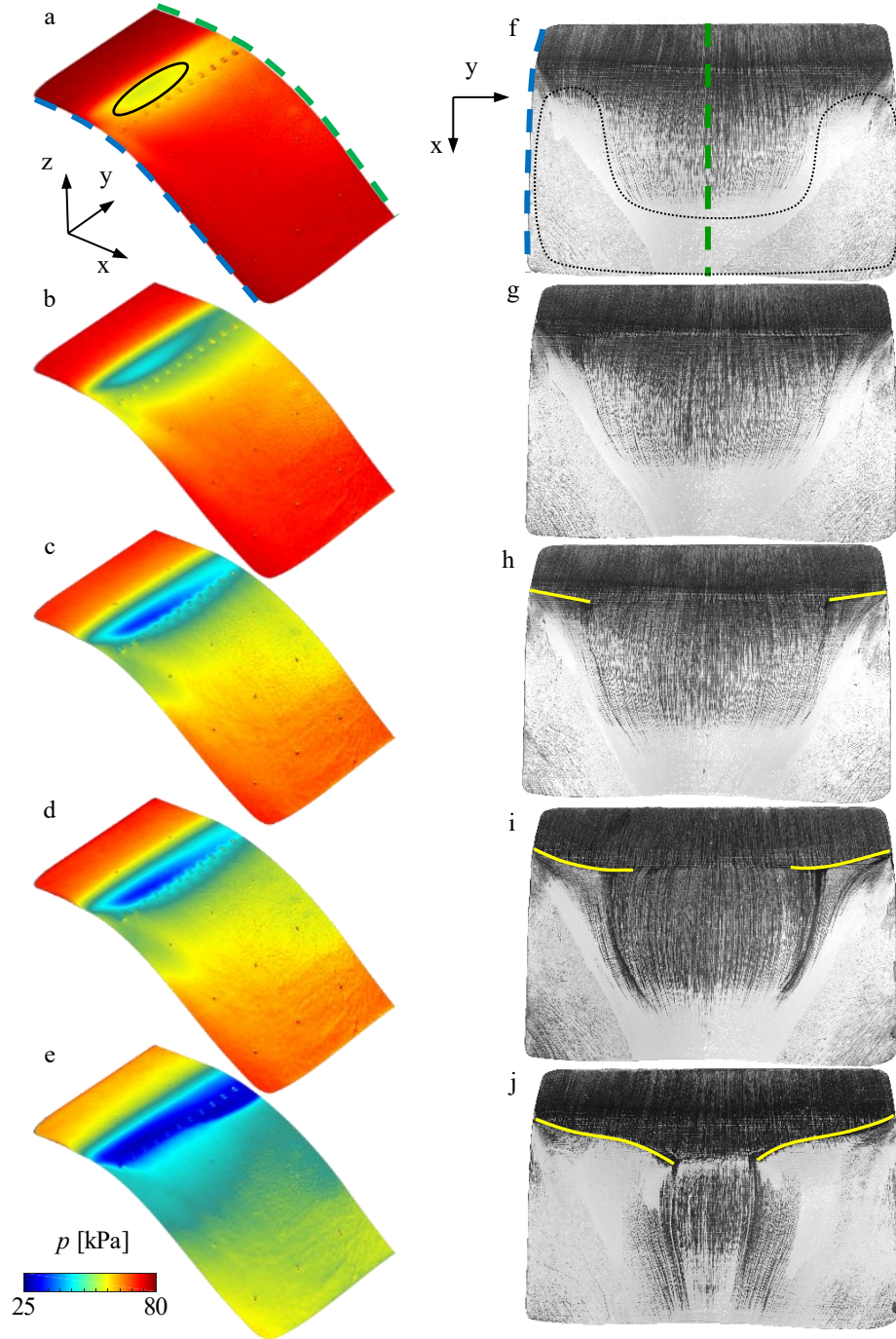


**Figure 5.3** Color raster plots of surface pressure distributions over half the span of the base flow over the bottom surface of SD-2 first turn measured using PSP (a-e), and corresponding surface oil visualization (f-j) at  $M_{AIP} = 0.54$  (a,f), 0.58 (b,g), 0.6 (c,h), 0.61 (d,i), and 0.66 (e,j). The solid black ellipse marks low pressure region (a). The blue dashed line marks diffuser corner, green dashed line marks the center span ( $y = 0$ ). In the oil visualization images, the black dotted line marks the horseshoe-shaped separation region, and the yellow solid lines mark the shock wave footprints.

To investigate the presence of a shock on the bottom surface of the first turn, the surface topology is characterized using PSP and surface oil visualization (Figure 5.3) at  $M_{AIP} = 0.54, 0.58, 0.6, 0.61, \text{ and } 0.66$ . Figure 5.3a-e shows color raster plots of the surface pressure distributions from over the half the span,  $-3.45 < x/D < -2.71$ ,  $0 < y/D < 0.76$ , where the diffuser's corner is marked with a blue dashed line and the centerline with a green dashed line in Figure 5.3a, and the flow direction is down to the right. It is noted that the orifices of the inactive actuation jets are visible in the surface pressure images. Corresponding images of surface oil-flow visualizations across the entire span of the actuation insert are shown in Figure 5.3f-j where the left half of each oil-visualization image corresponds to the pressure raster plots shown next to it. Table 5.1 shows corresponding pressure ratios of pressure just downstream of each shock front (high-pressure region) divided by the pressure upstream of the front, (low pressure region). This is used to estimate the shock strength.

At  $M_{AIP} = 0.54$  (Figure 5.3a and f), the pressure pattern indicates mild flow acceleration just downstream from the throat as is evidenced by the marked region of lower pressure just upstream of the jet array (solid black ellipse, Figure 5.3a). This low-pressure region is followed by three-dimensional separation in a horseshoe-like pattern as marked by a black dotted line in Figure 5.3f and discussed in Chapter 4 in connection with Figure 4.2. As  $M_{AIP}$  is increased (Figure 5.3b and g), the local flow acceleration becomes more pronounced by the sharper pressure gradients at about  $x/D = -3.4$ , and the span of the attached region slightly widens, which is marked by wider spanwise extent of oil streaks (Figure 5.3g).

When  $M_{AIP} = 0.6$  (Figure 5.3c and h) the surface pressure pattern indicates the presence of a shock front at the downstream edge of the low-pressure region, based on the higher pressure gradient at the interface, and higher pressure ratio (cf. Table 5.1). The imprint from this shock front can be seen at the corner on each side of the oil-flow visualization (Figure 5.3h, solid yellow line). A slight increase in the Mach number to  $M_{AIP} = 0.61$ , results in stronger shock that has a greater spanwise extent as evidenced by the increased pressure ratio (Table 5.1), and the spreading of the lower pressure region in Figure 5.3d towards the centerline. In addition, the shock line in the oil flow visualization in Figure 5.3i (solid yellow line) extends further towards the centerline. Finally, Figure 5.3j represents a state of a strong shock formation, as determined by the spanwise extent, sharp pressure gradient, and high pressure ratio. Only about a quarter of the span remains attached (solid yellow line marking shock imprint). It is also clearly visible that the most upstream portion of the shock front is in the corner and it progresses downstream as it approaches the centerline. This behavior is conjectured to be because of the higher velocity in the throat corners, which triggers the shock earlier in these regions. When examining the corresponding surface pressure color raster plot in Figure 5.3e, it is notable that the sharp gradient of pressure transition from low to high through the shock forms the same shape that is captured in the oil visualization, and the high-to-low pressure ratio for this case is the highest, at 1.46.

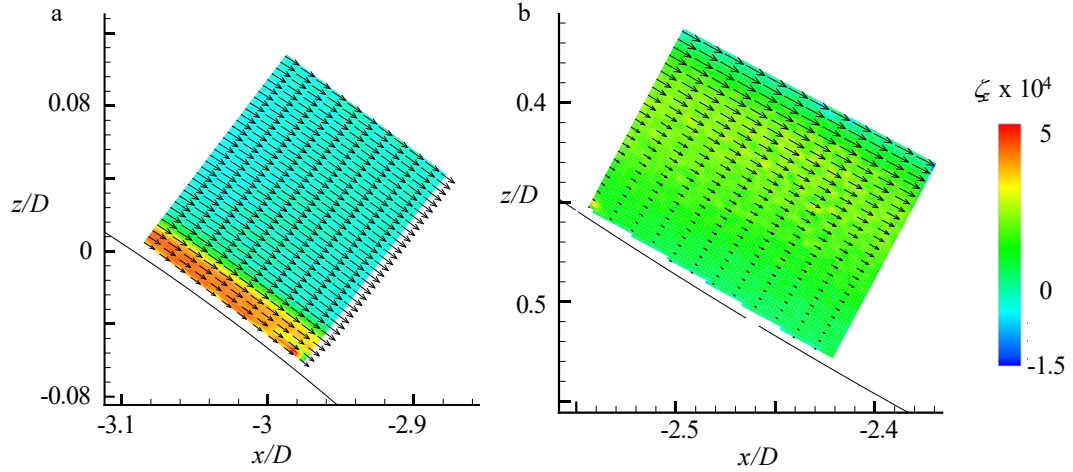


**Figure 5.4** Color raster plots in cross stream ( $z$ - $x$ ) planes (referenced to the diffuser's global coordinates) of the time-averaged distributions of the spanwise vorticity overlaid with equidistant grid of vectors of the time-averaged velocity at  $M_{AIP} = 0.54$  measured at: a)  $x/D = -3$ ,  $12 \times 15$  mm, and b)  $x/D = -2.5$ ,  $12 \times 10$  mm (cf. Figure 5.1b).

The effect of the first-turn separation found in Figure 5.3 on the downstream near-wall velocity along the bottom surface is investigated using PIV within the domain  $x/D = -3$  measuring  $12 \times 15$  mm (Figure 5.4a), and  $x/D = -2.5$  measuring  $12 \times 10$  mm (Figure 5.4b), at  $M_{AIP} = 0.54$  (cf. Figure 5.1b). The velocity field immediately next to the wall ( $\sim 1$  mm) cannot be resolved due to the surface reflections. The diffuser surface is shown by a line in each of the images for reference. As the base flow remains attached along the central plane shown in the oil visualization (green line in Figure 5.3f), the measured flow field in Figure 5.4a reflects the attachment, showing vorticity concentrations near the surface (Figure 5.4a). The measurement domain farther downstream at  $x/D = -2.5$  (Figure 5.1b) indicates that the boundary-layer has grown, and that the time-averaged flow it is not quite separated, which is the lack of reverse flow near the surface. This is in agreement with the surface oil-flow visualization in Figure 5.3f, where the downstream end is at  $x/D = -2.5$ ,

and in this region oil streaks were not created by the flow, indicating surface velocity deficit.

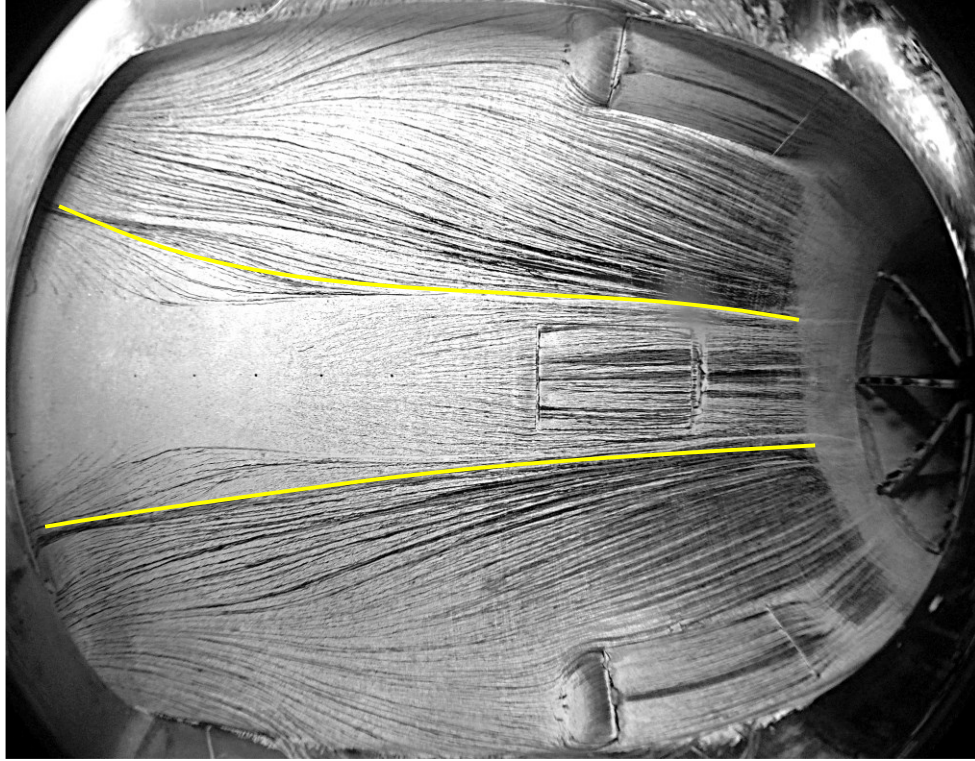


**Figure 5.5** Surface oil visualization at  $M_{AIP} = 0.54$  on the bottom surface of the diffuser's first turn extending from  $x/D = -2.5$  (left) to 0 (right). Solid yellow lines mark signatures of streamwise counter-rotating vortices. The image also shows the 40-probe total pressure rake at the AIP on the far right.

Surface oil-flow visualization along the bottom surface helps characterize the evolution of streamwise vortices that are engendered at the first turn. Figure 5.5 illustrates the flow topology immediately downstream from the first-turn actuation module up to the AIP (the AIP total pressure rake is visible at the downstream end on the right). A fisheye lens was used to capture the full axial extent of the surface flow causing image distortion. The oil-flow visualization is acquired at  $M_{AIP} = 0.54$ , i.e., in the absence of the first-turn shock. The visualization starts where the visualization in Figure 5.3f ends ( $x/D = -2.5$ ). It



is seen that the separation that originated in Figure 5.3f in the corners becomes confined near the centerline as marked by the solid yellow lines. The flow reattaches shortly downstream, as indicated by the appearance of oil streaks within the yellow bounds about halfway through the image. The bottom-surface streamwise vortices, which originate at the corners of the diffuser near the throat as discussed in Chapter 4 (cf. arrows and reverse flow in Figure 4.2a) leaves signatures on the surface (marked by yellow lines), which effects a boundary between the attached flow outside the bounds, and the reattaching flow within the bounds. The outer attached flow is drawn in towards the vortices, as evidenced by the streaks flowing towards the marked boundaries. This lower-surface vortex pair lifts lower-momentum fluid away from the surface, producing the region of pressure deficit seen in the lower halves of the AIP color raster plots in Figure 5.6.

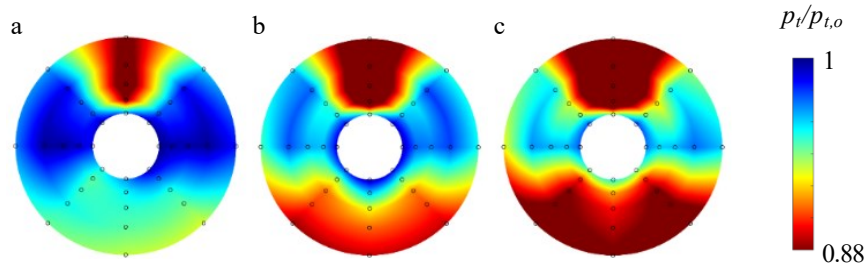


**Figure 5.6 Color raster plots of the total pressure distribution at the AIP in the base flow at  $M_{AIP} = 0.54$  (a),  $0.61$  (b),  $0.66$  (c).**

The effect of the streamwise vortices that originate at the corners of the diffuser's first turn are examined at the AIP using distributions of the total pressure for three characteristic flow conditions: in the absence of a shock (Figure 5.6a), and in the presence of a moderate and a strong shocks (Figure 5.6b and c, respectively. As noted in connection with Figure 4.4, the main source of pressure deficit and distortion at the AIP is the vortex

pair that forms on the upper surface of the second turn (cf. Chapter 4). In the absence of a shock at the first turn (Figure 5.6a), lower pressure deficit and distortion at the AIP are effected by separation along the first turn, but the deficit is not severe, relative to the top surface. At  $M_{AIP} = 0.61$  (Figure 5.6b), two connected lobes of pressure deficit form along the lower surface, while the upper-surface deficit widens and intensifies. The same trend continues at  $M_{AIP} = 0.66$  (Figure 5.6c), where the total pressure deficit along the lower surface becomes as pronounced as the deficit near the upper surface. The investigations reported in this chapter focus on the uses of fluidic actuation to mitigate this pressure deficit by reducing the shock-induced separation and indirectly affecting the strength of the shock.

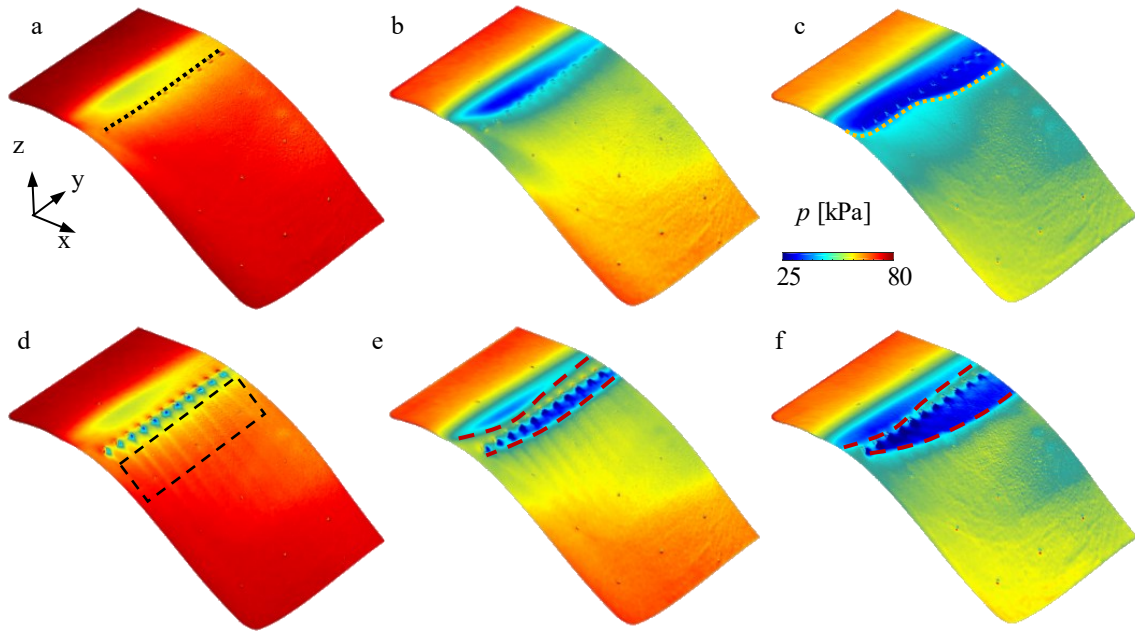


**Figure 5.7** Color raster plots of surface pressure distributions over half the span of the base flow over the concave surface of the diffuser's first turn measured using PSP in the absence (a-c) and presence (d-f) of fluidic actuation at  $C_q = 0.75\%$ , and  $M_{AIP} = 0.54$  (a, d),  $0.61$  (b, e),  $0.66$  (c, f). Dotted black line in (a) indicates the position of the jet array, orange dotted line in (c) marks shock front, the dashed rectangle in (d) marks traces of low pressure streaks induced by the actuation jets, and the red dashed lines in (e) and (f) mark the edges of low-pressure regions.

### 5.3 Effects of Fluidic Actuation

The flow control approach for mitigation of the effects of the first turn shock is based on earlier investigations of controlling a transonic shock over a curved surface by Gissen et al. [5]. In the present investigations, an array of  $n = 23$  equally-spaced (6.35 mm apart) fluidically oscillating jets is integrated across the span of the diffuser's bottom surface at  $x/D = -3.4$ , such that they are positioned near the expected streamwise position of the shock formation (Figure 5.7a, marked by dotted black line). The position was chosen based on the proximity to the shock, but since the shock position varies with  $M_{AIP}$ , the array position relative to the shock could not be fixed. As shown in Figure 5.3, the shock migrates downstream with increasing diffuser AIP Mach number from 0.54 to 0.66 (cf. Figure 5.3). The effect of the actuation on the shock is illustrated first by the surface static pressure distributions measured by the PSP. Figure 5.7 shows three pairs of such color raster plots in the absence and presence of actuation jets ( $C_q = 0.75\%$ ), at  $M_{AIP} = 0.54, 0.61, 0.66$ . The main features of shock formation in the absence of actuation at these  $M_{AIP}$  are discussed in connection with Figure 5.3a,c,e which are repeated in Figure 5.7a–c. In the absence of the shock formation at  $M_{AIP} = 0.54$  (Figure 5.7d), the changes in surface pressure due to the presence of the actuation jets is marked by local low-pressure streaks immediately downstream from the orifices. A noteworthy feature of these streaks is the thin persistent traces of lower pressure further downstream from the jet orifices, which are attributed to the formation of streamwise vortices by the jets (marked by dashed rectangle). Besides these features that are brought about by the presence of the jets, there is no significant change in the structure of the flow upstream and downstream of the jets compared to the corresponding flow in the absence of actuation in Figure 5.7a.



Once the shock is present at  $M_{AIP} = 0.61$  (Figure 5.7b), the actuation significantly alters the surface pressure associated with the shock, as seen in Figure 5.7e. In the immediate vicinity of the jet array, the active jets effect a region of compression, which is indicated by the strip of higher surface pressure. This higher-pressure region seems to split the previous single low-pressure region into two – one upstream of the jets and one downstream. This could indicate a change in the three-dimensional shock structure, which now has two distinct surface pressure signatures. More pronounced changes are effected by the actuation at  $M_{AIP} = 0.66$  compared to the base flow in Figure 5.7c, and the low-pressure fronts are marked by red dashed lines in Figure 5.7f. A feature of the actuation is reflected in the moderate changes in the second front where the shape of the base front (orange dotted lines, Figure 5.7c) is transformed into a smooth arc in the presence of actuation (red dashed line, Figure 5.7f).

In both cases  $M_{AIP} = 0.61$  and  $0.66$ , the second front has a sharper pressure gradient and higher pressure-ratio (1.66 in both cases) than the single front in the corresponding base flow (cf. Table 5.1), which could indicate that actuation effects a stronger shock. In addition, the position of the second front is consistently further downstream from the original shocks. The change in the surface shock signatures indicates an alteration of the three-dimensional shock structure, which could resemble that of a lambda shock.

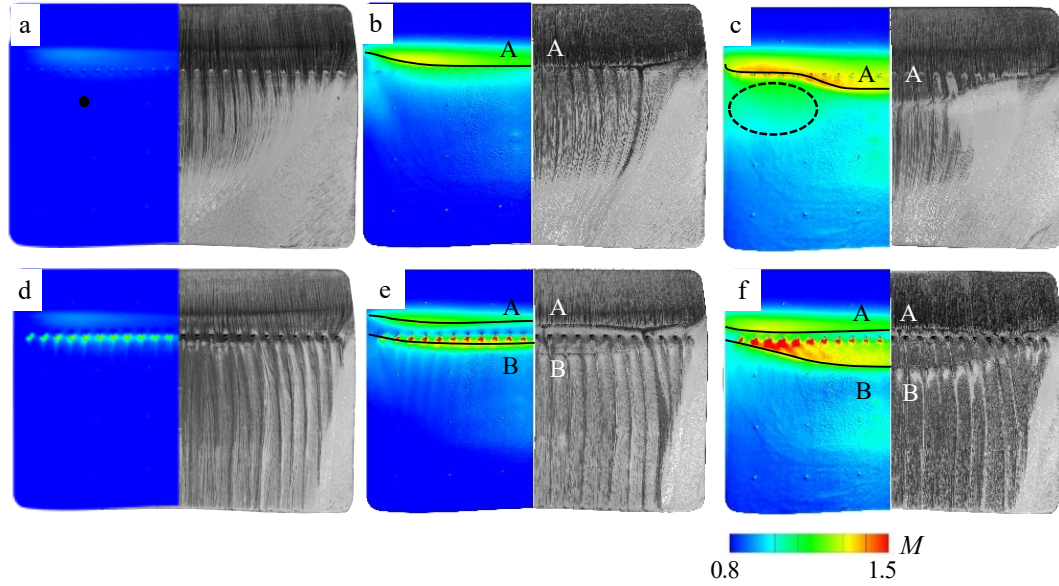


**Figure 5.8** Surface oil visualization on the first turn convex (bottom) surface at  $M_{AIP} = 0.54$  with inactive (a-c) and active ( $C_q = 0.75\%$ , d-f) actuation jets (a, d), 0.61 (b, e), 0.66 (c, f). Each of the oil visualization images is matched with color raster plots of distributions of the estimated local Mach number near the surface that are overlaid over the half-span of the flow. In b, c, e, and f black lines mark the approximate location of the shock across half the span. The first and second shock fronts are labeled A and B, respectively. Dashed ellipse in (c) marks region of constant Mach number. Dot in (a) marks position of dynamic pressure sensor.

Further insight into the flow topology over the first turn is sought through surface oil visualization in the absence and presence of actuation. The three pairs of flow fields in Figure 5.7 are shown in Figure 5.8 for  $M_{AIP} = 0.54$  (a, d), 0.61 (b, e), and 0.66 (c, f) and are characterized by the oil traces and color raster plots of distributions of the local Mach number near the surface that are estimated from the surface pressure measurements and overlaid over half the flow span. These Mach number distributions are estimated from the PSP measurements of surface pressure using the total pressure at the inlet to the contraction, assuming that the total pressure loss up to the diffuser's inlet is negligible. The computed distributions of the Mach numbers are used to determine lines of local Mach number maxima across the span that are overlaid on the color raster plots as the best

estimates of the positions of the local shock over the surface. As shown in Figure 5.8a,d, for  $M_{AIP} = 0.54$  the flow over the first turn is subsonic in the absence and presence of actuation, with the highest Mach number region being the jet orifices themselves. The base flow in the absence of actuation (Figure 5.8a) is similar to the corresponding flow over the smooth first turn surface (Figure 5.3f) indicating that the presence of inactive jet orifices on the surface does not affect the global flow topology. As noted in connection with Figure 5.3f, the flow separation pattern resembles a horseshoe, where the flow separates first closest to the corners and the separation extends toward the centerline as the flow evolves in the streamwise direction. When actuation is applied (Figure 5.8d), most of the spanwise nonuniformity is eliminated as the flow remains attached across most of the span, and the interface between the attached at separated flow is displaced and confined to the spanwise corners.

The shock induced over the first turn is shown in Figure 5.8b, for  $M_{AIP} = 0.61$ . In the absence of actuation, the spreading of flow separation from the corners towards the centerline is reduced compared to  $M_{AIP} = 0.54$  and more of the base flow is attached across the span until the flow becomes fully separated. The distribution of the near-surface Mach number indicates the shock location as marked by “A” and indicate that the shock’s upstream-most formation is in the corner. The shock is stronger close to the diffuser’s corner and progressively weakens towards the centerline, as indicated by maximum local Mach number regions being close to the corner. The corresponding oil visualization shows that flow separation is induced in the corners of the shock, while the shock in the rest of the span is of insufficient strength to induce separation. As shown in Figure 5.8e, actuation results in the formation of two distinct surface shock signatures, as is evidenced by the split

in the surface pressure traces in Figure 5.7e where the two shock fronts are labeled *A* and *B*. As noted in connection with Figure 5.7e the separation in the presence of actuation becomes more confined to the corner, and the shock has potentially increased in strength, as indicated by the higher local Mach numbers and higher surface pressure gradient. As indicated in the oil visualization image in the presence of actuation the flow remains mostly attached across the span, despite of formation of the stronger shock.

The base flow at  $M_{AIP} = 0.64$  (Figure 5.8c) shows that the shock front spans a greater distance than that of  $M_{AIP} = 0.61$ . There are also differences in the Mach number distributions just downstream from the shock in the corner in Figure 5.8b and c. In Figure 5.8c, there is a region of elevated Mach number just downstream from the shock in the corner, marked by the dashed ellipse. When compared with the oil visualization, this region appears to coincide with the extended separation that spreads much farther towards the center plane from the corners. The attached flow is now reduced to about the central third of the span. Once the jets are activated however (Figure 5.8f), the higher pressure region effected by the jet array leads to a split of the base flow shock in two shock signatures marked *A* and *B* in Figure 5.8f. As an indication of the weaker shock *B* close to the corners, the previously mentioned corner region of higher Mach number is no longer present, and the corner separation captured by the oil visualization is about as confined to the corner as it is in the presence of actuation in the absence of a shock (compare the oil traces on the far-right of Figure 5.8f and d). It is remarkable that in the presence of actuation the split shock (possibly owing to the formation of a lambda-shock) aren't strong enough to induce flow separation and the flow remains attached for most of the first turn span past the jet array. It should be noted that in Figure 5.8b,c,e, and f the estimated shock

positions from the distributions of the Mach number appear somewhat offset upstream relative to the corresponding oil traces on the right. This may suggest that oil accumulation due to flow deceleration may be spatially offset relative to the changes in pressure that are reflected in the Mach number distributions.

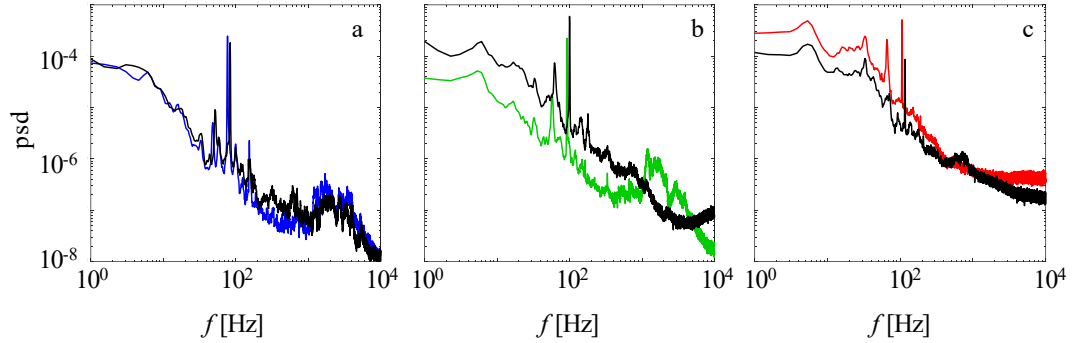


**Figure 5.9 Power spectra of surface pressure fluctuations downstream of the shock at  $C_q = 0$  (black) and 0.75% (color) for  $M_{AIP} = 0.54$  (a), 0.61 (b), 0.66 (c).**

Some insight into the flow dynamics in the absence and presence of actuation is gained from dynamic pressure traces measured downstream of the shock for the  $M_{AIP}$  in Figure 5.7 and Figure 5.8 and the resulting spectra of the pressure fluctuations are shown in Figure 5.9. The approximate dynamic pressure sensor position is shown in Figure 5.1a and Figure 5.7a. When no shock is formed over the first turn (Figure 5.9a), there is only a marginal difference between the spectra in the absence and presence of actuation since the flow remains nearly attached (cf. Figure 5.8a,e). These spectra include a prominent spectral peak near 100 Hz, which is attributed to facility signal noise. Once the shock is formed at  $M_{AIP} = 0.61$  (Figure 5.9b), there is a significant change in the spectral energy distribution when actuation is applied. The low frequency spectral power of the base flow pressure fluctuations is reduced when actuation is present, as shown in Figure 5.9b. In

addition, the power spectrum from the controlled case resembles that of the controlled  $M_{AIP} = 0.54$  spectrum. Despite a shock still being present in this controlled case, dynamics near this sensor seem to revert to that of flow without the presence of a shock. In the base flow strong shock case at  $M_{AIP} = 0.66$ , the pressure sensor is positioned separated flow and the spectrum contains a minor peak just below 1 kHz, which could be associated with the separation. Interestingly, when actuation is enabled and the flow is attached, this peak is suppressed but much of the spectrum fluctuations are amplified. This difference in controlled spectra from  $M_{AIP} = 0.61$  could be associated with the position and structure of the shock that is clearly different, as discussed in connection with Figure 5.8. As the sensor position is fixed and the shock front moves downstream with increasing  $M_{AIP}$ , the closer proximity may alter the measured dynamics.

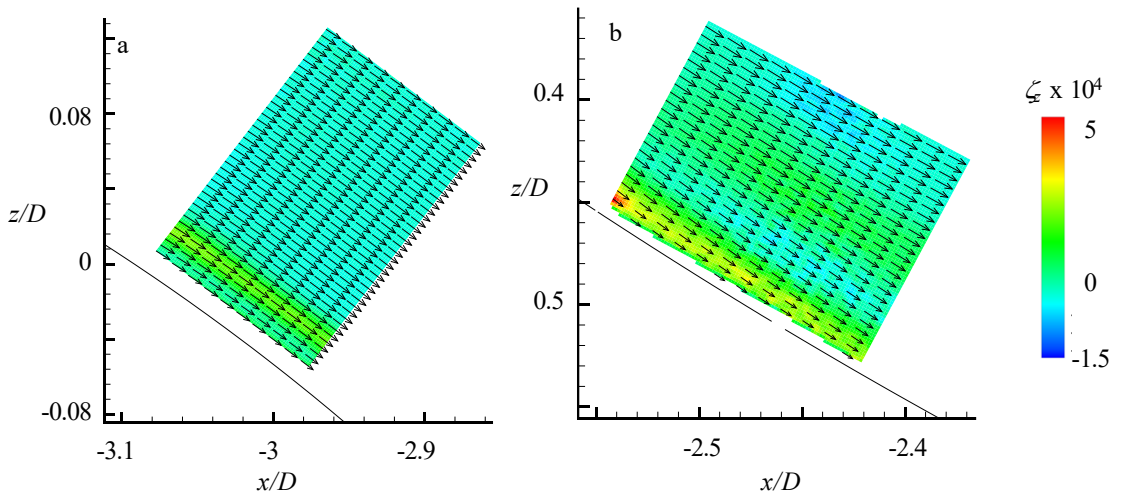


**Figure 5.10** Color raster plot of the mean spanwise vorticity component with overlaid mean velocity profiles as in Figure 5.4a and b, respectively.

The effect of the actuation on the near-wall vorticity and velocity over bottom surface is examined using planar PIV in the same cross stream planes as in Figure 5.4 and is shown in Figure 5.10. The primary difference between the flow in Figure 5.4a and 5.10a

is the thinning of the boundary layer, which becomes compressed closer to the surface. This, in turn, suggests that the boundary layer is less susceptible to separation in the presence of actuation since its streamwise growth as a result of the adverse pressure gradient is somewhat suppressed. The effect of the actuation on the diffuser flow becomes more prominent at  $x/D = -2.5$ , in Figure 5.10b. As noted in connection with Figure 5.4b, the base flow is about to separate or reattach in the time-averaged sense, and the actuation leads to clear attachment (Figure 5.10b).

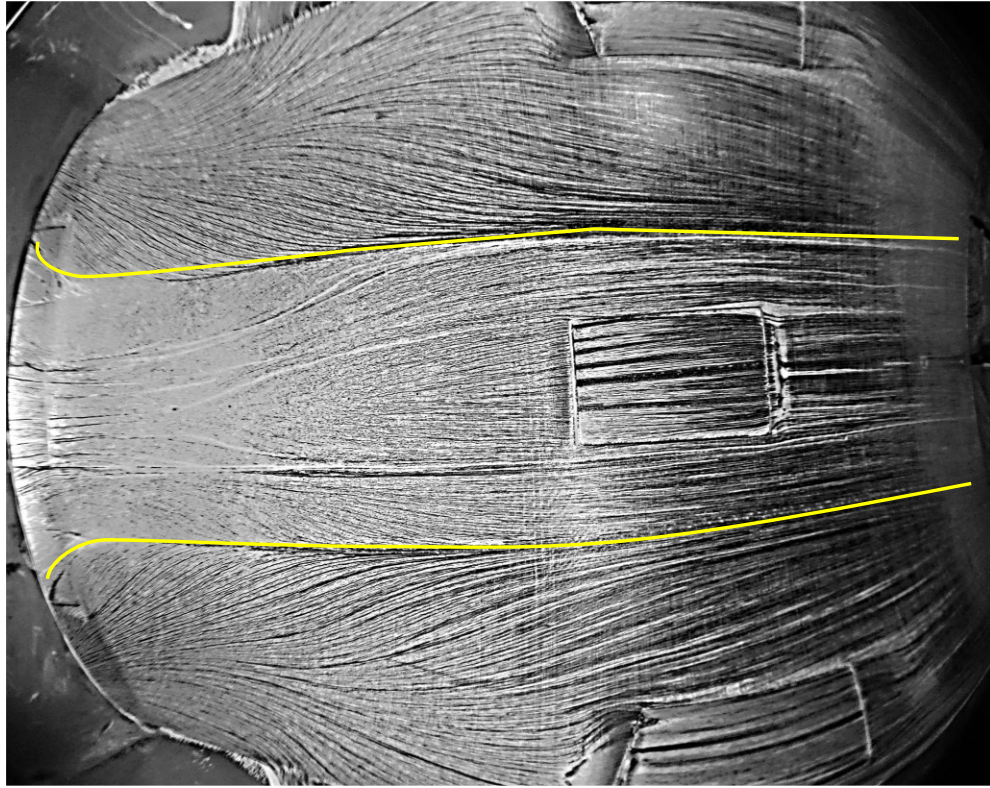


**Figure 5.11 Oil visualization on the concave (bottom) diffuser surface for  $-2.5 < x/D < 0$  at  $M_{AIP} = 0.54$  with  $C_q = 0.35\%$ . The yellow lines mark vortex trajectories.**

After assessing the effectiveness of the actuation on the flow along the first turn in the absence and presence of the shock formation, an important question is how those local



flow changes couple to the global diffuser flow and its integral measures of performance. The global topological changes in the presence of actuation are shown using surface oil visualization along the bottom surface between the first-turn flow control insert and the AIP at  $C_q = 0.35\%$  (the qualitative features of the flow topology in the presence of actuation are nearly the same as for higher  $C_q$ ). There are two main topological changes compared to the corresponding base flow topology in Figure 5.5. First, since in the presence of actuation the controlled flow remains attached throughout the central diffuser flow (between yellow lines), flow separation coupled to the secondary streamwise vortices remains confined only to the diffuser corners from Figure 5.8d-f. Another important topological change is that the attached flow about center span leads to increased spanwise separation between the vortices (as depicted by yellow lines in Figure 5.11). The increased separation limits the interaction between the vortex pair (spanwise separation nearly doubled at the AIP, Figure 5.11) leading to separation of vortices and reduced upwash of low-momentum fluid.

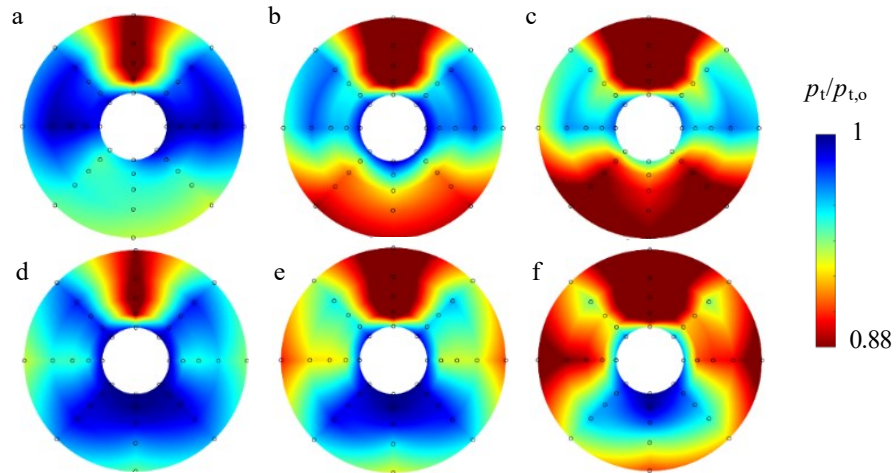


**Figure 5.12** Color raster plots of distributions of the total pressure at the AIP in the absence (a-c) and presence (d-f) of actuation ( $C_q = 0.75\%$ ), at  $M_{AIP} = 0.54$  (a, d), 0.61 (b, e), and 0.66 (c, f).



Perhaps the most important measures of the flow quality in the diffuser are the AIP total pressure distortion and losses. Figure 5.12 shows color raster plots of the total pressure distributions for the same previously discussed Mach numbers  $M_{AIP} = 0.54, 0.61$ , and  $0.66$  where the distributions of the base flows are repeated from Figure 5.6 for reference (Figure 5.12a-c). These data show that for all Mach numbers, actuation at the first turn can suppress and redistribute the total pressure deficit above the lower surface. Even in the absence of shock (Figure 5.12d), most of the lower surface deficit is broken up and redistributed upward along the side surfaces and thereby increasing the total pressure level in the bottom central region. Similar effect is visible when the increased total pressure deficit is caused in the presence of a shock at  $M_{AIP} = 0.61$  (Figure 5.12e). High total-pressure is recovered in most of the lower central domain, while the remnants of the lowered total pressure are pushed upward along the side walls. These changes are related to the altered flow topology in the first-turn streamwise vortices as shown in Figure 5.8. As discussed in connection with Figure 4.2 in Chapter 4, the close spanwise spacing between the two base flow vortices (Figure 5.8b) drives low-momentum fluid downward along the side surfaces and carries it towards the lower central region. However, the first turn vortices are not as closely coupled as the second turn vortices (along the upper surface, cf. Figure 5.8a) and consequently the induced deficit is not as high as over the top surface of the AIP. When actuation is applied, the first-turn vortices are displaced away from each other (see Figure 5.8e) and therefore their sweeping action is diminished and they lead to lower total-pressure deficit. Similar actuation effect is effected at  $M_{AIP} = 0.66$  (Figure 5.12f), but there is a stronger deficit along the side walls as the vortices are displaced by the flow control.

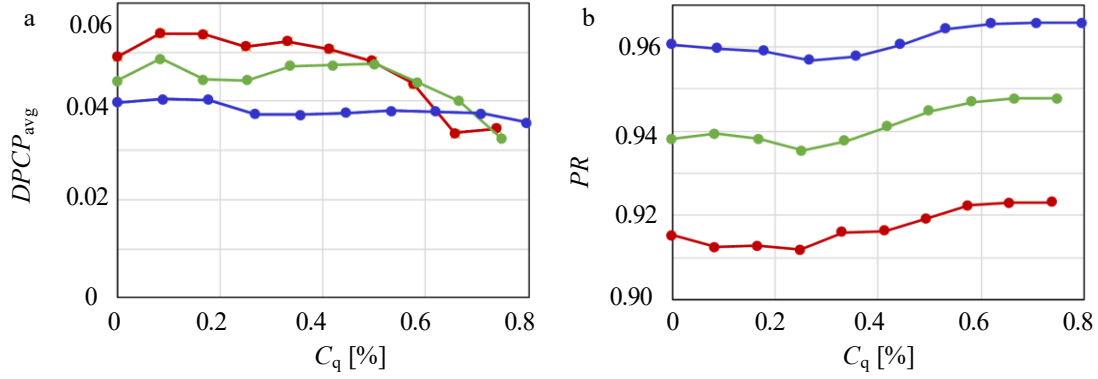


**Figure 5.13** Variations with  $C_q$  of the average circumferential distortion  $DPCP_{avg}$  (a) and total pressure recovery  $PR$  (b) for  $M_{AIP} = 0.54$  (●),  $0.61$  (●), and  $0.66$  (●).

Figure 5.13 shows variations of the time-averaged circumferential distortion  $DPCP_{avg}$  (a) and total pressure recovery  $PR$  (b) with  $C_q$  for  $M_{AIP} = 0.54$ ,  $0.61$ , and  $0.66$ . As expected, the distortion parameter increases with Mach number in the absence of actuation ( $C_q = 0$ ). In the absence of the first-turn shock formation,  $DPCP_{avg}$  is about 0.04, and when actuation is applied there is only a modest reduction with increasing  $C_q$ . Knowing how small the contribution of the lower surface total pressure deficit to the total distortion is (Figure 5.12), it is not surprising that the actuation does not significantly effect distortion parameter because the actuation does not target the main source of the distortion at the second turn surface. As the Mach number is increased to  $M_{AIP} = 0.61$  and a shock is present, a  $C_q$  leads to a marginal difference up to about 0.5%, and above this level  $DPCP_{avg}$  drops monotonically to the level at  $M_{AIP} = 0.54$  and  $C_q = 0.8\%$ . Similar response is also attained at  $M_{AIP} = 0.66$  for  $C_q > 0.3\%$  down to about  $DPCP_{avg} = 0.035$  (regardless of the different base distortion). This indicates that even though higher pressure deficit is induced at higher Mach numbers, the actuation is capable of reducing it. Again, the distortion parameter is primarily tied to the total-pressure deficit effected at the second turn, but this source of distortion is not addressed by actuation in the present study (cf. Chapter 4). The

second parameter that characterizes the flow at the AIP face is the total-pressure recovery which is shown in Figure 5.13b. As expected, in the absence of actuation, the pressure recovery decreases with increasing Mach number. However, the actuation has only a weak effect on  $PR$  which appears to plateau at the highest levels of  $C_q$ , regardless of the Mach number.

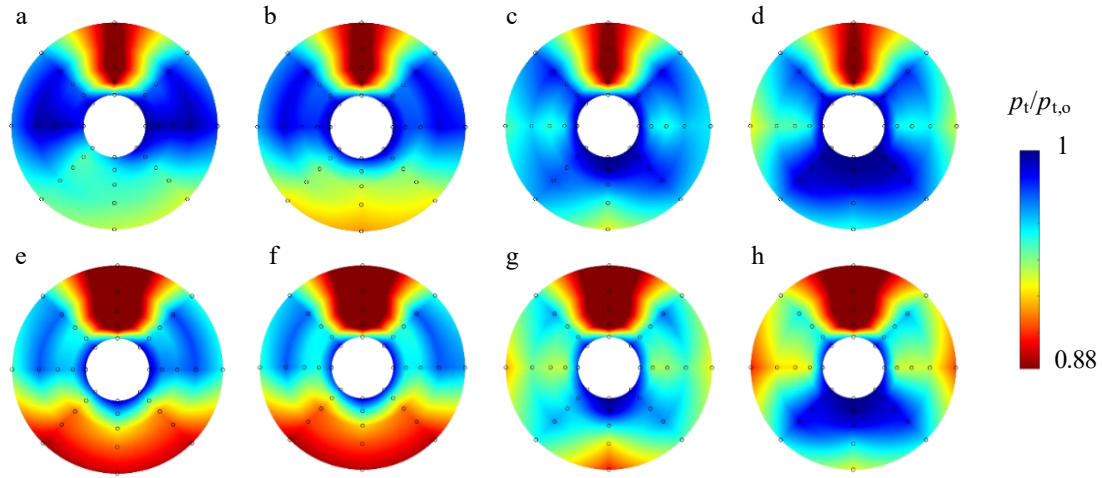


**Figure 5.14** Color raster plots of distributions of the total pressure at the AIP for  $M_{AIP} = 0.54$  (a-d), and  $0.61$  (e-h), for  $C_q = 0$  (a, e),  $0.25\%$  (b, f),  $0.5\%$  (c, g), and  $0.75\%$  (d, h).

To probe how the flow control effect varies with  $C_q$ , flow in the absence and presence of the shock are tested at the same sequence of  $C_q$ . Clearly, if  $C_q$  is constant between two different Mach numbers, the flow rate of the actuation is proportional to the diffuser flow rate. Figure 5.14 shows color raster plots of the AIP total pressure for  $M_{AIP} = 0.54$  (Figure 5.14a–d) and  $0.61$  (Figure 5.14e–h). Despite the different flow characteristics at these two Mach numbers, the responses of the AIP total pressure deficit to the actuation are similar at the same  $C_q$ . For  $C_q = 0.25\%$  (Figure 5.14b and f), there is either a small difference (at higher  $M_{AIP}$ , Figure 5.14e) or perhaps an adverse effect (at

lower  $M_{AIP}$ , Figure 5.14a), but as  $C_q$  increases to 0.5% (Figure 5.14c and g) there is a dramatic shift in the total pressure deficit, where most of the central lower region is cleared except for a very narrow region near the wall. This residual deficit becomes fully cleared at  $C_q = 0.75\%$  (Fig 12d, h). This similarity in the total pressure deficit response to actuation, regardless of the presence of the first turn shock further points to the important role of the streamwise vortices that form in the diffuser's first turn, and not directly to the shock.

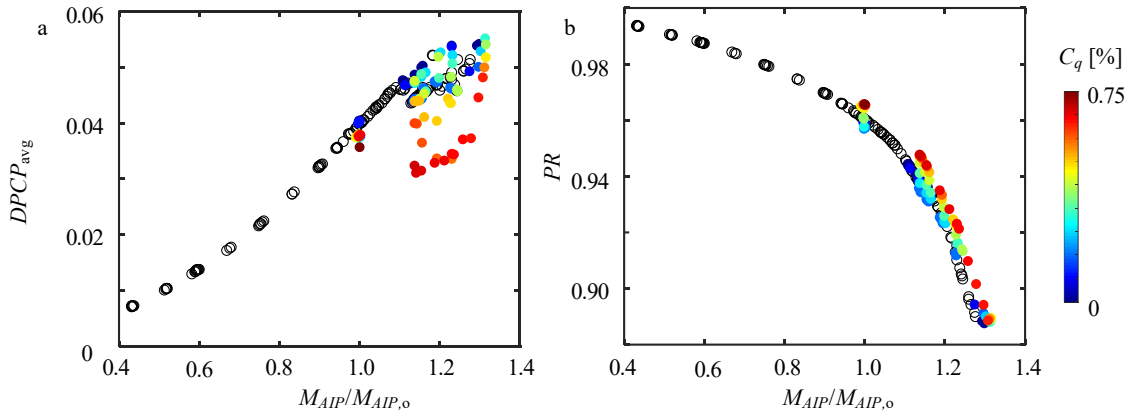


**Figure 5.15 Effects of actuation at varying  $M_{AIP}$  (normalized by  $M_{AIP,o} = 0.54$ ) on  $DPCP_{avg}$  (a), and total  $PR$  (b) in the base and controlled flows (open and solid symbols, respectively).**

Finally, to illustrate robustness of the present flow control approach, the two main AIP flow descriptors,  $DPCP_{avg}$  and  $PR$ , are plotted over a range of Mach numbers and several different values of  $C_q$ . These results are shown in Figure 5.15, where the Mach number is normalized by the nominal operational AIP Mach number  $M_{AIP,o} = 0.54$ . The base flow distortion (Figure 5.15a) increases monotonically with Mach number until shocks are formed at the highest range, where  $DPCP_{avg}$  generally increases but not monotonically. Different  $C_q$  decrease  $DPCP_{avg}$  by up to 30%. The only actuation case for

which  $M_{AIP}/M_{AIP,0} < 1$  (prior to the shock formation) effects only a moderate improvement. Another interesting outcome of the actuation is its effect on the total pressure recovery (Figure 5.15b), where there is a relatively small 1% increase in the total pressure recovery for most of the actuation cases.

## **CHAPTER 6.    SERPENTINE DIFFUSER WITH COWL INLET**

In the final stage of this research, an additional step is taken to mimic the effects of aircraft-integrated diffusers, by drawing the flow into the diffuser through a serrated cowl inlet. While such inlets are typically optimized for other parts of the flight envelope, during takeoff they form secondary streamwise vortices that can significantly hinder engine operation. The inlet vortices that form along the cowl lips are similar to the vortices that are formed over delta wings, and they subsequently dominate the flow dynamics within the diffuser. The cowl-induced flow effects are addressed by using aerodynamic bleed across the cowl's outer shell that directly interact with the cowl lip vortices by introduction of momentum and small-scale vorticity near the surface and thereby significantly mitigating the effects of these vortices on the diffuser flow. In addition, second turn fluidic actuation is tested in conjunction with the cowl aerodynamic bleed to enable further reduction of losses and distortion through the inlet system.

### **6.1    Introduction**

This final stage of research is the investigation of flow through a serpentine diffuser with a cowl inlet. The investigations in Chapters 3-5 used a contraction at the diffuser's inlet to isolate from and minimize inlet nonuniformities. An aircraft-integrated diffuser is more closely approximated by drawing air through a serrated cowl inlet that is mounted to a ground plane, which is studied in the present chapter, effectively emulating an aircraft inlet in static conditions (zero free-stream velocity). A section view of the test section is shown in Figure 6.1, showing the cowl that is attached to an identical serpentine diffuser

geometry to that studied in Chapter 4 and 5. Further detail on the experimental setup can be found in Chapter 2.

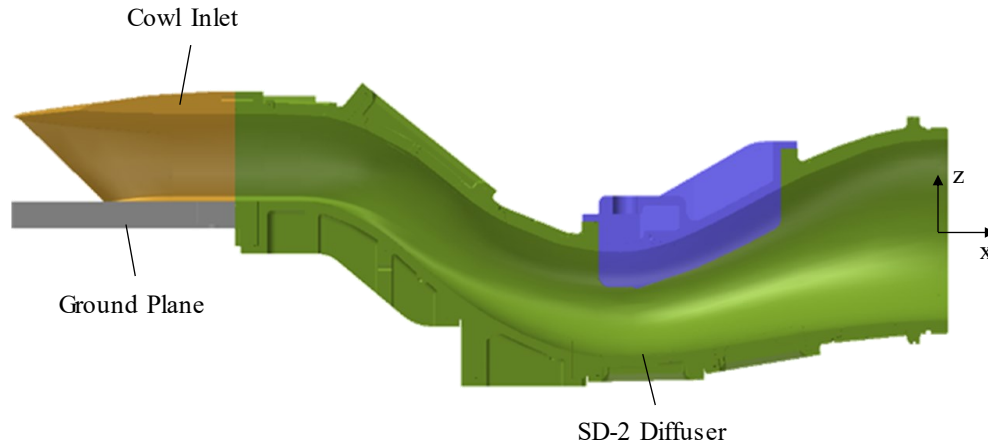


**Figure 6.1** Section view of the serrated cowl and ground plane serving as an inlet for the SD-2 diffuser.

The dominant flow features within the combined cowl-diffuser are visualized using iso-surfaces of streamwise vorticity ( $x$ -direction) from the numerical simulation of Lakebrink and Mani, [79] shown in Figure 6.2. These data demonstrate that the flow within the diffuser is dominated by four streamwise vortices whose sense of rotation is marked with arrows. As the flow is drawn into the diffuser, streamwise vortices are formed in the corners of the diffuser D-shape and evolve along the diffuser surface, steadily growing in size to the AIP. In addition to these two corner vortices, a counter-rotating vortex pair is formed over the cowl centerline and continues to grow and interact with the corner vortices.

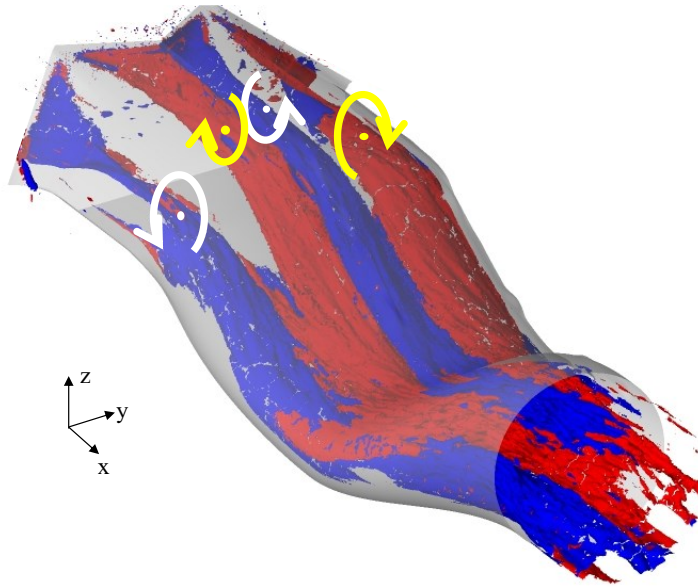


**Figure 6.2** The evolution of streamwise vortices within the coupled cowl-diffuser captured in the simulations of Lakebrink and Mani, [79]. The vortices are visualized using surfaces of streamwise vorticity (red is positive, blue is negative) originating at the serrated edges of the cowl and at the corner between the cowl and the inlet ground plane. The sense of each vortex is marked by arrows.

## 6.2 Base Flow Characterization

The integration of the diffuser with the serrated cowl inlet introduces inlet vortices that significantly alters the base flow as compared to that of the isolated diffuser with an inlet contraction (cf. Chapters 4 and 5). The serrated cowl inlet has four straight edges that form two triangular streamwise protrusions that connect at the center plane and at the corners of the cowl with the ground plane (cf. Figure 2.3, Figure 6.3, and Figure 6.4). These sharp edges engender two pairs of counter-rotating streamwise vortices- one pair about the center plane and a single vortex in each corner. The surface topology effected by these vortices is characterized using surface oil visualization at  $M_{AIP} = 0.5$  and is shown in Figure 6.3a and b, of the inner surface of the cowl and of the ground plane underneath



the cowl (the flow is from left to right). The dark streaks that originate at the cowl's upstream edges are the surface signatures of the vortex trajectories (marked by yellow dashed lines in Figure 6.3a) that proceed towards the center plane and each of the corners. It is apparent that the vortices are strong enough to produce near-wall flow that is orthogonal to bulk flow in the vortices, where some streaks near the corner and center plane (within the red boxes) have no streamwise component (bulk flow is in  $+x$  direction but streaks bounded in red dashed lines are in  $+y$  direction). This highlights the losses that the vortices engender – orthogonal streaks indicate an effective blockage in the flow, where there is zero velocity in the  $+x$  direction. In addition, complex patterns are found between yellow dashed lines and cowl edge (cf. enlarged region in Figure 6.3b), which are similar to those on a delta wing [80] and are most likely secondary or tertiary separation and/or attachment lines.

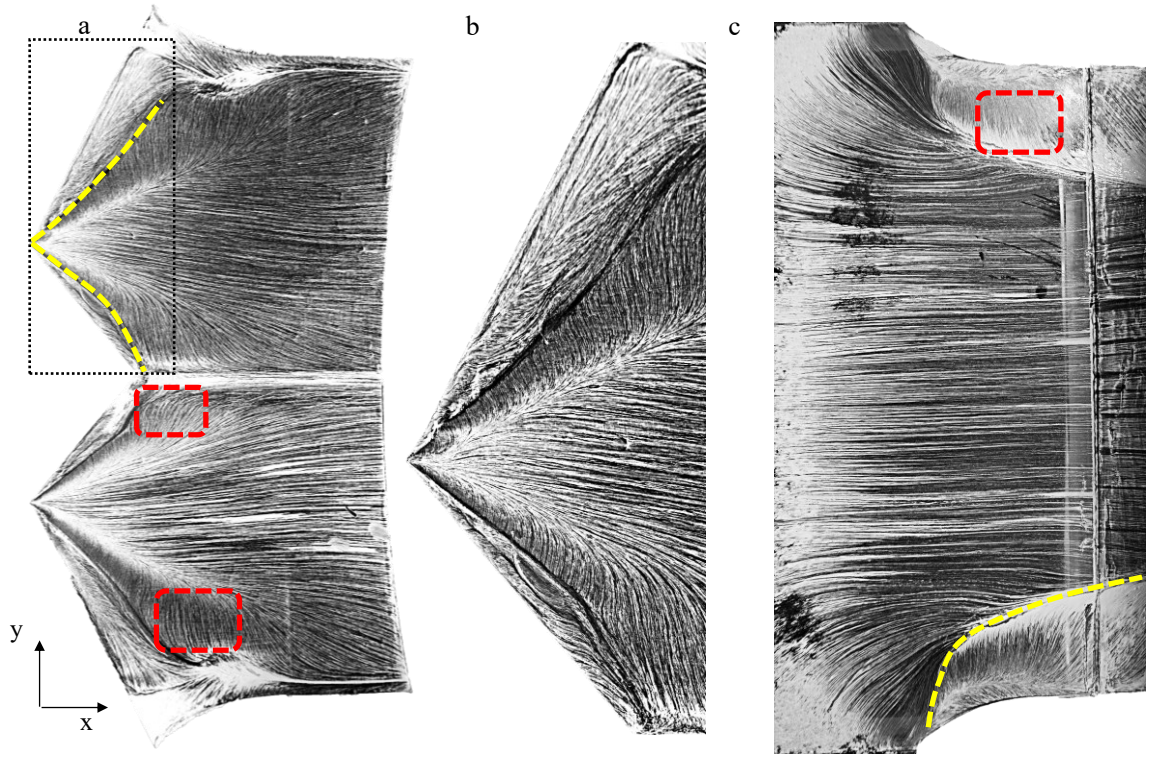


**Figure 6.3 Surface oil visualization on the inner cowl surface (a) and the ground plane underneath (c) at  $M_{AIP} = 0.5$ . Black dotted rectangle in (a) marks the enlarged region shown in (b). Yellow dashed lines highlight the surface markings of the vortex path. Red rectangle mark regions in which the oil traces point normal to the streamwise direction.**

The surface oil visualization on the ground plane (Figure 6.3c) shows a surface signature of the corner vortices, one of which is marked by a yellow dashed line. This line is a near-surface interface of the corner vortices ( $y$ -direction streaks below line) with the bulk flow ( $x$ -direction streaks above line) and is moving away from the corner as it progresses in the streamwise direction. This indicates that the corner vortex is growing in size, because the on-surface vortex extent stretches from the edge of the oil domain to the yellow line). This visualization also shows the high angularity of the flow in the vortex indicated by the streaks in the corner that are perpendicular to the bulk, centerline flow (marked by a red rectangle). This creates an effective blockage in the flow because flow

in this region is stagnant in the  $+x$  direction, resulting in reduced test section mass flow rate and total pressure recovery.

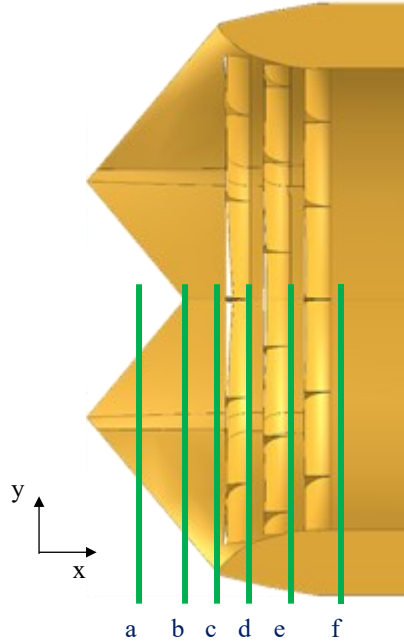


**Figure 6.4 Spanwise projection of cross-stream and streamwise-normal SPIV planes relative to the bleed slots on the surface of the cowl (cf. Sections 2.4.2, 6.3), at  $x/D = -4.89$  (a),  $-4.7$  (b),  $-4.58$  (c),  $-4.43$  (d),  $-4.28$  (e),  $-4.12$  (f).**

The vortex evolution was also characterized using stereo particle image velocimetry (SPIV) that was conducted at six cross stream planes normal to the streamwise direction. The PIV domain included half the span of the cowl inlet, shown in Figure 6.4 relative to the auxiliary bleed slots on the surface of the cowl, which were mentioned in Section 2.4.2 and will be discussed further in Section 6.3. The base cowl has the same geometry and does not have these slots. In the present experiments, the flow through each of these six planes is measured at  $M_{AIP} = 0.4$  and  $0.5$  for the base cowl (in the absence of the bleed ports) where the maximum reachable AIP Mach number is  $0.5$  because of the limitations of the facility blower and the losses created by the base cowl.

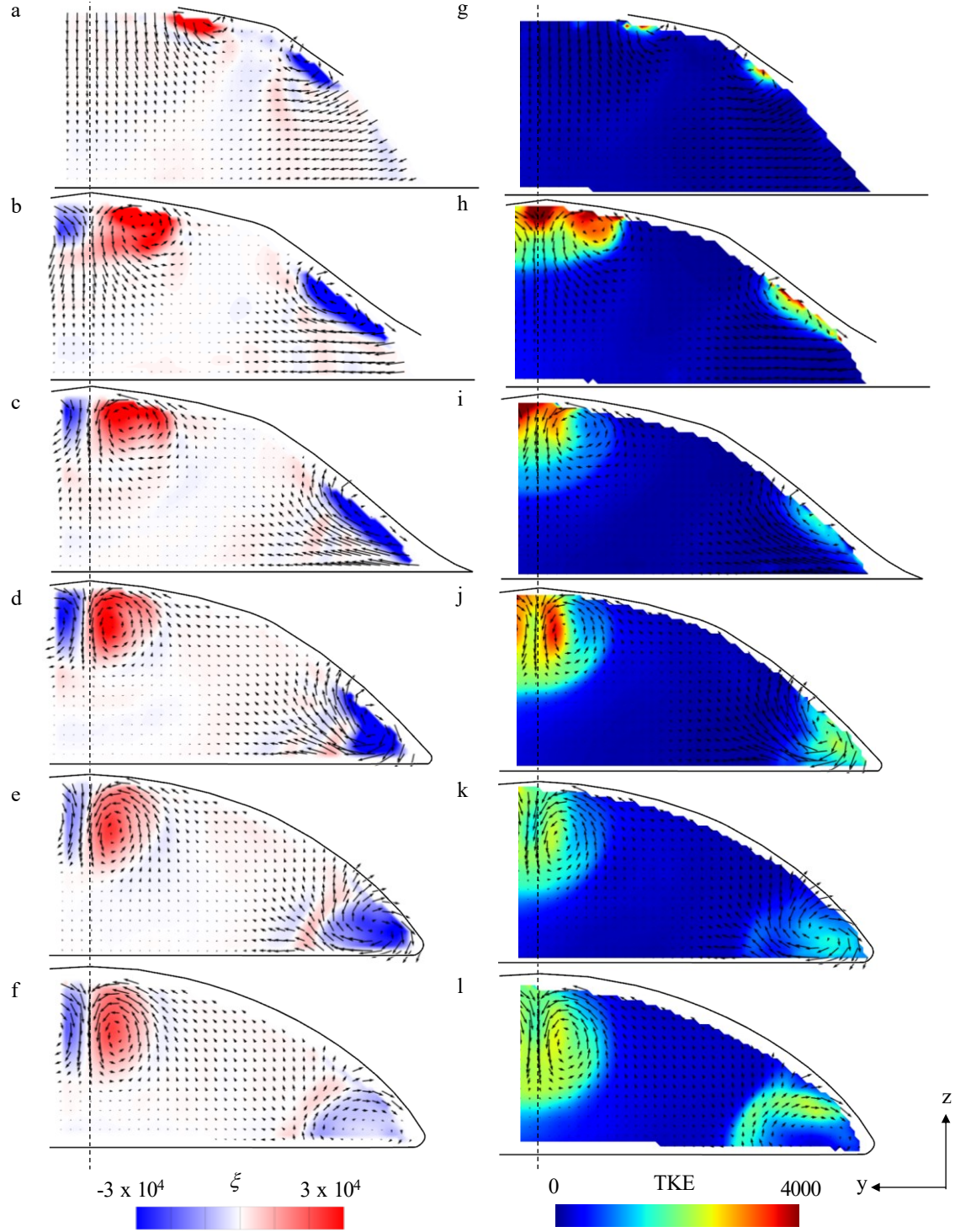


**Figure 6.5** Color raster plots of distributions of the streamwise vorticity (a-f), and TKE (g-l) of the base flow within the spanwise planes at  $x/D = -4.89$  (a, g),  $-4.7$  (b, h),  $-4.58$  (c, i),  $-4.43$  (d, j),  $-4.28$  (e, k),  $-4.12$  (f, l), at  $M_{AIP} = 0.5$ . The dashed line in each image marks the centerline  $y = 0$ , and solid lines bounding the domains mark the intersection of the diffuser's inner surface with the measurement planes.

Color raster plots of distributions of the streamwise vorticity and TKE in the base flow within the SPIV measurement planes (cf. Figure 6.4) are shown in Figure 6.5a-f and Figure 6.5g-l, respectively, ordered from upstream (a,g) to downstream (f,l). Figure 6.5a shows the vortices originating on the edge of the serrated cowl (cf. Figure 6.4a). As these vortices extend in the streamwise direction, they are oblong in shape and follow the cowl edge until they connect at the centerline (Figure 6.5b) or connect to the corner (Figure 6.5c). When the cowl edges connect at the centerline, the individual vortices of opposite sense coalesce into a counter-rotating vortex pair that remains at the centerline (Figure 6.5d-f), where the centerline vortex fully in the SPIV domain is rotating counterclockwise. The corner vortex rotates clockwise and remains in the corner through all planes. In the final two planes (Figure 6.5e,f), lower vorticity levels are apparent, which coincide with higher TKE levels (Figure 6.5k,l), indicating that the vortices are exhibiting increasing turbulent fluctuations.

The TKE in Figure 6.5g-l shows the turbulent fluctuations associated with each pair of vortices. The center plane vortices have more fluctuation energy than the corner, but both regions have significantly more turbulent energy than the bulk flow in the rest of the field, in which the magnitude of the TKE is negligible. Turbulent fluctuations are most concentrated in the more upstream planes (Figure 6.5h-j), where there are small regions of high energy (central vortices), after which those regions grow with the vortices into larger regions with lower TKE as the flow progresses through the cowl.

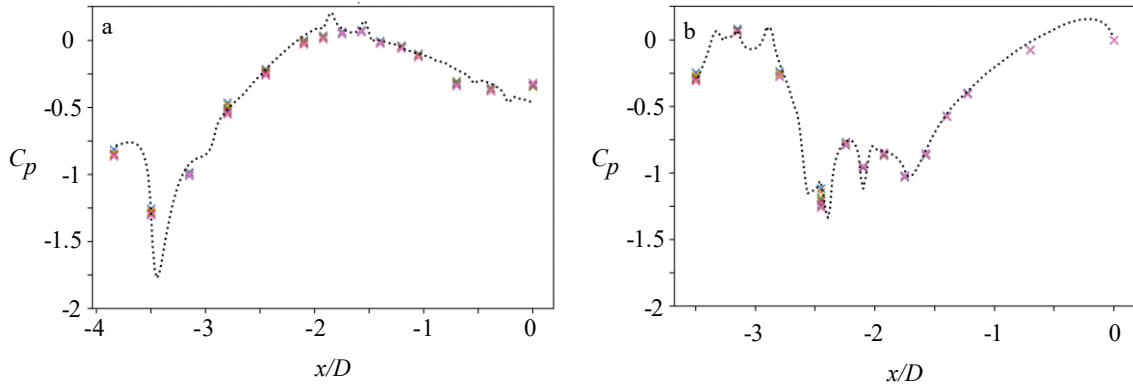


**Figure 6.6** Streamwise distributions of the centerline pressure coefficient  $C_p$  along the lower (a) and upper (b) surfaces of the diffuser in the base flow measured at  $M_{AIP} = 0.3$  ( $\times$ ), 0.35 ( $\times$ ), 0.4 ( $\times$ ), 0.45 ( $\times$ ), and 0.5 ( $\times$ ). The experimental measurements are compared with numerical simulations for  $M_{AIP} = 0.5$  (dashed line, Lakebrink and Mani [79]).

The streamwise evolution of the flow within the diffuser is characterized along the centerline by distributions of the pressure coefficient along its lower and upper surfaces in Figure 6.6a and b, respectively (the diffuser's throat and AIP are at  $x/D = -3.5$  and 0, respectively). The pressure coefficient is computed from  $C_p = 2(p/p_{ref} - 1)/(1.4 \cdot M_{AIP}^2)$  where the static reference pressure  $p_{ref}$  is acquired at the top surface of the AIP, and the data are measured at five equal increments of  $M_{AIP}$  from 0.3 to 0.5. The corresponding pressure distributions from the numerical simulations of Lakebrink and Mani for  $M_{AIP} = 0.5$  [79] are overlaid on the experimental data and exhibits a good agreement between the simulations and the measurements. As the flow enters the cowl, the pressure on the lower surface (Figure 6.6a) indicates that the flow begins to accelerate even prior reaching the diffuser throat ( $x/D = -3.5$ ) as is evidenced by the negative static pressure slope. A suction peak is reached just past the throat at  $x/D = -3.48$  and is followed by a sharp streamwise pressure rise or adverse pressure gradient although these data do not indicate local flow separation. Thereafter for  $x/D > -3.48$ , the pressure increases up to

about  $x/D = -1.6$  and then begins to decrease monotonically towards the AIP indicating flow deceleration. The pressure distribution on the upper surface is more complex ostensibly as a result of the streamwise vortices that form at the sharp edges of the cowl (cf. Figure 6.2). These data show that the flow decelerates along the upper surface immediately downstream of the diffuser's throat, as is evidenced by the sharp increase in static pressure. Following the relatively flat extent at  $-3.4 < x/D < -2.9$ , the flow sharply accelerates over a short distance ( $-2.9 < x/D < -2.6$ ). For  $x/D > -2.6$  the pressure distribution exhibits several consecutive accelerations and decelerations before reaching the diffuser geometry's centerline  $z$ -direction minimum point at  $x/D = -1.7$  (cf. Figure 6.1), after which it has its final acceleration. Past the second turn, the flow faces a steady adverse pressure gradient to just about the AIP plane. The highly disparate trends between the bottom surface and the top surface static pressure shows the highly non-uniform nature of offset diffuser flow, where at a given  $x/D$  position, each surface is locally experiencing different flow.



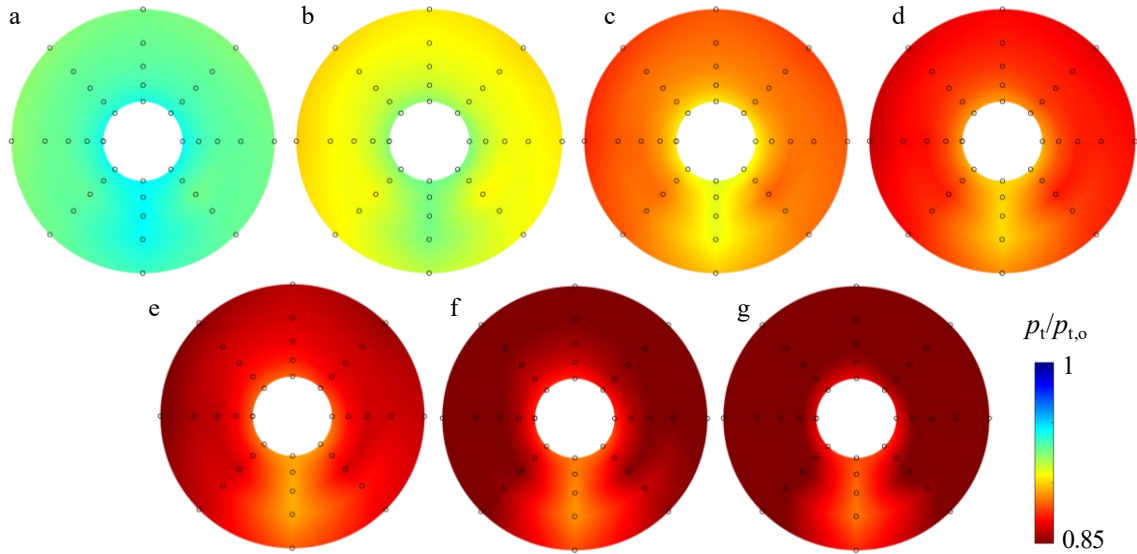


**Figure 6.7** Color raster plots of time-average total pressure at the AIP for  $M_{AIP} = 0.3$  (a), 0.35 (b), 0.4 (c), 0.425 (d), 0.45 (e), 0.475 (f), and 0.5 (g).

The flow distortion through the diffuser's AIP is assessed from distributions of the total pressure measured by the 40-probe rake at the AIP (cf. Chapter 2). Color raster plots of distributions of the time-averaged total pressure at the AIP are shown in Figure 6.7a-g for  $M_{AIP} = 0.3, 0.35, 0.4, 0.425, 0.45, 0.475$ , and  $0.5$ , respectively. A common aspect of these distributions is the absence of any dominant features that would normally indicate the presence of coherent secondary flows (e.g., streamwise vortices) except perhaps a region of somewhat lower pressure along the lower segment of the AIP plane. This is in stark contrast to the color raster plots of the AIP total pressure associated with this diffuser in the absence of the cowl, which exhibits signatures of streamwise vortices that form as a result of separation at the diffuser's first and second turns (cf. Chapters 5 and 4, respectively). The raster plots in Figure 6.7 support the assertion that the streamwise vortices that form in the presence of the cowl become unstable as the flow expands through the diffuser and therefore their features are smeared in the time-averaged measurements.



This indicates the need for the time-resolved total pressure measurements to adequately capture variations of the total pressure across the AIP. A second common feature in contrast to the diffuser's flow in the absence of cowl is that there is a significant drop in the magnitude of the total pressure between the diffuser's inlet and the AIP. As is evident from the data in Figure 6.7, this reduction in total pressure is proportional to the diffuser's Mach number, where there is a pressure loss of about 15% at the  $M_{AIP} = 0.5$  (Figure 6.7g). For comparison, there was only about 4% decrease in the average total pressure in the presence of a contraction at the diffuser's inlet at  $M_{AIP} = 0.5$  (Chapter 4), which points to a shift in the objectives of the flow control approaches in the two diffuser configurations. While in the presence of the contraction the total pressure distortion was the primary target, in the presence of the cowl inlet the primary goal is minimization of the total pressure losses, or improvement of total pressure recovery.

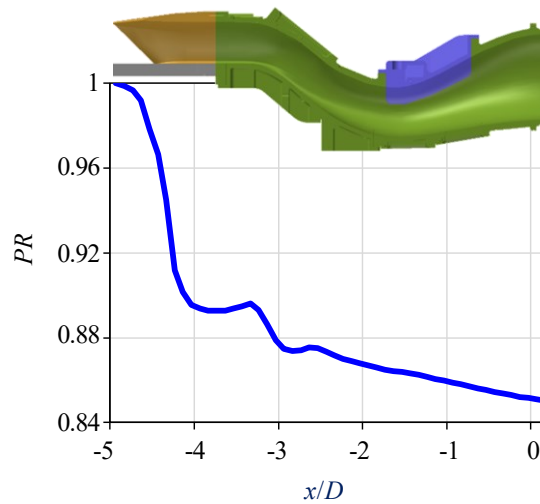


**Figure 6.8** Streamwise variation of average total pressure recovery from the numerical simulations of Lakebrink and Mani [79] at  $M_{AIP} = 0.5$ , along the diffuser with the cowl inlet diffuser shown for reference above.

The streamwise evolution of the total pressure loss is shown in Figure 6.8 in terms of the pressure recovery  $PR = \frac{\overline{P_T}}{P_{T,ref}}$  computed from the numerical simulations of Lakebrink and Mani, [1] at  $M_{AIP} = 0.5$ . Of the 15% total pressure drop in the diffuser, 73% of it occurs within the cowl inlet ( $-5 < x/D < -4.2$ ). This finding clearly indicates that flow control should be implemented within the cowl.

The unsteady characteristics of the flow within the AIP are revealed by using time-resolved measurements of the total pressure over a range of  $M_{AIP}$  using a dynamic pressure rake described in Section 2.3.1.2. The time-resolved pressure is used to compute the instantaneous and time-averaged  $DPCP_{avg}$  and pressure recovery.

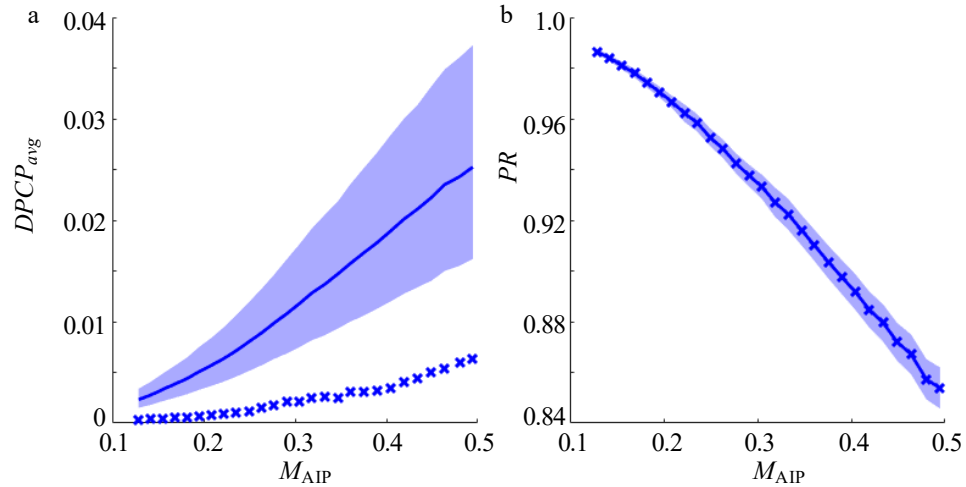


**Figure 6.9** Steady state (×) and time-averaged (—) circumferential distortion  $DPCP_{avg}$  (a), and pressure recovery  $PR$  (b), for  $0.12 \leq M_{AIP} \leq 0.5$ . The 95% confidence interval is marked with a blue shaded region about the time-averaged data.

The disparities between the time-average and instantaneous distortion and pressure recovery are compared in Figure 6.9. Each parameter is calculated on the time-averaged total pressure (in this discussion this is coined steady-state), and each is calculated on the

instantaneous total-pressure realization, and then averaged (time-averaged, in this discussion). To further clarify the difference, steady-state is calculated as  $X(\bar{p})$ , and time-average is calculated as  $\overline{X(p)}$ , where  $X$  is a calculated parameter,  $p$  is the instantaneous pressure, and the bar notates a time-average. In addition to these calculations, the 95% confidence interval representing 95% of the range of instantaneous parameter values is shown by the filled region. The confidence interval is calculated with percentiles to produce range of parameter values from the 2.5% to 97.5% percentiles. The parameters and their confidence intervals in the range  $0.12 \leq M_{AIP} \leq 0.5$  are shown in Figure 6.9.

The data in Figure 6.9a show that there is a significant disparity between the steady-state  $DPCP_{avg}$  and its corresponding time-averaged and 97.5% percentile values. The steady-state  $DPCP_{avg}$  is low — (less than 0.007 at  $M_{AIP} = 0.5$ ) throughout the range of  $M_{AIP}$  as anticipated from the relative uniformity and symmetry of the total pressure distributions at the AIP in Figure 6.7. However, the time-averaged distortion is much higher, reaching about 0.025 at  $M_{AIP} = 0.5$ . Besides the disparity in magnitudes, there is also a difference in the rate of change of the distortion with  $M_{AIP}$ , where the top bound of the confidence interval (97.5% percentile) increases at a much steeper rate than the steady state  $DPCP_{avg}$ . The distortion unsteadiness also increases with  $M_{AIP}$  as is evidenced by the increasing width of the confidence interval (e.g., from 0.002 at  $M_{AIP} = 0.12$  to 0.02 at  $M_{AIP} = 0.5$ ).

Similar to the variation of the total pressure distortion with  $M_{AIP}$  in Figure 6.9a, the variation of the pressure recovery  $PR$  is shown in Figure 6.9b. These data show that  $PR$  decreases nearly linearly with  $M_{AIP}$ , exceeding a 10% loss already at about  $M_{AIP} = 0.375$ . In this case, the time-average  $PR$  coincides with the steady-state  $PR$  because the parameter

is linear, meaning the two methods of calculation discussed above results in the same value, unlike  $DPCP_{avg}$ . Like with distortion, the instantaneous variation in pressure recovery increases with  $M_{AIP}$ .

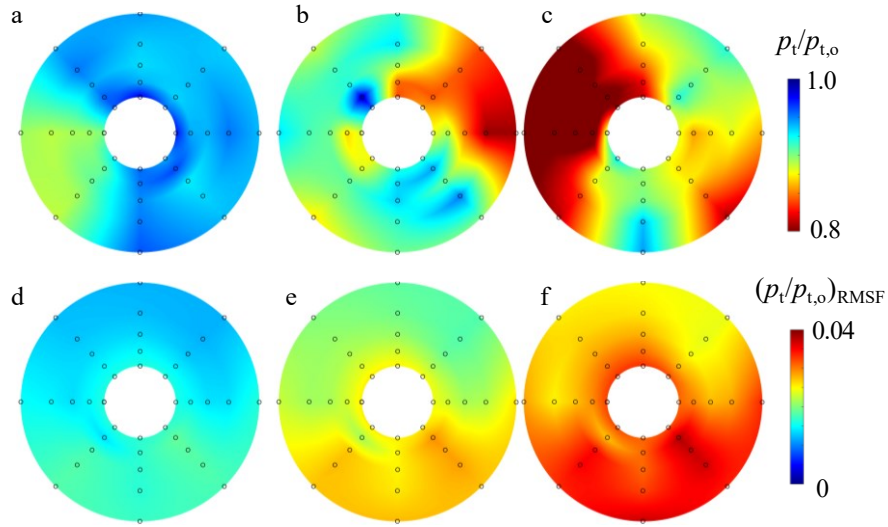


**Figure 6.10** Color raster plots of the total pressure distributions at the AIP at the instant of peak  $DPCP_{avg}$  (a, b, c) and AIP total pressure RMS fluctuations (d, e, f) for  $M_{AIP} = 0.3$  (a, d), 0.4 (b, e), 0.5 (c, f).

Figure 6.7 shows that there is a significant loss of total pressure at the AIP, and that this loss is nearly uniformly distributed across the AIP face, except at its lower central region that exhibits a slightly lower drop in pressure. As discussed in connection with Figure 6.9, there are significant deviations from the time-averaged total pressure distributions. Distributions of the instantaneous total pressure at an instance in time that correspond to the maximum  $DPCP_{avg}$  are plotted in Figure 6.10a-c for  $M_{AIP} = 0.3, 0.4, 0.5$  and are highly nonuniform and asymmetric. However, when considering the 40-probe average of the total pressure, the instantaneous measurements do not differ much from the time-average in Figure 6.7, which is corroborated by the small variation of pressure recovery shown by the confidence interval in Figure 6.9b). This highly non-uniform

distribution results in high instantaneous circumferential distortion that clearly becomes worse with increasing  $M_{AIP}$  (cf. Figure 6.9). The unsteadiness of the AIP total pressure is evident in color-raster plots of the RMS of the total pressure fluctuations are shown in Figure 6.10d-f. The RMS fluctuations are consistently higher along the lower segment of the AIP over the range of  $M_{AIP}$ .

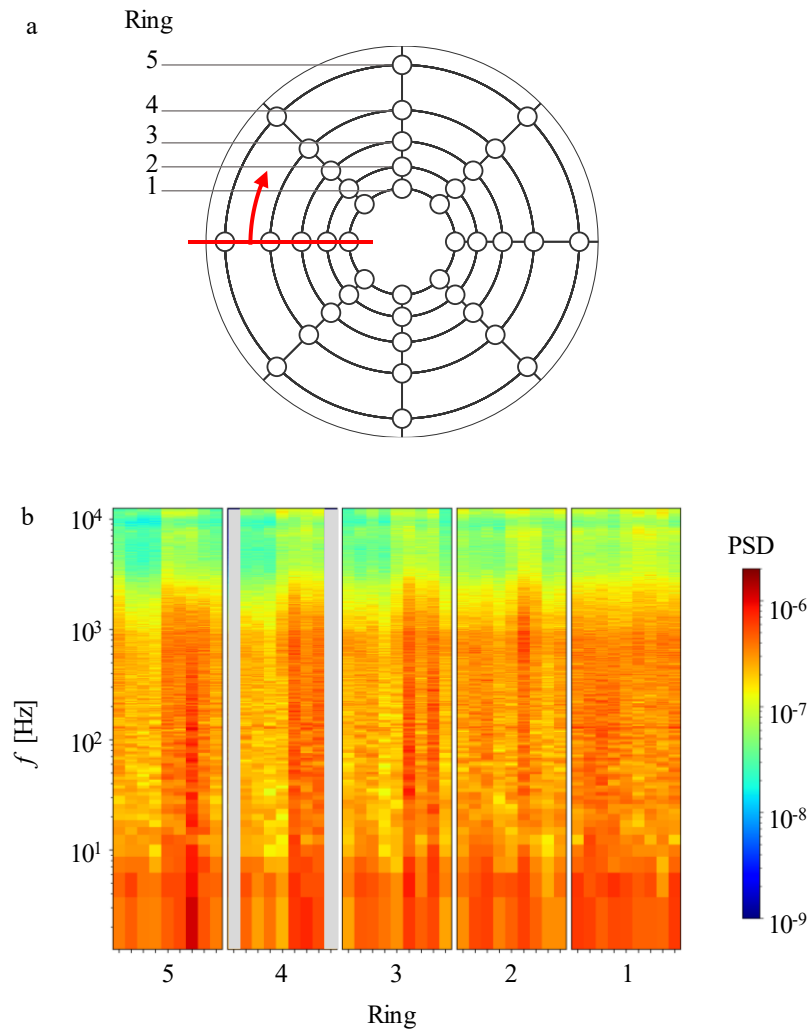


**Figure 6.11** Vertical color raster bars of spectral magnitudes (b, up to 10 kHz) of the total pressure measured by each of the AIP sensors at  $M_{AIP} = 0.5$  in each of the circumferential rings as shown schematically above in (a). The bars are grouped by ring number and the data for each sensor are arranged in CW order starting at the red line in (a). The bars shaded in gray represent missing data.

Spectral magnitudes (up to 10 kHz) of the total pressure fluctuations measured at  $M_{AIP} = 0.5$  by each of the AIP sensors are shown in Figure 6.11b. The data are arranged in vertical bars and the sensors are grouped in each of the circumferential rings of the array as shown schematically in Figure 6.11a (the data for each sensor are arranged in CW order starting at the red line in Figure 6.11a and the bar for the first port is repeated at right the end of the group). These data show that the power levels are fairly uniform in value for frequencies up to about 2 kHz, where the power drops by an order of magnitude. When comparing the variation in the angular direction, the outer two rings (rings 4 and 5) show that the portion at the top half of the AIP (left half of each ring group in plot) has a lower power than at the bottom half of AIP, which is consistent with the corresponding RMS AIP distributions in Figure 6.10f. This trend can be identified in ring 3, but less so. At the innermost rings, there is high azimuthal uniformity, indicating that there are not particular spatial differences in the fluctuations in the inner core flow.

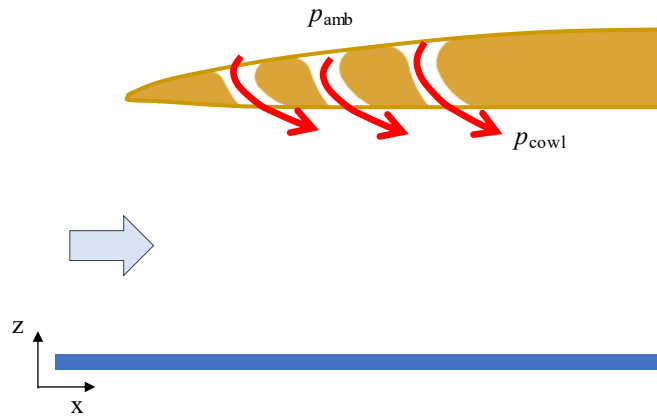


**Figure 6.12 Schematic of bleed flow through the three auxiliary inlet slots.**

### **6.3 Aerodynamic Bleed using Auxiliary Inlets**

Guided by the sharp drop in the total pressure along the inlet section of the cowl (cf. Figure 6.8) and an indication that the counter-rotating vortex pair that forms along the along the upper surface of the cowl (cf. Figure 6.2) leads to flow blockage within the cowl as demonstrated in Figure 6.6b, it is desirable to use flow control to disrupt the formation of this vortex pair and thereby mitigate the blockage effects. To this end, three auxiliary inlet slots are opened across the cowl upper surface, as shown schematically in Figure 6.12. These inlets exploit the existing pressure difference across the surface of the cowl and draw outer air through the cowl walls and into the diffuser. In principle, the flow through these slots can be actively regulated by electromechanically or piezoelectrically-operated louvers, or passive doors (or blow-in doors), however, in the present experiments they are kept open. The inlet cross section of the slots on the outer surface is bell-mouth-like to minimize pressure losses, and on the inner flow-side they are contoured to guide the air flow smoothly into the cowl to disrupt the formation of the streamwise vortices.

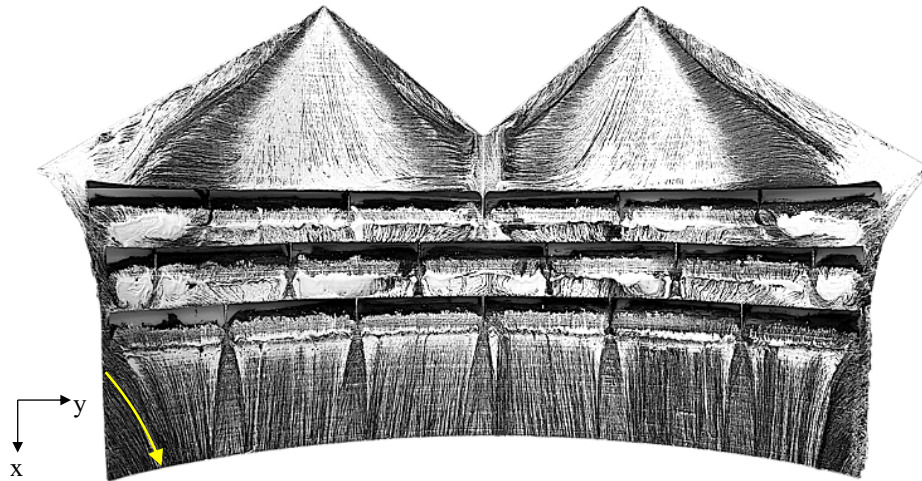


**Figure 6.13 Surface oil visualization on the inner surface of the cowl with three auxiliary spanwise inlet slots at  $M_{AIP} = 0.5$ . Yellow arrow highlights direction of oil streaks in the corner downstream of slots.**

### 6.3.1 *Bleed Effect within the Cowl Inlet*

The effect of the bleed through the auxiliary inlet slots is first investigated using surface oil visualization, and the topology of the oil streaks on the curved inlet surfaces at  $M_{AIP} = 0.5$  is shown in Figure 6.13 (equivalent to the base flow visualization in Figure 6.3a). Though the topology upstream of (above) the slots is similar to that of the base flow, there are some differences. In particular, the upstream slot appears to create blockage as is evidenced by the fact that the oil streaks are parallel to the slots along the upstream edge of the first slot, which is most noticeable near the center plane. Another observation is that the darker streaks that mark the vortex position along the two outer cowl edges is closer to the edge of the cowl lip edge than in the base flow. It is conjectured that this is the case because the slots effectively provide a flow bypass to the cowl inlet so that the flow rate through the front inlet is lower. In addition, though somewhat obfuscated by the slots, it appears that the flow downstream of the slots is straighter than in the base flow. It should be noted that some flow angularity is present in the wake of the structural fins that partition the slots for support. The biggest difference between base flow (Figure 6.3a) and the auxiliary inlet oil visualization (Figure 6.13) downstream of the slots is the direction of the flow in the corners. In the presence of the auxiliary inlets, the streaks are directed towards the centerline (as marked by the yellow arrow), rather than towards the corner as in the base cowl in Figure 6.3a. This change in the trajectory of the corner vortex is further characterized using stereo PIV.



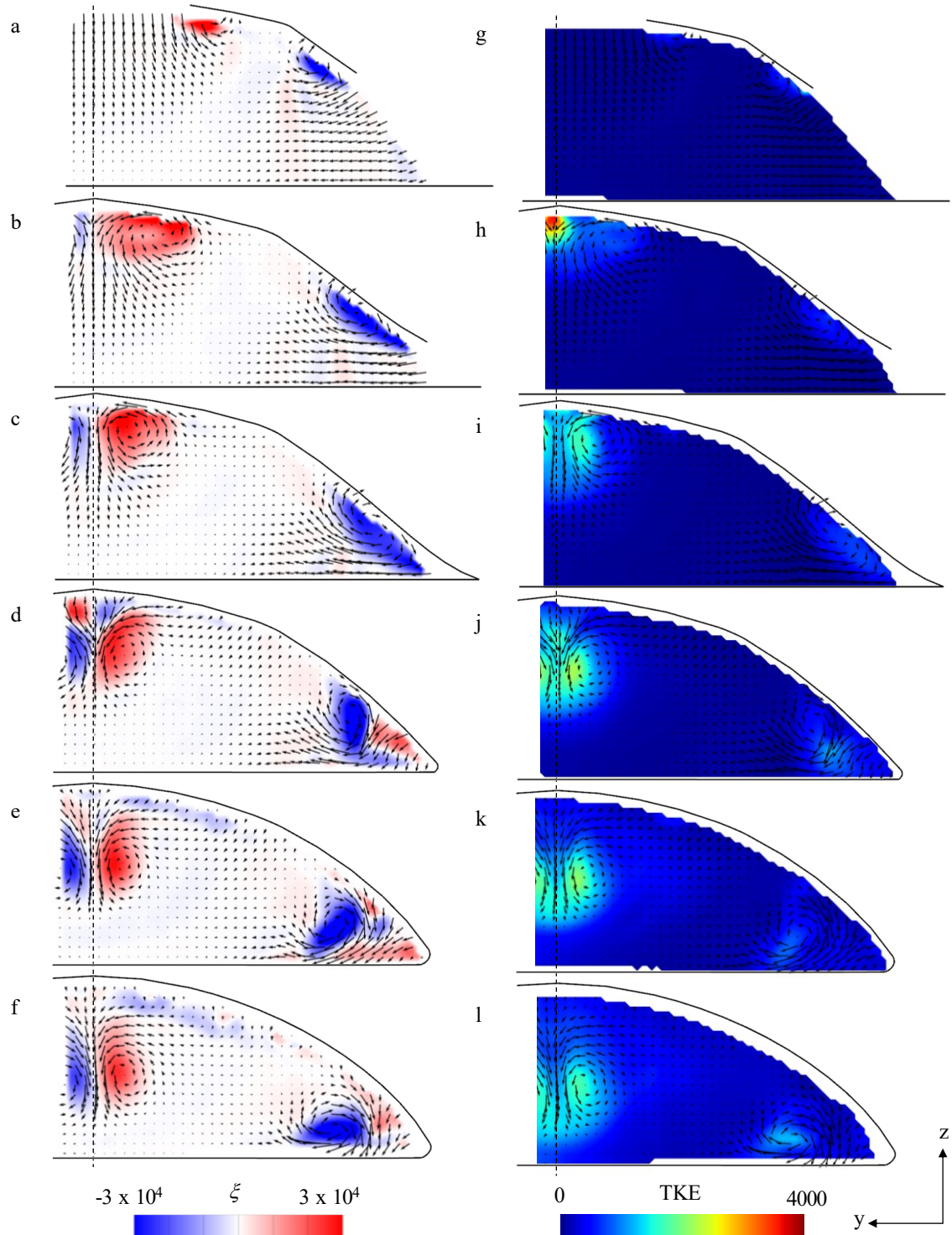


**Figure 6.14** Color raster plots of vorticity (a-f), and TKE (g-l) fields within the auxiliary inlet cowl, within the spanwise planes at  $x/D = -4.89$  (a, g),  $-4.7$  (b, h),  $-4.58$  (c, i),  $-4.43$  (d, j),  $-4.28$  (e, k),  $-4.12$  (f, l), at  $M_{AIP} = 0.5$ . Dashed line is test section centerline  $y = 0$ , and the bounding solid lines mark the intersection of the diffuser's inner surface with the measurement planes.

The effects of the auxiliary inlet slots are investigated using SPIV at the same planes as in the base flow in Figure 6.5. The bleed flow through auxiliary inlet has significant effects on the evolution of the strength and scale of the streamwise vortices that form in the base cowl flow as shown in Figure 6.14a-f. While the vorticity distributions in the measurement planes upstream of the slots in Figure 6.5a-c and Figure 6.14a-c are similar, their evolution downstream of the slots is different. The additional momentum flux and concomitant vorticity effected by the flow through the slots along the upper surface alters the trajectory of the center vortex pair by displacing them farther away from the top surface compared to the base flow. The additional momentum flux near the surface corners of the cowl alters the vorticity distributions within the cores of these vortices which rotates through the measurement planes as it is advected away from the corner towards the bulk flow in Figure 6.14d-f. Furthermore, the bleed flow effects also lead to a clear reduction in the turbulence intensity within and around the cores of the streamwise vortices as shown by the distributions of TKE in upstream and downstream of the slots, in Figure 6.5g-l. Similar to the base flow, TKE spreads about the cores and diminishes as the flow moves downstream.

$$\Gamma_1(\mathbf{x}) = \frac{1}{S} \int_{\mathbf{x}' \in S} \sin \alpha \, d\mathbf{x}' \quad (6.1)$$

$$\Gamma_2(\mathbf{x}) = \frac{1}{S} \int_{\mathbf{x}' \in S} \sin \beta \, d\mathbf{x}' \quad (6.2)$$

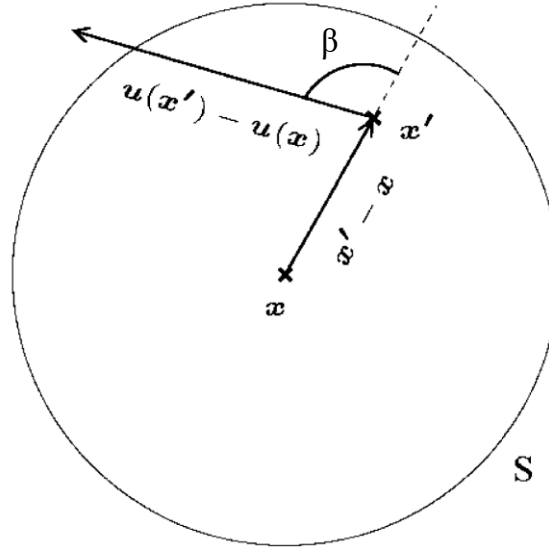


**Figure 6.15 Definition of  $\beta$  for  $\Gamma_2$  in Equation 6.2 [81].**

The effect of the bleed auxiliary inlets on the center and extent of the cowl lip vortices is quantified using vortex scalar functions  $\Gamma_1$  and  $\Gamma_2$ , respectively [81-83], where the extent is defined as the domain of the vortex. The  $\Gamma_1$  and  $\Gamma_2$  dimensionless scalars are computed using Equations 6.1 and 6.2, respectively, where  $S$  is a circle with center  $x$  and a chosen radius  $R$ , which is an adjustable parameter. For every point within that circle of radius  $R$  centered at point  $x$ , the sine an angle is integrated and divided by the area of  $S$ . The angle used in  $\Gamma_1$ ,  $\alpha$ , is defined as the angle between the vector pointing from  $x$  to  $x'$  and the velocity vector at  $x'$ ,  $u(x')$ . In the angle  $\beta$ , the absolute velocity vector  $u(x')$  is replaced with a velocity relative to that at  $x$ , or  $u(x') - u(x)$ . An illustration of this concept is shown in Figure 6.15. Both scalars vary from -1 to 1, and the peak values of both criteria is reached at the vortex center.

	$x_{wc} = \frac{\sum_{i=1}^N x_i P_i}{\sum_{i=1}^N P_i}$	(6.3)
--	--	-------

The  $\Gamma_1$  and  $\Gamma_2$  criteria are computed for every point in the PIV field, such that regions without vortices have low  $\Gamma_1$  and  $\Gamma_2$  magnitudes, while regions within vortices have higher values. To identify the extent of each vortex, the criteria are thresholded by  $|\Gamma_1| > 0.75$  and  $|\Gamma_2| > 0.75$ . When these criteria are satisfied at a given point in the measurement plane, this point is considered part the vortex domain. While the choice of this threshold affects the defined absolute vortex domain size, the trends used for analysis remain the same. The center of the vortex is found by finding the  $\Gamma_1$ -weighted centroid of the previously defined extent, where a weighted centroid is defined in Equation 6.3 for  $N$  points that each have a location  $x_i$  and a property  $P_i$ . This method was chosen to reduce possible noise associated with instantaneous PIV measurements. The computed centers and extents of the vortices shown in Figure 6.5 and Figure 6.14 are shown in Figure 6.16 a-f and g-l, respectively.

In connection with the discussion of Figure 6.5 and Figure 6.14, Figure 6.16 shows that the slots effect a change in trajectory of both the center vortices and the corner vortex. In addition, the vortex extents in the case with auxiliary inlet slots (Figure 6.16g-l) are smaller for both the center and corner vortices, in particular starting in the fourth plane  $x/D = -4.43$  (Figure 6.16d,j), which is just downstream of the first auxiliary inlet slot (cf. Figure 6.4). The smaller vortex cores in the presence of the bleed flow effects overall lower losses, as a larger ratio of the inlet flow is not in the vortex cores and has a higher streamwise ( $x$ -direction) momentum. The difference is most noticeable in the most downstream plane after all three slots, in Figure 6.16 f and l.

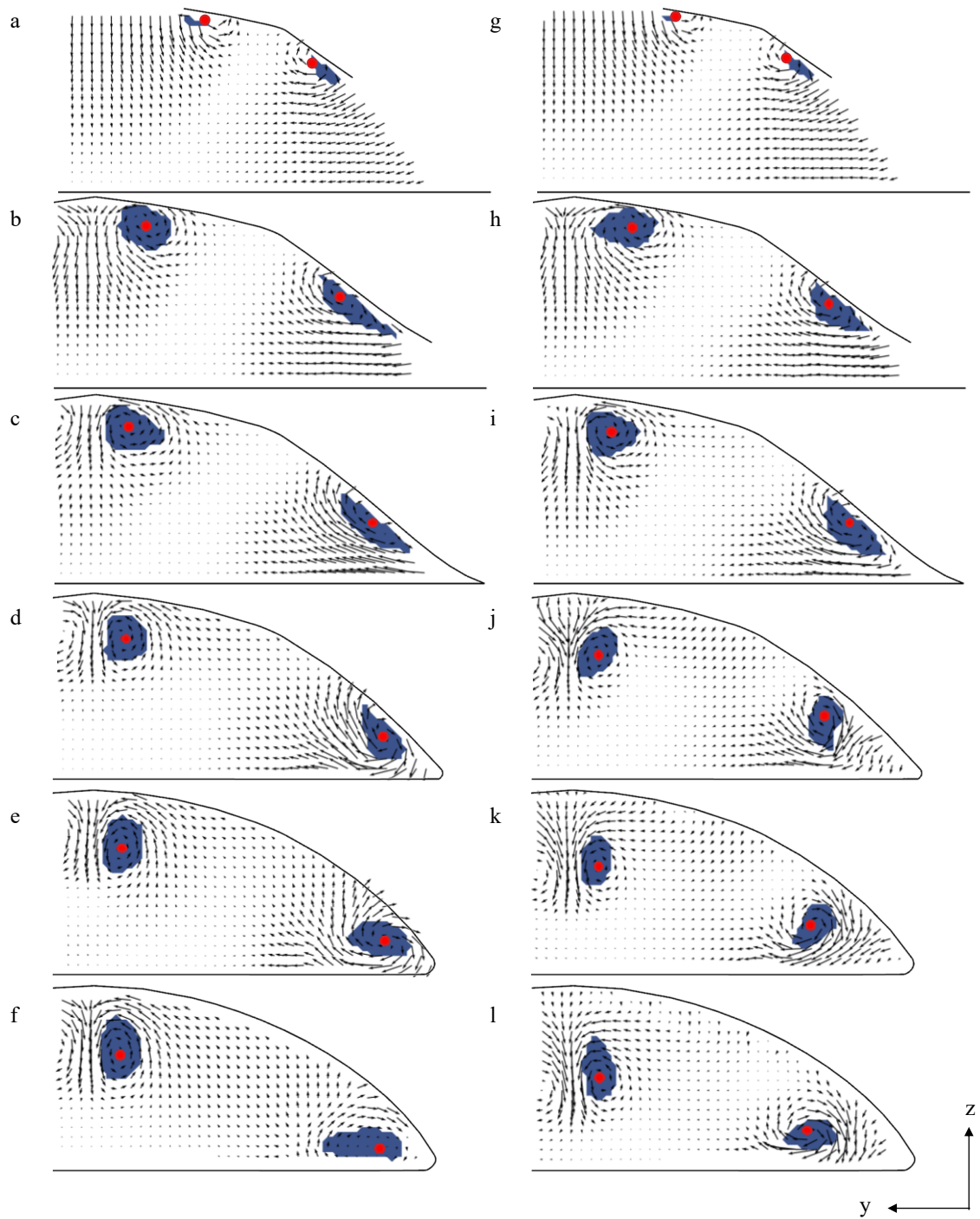


**Figure 6.16** The extent of the vortex cores as defined by Equation 6.2 marked by blue shading and the vortex centers marked by red dots in the flows through the base cowl (a-f, cf. Figure 6.5) and the cowl with the auxiliary bleed inlets (g-l, cf. Figure 6.14), at  $x/D = -4.89$  (a, g),  $-4.7$  (b, h),  $-4.58$  (c, i),  $-4.43$  (d, j),  $-4.28$  (e, k),  $-4.12$  (f, l).

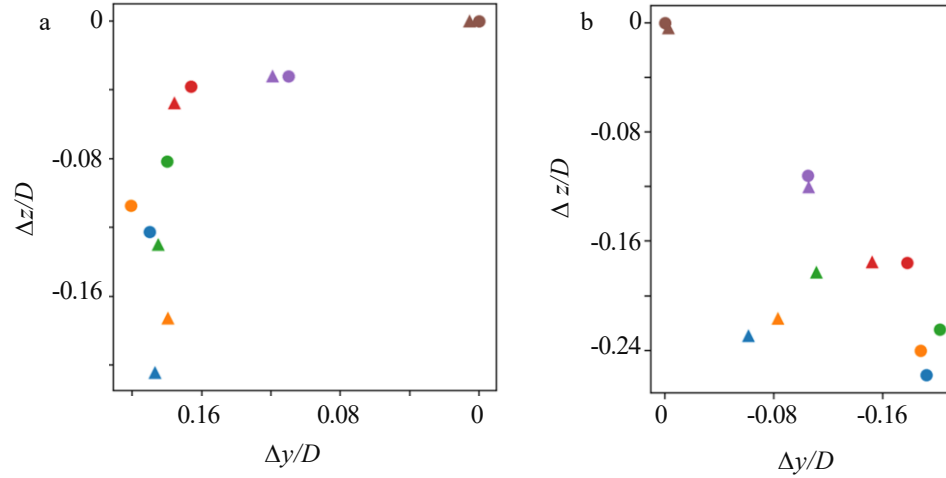


**Figure 6.17** The change in the  $y$  and  $z$  positions of the centers of the vortex cores relative to the vortex position in the base flow plane at  $x/D = -4.8$  (●), and scaled by  $D$ , for center vortex pair (a) and the corner vortices (b) for base (●) and auxiliary inlet (▲) at  $x/D = -4.89, -4.7, -4.58, -4.43, -4.28, -4.12$ .

The trajectories of the vortex centers computed using the  $\Gamma_1$  criterion (cf. red dots in Figure 6.16) are shown in Figure 6.17, with their position being relative to the base flow vortex position in the plane  $x/D = -4.8$  (notice the position of this reference vortex is at (0,0)), and this relative position being scaled by the AIP diameter  $D$ . These data highlight how the positions of the center (Figure 6.17a) and corner (Figure 6.17b) vortices are similar between the base and auxiliary inlet cowls for the first three planes ( $x/D = -4.89, -4.7, -4.58$ ), which are all upstream of the auxiliary inlet slots. As can be seen in Figure 6.16, the center vortex is engendered on the serrated cowl lip and follows the lip towards the centerline as the edges of the serrated inlet converge at the center plane of the cowl (cf. Figure 6.4). The base and controlled vortices are essentially in the same position through plane  $x/D = -4.58$  (Figure 6.16 d and j) where it becomes apparent that in the presence of the auxiliary inlet the vortex is moving away from the wall at a greater rate than that of the base flow. The disparity is the greatest in the plane  $x/D = -4.12$  (Figure 6.16 f and l), where

there the vortices in the base cowl flow and in the presence of the bleed are offset by about  $0.1 \cdot D$ .

While the effect of the bleed flow on the center vortex pair is the increased  $z$ -direction displacement relative to corresponding vortices in the base flow, there is a significant change in the position of the corner vortex past the measurement plane  $x/D = -4.58$ . While the corner vortex in the base flow resides within the corner (bottom right) along the cowl as is evidenced by the corner vortex position in the last three planes indicated in Figure 6.17b, in the presence of the bleed, the vortex deviates from the base flow trajectory by taking a turn at  $x/D = -4.43$ . At the most downstream PIV plane  $x/D = -4.12$ , it becomes displaced by greater than  $0.1 \cdot D$  in the  $y$  direction relative to the center of the corner vortex in the base flow.

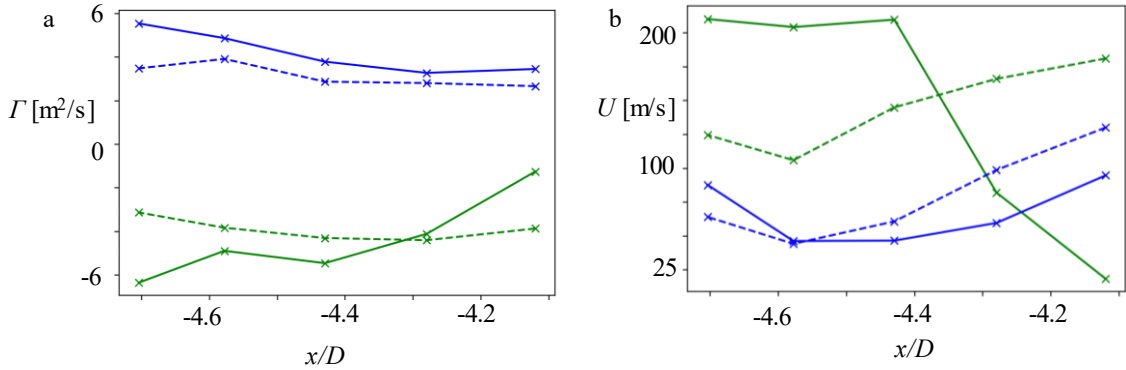


**Figure 6.18** The circulation  $\Gamma$  of the streamwise vortices (a) and the corresponding streamwise velocity  $U$  through their cores as defined in Figure 6.16 (b) for the **center** and **corner** vortices in the base cowl (solid lines) and the cowl with the auxiliary bleed inlet (dashed lines).

The streamwise variation of the circulation  $\Gamma$ , a measure of the vortex strength, is calculated with Equation 6.4 about the vortex cores in Figure 6.16 in the absence and presence of the bleed through their cross sections (Figure 6.18a). In addition, the

streamwise component ( $x$ -direction) of velocity through the vortex cores in Figure 6.16 is computed and shown in Figure 6.18b (Equation 6.4).

$$\Gamma = \iint_S \omega \, dS \quad 6.4$$

The streamwise variation of the circulation  $\Gamma$  of the corner and center vortices ( $\Gamma > 0$ , is counterclockwise) is shown in Figure 6.18a. These data show that the circulation of the streamwise center vortices diminishes nearly monotonically and that in the presence of bleed leads to a reduction in  $\Gamma$  arguably due to the reduction in the flow rate through the inlet. The respective circulations of the corner and center vortices in the absence and presence of bleed are similar in magnitude except that at  $x/D > -4.3$  the circulation magnitude of the corner vortex in the absence of bleed decreases below the level of the circulation in the presence of bleed. This could be due to unsteadiness in the vortex in the base flow, as compared to a steadier vortex in the corner vortex of the actuated flow where the vorticity remains more concentrated on the average.

The variation of streamwise velocity  $U$  through the vortex cores in Figure 6.18b shows that while the trend of  $U$  in the center vortices is nearly unchanged in the presence of bleed (a reduction through  $x/D = -4.58$  is followed by monotonic increase), there is a significant reduction in  $U$  in the corner vortex. However, for  $x/D \approx -4.43$ ,  $U$  of the base flow decreases abruptly where the vortex that forms on the other edge of the serrated cowl inlet merges with the corner vortex as shown in Figure 6.3a. In fact,  $U$  in this vortex continues to drop through  $x/D = -4.12$ . In contrast, in the presence of bleed,  $U$  of the corner vortex is initially lower than base flow, partially because of flow bypass through the bleed



ports, but  $U$  increases monotonically and at a similar rate as the increase in the center vortex.

Instantaneous PIV measurements are exploited to investigate the time variation in the position of the vortex centers, for the base cowl and auxiliary inlet cowl (Figure 6.16b-f and g-l). The  $I_2$  and  $I_1$  criteria discussed in connection with Figure 6.16 are used to determine the distributions of the vortex centers using each instantaneous velocity field out of 6,000 realizations. These distributions are used to form a 2D probability density function (PDF), where the integral of the two-dimensional distribution equals 1, like a conventional one-dimensional PDF. A method called Highest Density Region, outlined by Hyndman [84], is used to draw a boundary which describes the region of 75% of the realized positions. These regions which statistically represent 75% of the realized vortex positions are plotted in Figure 6.19 for planes  $x/D = -4.7, -4.58, -4.43, -4.28$ , and  $-4.12$  in the absence and presence of bleed, in addition to the statistical mode (the most probable point), marked by solid circles.

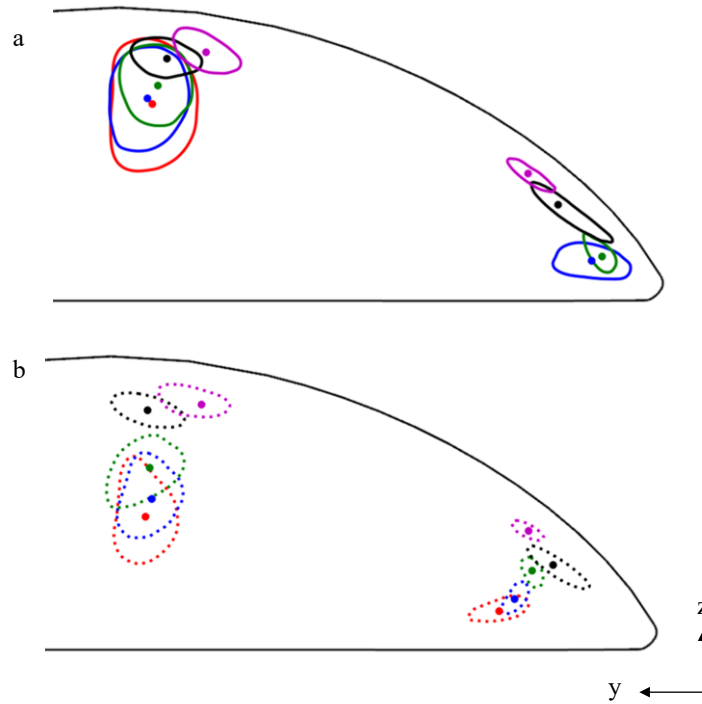


**Figure 6.19 Highest density regions [84] representing 75% of the distribution of the vortex positions in the base (a) and auxiliary inlet cowl (b) at  $x/D = -4.7, -4.58, -4.43, -4.28, -4.12$ , where the most probable point (mode) is marked with a solid circle.**

In the planes before the first bleed slot ( $x/D = -4.7, -4.58$ ), the distributions of vortex positions in the base (Figure 6.19a) and controlled (Figure 6.19b) are quite similar. As they progress downstream, they begin to diverge, which highlights the effect of the slots on the auxiliary inlet cowl vortices. The corner vortex moves away from the corner, and the central vortex is displaced further away from the top wall where it was engendered. In addition to these effects which can be observed with time-averaged SPIV data, Figure 6.19 shows the relative shape and size of the instantaneous distributions of vortex positions as they evolve through the planes. In the corner, the base flow distribution of vortex locations produces an oblong shape, which aligns with the cowl lip to which the vortex is fixed in the first two upstream planes ( $x/D = -4.7, -4.58$ ). As it progresses downstream, at first the

distribution tightens, indicating less unsteadiness, but later increases again (blue contour in corner of Figure 6.19a). The vortex distributions associated with the auxiliary inlet however maintain a small-sized distribution, indicating not only lower absolute unsteadiness through all PIV planes, but also streamwise increase as was seen in the base flow. This effect is also observed with the central vortex. At first, the vortex position is fairly steady when it is locked to the cowl lip, but when it starts to separate from the wall, the base flow vortex position varies widely, with unsteadiness further increasing with each PIV plane, as indicated by the size of the areas enclosed by the HDR contour lines. The central vortices are rendered much steadier in the auxiliary inlet cowl, which is indicated by the smaller-area regions (dashed contours), and has the greatest difference to the base flow in the most downstream planes (blue and red contours).

### 6.3.2 Bleed Effect within the Diffuser and at the AIP

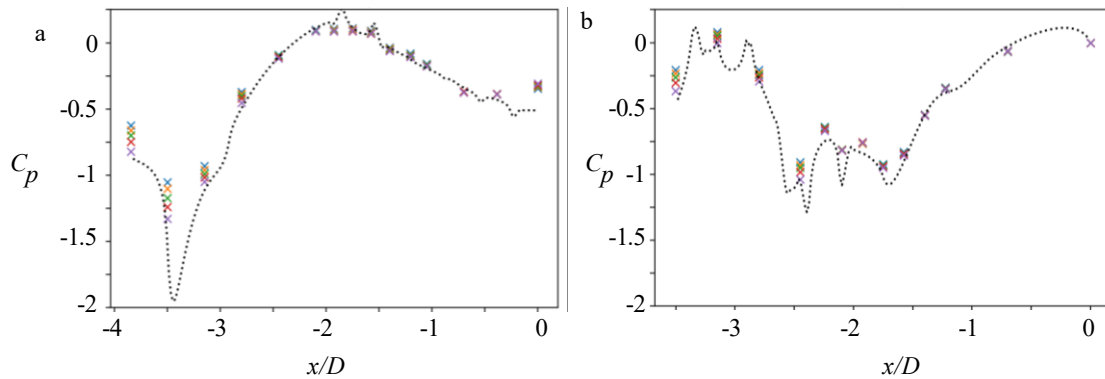


**Figure 6.20** Streamwise distributions of the centerline pressure coefficient  $C_p$  along the lower (a) and upper (b) surfaces of the diffuser in the presence of bleed through the cowl's surface measured at  $M_{AIP} = 0.3$  (×),  $0.35$  (×),  $0.4$  (×),  $0.45$  (×), and  $0.5$  (×). The experimental measurements are compared with numerical simulations for  $M_{AIP} = 0.5$  (dashed line) (Lakebrink and Mani [79]).

The global effect of the cowl bleed is assessed using distributions of the pressure coefficient along the centerlines ( $y = 0$ ) of the diffuser's lower and upper surfaces (Figure 6.20a and b, respectively similar to Figure 6.6 for the base flow) for  $0.3 < M_{AIP} < 0.5$ . As in Figure 6.6, the pressure coefficient traces assessed from the numerical simulations of Lakebrink and Mani [79] for  $M_{AIP} = 0.5$  are also included. Similar to the base flow, the data in Figure 6.6 exhibit a good agreement between the simulations and the measurements.

Both the lower and upper surface pressure coefficient distributions in the presence of bleed are similar in shape to the corresponding distributions in the base flow in Figure 6.6. The main difference along the lower surface is in the higher initial flow acceleration, resulting in the lower suction peak along the diffuser throat ( $x/D = -3.5$ ). Although the upper surface central  $C_p$  profile (Figure 6.20b) is also similar in shape to the corresponding base flow profile (Figure 6.6b), there are two domains where the pressure levels deviate. The stagnation region with elevated pressure levels immediately upon the flow entrance into diffuser ( $x/D = -3.5$ ) is lowered in magnitude, indicating enhanced flow acceleration. Conversely, flow acceleration around  $x/D = -2.5$  becomes less pronounced in the controlled flow, preceding the successive flow accelerations and decelerations.

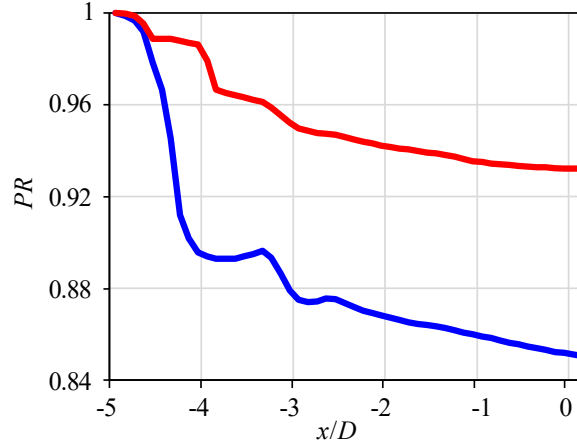


**Figure 6.21 Streamwise variation of average pressure recovery along the diffuser with the cowl inlet in the absence (—) and presence (—) of bleed from the numerical simulations of Lakebrink and Mani [79] at  $M_{AIP} = 0.5$ .**

In addition to the experimental centerline static pressure profiles, numerical face-averaged pressure recovery (Lakebrink and Mani, [79]) is used to help understand the evolution of pressure loss through the diffuser, which is shown in Figure 6.21 in the absence (blue, repeated from Figure 6.8) and presence of bleed (red) at  $M_{AIP} = 0.5$ . As air outside the cowl is drawn in, both cases exhibit about the same loss in recovery up to the first auxiliary inlet slot in the controlled flow ( $x/D \approx -4.6$ ). The following sharp drop in pressure recovery of the base flow becomes fully suppressed by the auxiliary inlet, which maintains almost invariant recovery over the streamwise extent of the bleed slots, until about  $x/D = -4$ . The bleed flow does not only affect the vortex formation and interaction but also adds mass flow rate such that only downstream from the last bleed slot the mass flow rate matches that of the base flow diffuser. The position just after the last bleed slot is marked by a notable drop in recovery immediately after about  $x/D = -4$ . A local drop in recovery of similar scale in the base flow is seen just as the flow turns about the first diffuser bend (cf. Figure 6.8), starting at about  $x/D = -3.3$ . Interestingly, this feature is

suppressed or nonexistent in the controlled flow. For the remaining flow downstream, there is not just an offset in the absolute levels of recovery, but the controlled flow continues to incur less losses of total pressure, as the recovery decreases at a lower rate than in the base flow. Overall, the flow control effects a large increase in recovery, up to 93% from 85% at the AIP ( $x = 0$ ).

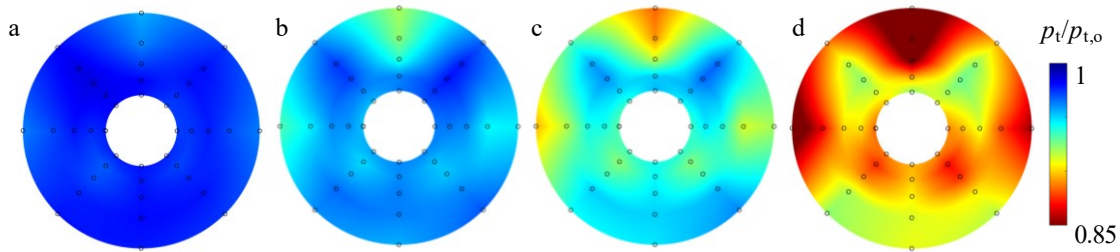


**Figure 6.22 Color raster plots of the time-average total pressure at the AIP in the presence of cowl bleed for  $M_{AIP} = 0.3$  (a),  $0.4$  (b),  $0.5$  (c), and  $0.6$  (d).**

To illustrate how the bleed flow ultimately affects the flow structure at the AIP, Figure 6.22 shows color raster plots of total pressure for  $M_{AIP} = 0.3, 0.4, 0.5$ , and  $0.6$  (Figure 6.22a-d, respectively). First, and arguably the most important difference when comparing the pressure distributions in Figure 6.22a-c to their base flow counterparts in Figure 6.7a,c,g is the higher overall magnitude of the total pressure across the AIP plane. This is a clear indication that the applied flow control bleed has a significant effect on the total pressure losses through the diffuser, as indicated in Figure 6.21. Second, some interesting features appear at  $M_{AIP} = 0.4$  and  $0.5$  (Figure 6.22b and c). These data show concentration of total pressure deficit over the top central surface, much like in the isolated diffuser with the contraction inlet (cf. Chapter 4, [85]). Although there are several isolated regions of reduced total pressure across the AIP plane, they exhibit lower deficit. As a consequence of the reduced losses, the diffuser flow in the presence of the bleed can be

driven up to  $M_{AIP} = 0.6$  and the corresponding pressure distribution is shown in Figure 6.22d. In contrast, in the absence of the bleed, the diffuser could be driven at most at just over  $M_{AIP} = 0.5$  before reaching the blower power limit.

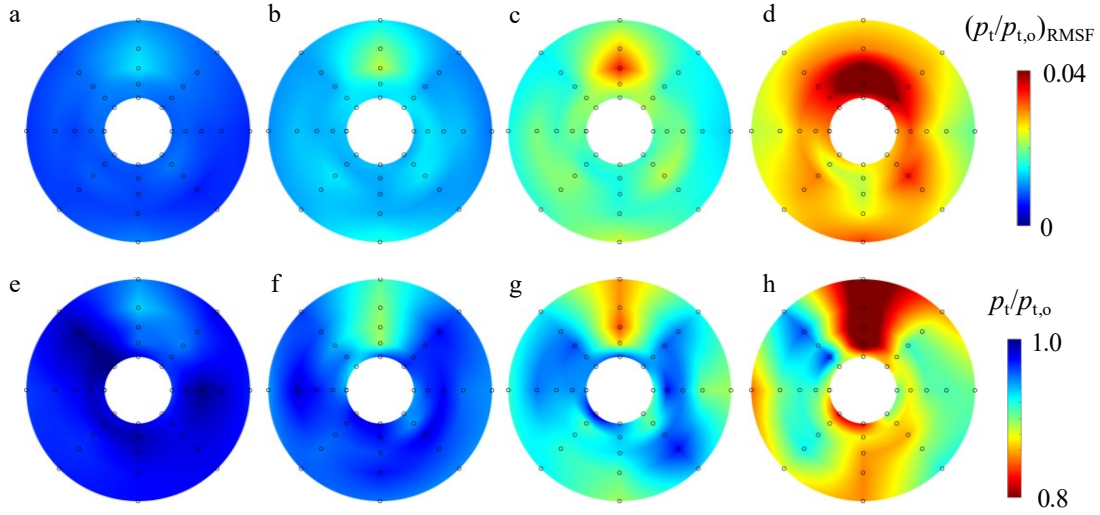


**Figure 6.23** Color raster plots of the RMS fluctuations of the total pressure (a-d) and total pressure distribution associated with peak  $DPCP_{avg}$  distortion (e-h), at  $M_{AIP} = 0.3$  (a,e), 0.4 (b,f), 0.5 (c,g), 0.6 (d,h) in the presence of bleed actuation.

In addition to time-average measures, characteristics of the time-resolved total pressure at the AIP yield AIP distributions of the RMS fluctuations (Figure 6.23a-d) and of the instantaneous total-pressure associated with maximum  $DPCP_{avg}$  (Figure 6.23e-h) for  $M_{AIP} = 0.3, 0.4, 0.5$ , and 0.6. The corresponding distributions at  $M_{AIP} = 0.3, 0.4, 0.5$  for the base flow shown in Figure 6.10. Comparison of the RMS fluctuations of the total pressure at the AIP in the presence (Figure 6.23a-d) and absence (Figure 6.10d-f) of bleed shows two main differences. First, the magnitude of the RMS fluctuations of fluctuation are much lower than in the base flow for all  $M_{AIP}$ , indicating lower unsteadiness of the streamwise vortices in the flow. This enhanced stability of the vortex cores may be connected with the lower TKE in their cores as they are formed at the inlet (Figure 6.14).

Secondly, the topology of the distribution of the total pressure is different in the presence of bleed. These data show a distinct peak of RMS fluctuations in the top center of the AIP, which is reminiscent of the distribution of the base of the isolated diffuser in the absence of the cowl (cf., Figure 4.27, Chapter 4). This peak could be associated with the formation of a pair of counter-rotating streamwise vortices, which form along the separation at the second turn.

The differences between the spectral content of the total pressure fluctuations at the AIP are compared in the absence and presence of the bleed using color raster bar plots of power spectral density as shown in Figure 6.24 (similar to Figure 6.11). These data show that in the presence of bleed there is a spectral peak at about 90 Hz in the spectra of all the AIP sensors which is attributed to noise from the tunnel blower. It is noted that this spectral component is not detected in the absence of bleed because it is masked by the higher pressure fluctuations. In agreement with the discussion in connection with Figure 6.23, the spectral data in Figure 6.24 show that the power in the fluctuations is reduced significantly over the entire AIP plane and at almost all frequencies. Certain ports stand out as having an elevated fluctuation level, the highest of which is port number (1,3), which is marked with a rectangle in Figure 6.24a,b.



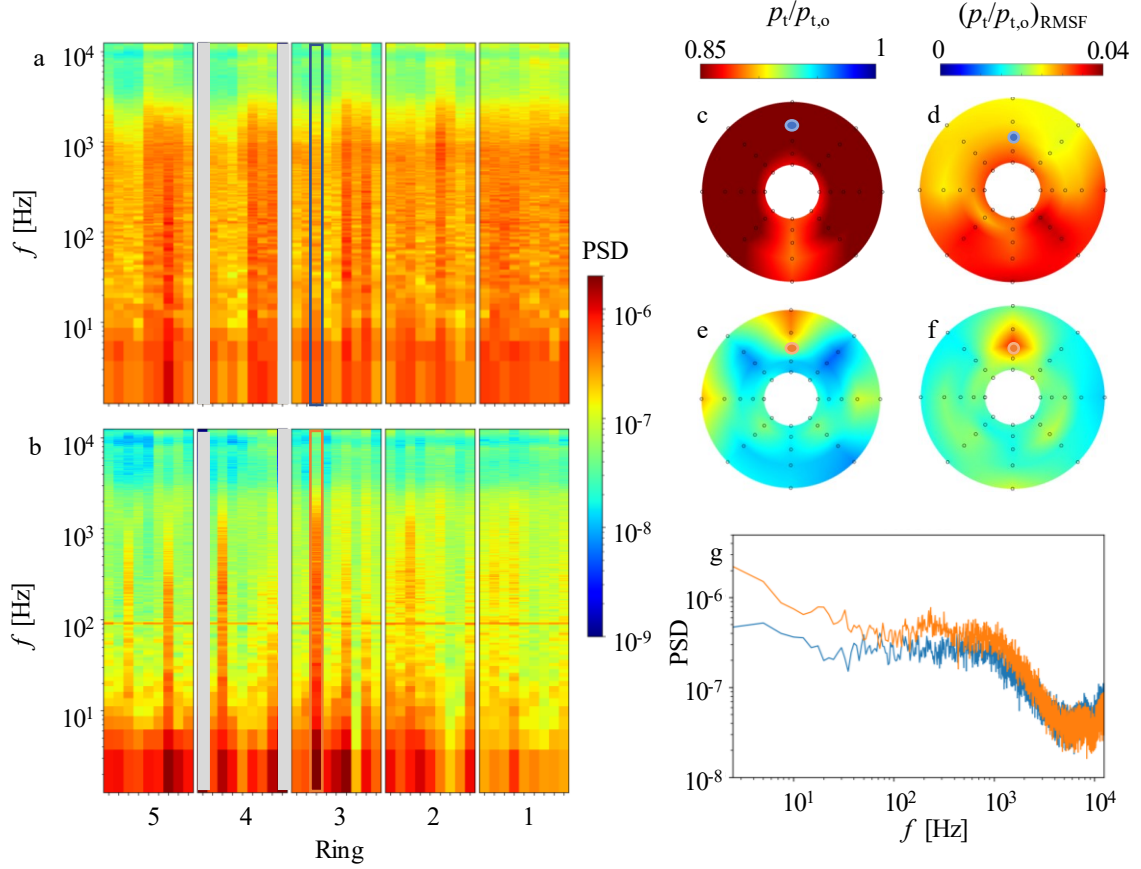


**Figure 6.24** Vertical color raster bars of spectral magnitudes (up to 10 kHz) of the total pressure measured by each of the AIP sensors in each of the circumferential rings as shown schematically in Figure 6.11a at  $M_{\text{AIP}} = 0.5$ . The bars are grouped by ring number and the data for each sensor are arranged in CW order (cf. Figure 6.11a). The bars shaded in gray represent missing data. The data in the absence and presence of bleed are shown in (a) and (b), respectively. Also shown are corresponding color raster plots of distributions of the time-averaged total pressure (c,e) and total pressure RMS fluctuations (d,f) at the AIP, and a power spectra for the two previously mentioned cases at the port marked in the spectra bars (a,b) and AIP plots (c-f).

Figure 6.24 also includes color raster plots of the AIP total pressure distributions in the absence and presence of bleed in Figure 6.24c and e, AIP total pressure RMS fluctuations shown in Figure 6.24 d and f, and corresponding spectra for the single sensor (3,1) shown in Figure 6.24g. The spectra at port (3,1) shows that in the presence of bleed, the spectral power of the pressure fluctuations between 100 Hz and 1000 Hz actually

increases, with a spectral peak occurring at about 250 Hz. It is conjectured that the increased fluctuations result from interaction between a pair of adjacent vortices near the upper surface that would normally be smeared out in the base flow. Other regions of elevated pressure fluctuations are noticeable in rings 1 and 2 (cf. Figure 6.24b), at the upper half of the AIP, which correspond to sensors (1-2, 1), (1-2, 2), and (1-2, 8) shown in the left half of the bar plot in each of the ring groups in Figure 6.24b.

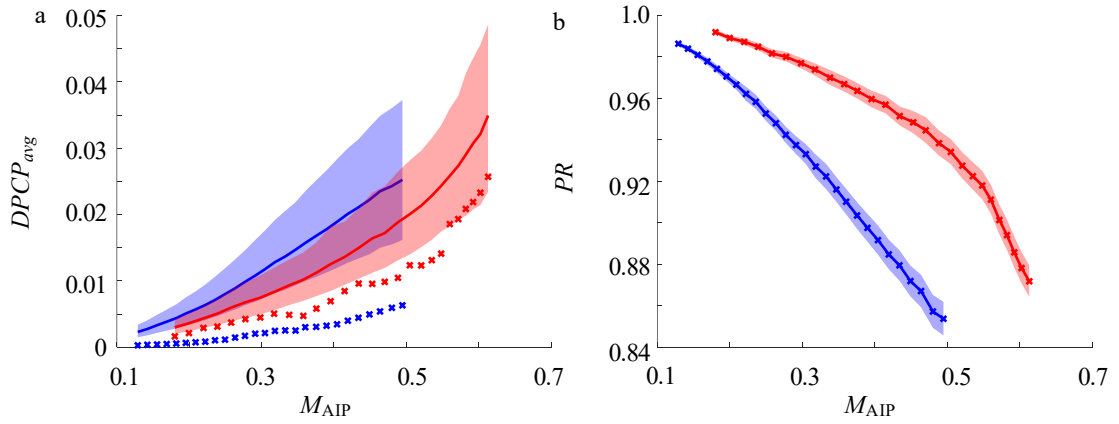


**Figure 6.25 Base cowl and auxiliary inlet bleed  $DPCP_{avg}$  (a) and pressure recovery (b) steady state (×), time-averaged (—), and 95% confidence interval (shaded) for  $M_{AIP} = 0.12 - 0.6$ .**

The variations of instantaneous and time-averaged distortion and recovery over the range  $0.12 \leq M_{AIP} \leq 0.6$  in the absence and presence of bleed are shown in Figure 6.25, where the base data from Figure 6.9 are repeated for reference. As discussed in connection to Figure 6.9, the term steady-state in this figure discussion refers to the parameter being calculated on the time-average total-pressure values, and time-average refers to the time-average of the parameter which is calculated for each instantaneous total-pressure realization. To clarify, steady-state is calculated as  $X(\bar{p})$ , and time-average is calculated

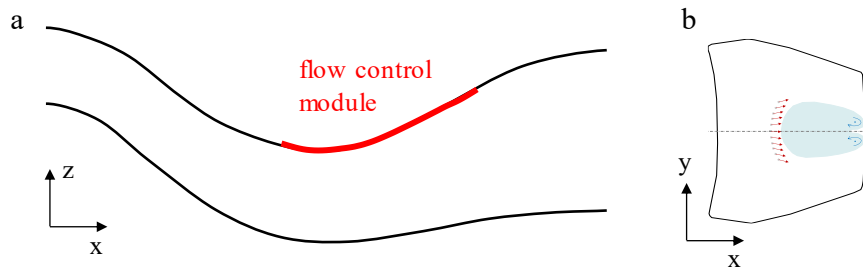
as  $\overline{X(p)}$ , where  $X$  is a calculated parameter,  $p$  is the instantaneous pressures, and the bar notates a time-average.

Figure 6.25a shows the steady-state, time-average, and 95% confidence interval of instantaneous  $DPCP_{avg}$ . Perhaps not surprisingly, the steady-state distortion increases in the controlled flow, arguably due to a combination of the extremely low absolute distortion levels in the base flow and the steadying of the vortices with auxiliary inlet bleed. As already seen in Figure 6.22, the controlled flows form distinct total pressure signatures at the AIP, which lead to the increased distortion levels. Still, the overall levels of the distortion in the presence of bleed remain low in the absolute sense. The main effect of the bleed on distortion is seen as the significant lowering of the instantaneous distribution of distortion. At most Mach numbers, the time-average distortion of the controlled flow about matches the bottom edge of the base flow confidence interval, corresponding to the bottom 2.5% magnitudes in the base flow. It is important to note that the time-average differs from the steady-state because of the non-linearity of the  $DPCP_{avg}$  parameter ( $X(\bar{p}) \neq \overline{X(p)}$ ). At  $M_{AIP} = 0.5$ , the highest end of the base flow range, the top end of the confidence interval is reduced from above 0.35 to about 0.25. In addition, it is noticeable that the range that the confidence interval encapsulates is smaller than that of the base flow for a fixed  $M_{AIP}$ , which is another indicator of increased flow steadiness.

The equivalent total pressure recovery variation with Mach number is shown in Figure 6.25b. In this case, as pressure recovery is a linear parameter ( $X(\bar{p}) = \overline{X(p)}$ ) the steady-state and time-average values coincide. As already assessed in connection with Figure 6.22, there is a notable increase in the total pressure recovery across the full range

of the diffuser Mach numbers. While the base flow recovery decreases in a nearly linear fashion with  $M_{AIP}$ , it is seen that the controlled flow recovery initially decreases at the lower rate with the increase in  $M_{AIP}$ , up to about  $M_{AIP} = 0.54$ . Its slope changes for the highest diffuser flow rates, and it appears that the recovery decreases thereafter at the rate comparable to the base flow. Consequently, the relative improvement in recovery is lowest at the lowest Mach numbers and then progressively increases with the increasing Mach number up to about  $M_{AIP} = 0.54$ . It should be noted that an alternative view of the achieved increase in recovery would be stated in terms of the enabled higher flow rates through the diffuser. The facility is capable achieving  $M_{AIP} = 0.6$  with the bleed slots, compared to the limit of about  $M_{AIP} = 0.5$  in the uncontrolled flow. In addition to steady-state recovery, the confidence interval shows that despite significant variation in the base flow total pressure pattern, as discussed in connection with Figure 6.10 and Figure 6.23, the face-averaged total pressure deficit does not significantly vary in time in both the base and controlled flows.

#### 6.4 Auxiliary Inlet Slots with Active Flow Control



**Figure 6.26** Schematic diagram of the diffuser cross section (a) and the location of the spanwise actuation jet array in the second turn (b, as in Chapter 4).

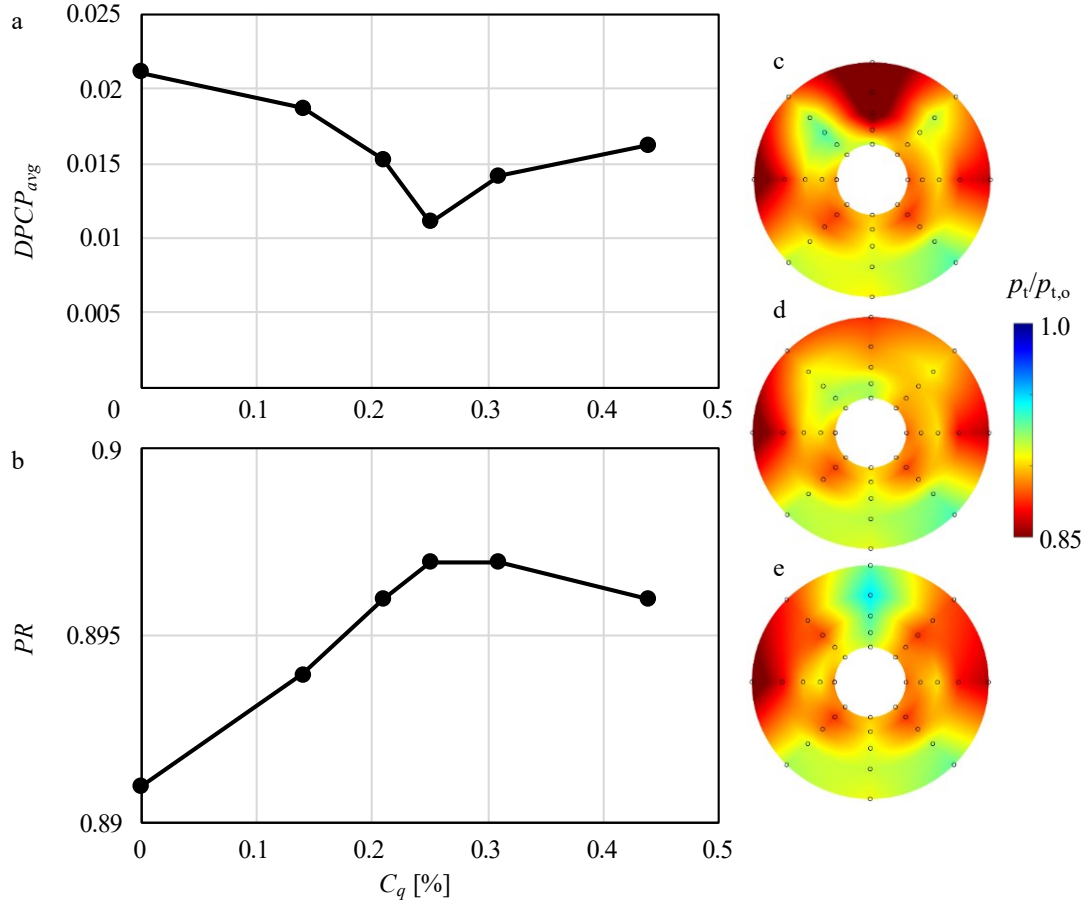


**Figure 6.27** Variation with  $C_q$  of the  $DPCP_{avg}$  (a) and of the pressure recovery  $PR$  (b), and corresponding color raster plots of the total pressure at the AIP for  $C_q = 0$  (c),  $0.25\%$  (d), and  $0.45$  (e) all for  $M_{AIP} = 0.6$ .

As discussed in connection with Figure 6.22, the distributions of the AIP total-pressure in the presence of bleed through the auxiliary inlet ports are reminiscent of those of the diffuser flow in the absence of the cowl (Chapter 4). These distributions were attributed to the formation of pair of counter-rotating vortices that are engendered at a separation region along the second turn. Therefore, the same flow control technique used in Chapter 4 is also added to the present diffuser configuration for further reduction in distortion. A schematic is shown in Figure 6.26, which describes the flow control insert

location (Figure 6.26a) and fluidic oscillating jet array position (Figure 6.26b) which was used in Chapter 4.

To demonstrate effectiveness of the actuation at the second turn in further improvement of the bleed effects diffuser flow of the assisting the auxiliary inlet bleed is demonstrated at the  $M_{AIP} = 0.6$  for which the highest steady state  $DPCP_{avg}$  is measured (cf. Figure 6.25). The effects of the additional second turn actuation are shown in Figure 6.27a,b with increasing  $C_q$ . In addition, color raster plots of the total pressure distribution at the AIP are also shown in Figure 6.27c–e. The data in Figure 6.27a,b show that there appears to be an optimum  $C_q$  for which the distortion  $DPCP_{avg}$  is minimized. In the absence of second turn actuation ( $C_q = 0$ ),  $DPCP_{avg} = 0.022$ . As  $C_q$  is increased,  $DPCP_{avg}$  decreases monotonically to  $DPCP_{avg} = 0.012$  at  $C_q = 0.25\%$ . The corresponding distribution of total pressure at the AIP is shown in Figure 6.27d and compared to the corresponding distribution with bleed alone ( $C_q = 0$ , Figure 6.27c). It is clear that the second-turn actuation successfully suppresses the low pressure domain along the central upper surface (Figure 6.27c). Interestingly, for  $C_q > 0.25\%$ , actuation at the second turn further decreases the top-center pressure deficit but the distortion increases. The total pressure AIP distribution at  $C_q = 0.45\%$  (Figure 6.27e) indicates that higher circumferential (azimuthal) variation. These two competing effects somewhat diminish the overall effect of the actuation. In addition, it is interesting to note that the total pressure recovery has a peak at the same optimal  $C_q = 0.25\%$ . Although the change is within 1%, the recovery increases monotonically up to the optimum  $C_q$ , followed by a weak decrease  $C_q > 0.25\%$ .

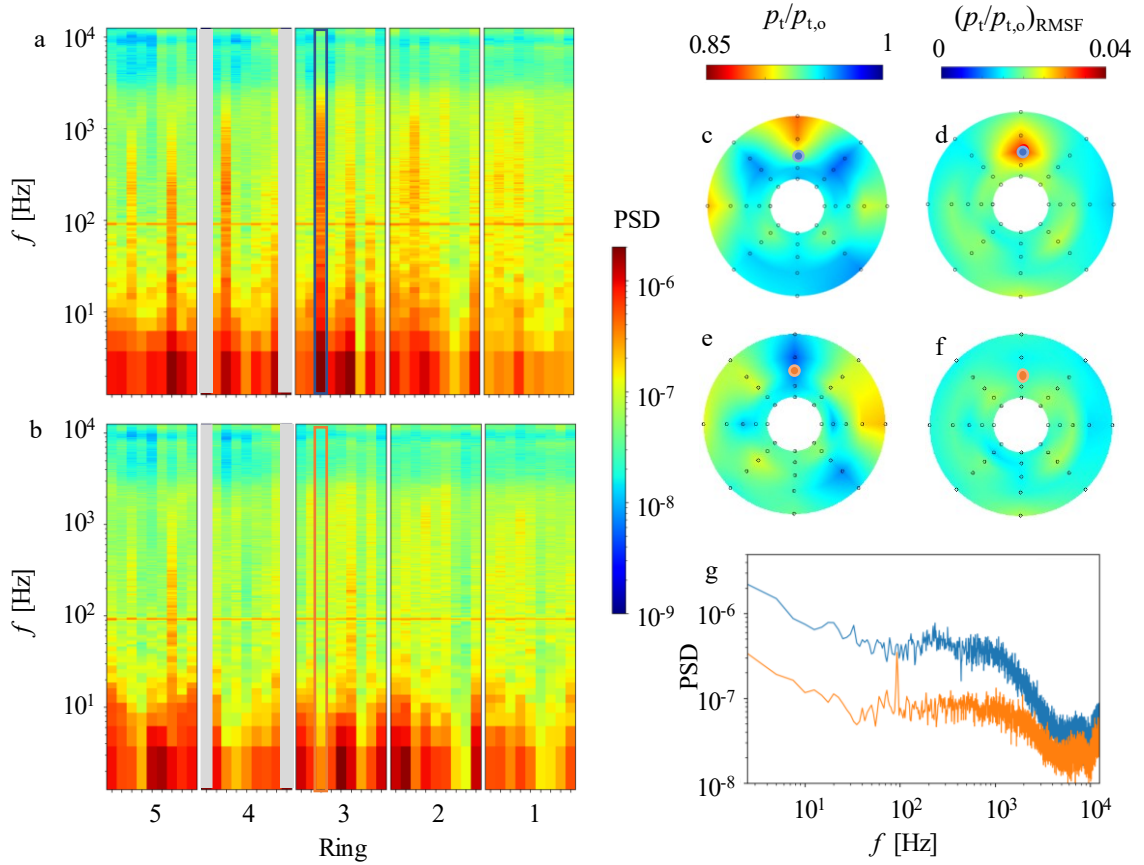


**Figure 6.28** Vertical color raster bars of spectral magnitudes (up to 10 kHz) of the total pressure measured by each of the AIP sensors in each of the circumferential rings (a,b) as shown schematically in Figure 6.11a at  $M_{AIP} = 0.5$ . The bars are grouped by ring number and the data for each sensor are arranged in CW order starting (cf. Figure 6.11a). The bars shaded in gray represent missing data. The data in the absence and presence of bleed are shown in (a) and (b), respectively. Also shown are corresponding color raster plots of the time-averaged total pressure (c,e) and total pressure RMS fluctuations (d,f) at the AIP, and power spectra for the two previously mentioned cases at the port marked in the spectra bars (a,b) and AIP plots (c-f).

Similar to the discussion of Figure 6.24, the dynamic effects of the second turn actuation are investigated at  $M_{AIP} = 0.5$  with AIP total pressure power spectra are shown in Figure 6.28. Figure 6.28a shows the spectra in color bar form, grouped by ring for the auxiliary inlet bleed (repeated from Figure 6.24b for reference) and the equivalent plot for combined flow control (auxiliary inlet and AFC,  $C_q = 0.5\%$ ) in Figure 6.28b. As discussed

in connection to Figure 6.24, the auxiliary inlet bleed greatly reduces the magnitude of fluctuations from that of the base flow, and the use of active flow control along the second turn further reduces these fluctuations. The bleed flow without active flow control (Figure 6.28a) contains some spatial peaks of power spectral density with fluctuation in rings 3-5, and slightly lower but noticeable levels in rings 4 and 5. Most of these noticeable regions have been suppressed when active flow control is used, which is observed in Figure 6.28b.

The top central port (3,1), which was investigated in detail in Figure 6.24, is shown again for closer examination of the effect of active flow control. The top central region of the AIP color raster plot has a much higher total pressure when AFC is used (Figure 6.28e), and also has suppressed the RMS fluctuation peak found in the bleed-only case (Figure 6.28d vs f). The change in color shown in the bars in Figure 6.28a and b is represented directly in a line plot in Figure 6.28g for port (3,1), showing the dramatic reduction in fluctuations in this region, which is almost an order of magnitude for frequencies below 1000 Hz. The relatively high fluctuations in the  $C_q = 0$  case is attributed to unstable vortices in this region. When flow control is used ( $C_q = 0.5\%$ ), this fluctuation is suppressed, which is attributed to the displacement of the pair of vortices to the sidewalls of the diffuser, whose high pressure deficit signatures are visible on the sides of the time-average total pressure color raster plot in Figure 6.28e.



## CHAPTER 7. CONCLUSIONS

The performance of aggressive diffusers designed for advanced supersonic propulsion systems is hampered by internal flow separation domains on the concave surfaces of their internal turns which is coupled with the formation of secondary-flow vortices and consequently in significant flow distortion at the AIP. The presence of streamwise vortical structures within the diffuser's core flow results in significant flow losses, distortion, and angularity. The present investigations demonstrated that the separated flow domains that give rise to the streamwise vortices are susceptible to fluidic actuation which provides an efficient mechanism for controlling the separation and thereby the evolution of the secondary vortices. Targeting the coupling between the separated flow and the streamwise vortices, can significantly weaken these vortices and therefore diminish the inherent flow distortion and losses that are brought about by their presence. The experimental investigations were accompanied by detailed numerical simulations at the Boeing Company that helped shed light on complex three-dimensional flow topology within the diffuser where access for optical velocimetry is limited.

### 7.1 Offset Diffuser (SD-1)

In the early investigations, the coupling between concentration of trapped vorticity and the streamwise vortices was investigated in a milder diffuser in which the base flow was not separated (SD-1). The trapped vorticity was deliberately formed by a recess in the diffuser's inner surface and was controlled using a spanwise array of surface-integrated fluidically-oscillating jets. The local and global characteristics of the diffuser's flow in the

absence and presence of the actuation were investigated up to  $M_{AIP} = 0.7$  using a forty-probe AIP total pressure rake, surface oil-flow visualization and hot-wire anemometry.

The measurements coupled with numerical simulations at the Boeing Company demonstrated that actuation controls the strength, scale, and structural topology of the trapped vorticity within the surface recess, and consequently its interactions with the cross flow. These interactions were leveraged to control separation and thereby diminished the strength of the secondary flow within the diffuser. As a result, diminution of nominally-vertical up- or down-welling of low-momentum fluid from the inner surfaces of the diffuser that is normally induced by the streamwise vortices leads to significant reduction in total-pressure distortion at the AIP. It was also shown that the effectiveness of fluidic actuation increases with AIP Mach number, reaching distortion ( $DPCP_{avg}$ ) reduction of about 80% at  $M_{AIP} = 0.7$  at actuation mass flow rate ratio  $C_q$  below 0.7%. Another important finding of the present investigations is that conforming the spanwise shape of jet array to the structure of upstream boundary of the separated flow in the base flow significantly enhances the receptivity of the flow to actuation. Thus, the actuation could be tuned to optimize its effectiveness by varying the number or spacing of the actuation jets. For example, it was shown that distortion reduction of about 67% in can be attained with half the active jets at almost a third of the actuation flow rate (or reduction of  $C_q$  from 0.7% to about 0.25%). These findings demonstrate the methodology for optimizing the effects of actuation in similar offset diffusers.

## 7.2 Serpentine Diffuser (SD-2)

Following the application of flow control actuation in the mildly offset diffuser, the present investigations were extended to mitigation of flow distortion and losses that are effected by internal separation and the formation of streamwise vortices over the concave inner surfaces of serpentine diffusers. Similar to the offset diffuser, it was demonstrated that the secondary vortices form in the outboard segments of the vorticity layer that bounds the separated flow domain. While the separation induces losses that predominantly affect total pressure recovery, the streamwise vortices advect low-momentum fluid from the boundary layer over the inner surface into the core flow resulting in flow distortion. The present investigations demonstrated that the streamwise vortices that are linked to separation over the diffuser's second turn are the major contributor to distortion at the diffuser's AIP, and therefore the control was applied first at this turn. Similar to SD-1, this was accomplished by using fluidic actuation based on a spanwise array of oscillating jets that is integrated into the diffuser's inner surface just upstream of separation. The actuation jets on each side of the diffuser's center plane were skewed towards the outboard relative to the direction of the core flow so that each segment leads to the formation of an array of streamwise vortices that have opposite sense relative to the sense of the streamwise vortex that is formed at the outboard edge of the separation domain. These control jets alter the distributions and topology of vorticity concentrations within the separated flow, thereby controlling the formation, evolution, and intensification of the streamwise vortices.

The local and global characteristics of the diffuser flow in the absence and presence of actuation were investigated at Mach number up to  $M_{AIP} = 0.64$  using the AIP total pressure rake, surface static pressure ports, and surface oil visualization. These

investigations demonstrated that the array of single-sense streamwise vortices that are engendered by the actuation jets on each side of the centerline significantly modifies the structure and scale of the separated domain, and of the dominant streamwise vortex that forms along each of its spanwise edges in the absence of actuation. As a result of the actuation, the distortion measured at the AIP is reduced by up to 60% at  $M_{AIP} = 0.54$  using actuation mass flow rate ratio as low as  $C_q = 0.54\%$ . It is also shown that the actuation effectiveness is optimized by adapting the spanwise extent of the actuator array to the characteristic width of the separation.

Further insight into dynamics and intensity of coherent motions that are associated with the presence of the streamwise vortical structures in the base and controlled flows is gained by time-resolved measurements of the total pressure distribution at the AIP by a 40-probe rake of dynamic pressure sensors. These measurements (acquired at 25 kHz) revealed that the local deficits of total pressure at the AIP that are effected by the presence of streamwise vortices are unstable and meander laterally within the diffuser's core flow with characteristic frequencies within a band centered at about 1 kHz. Spectral and SPOD analysis of the time-dependent measurements reveal the changes in the coupled spatio-temporal changes in the AIP flow in the absence and presence of actuation. The present measurements show that the actuation has a profound effect on the topology and stability of these vortices and suppresses much of their apparent instability. Along with the time-averaged descriptors that are based on the total pressure distribution at the AIP, there is an attenuation of over 25% of the instantaneous variations in the circumferential distortion.

The changes in the global, three-dimensional structure of the time-averaged diffuser flow that are brought about by the actuation, are elucidated by the numerical

simulations. As noted above, the simulation confirm that in the base flow the secondary counter-rotating vortices roll up from concentrations of streamwise vorticity of opposite sense that form within the outboard spanwise segments of the boundary layer outside the closed separated flow domain in the diffuser's second turn. The transport of low-momentum fluid from the diffuser's inner surface by the vortex pair results in the distortion of the total-pressure distribution. In the presence of actuation, the single-sign streamwise vorticity formed by the skewed off-center actuation jets on each half of the span are of opposite sense relative to the streamwise vortex that is already present in that spanwise half of the boundary layer. These concentrations of streamwise vorticity diminish the separation and alter the rollup of each streamwise vortex leading to significant spanwise displacement and weakening of its core resulting in reduction of the total pressure distortion at the AIP.

### **7.3 Transonic Shock in a Serpentine Diffuser (SD-2)**

Above a critical Mach number  $M_{AIP} = 0.6$ , it is found that a transonic shock forms at the diffuser first turn, which induces increases flow losses and distortion. This investigation focused on the use of flow control to minimize these induced effects. In particular, the flow control methodology focused on mitigation of the shock strength and of the extent of the separation domain induced by the shock and the associated streamwise vortices to minimize total pressure losses and distortion. Actuation is effected using an array of surface-mounted fluidic-oscillating jets that are nominally positioned just downstream from where the shock forms with the objective of controlling the separation domain, and thereby also affect the shock itself. The local and global characteristics of the diffuser flow in the absence and presence of actuation are investigated at Mach numbers

up to  $M_{AIP} = 0.66$ . In addition to the diagnostics that were used in the investigations of the effects of actuation at the second turn, the investigations at the first turn also included pressure-sensitive paint (PSP) and limited measurements of the diffuser flow in three cross stream segments of the center plane were acquired using high-resolution PIV.

When the Mach number is below the limit for first-turn shock formation, the major contribution of the flow over the bottom surface to total pressure distortion arises from the formation the counter-rotating streamwise vortices at the spanwise edges of the separated flow domain at the second turn. A pair of similar counter-rotating streamwise vortices that form at the upstream corners of the diffuser's D-shaped inlet has a much lower impact on distortion at the AIP. However, when the diffuser's flow rate is increased such that a transonic shock is formed at its upstream turn, the effects of these vortices on the AIP pressure distribution is amplified by coupling to a separation domain downstream of the shock. PSP measurements show that the shock initially forms close to the diffuser's spanwise corners and spreads towards its center plane and its strength decreases monotonically towards the centerline. Therefore, the separation induced by the shock is concentrated off-center at each spanwise edge and leads to intensification of the corner vortices and of their effects on the total pressure deficit and distortion at the AIP that is combined with an increase in the total pressure loss once the transonic shock is formed.

The effects of the actuation on the structure of the shock is reflected in the surface pressure distributions downstream of the shock in the base flow. The surface pressure maps indicate the formation of a second shock front downstream of the shock in the base flow which indicates the formation of a lambda-shock with locally decelerated flow between the two branches. More importantly, flow control reattaches the central flow over

the diffuser first turn, much like the base flow in the absence of transonic shock. As a result of the actuation and attachment of the separated flow, the first-turn streamwise vortices become displaced farther apart across the span which significantly diminishes their spanwise interactions. As a result, their effects of upwelling low-momentum fluid from the wall layer diminishes and the total pressure distortion at the AIP is reduced by about 30% in the controlled flow. In addition, there is a small but consistent increase in the total pressure recovery of about 1%. Because the actuation can offset most of the first-turn sources of AIP distortion at elevated diffuser flow rates, the diffuser can be operated beyond the current shock limits

#### **7.4 Serpentine Diffuser with Cowl Inlet**

Up to this point, the flow in the serpentine diffuser was investigated in an “isolated” diffuser in which the inlet flow is nearly-uniform with exceedingly thin boundary layers on the inner surfaces. These investigations were extended to include a typical cowl inlet which introduces a system of strong streamwise vortices that complicate the flow within the diffuser and contributes significantly to pressure losses. It is shown that the inlet cowl leads to the formation of four streamwise vortices. One vortex is formed at each corner of the cowl with the inlet ground plane and evolve along the diffuser’s spanwise corners to the AIP. In addition, a pair of counter-rotating vortices is formed over the center of the cowl and continues to grow and interact with the corner vortices through the AIP. The present results show that the cowl vortex system is a major source of losses in total pressure resulting in about a 15% loss in the overall diffuser pressure recovery at the AIP. It is noteworthy that despite the formation of the strong vortices, their evolution through the

diffuser leads to surprisingly low time-averaged circumferential distortion which is attributed to strong unsteadiness and mixing.

The evolution of the vortices within the cowl is deliberately disrupted by enabling autonomous injection of ambient bleed air by exploiting the pressure difference across the cowl surface between the outer and inner flows. Surface jets of ambient air are formed at several successive spanwise slots in the cowl's surface. This autonomous bleed flow introduces a layer of small-scale vorticity on the cowl's inner surface and the bleed momentum alters the trajectories the central vortex pair by deflecting them towards the cowl's centerline. The presence of the slots significantly weakens the formation of the vortices at the entrance. As a result, the actuation effects a large increase in recovery, up to 93% from 85% which could enable higher thrust for a given engine power. Furthermore, the autonomous bleed lowers the peak circumferential distortion  $DP_{CP_{avg}}$  by about 35% across the full range of overall flow rates that is accompanied by a somewhat increased level of time-averaged distortion indicating that the vortex system through the diffuser is more stable. In fact in the presence of actuation, the pattern of total pressure distribution at the AIP is reminiscent of corresponding distributions in the absence of the cowl, indicating that the effects of the streamwise vortices may be further mitigated by fluidic actuation similar to the flow in the isolated diffuser.

Therefore, the final step of the current study assessed the effects of a dual flow control approach where the vortex system formed by the cowl was affected by autonomous bleed while the rise of the losses in total pressure past the second turn of the diffuser are controlled by an array of fluidic oscillating jets. It is shown that the autonomous bleed alone results in the time-averaged distortion  $DP_{CP_{avg}} = 0.022$  at the highest diffuser flow



rate, and the addition of fluidic actuation at the second turn monotonically decreases  $DPCP_{\text{avg}}$  with increasing  $C_q$  down to  $DPCP_{\text{avg}} = 0.012$  at  $C_q = 0.25\%$  with a corresponding small improvement in recovery.

## 7.5 Closing Remarks

This work has shown that surface-mounted fluidic actuation can effect large-scale changes to flow topology through offset and serpentine diffusers through manipulation of surface-coupled flow features like flow separation and associated vortices which lift off the surface at critical points. When using this flow control technique to target the characteristic streamwise vortices of offset and serpentine diffusers, the effects can be significant, particularly in reduced pressure distortion at the AIP. Additionally, work on flow control optimization has found that fluidic-oscillating jets which are closer to the targeted flow features have a greater effect than those slightly laterally displaced, such that smaller arrays of jets can induce the same effect with less  $C_q$ . When fixing the jet array positions, there is also an optimal  $C_q$ , above which the jets induce increased flow losses.

Future investigations should extend the present studies by including the effects of cross wind on the inlet flow into the cowl and specifically on the formation and stability of the streamwise vortices. It is well known that cross flow can lead to internal flow separation within inlets of engines that are mounted externally on aircraft wings, and it stands to reason that cross flow on the inlets of embedded propulsion systems could potentially be even more susceptible to such adverse effects. An important question is what method of flow control should be selected for mitigation of internal separation, and specifically what would be the effectiveness of the autonomous bleed across the surface of

the cowl. It is anticipated that the actuation will have to overcome asymmetry of the cowl lip vortices (of their position and/or strength), and therefore regulation of the bleed across the cowl will be paramount. Exploring active control techniques including sensitivity analysis of the flow within the diffuser to the inlet flow conditions would be an important contribution.

## APPENDIX A: PRESSURE SENSITIVE PAINT

### A.1 Background

Pressure sensitive paint (PSP) measurements, based on molecular photoluminescence [60], are conducted over the flow control module installed in the second turn of the diffuser yielding spatial distribution of the static pressure over the flow control insert (capturing the central separation domain and the outboard spanwise attached domain). In this experimental technique that was developed in the 1980s and 90s (Peterson and Fitzgerald [61], Kavandi et al. [62]) and later refined by Liu and Campbell [60], and Bell [63], the illuminated paint absorbs and emits light proportional to oxygen or thermal quenching at the surface. The thermal bias is typically compensated for through a second component of the paint that is only sensitive to temperature (TSP), where, in principle, both the PSP and TSP components have identical temperature sensitivity such that the paint/surface pressure ratio is related to the PSP and TSP intensity ratios as in Equation A.1 [63, 64], where the subscripts  $P$  and  $T$  refer to the intensities of the PSP and TSP components and subscript  $o$  refers to the tunnel off case. The coefficients  $A$  and  $B$  must be determined experimentally through calibration.

$$\frac{I_{P,o}}{I_P} \cdot \frac{I_T}{I_{T,o}} = A + B \frac{p}{p_o} \quad \text{A.1}$$

## A.2 Hardware

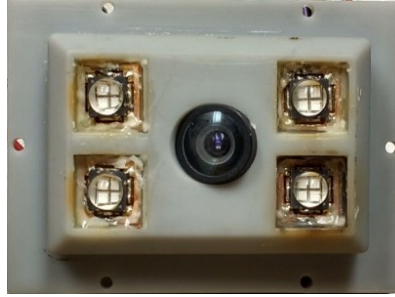


**Figure A.1 Flow-facing side of the integrated stereolithography PSP insert containing a camera and four LEDs.**

A custom-built PSP system was necessary for this facility because commercial systems are meant for external flow applications and are too large to integrate into the diffuser test section. A stereolithography insert was designed that houses a camera and array of UV LEDs for PSP surface illumination. The first iteration (Figure A.1), used in Chapter 4, consists of board-level CMOS camera from The Imaging Source that uses the Aptina MT9P006 CMOS sensor, surrounded by 4 LED Engin LZ4-00UA00 UV LEDs. The second design, used in Chapter 5, utilized a larger camera (FLIR GS3-U3-14S5C-C), that uses a 2/3" Sony ICX285 sensor and 14-bit analog-to-digital converter. The LEDs were chosen for their small size (7mm x 7mm) and high power (10W). The wavelength chosen is 400nm, which is the elimination wavelength required by the paint. The LEDs are air-cooled with impinging jets to the LED, fed from lab compressed air, to hold them at a stable temperature, since their brightness is dependent on temperature. A bandpass or high-pass filter is used to prevent the 400nm illumination light from being captured by the camera and contaminating the emitted light from the paint.

When choosing a camera for PSP, many considerations must be made. If only one camera will be used to capture two separate wavelengths (the present study), the camera must be color, and the quantum efficiency of the RGB filters embedded in the sensor must satisfactorily separate the wavelengths into different colors. Assuming this is achieved, the other most important consideration is how well the sensor can discretize the captured light. Maximum number of electrons per pixel bucket (well depth), a high bit-depth, and a high signal-to-noise ratio help in this aspect. Often there is a tradeoff between camera spatial resolution and the quality of the light discretization. In this application, the latter is more important, as it directly effects the pressure resolution. To achieve the desired field of view, fisheye lenses were used.

The camera and illumination were triggered in LabView to light the PSP surface like a camera flash. The pulsed light was implemented in part to avoid LED overheating. The camera, which communicates over USB, is managed in MATLAB and the images are streamed in real time as an image sequence is acquired. To increase the signal-to-noise ratio, for each pressure measurement, a series of images was taken and then averaged. For each dataset, a tunnel-off case is taken at a known ambient pressure for calculating the ratios in the Equation A.1. In addition, in each dataset a range of mass flow rates were measured to generate the calibration curve. Simultaneous to the image acquisition, steady state static pressure measurements are conducted at an array of points on the surface for correlating static pressure to the pixel ratio value.

Many camera settings must be chosen before acquiring images for PSP. These include gain, exposure time, and shutter settings. In general, gain should be set to zero, because generally it increases noise. For best image quality, the image brightness should

be increased by increasing exposure time. Exposure should be chosen such that the image is as bright as possible but does not saturate pixels. This requires experimentation to determine the best settings. Sometimes there are color-by-color gain or gamma settings, which treat each color differently. For PSP, it is desired that the colors are treated the same, so these individual color settings should be set to the same value. Lastly, there are typically different types of shutters. A rolling shutter records each pixel value in series, rolling across the image very quickly. In these experiments, a global shutter was used instead, which shutters the whole pixel array at once, to avoid time dependency in the images.

Each time a case or series of cases are taken, a tunnel-off case must be taken, in addition to a range of flow rates for the purposes of calibration. Before starting, an exposure time must be chosen, which depends on what pressures will be experienced during the data-taking run. The lower the pressure, the higher the image light intensity. Because it is desired that the highest image intensity is close to saturation but not saturated, a preliminary step is to run the tunnel at the fastest flow rate (lowest pressure) that is planned for the test to experimentally determine the exposure time.

After this exposure time is chosen, no camera settings are changed during the acquisition run, or calibration will not be consistent. Next, the tunnel-off images are taken, along with tunnel-off pressure and temperature. The purpose of the tunnel-off image is that this is the only case where the actual pressure is known for the whole image (ambient pressure), unlike when the tunnel is on, and pressure is only known at the static pressure ports on the surface. In addition, an approximation is made that the measured ambient or surface temperature is uniform across the PSP surface.

Once the tunnel-off case is taken, the tunnel-on cases are taken, in addition to a range of mass flow rates that exceed the lower and upper bounds of the cases intended for measurement, for the purposes of calibration. Simultaneous to every image acquisition is steady-state measurement of the static pressures on the surface that are in the camera field of view.

### **A.3 Postprocessing**

To convert raw PSP images into pressure fields, one must have images corresponding to the tunnel-off case, the cases desired for measurement, and the extra flow rate cases for calibration. The first step is to convert each of the image series into a single image through averaging. Depending on the specifics of the experimental setup, there might be vibrations, resulting in either images within an image series not lining up exactly, or images between cases not lining up. Images can be aligned after the fact using a process called automatic image registration. This is a method of automatically determining the translational, rotational, scale, and/or shear necessary to align the images. If there is vibration within an image series that causes blurring when averaged, use this technique to align all images in the sequence to a target image, which can be chosen as the first image in the series. This will yield images of the same size as the originals. The same procedure can be used between cases to ensure that all images are aligned. After images are aligned and averaged, an optional smoothing step can be performed. This might be necessary, depending on the texture of the PSP surface, which might create undesirable patterns in the pressure contour.

Once a set of aligned images are obtained, the quantity on the left side of Equation 2.1 can be computed. For each average image, produce a new quantity which is the PSP component of the tunnel-off case divided by the PSP component of each tunnel-on case, and multiplied by the corresponding inverse ratio of the TSP image components. This inverse ratio of the TSP components represents the temperature variation between cases and is removed from the pressure signal by multiplying by the inverse, because the PSP paint component has the same temperature sensitivity as the TSP component. In theory, this quantity is linearly proportional to pressure. Now, the calibration curve must be computed so that pressure can be calculated.

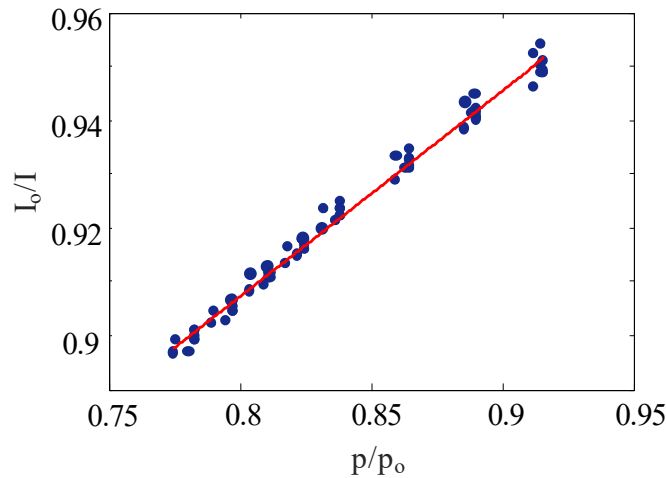


**Figure A.2 PSP calibration curve relating intensity ratio to pressure ratio.**

To compute the calibration curve, one must sample the pixels of the ratio quantity near each pressure port contained in the image that was measured alongside the image acquisition. These pixels are assumed to have the same pressure as measured by the pressure port itself. With each image containing ideally an array of pressure ports, the pressure measurements from the ports can be plotted against the previously mentioned ratio



quantity, with all ports from every flow rate earmarked for calibration on the same plot. A curve can be fit through these points (Figure A.2) to obtain an equation to use for converting the rest of the pixels to absolute pressure (Equation A.1). Ideally, it is found that all pressure ports in the image line up on the same curve, implying that all parts of the image correlate the same way to pressure. This was the case in this study, though it is theoretically possible to apply different calibration curves to different parts of the image. Once this calibration curve is generated from the images earmarked for calibration, the calibration equation can be applied to the images earmarked for measurement, and the fields of pressure are now obtained (Figure A.3).

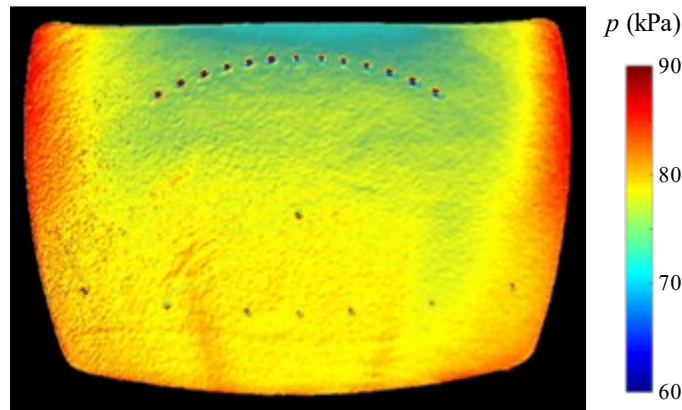


**Figure A.3 Color raster plot of pressure from PSP, showing an inactive jet array on top, and static pressure ports in central and lower parts of domain.**

#### **A.4 Image De-warping**

It is often desirable to map the pressure field onto a known coordinate system, like CAD or CFD for comparison or plotting. A raw image might be quite warped (Figure A.4a) depending on the lens used and is difficult to use in comparisons. This subsection goes over the process of transforming to another coordinate system.

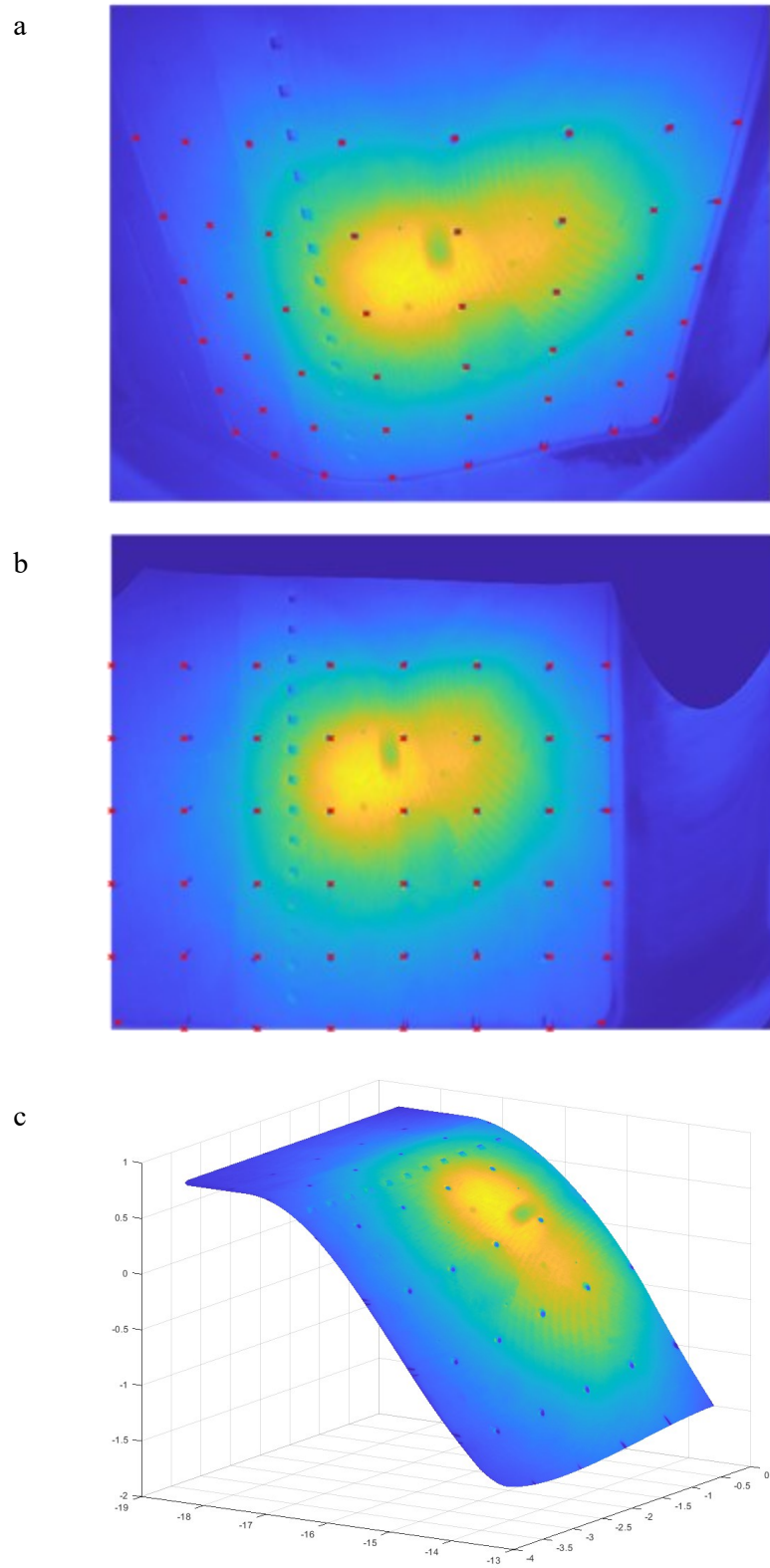


**Figure A.4 Colorized PSP camera image before correction (a), after 2D dewarping (b), and after mapping to 3D (c). Points on surface (●) were used for mapping.**

A given PSP image most likely has many recognizable features in it, including edges of geometries and pressure ports integrated into the PSP surface. If a CAD model exists for these features, in the coordinate system desired to transform the pressure to, it can be used for the transformation. For a set of recognizable features that can be found both in a CAD coordinate system and on the PSP image, a list of this set of features must be generated, which contains the pixel location of each in the PSP image, as well as the 2D or 3D coordinate in CAD. For the present study, an insert was modified to have a regular grid of dimples, shown in the warped (Figure A.4a) and corrected (Figure A.4b) images. Ideally, there are two of the three dimensions in CAD that best describe the view of the camera. To perform the transform, a MATLAB function called *fitgeotrans* is used to generate a coordinate system transform from the set of PSP coordinate and CAD coordinates. Only two CAD dimensions can be provided, because the PSP image is 2D. Once the PSP coordinates are transformed into two of the three CAD coordinates (Figure A.4b), the other coordinate can be mapped, based on knowing that the PSP image lies on a specific surface in CAD. The 3D CAD surface can be extracted and used to interpolate the third dimension from the two used in the original transform (Figure A.4c). This is the method used to produce the Chapter 5 PSP contours.

## REFERENCES

- [1] Wellborn, S., Reichert, B., and Okiishi, T. "An experimental investigation of the flow in a diffusing S-duct," *28th Joint Propulsion Conference and Exhibit*. 1992.
- [2] Tindell, R. H. "Highly compact inlet diffuser technology," *Journal of Propulsion and Power* Vol. 4, No. 6, 1988, pp. 557-563.
- [3] Lee, C. C., and Price, W. A. "Subsonic Diffusers for Highly Survivable Aircraft," *Air Force Wright Aeronautical Laboratories*, 1986.
- [4] DeSalvo, M., Whalen, E., and Glezer, A. "High-Lift Enhancement Using Fluidic Actuation," *48th AIAA Aerospace Sciences Meeting Including the New Horizons Forum and Aerospace Exposition*. American Institute of Aeronautics and Astronautics, 2010.
- [5] Gissen, A. N., Vukasinovic, B., Glezer, A., and Sivaram, G. "Active Shock Control in a Transonic Flow," *43rd Fluid Dynamics Conference*. American Institute of Aeronautics and Astronautics, 2013-3116.
- [6] Zhang, X., Wang, Z., and Gursul, I. "Control of Multiple Vortices over a Double Delta Wing," *47th AIAA Fluid Dynamics Conference*. American Institute of Aeronautics and Astronautics, 2017.
- [7] Gursul, I., and Wang, Z. "Flow Control of Tip/Edge Vortices," *AIAA Journal* Vol. 56, No. 5, 2018, pp. 1731-1749.
- [8] Çelik, A., Çetin, C., and Yavuz, M. M. "Effect of Passive Bleeding on Flow Structure over a Nonslender Delta Wing," *AIAA Journal* Vol. 55, No. 8, 2017, pp. 2555-2565.
- [9] Henne, P. "Low-speed test of translating lip axisymmetric inlets for subsonic transports," 1974.
- [10] Fradenburgh, E. A., and Demarquis, D. W. "Theoretical performance characteristics of sharp-lip inlets at subsonic speeds," 1954.
- [11] Brown, A. C., Nawrocki, H. F., and Paley, P. N. "Subsonic diffusers designed integrally with vortex generators," *Journal of Aircraft* Vol. 5, No. 3, 1968, pp. 221-229.
- [12] Vakili, A., Wu., J., Liver, P., and Bhat, M. "Flow control in a diffusing S-Duct," *Shear Flow Control Conference*. American Institute of Aeronautics and Astronautics, 1985-524.

- [13] Reichert, B. A., and Wendt, B. J. "Improving curved subsonic diffuser performance with vortex generators," *AIAA Journal* Vol. 34, No. 1, 1996, pp. 65-72.
- [14] Anderson, B. H., and Gibb, J. "Vortex-Generator Installation Studies on Steady-State and Dynamic Distortion," *Journal of Aircraft* Vol. 35, No. 4, 1998, pp. 513-520.
- [15] Hamstra, J. W., Miller, D. N., Truax, P. P., Anderson, B. A., and Wendt, B. J. "Active inlet flow control technology demonstration," *The Aeronautical Journal (1968)* Vol. 104, No. 1040, 2000, pp. 473-479.
- [16] Jirasek, A. "Design of Vortex Generator Flow Control in Inlets," *Journal of Aircraft* Vol. 43, No. 6, 2006, pp. 1886-1892.
- [17] Holden, H., and Babinsky, H. "Effect of Microvortex Generators On Separated Normal Shock/ Boundary Layer Interactions," *Journal of Aircraft* Vol. 44, No. 1, 2007, pp. 170-174.
- [18] Yi, J., Kim, C., and Lee, B. J. "Adjoint-Based Design Optimization of Vortex Generator in an S-Shaped Subsonic Inlet," *AIAA Journal* Vol. 50, No. 11, 2012, pp. 2492-2507.
- [19] Tanguy, G., MacManus, D. G., Zachos, P., Gil-Prieto, D., and Garnier, E. "Passive Flow Control Study in an S-Duct Using Stereo Particle Image Velocimetry," *AIAA Journal* Vol. 55, No. 6, 2017, pp. 1862-1877.
- [20] Gil-Prieto, D., Zachos, P., MacManus, D. G., and Tanguy, G. "Convolved Intake Distortion Measurements Using Stereo Particle Image Velocimetry," *34th AIAA Applied Aerodynamics Conference*. American Institute of Aeronautics and Astronautics, 2016-3560.
- [21] Tanguy, G., MacManus, D. G., Garnier, E., and Martin, P. G. "Characteristics of unsteady total pressure distortion for a complex aero-engine intake duct," *Aerospace Science and Technology* Vol. 78, 2018, pp. 297-311.
- [22] Ball, W. H. "Tests of wall suction and blowing in highly offset diffusers," *Journal of Aircraft* Vol. 22, No. 3, 1985, pp. 161-167.
- [23] Scribner, A., Ng, W., and Burdisso, R. "Effectiveness of a Serpentine Inlet Duct Flow Control Technique at Design and Off- Design Simulated Flight Conditions," *Journal of Turbomachinery* Vol. 128, No. 2, 2006, pp. 332-339.
- [24] Anderson, B. H., Miller, D. N., Addington, G. A., and Agrell, J. "Optimal Micro-Jet Flow Control for Compact Air Vehicle Inlets." NASA Glenn Research Center, 2004.

- [25] Gartner, J., and Amitay, M. "Flow Control in a Diffuser at Transonic Conditions," *45th AIAA Fluid Dynamics Conference*. American Institute of Aeronautics and Astronautics, 2015-2484.
- [26] Rabe, A. "Effectiveness of a serpentine inlet duct flow control scheme at design and off- design simulated flight conditions." ProQuest Dissertations Publishing, 2003.
- [27] Harrison, N., Anderson, J., Fleming, J., and Ng, W. "Active Flow Control of a Boundary Layer- Ingesting Serpentine Inlet Diffuser," *Journal of Aircraft* Vol. 50, No. 1, 2013, pp. 262-271.
- [28] Garnier, E. "Flow Control by Pulsed Jet in a Curved S-Duct: A Spectral Analysis," *AIAA Journal* Vol. 53, No. 10, 2015, pp. 2813-2827.
- [29] Souverein, L. J., and Debiève, J.-F. "Effect of air jet vortex generators on a shock wave boundary layer interaction," *Experiments in Fluids* Vol. 49, No. 5, 2010, pp. 1053-1064.
- [30] Narayanaswamy, V., Raja, L. L., and Clemens, N. T. "Control of a Shock/Boundary-Layer Interaction by Using a Pulsed-Plasma Jet Actuator," *AIAA Journal* Vol. 50, No. 1, 2012, pp. 246-249.
- [31] Amitay, M., Pitt, D., and Glezer, A. "Separation control in duct flows," *Journal of Aircraft* Vol. 39, No. 4, 2002, pp. 616-620.
- [32] Mathis, R., Duke, D., Kitsios, V., and Soria, J. "Use of zero-net-mass-flow for separation control in diffusing S-duct," *Experimental Thermal and Fluid Science* Vol. 33, No. 1, 2008, pp. 169-172.
- [33] Owens, L. R., Allan, B. G., and Gorton, S. A. "Boundary-Layer-Ingesting Inlet Flow Control," *Journal of Aircraft* Vol. 45, No. 4, 2008, pp. 1431-1440.
- [34] Anderson, B. H., Mace, J. L., and Mani, M. "Active Fail- Safe Micro- Array Flow Control for Advanced Embedded Propulsion Systems - NASA/TM-2009-215596." Sponsoring Organization: NASA Glenn Research Center, 2009-741.
- [35] Anderson, B., Tinapple, J., and Surber, L. "Optimal Control of Shock Wave Turbulent Boundary Layer Interactions Using Micro-Array Actuation," *3rd AIAA Flow Control Conference*. American Institute of Aeronautics and Astronautics, 2006.
- [36] Godard, G., and Stanislas, M. "Control of a decelerating boundary layer. Part 1: Optimization of passive vortex generators," *Aerospace Science and Technology* Vol. 10, No. 3, 2006, pp. 181-191.
- [37] Anabtawi, A., Blackwelder, R., Lissaman, P., and Liebeck, R. "An experimental investigation of boundary layer ingestion in a diffusing S-duct with and without

- passive flow control," *37th Aerospace Sciences Meeting and Exhibit*. American Institute of Aeronautics and Astronautics, 1999.
- [38] Anderson, B. H., Addington, G. A., Agrell, J., and Miller, D. N. "Optimal Micro-Vane Flow Control for Compact Air Vehicle Inlets - NASA/TM-2004-212936." Sponsoring Organization: NASA Glenn Research Center, 2004.
  - [39] Tournier, S., Paduano, J., and Pagan, D. "Flow Analysis and Control in a Transonic Inlet," *23rd AIAA Applied Aerodynamics Conference*. American Institute of Aeronautics and Astronautics, 2005.
  - [40] Geiselhart, K. A., Daggett, D. L., Kawai, R., and Friedman, D. "Blended Wing Body Systems Studies: Boundary Layer Ingestion Inlets With Active Flow Control - NASA/CR-2003-212670." Sponsoring Organization: NASA Langley Research Center, 2003.
  - [41] Delot, A.-L., Garnier, E., and Pagan, D. "Flow Control in a High-Offset Subsonic Air Intake," *47th AIAA/ASME/SAE/ASEE Joint Propulsion Conference & Exhibit*. American Institute of Aeronautics and Astronautics, 2011.
  - [42] Gissen, A. N., Vukasinovic, B., McMillan, M. L., and Glezer, A. "Distortion Management in a Boundary Layer Ingestion Inlet Diffuser Using Hybrid Flow Control," *Journal of Propulsion and Power* Vol. 30, No. 3, 2014, pp. 834-844.
  - [43] Gartner, J., and Amitay, M. "Effect of boundary layer thickness on secondary structures in a short inlet curved duct," *International Journal of Heat and Fluid Flow* Vol. 50, 2014, pp. 467-478.
  - [44] Burrows, T. J., Vukasinovic, B., Lakebrink, M. T., Mani, M., and Glezer, A. "Control of flow distortion in offset diffusers using trapped vorticity," *International Journal of Heat and Fluid Flow* Vol. 75, 2019, pp. 122-134.
  - [45] G., S. P., and S., S. J. "Flow over a Wing with an Attached Free Vortex," *Studies in Applied Mathematics* Vol. 57, No. 2, 1977, pp. 107-117.
  - [46] Hurley, D., and Lachmann, G. "The use of boundary layer control to establish free streamline flows," *Advances in Aeronautical Sciences* Vol. 2, 1959, pp. 662-708.
  - [47] Cox, J. "The revolutionary Kasper wing," *AIAA Soaring*, 1973.
  - [48] Rossow, V. J. "Lift Enhancement by an Externally Trapped Vortex," *Journal of Aircraft* Vol. 15, No. 9, 1978, pp. 618-625.
  - [49] Ringleb, F. O. "Two-Dimensional Flow With Standing Vortexes in Ducts and Diffusers," *Journal of Basic Engineering* Vol. 82, No. 4, 1960, pp. 921-927.
  - [50] Adkins, R. C. "A Short Diffuser With Low Pressure Loss," *J. Fluids Eng.* Vol. 97, No. 3, 1975, p. 297.

- [51] Heskestad, G. "Remarks on Snow Cornice Theory and Related Experiments With Sink Flows," *Journal of Basic Engineering* Vol. 88, No. 2, 1966, pp. 539-547.
- [52] Adkins, R. C., Matharu, D. S., and Yost, J. O. "The Hybrid Diffuser," *Journal of Engineering for Power* Vol. 103, No. 1, 1981, pp. 229-236.
- [53] Mariotti, A., Buresti, G., and Salvetti, M. V. "Control of the turbulent flow in a plane diffuser through optimized contoured cavities," *European Journal of Mechanics / B Fluids* Vol. 48, 2014, pp. 254-265.
- [54] Fozard, J. W. "The Hawker P1127 vectored thrust fighter program - Lessons learned," *Aircraft Design, Systems and Operations Conference*. 1990.
- [55] Bore, C. "Intakes for Vertical Landing Aircraft," *Practical Intake Aerodynamic Design*. 1993.
- [56] Sóbester, A. "Tradeoffs in Jet Inlet Design: A Historical Perspective," *Journal of Aircraft* Vol. 44, No. 3, 2007, pp. 705-717.
- [57] Hawkins, J. E. "YF-16 Inlet Design and Performance," *Journal of Aircraft* Vol. 13, No. 6, 1976, pp. 436-441.
- [58] Powell, A. G., Welge, H. R., and Trefny, C. J. "Low-speed aerodynamic test of an axisymmetric supersonic inlet with variable cowl slot," *21st Joint Propulsion Conference*. Monterey, CA, 1985.
- [59] Garzon, A. "Use of a Translating Cowl on a SSBJ for Improved Takeoff Performance," *45th AIAA Aerospace Sciences Meeting and Exhibit*. 2007.
- [60] Liu, T., Campbell, B. T., Burns, S. P., and Sullivan, J. P. "Temperature- and Pressure- Sensitive Luminescent Paints in Aerodynamics," *Appl. Mech. Rev.* Vol. 50, No. 4, 1997, p. 227.
- [61] Peterson, J. I., and Fitzgerald, R. V. "New technique of surface flow visualization based on oxygen quenching of fluorescence," *Review of Scientific Instruments* Vol. 51, No. 5, 1980, p. 670.
- [62] Kavandi, J., Callis, J., Gouterman, M., Khalil, G., Wright, D., Green, E., Burns, D., and McLachlan, B. "Luminescent barometry in wind tunnels," *Review of Scientific Instruments* Vol. 61, No. 11, 1990, p. 3340.
- [63] Bell, J. H., Schairer, E. T., Hand, L. A., and Mehta, R. D. "Surface Pressure Measurements Using Luminescent Coatings," *Annual Review of Fluid Mechanics* Vol. 33, No. 1, 2001, pp. 155-206.
- [64] Khalil, G. E., Costin, C., Crafton, J., Jones, G., Grenoble, S., Gouterman, M., Callis, J. B., and Dalton, L. R. "Dual-luminophor pressure-sensitive paint," *Sensors and Actuators B: Chemical* Vol. 97, No. 1, 2004, pp. 13-21.



- [65] Sciacchitano, A., and Scarano, F. "Elimination of PIV light reflections via a temporal high pass filter," *Measurement Science and Technology* Vol. 25, No. 8, 2014, p. 084009.
- [66] Wieneke, B. "PIV uncertainty quantification from correlation statistics," *Measurement Science and Technology* Vol. 26, No. 7, 2015, p. 074002.
- [67] Wilson, B. M., and Smith, B. L. "Uncertainty on PIV mean and fluctuating velocity due to bias and random errors," *Measurement Science and Technology* Vol. 24, No. 3, 2013, p. 035302.
- [68] Lakebrink, M. T., Mani, M., and Winkler, C. "Numerical Investigation of Fluidic Oscillator Flow Control in an S-Duct Diffuser," *55th AIAA Aerospace Sciences Meeting*.
- [69] Cattafesta, L. N., and Sheplak, M. "Actuators for Active Flow Control," *Annual Review of Fluid Mechanics* Vol. 43, No. 1, 2011, pp. 247-272.
- [70] Kearney, J. M. "Aerodynamic control using distributed active bleed." Georgia Institute of Technology, 2015.
- [71] Gissen, A., Vukasinovic, B., and Glezer, A. "Dynamics of flow control in an emulated boundary layer- ingesting offset diffuser," *Exp Fluids* Vol. 55, No. 8, 2014, pp. 1-19.
- [72] Moffatt, H. K., and Tsinober, A. "Helicity in Laminar and Turbulent Flow," *Annual Review of Fluid Mechanics* Vol. 24, No. 1, 1992, pp. 281-312.
- [73] Chong, M. S., Perry, A. E., and Cantwell, B. J. "A general classification of three-dimensional flow fields," *Physics of Fluids A: Fluid Dynamics* Vol. 2, No. 5, 1990, pp. 765-777.
- [74] M Tobak, a., and Peake, D. J. "Topology of Three-Dimensional Separated Flows," *Annual Review of Fluid Mechanics* Vol. 14, No. 1, 1982, pp. 61-85.
- [75] Vukasinovic, B., Rusak, Z., and Glezer, A. "Dissipative small-scale actuation of a turbulent shear layer," *Journal of Fluid Mechanics* Vol. 656, 2010, pp. 51-81.
- [76] Wellborn, S. R., Okiishi, T. H., and Reichert, B. A. "A study of the compressible flow through a diffusing S-duct," *NASA Technical Report*, No. 19940017118, 1993.
- [77] Towne, A., Schmidt, O. T., and Colonius, T. "Spectral proper orthogonal decomposition and its relationship to dynamic mode decomposition and resolvent analysis," *Journal of Fluid Mechanics* Vol. 825, 2017, pp. 1113-1152.
- [78] Lakebrink, M. T., Mani, M., Rolfe, E., Spyropoulos, J., Philips, D., Bose, S., and Mace, J. L. "Toward Improved Turbulence-Modeling Techniques for Internal-Flow Applications," *2019 Flow Control Conference*. 2019.

- [79] Burrows, T. J., Vukasinovic, B., Glezer, A., Lakebrink, M. T., and Mani, M. "Controlled Flow Dynamics in a Serpentine Diffuser with a Cowl Inlet," *AIAA AVIATION 2020 FORUM*. 2020.
- [80] Woodiga, S. A., and Liu, T. "Skin friction fields on delta wings," *Experiments in Fluids* Vol. 47, No. 6, 2009, p. 897.
- [81] Berson, A., Michard, M., and Blanc-Benon, P. "Vortex identification and tracking in unsteady flows," *Comptes Rendus Mécanique* Vol. 337, No. 2, 2009, pp. 61-67.
- [82] Graftieaux, L., Michard, M., and Grosjean, N. "Combining PIV, POD and vortex identification algorithms for the study of unsteady turbulent swirling flows," *Measurement Science and Technology* Vol. 12, No. 9, 2001, pp. 1422-1429.
- [83] Depardon, S., Lasserre, J. J., Brizzi, L. E., and Borée, J. "Instantaneous skin-friction pattern analysis using automated critical point detection on near-wall PIV data," *Measurement Science and Technology* Vol. 17, No. 7, 2006, pp. 1659-1669.
- [84] Hyndman, R. J. "Computing and Graphing Highest Density Regions," *The American Statistician* Vol. 50, No. 2, 1996, pp. 120-126.
- [85] Burrows, T. J., Vukasinovic, B., and Glezer, A. "Fluidic Control of an Aggressive Offset Diffuser for a Supersonic Inlet," *47th AIAA Fluid Dynamics Conference*. American Institute of Aeronautics and Astronautics, 2017-4304.